# CHARGE-SELECTIVE TRANSPARENT CONDUCTORS FOR SOLUTION-PROCESSED ORGANIC SOLAR CELLS

by

Rowshan Rahmanian

M.Sc., Sharif University of Technology, 2008

A THESIS SUBMITTED IN PARTIAL FULFILLMENT OF

THE REQUIREMENTS FOR THE DEGREE OF

DOCTOR OF PHILOSOPHY

in

THE FACULTY OF GRADUATE AND POSTDOCTORAL STUDIES

(Electrical and Computer Engineering)

THE UNIVERSITY OF BRITISH COLUMBIA

(Vancouver)

June 2017

## Abstract

Organic solar cells (OSCs) become increasingly popular for harvesting solar energy, due to their potential for low-cost manufacturing and mechanical flexibility. As the efficiency of laboratory-scale devices increases, developing materials and processes that would enable low-cost roll-to-roll fabrication of such devices gains increasing research interest. In order to promote OSCs as a viable substitute for silicon-based solar cells, it is necessary to synthesize materials that can offer high performances, roll-to-roll processability, and potential for flexibility, via processes that are scalable, and do not rely heavily on costly fabrication conditions, such as high temperature, vacuum processing, or inert atmospheres.

This research is focused on two related aspects within this goal. The first part of the research concerns the fabrication of highly stretchable transparent conductive electrodes (TCEs) as replacement for conventional indium tin oxide (ITO) TCEs. Sparse meshes of metallized polyacrylonitrile nanofibers (NFs) fabricated via the scalable electrospinnig method are used to realize TCEs with performances comparable to ITO electrodes (sheet resistance, $R_S$, of 155 Ω/□, with transparency, $T$, of 95%) and with unprecedented electromechanical stretchability (only 56% increase in resistance at 100% strain). Furthermore, by incorporating the metallized NFs into matrices of solution-processed, charge-selective layers, composite charge-selective TCEs are fabricated. Annealed at the appropriate temperature, these charge-selective TCEs achieve performances superior to ITO and on a par with the uncoated NF TCEs. Using ZnO as the matrix, electron-selective composite TCEs with $R_S$ = 23 Ω/□ at $T$ = 95% are fabricated. Using $MoO_3$, hole-selective TCEs with $R_S$ = 35.5 Ω/□ at $T$ = 94% are obtained. The second part of the research, involves the fabrication of OSCs using a scalable, low-temperature spray-coating

process in air. By employing an accelerated air drying post-deposition stage, we were able to achieve large-area pinhole-free coatings of P3HT:PCBM layers with sub-nanometer surface roughness, through single-pass spray-coating at 25 °C substrate temperature. OSCs fabricated in air through this process, achieve power conversion efficiencies up to 2.57%, comparable to the reference devices fabricated via spin-coating in nitrogen atmosphere. The introduced process is successfully used to fabricate fully-sprayed, as well as large-area OSCs.

## Preface

All the research projects presented in this dissertation are carried out in Flexible Electronics and Energy Lab (FEEL) in the Department of Electrical and Computer Engineering of the University of British Columbia, under the supervision of Dr. Peyman Servati.

Chapter 2 is based on an original idea published in Advanced Energy Materials journal (S. Soltanian, R. Rahmanian, B. Gholamkhass, N. Mohseni Kiasari, F. Ko, P. Servati, '*Highly Stretchable, Sparse, Metallized Nanofiber Webs as Thin, Transferrable Transparent Conductors*', Advanced Energy Materials, Vol. 3, Issue 10, pp. 1332-1337, 2013)[1], for which Dr. Saeid Soltanian is the originator and the primary investigator. The development and optimization of electrospinning and sputtering processes leading to low-sheet resistance, high-optical transmittance transparent conductors have been carried out by Dr. S. Soltanian. The study of the effects of post-fabrication thermal annealing on improving the sheet resistance and optical transmittance of the metallized nanofibers has been conducted by the author. In addition, the author has been responsible for the fabrication and characterization of mechanically stretchable transparent conductors based on the material introduced in [1], as well as for the analysis of the performance based on microstructural characterization of the nanofibers. Dr. B. Gholamkhass and Mr. N. Mohseni Kiasari have been responsible for the fabrication and characterization of organic solar cells based on the introduced transparent conductive electrode (TCE). Dr. P. Servati and Dr. F. Ko have supervised the research throughout various experimental, analysis and publication stages. The author was responsible for preparing the sections of the manuscript comprising the abstract, the introduction, and the discussion of the electromechanical response of the stretchable TCEs with reference to the material properties and

microstructural observations, including the discussion of the performance in comparison with the relevant literature. The experimental section as well as the discussions on the characterization of individual NFs was written by Dr. S. Soltanian. The section concerning the fabrication and characterization of organic solar cells using the introduced TCE was written by Mr. N. Mohseni Kiasari and Dr. B. Gholamkhass. All the authors were involved in the revision of the manuscript for publication, under the supervision of Dr. P. Servati.

Chapter 3 is based upon the further extension of the idea presented in Chapter 2, into the development of charge-selective transparent electrodes. The author has been the lead investigator and responsible for the design and implementation of all the experiments, characterizations and analyses of the results. Mr. Parham Pashaie has collaborated in the measurements of optical transmittance and sheet resistance of the transparent electrodes.

Chapter 4 is concerned with the development of the spray-coating process for the fabrication of organic solar cells. The author has been the lead investigator in this project and has had the primary role in the development of the spray-coating and drying process, including the design and implementation of the experiments. Dr. Saeid Soltanian has been a major collaborator in the implementation and improvement of the process at various stages of this project. Ms. Zenan Jiang has collaborated in the fabrication and characterization of the solar cells, including the substrate preparation, design and implementation of current-voltage measurements, and analysis of the performance for the devices fabricated on large substrates. Mr. Yan Wang has collaborated in substrate preparations, atomic force microscopy (AFM) of the spray-coated films, and current-voltage measurements of the solar cells. He and Ms. Jiang have also been responsible for the design and fabrication of the device holder and adaptation of the measurement setup for current-voltage measurements of large-area devices. Spray-coating

experiments as well as a part of thin film characterizations have been carried out using the facilities at the 4DLabs in Simon Fraser University.

## Publications and Presentations

**Journal Papers:**

- S. Soltanian, R. Rahmanian, B. Gholamkhass, N. Mohseni Kiasari, F. Ko, P. Servati, '*Highly Stretchable, Sparse, Metallized Nanofiber Webs as Thin, Transferrable Transparent Conductors*', Advanced Energy Materials, Vol. 3, Issue 10, pp. 1332-1337, 2013

**Conference Presentations:**

- R. Rahmanian, S. Soltanian, P. Servati, '*Low-roughness, Charge-selective Nanofibrous Transparent Conductors for Organic Solar Cells*', MRS Spring 2015 Meeting, San Fransisco, USA, 2015
- R. Rahmanian, S. Soltanian, P. Servati, '*Nanostructured Transparent Conductors on Pre-stretched Elastomer Substrates for Stretchable Solar Cells*', MRS Spring 2013 Meeting, San Fransisco, USA, 2013
- R. Rahmanian, S. Soltanian, B. Gholamkhass, P. Servati, '*Nanostructured Materials as Flexible Transparent Conductors*', 17th Annual PCAMM Meeting, Vancouver, BC, Canada, 2012

# Table of Contents

## List of Tables

## List of Figures

## List of Abbreviations

| | |
|---|---|
| **AFM** | Atomic Force Microscopy |
| **AM** | Air Mass |
| **CNT** | Carbon Nanotube |
| **CVD** | Chemical Vapor Deposition |
| **DCB** | Dichlorobenzene |
| **DMF** | Dimethylformamide |
| **EQE** | External Quantum Efficiency |
| **FF** | Fill Factor |
| **HOMO** | Highest Occupied Molecular Orbital |
| **IPA** | Isopropyl alcohol |
| **ITO** | Indium tin oxide |
| **LED** | Light-Emitting Diode |
| **LUMO** | Lowest Unoccupied Molecular Orbital |
| **MIM** | Metal-Insulator-Metal |
| **MPP** | Maximum Power Point |
| **NF** | Nanofiber |
| **NP** | Nanoparticle |
| **NW** | Nanowire |
| **OPV** | Organic Photovoltaic |
| **OSC** | Organic Solar Cell |
| **P3HT** | Poly(3-hexylthiphene) |

| | |
|---|---|
| **PAN** | Polyacrylonitrile |
| **PCBM** | Phenyl-C61-butyric acid methyl ester |
| **PCE** | Power Conversion Efficiency |
| **PDMS** | Polydimethylsiloxane |
| **PEDOT** | Poly(3,4-ethylenedioxylenethiophene) |
| **PSS** | Polystyrene sulfonic acid |
| **PV** | Photovoltaic |
| **SEM** | Scanning Electron Microscopy |
| **SWNT** | Single-Walled Carbon Nanotube |
| **TC** | Transparent Conductor |
| **TCE** | Transparent Conductive Electrode |
| **TCO** | Transparent Conductive Oxide |
| **TEM** | Transmission Electron Microscopy |

## Acknowledgements

I would like to express my most sincere gratitude to my supervisor, Dr. Peyman Servati who has provided me with more than scientific advice throughout various stages of my research. His insightful guidance, supportive patience, and empathic approach has helped me to see beyond what I used to see, and encouraged me to be beyond what I used to be.

I would like to express an inexpressible indebtedness to Dr. Saeid Soltanian, without whom neither this research, nor I as a researcher, would have been where we are now. He has been a mentor, a dear friend, and an inimitable model of academic dedication.

I also take this opportunity to offer my deepest appreciation to Drs. Frank Ko, John Madden, and Michael Wolf, the members of my dissertation committee, who have provided me with their invaluable feedback and support over the course of this research.

I hereby acknowledge the financial support provided for this work by the Peter Wall Institute for Advanced Studies at UBC and Dr. Reza Nouri. In addition, I would like to thank all my colleagues and collaborators who have contributed to various aspects of this work. I owe a special thanks to Dr. Bobak Gholamkhass for his expertise and advice at various junctures of this research, with which he has been always generous. I would like to thank my friends and colleagues, Ms. Zenan Jiang, Mr. Yan Wang, Dr. Amir Servati, Mr. Nima Mohseni Kiasari, as well as all the previous and present members of the Flexible Electronics and Energy Lab, whose help and friendship has been an inseparable part of my work.

Finally, I would like to thank my sister, Ms. Nazli Rahmanian, who has been my part-time professional adviser and full-time spiritual adviser for a period including, but not limited to, the duration of my doctoral program.

## Dedication

*To my parents, and to my sister, whose love and support is beyond a dedication.*

# Chapter 1: Introduction

## 1.1 Organic Solar Cells

### 1.1.1 Introduction

As the evidence for climate change continues to build, the need to find more environmentally-friendly ways to generate, transport, and store electricity becomes of increasing importance[2]. Harnessing solar energy is one of the most promising ways to tackle today's energy issues. Although the present dominant photovoltaic (PV) technology is based on inorganic materials, high material and manufacturing costs limit its wide acceptance. Intensive research has been conducted towards the development of low-cost PV technologies, which include emerging technologies such as dye-sensitized, perovskite, quantum dot, and organic solar cells[3, 4]. Organic photovoltaic (OPV) devices are one of the promising candidates due to the ease of processing, low cost, and mechanical flexibility they offer[5-7]. The cheap technology already well developed for plastic thin film applications can be adapted for low-cost fabrication of organic solar cells, and the mechanical flexibility offered by organic materials is crucial for emerging wearable and stretchable applications as well as architectural integration onto curved surfaces[6, 8]. Organic solar cells have reached confirmed power conversion efficiencies of over $11.2 \pm 0.3\%$, which is on a par with the latest dye-sensitized solar cells ($11.9 \pm 0.4\%$), and exceeds those of amorphous silicon ($10.2 \pm 0.2\%$) [3].

Interest in solution-processed organic solar cells (OSCs) is mounting as laboratory-based polymer:fullerene bulk heterojunction devices attain higher efficiencies. These high-performance devices are often obtained for small cell areas and rely on deposition techniques, such as spin coating[9] which involves a considerable waste of materials and is not scalable[9,

10]. Therefore, materials and manufacturing processes need to be developed, which can not only scale up the laboratory-scale devices without sacrificing performances but also minimize the manufacturing cost [7].

The goal of the present research is to develop novel materials and fabrication processes for organic solar cells, which offer high-performance, low-cost, and scalable alternatives to the materials and processes currently dominating the field of OPV devices. Within this goal, the research is focused on two objectives. The first is to develop high-performance, flexible and scalable transparent conductive electrodes (TCEs) as replacements for indium tin oxide TCEs. The second part of the research aims to develop a low-cost, low material consumption and scalable process for the deposition of organic solar cells, through developing a low-temperature spray-coating process.

In this chapter, fundamental working principles, materials and fabrication processes of organic solar cells will be reviewed.

### 1.1.2 Working Principles

Converting light into electric current in an organic photovoltaic cell is accomplished by four consecutive steps: (i) Absorption of a photon leading to the formation of an excited state, the electron-hole pair (exciton). (ii) Exciton diffusion to a region, where (iii) the charge separation occurs. (iv) Finally, charge transport to the anode (holes) and cathode (electrons), to supply a direct current for the consumer load.

The potential energy stored within one pair of separated positive and negative charges is equivalent to the difference in their respective quasi-Fermi levels, or in other words it corresponds to the difference in the electrochemical potentials[11]. The larger the quasi-Fermi

level splitting remains during charge transport through the interfaces at the contacts, the larger will be the photovoltage.

Though for ideal (ohmic) contacts no loss is expected, energy level offsets at non-ideal contacts can lead to a decrease in the photovoltage. The electric current that a photovoltaic solar cell delivers corresponds to the number of created charges that are collected at the electrodes. This number depends on the fraction of photons absorbed ($\eta_{abs}$), the fraction of electron-hole pairs that are dissociated ($\eta_{diss}$), and finally the fraction of separated charges that reach the electrodes ($\eta_{out}$) determining the overall photocurrent efficiency ($\eta_j$)

$$\eta_j = \eta_{abs} \times \eta_{diss} \times \eta_{out} \qquad \textbf{(Equation 1.1)}$$

The fraction of absorbed photons is a function of the absorption spectrum, the absorption coefficient, the absorbing layer thickness, and of internal multiple reflections at, for example, metallic electrodes. The fraction of dissociated electron-hole pairs on the other hand is determined by whether they diffuse into a region where charge separation occurs and on the charge separation probability there[12]. To reach the electrodes, the charge carriers need a net driving force, which generally results from a gradient in the electrochemical potentials of electrons and holes. Two "forces" contribute to this: internal electric fields and concentration gradients of the respective charge carrier species. The first leads to a field-induced drift and the other to a diffusion current. Though a detailed analysis requires the knowledge of charge carrier distributions over film depth, thin film devices (<100 nm) are mostly field drift dominated, whereas thick devices, having effective screening of the electrical fields inside the bulk, are more dominated by the diffusion of charge carriers in concentration gradients at the selective contacts.

To understand the rectifying behavior of an intrinsic semiconductor device in the dark, the MIM (metal-insulator-metal) model[13] is useful. In Figure 1.1, a semiconductor, sandwiched between two metal electrodes with different work functions is depicted for several situations. The metals are represented by their Fermi levels, whereas for the semiconductor the valence and conduction bands, corresponding to the molecular LUMO (lowest unoccupied molecular orbital) and the HOMO (highest occupied molecular orbital) levels, are shown. In Figure 1.1(a), there is no voltage applied (short-circuit conditions). Hence, there is no net current flowing in the dark, and the built-in electric field resulting from the difference in the metals' work functions is evenly distributed throughout the device. Under illumination, separated charge carriers can drift in this electric field to the respective contacts: the electrons move to the lower work function metal and the holes to the opposite. The device then works as a solar cell. In Figure 1.1(b), the situation is shown for open circuit conditions, also known as "flat band condition." The applied voltage is called the open circuit voltage $V_{OC}$, which corresponds in this case to the difference in the metals' work functions and balances the built-in field. As there is no net driving force for the charge carriers, the current is zero. In Figure 1.1(c) the situation is shown for an applied reverse bias and only a very small injected dark current $j_0$ can flow. Under illumination, the generated charge carriers drift under strong electric fields to the respective electrodes and the diode works as a photodetector. If a forward bias larger than the open circuit voltage is applied (Figure 1.1(d)), the contacts can efficiently inject charges into the semiconductor. If these can recombine radiatively, the device works as a light-emitting diode (LED). The asymmetric diode behavior results from the different injection of the two metals into the HOMO and LUMO levels, respectively, which depends exponentially on the energy barrier between them[14].

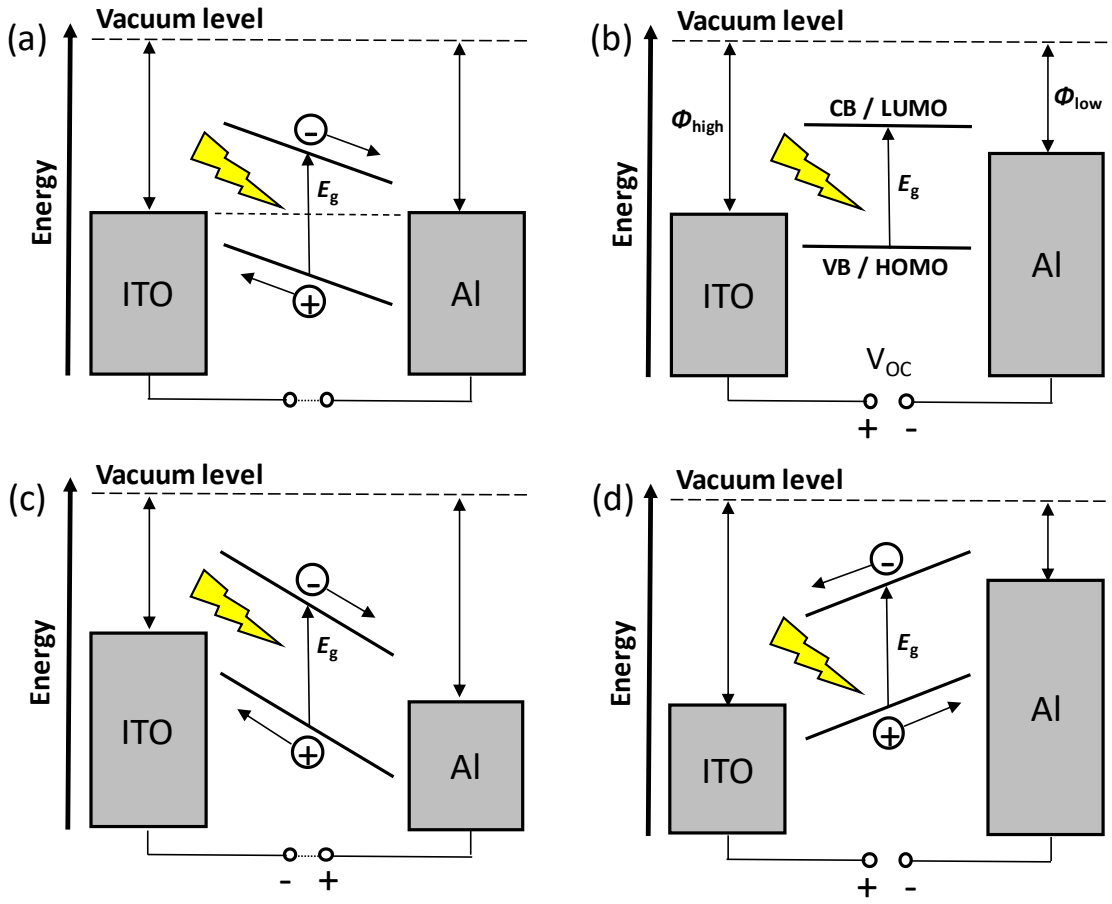


**Figure 1.1:** Metal-insulator-metal (MIM) picture of organic diode device function. (a) Closed circuit condition: under illumination photogenerated charges drift toward the contacts. (b) Flat band or open circuit condition: the current becomes zero. (c) Reversed bias: photogenerated charges drift in strong electric fields, the diode operates as a photodetector. (d) Forward bias larger than $V_{OC}$: the injection increases and the diode opens up.

In Figure 1.2, the current-voltage characteristics are shown for a solar cell in the dark and under illumination. In the dark, there is almost no current flowing, until the contacts start to inject heavily at forward bias for voltages larger than the open circuit voltage. Under illumination, the current flows in the opposite direction than the injected currents. At (a) the maximum generated photocurrent flows under short-circuit conditions; at (b) the photogenerated

current is balanced to zero (flat band condition). Between (a) and (b), in the fourth quadrant, the device generates power (i.e., current × voltage). At a certain point, denoted as maximum power point (MPP), the product between current and voltage and hence the power output is largest. To determine the efficiency of a solar cell, this power needs to be compared with the incident light intensity. Generally, the fill factor (*FF*) is calculated as $FF = V_{MPP} \times I_{MPP} / (V_{OC} \times I_{SC})$ to denote the part of the product of $V_{OC}$ and $I_{SC}$ that can be used. The power conversion efficiency can be written as

$$\eta_{POWER} = \frac{P_{OUT}}{P_{IN}} = \frac{I_{MPP} \cdot V_{MPP}}{P_{IN}} = \frac{FF \cdot I_{SC} \cdot V_{OC}}{P_{IN}} \qquad \textbf{(Equation 1.2)}$$

Generally, the *I-V* characteristics of a photovoltaic device can be described by

$$I = I_0 \cdot \left\{ \exp\left( \frac{e}{nkT} (U - IR_S) \right) - 1 \right\} + \frac{U - IR_S}{R_{SH}} - I_{PH} \qquad \textbf{(Equation 1.3)}$$

where $I_0$ is the dark current, *e* the elementary charge, *n* the diode ideality factor, *U* the applied voltage, $R_S$ the series, $R_{SH}$ the shunt resistance, and $I_{PH}$ is the photocurrent. The corresponding equivalent circuit is depicted in Figure 1.3. For a high *FF*, two things are required: (i) that the shunt resistance is very large to prevent leakage currents and (ii) that the series resistance is very low to get a sharp rise in the forward current. The series resistance simply adds up from all series resistance contributions in the device, that is, from bulk transport, from interface transfer and from transport through the contacts[15].

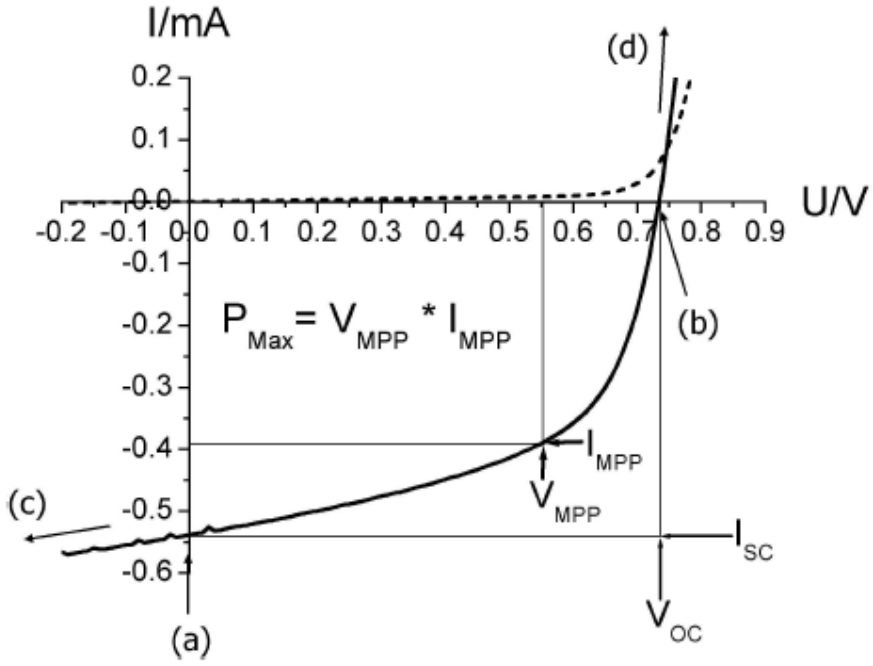


**Figure 1.2:** Current-voltage (*I*-*V*) curves of an organic solar cell (dark, dashed; illuminated, full line). The characteristic intersections with the abscissa and the ordinate are the open circuit voltage ($V_{OC}$) and the short-circuit current ($I_{SC}$), respectively. The largest power output ($P_{Max}$) is determined by the point where the product of voltage and current is maximized. Division of $P_{Max}$ by the product of $I_{SC}$ and $V_{OC}$ yields the fill factor *FF*. The letters (a–d) correspond to Figure 1.1[15].

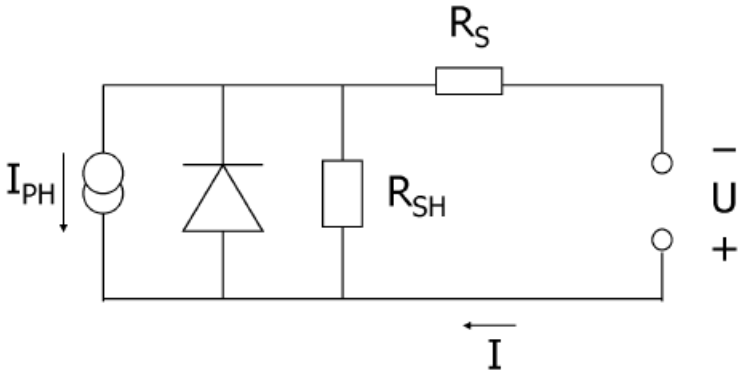


**Figure 1.3:** Equivalent circuit for a solar cell, described by Equation 1.3[15].

### 1.1.3 Device Architectures

As the exciton binding energy in organic semiconductors is generally large (0.1–1 eV) compared to silicon[11], the built-in electric fields (on the order of $10^6 – 10^7$ V/m) are usually not high enough to dissociate the excitons directly. Hence, a process should be introduced that efficiently separates electron-hole pairs. This is possible at the sharp drop of potential at donor–acceptor (D-A) as well as semiconductor–metal interfaces. In the following, the most basic device architectures are reviewed, and the individual advantages and disadvantages are discussed. Their main difference lies in the exciton dissociation or charge separation process, which occurs at different locations within the photoactive layer. A second issue is the consecutive charge transport to the electrodes[15].

#### 1.1.3.1 Single-Layer Organic Solar Cells

The first organic solar cells were based on single thermally evaporated molecular organic layers sandwiched between two metal electrodes of different work functions. The rectifying behavior of these devices can be explained by the MIM-model (for insulators) or by the formation of a Schottky barrier (for doped materials) between the metal with the lower work function and the p-type organic layer[13]. In Figure 1.4, the situation is depicted for the case of a Schottky junction at the aluminum contact. Close to the contact, in the depletion region *W*, a resulting band bending from the Schottky contact is depicted. This corresponds to an electric field in which excitons can be dissociated. Because the exciton diffusion length for most organic solar cell materials is below 20 nm, only those excitons generated in a small region within $\leq 20$ nm from the contacts contribute to the photocurrent[15].

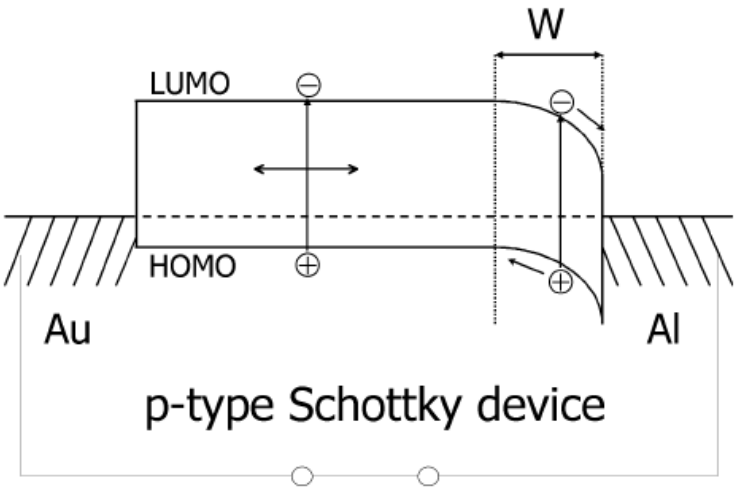


**Figure 1.4:** Schematic of a single layer device with a Schottky contact at the aluminum contact. Photogenerated excitons can only be dissociated in a thin depletion layer *W*, and thus the device is exciton diffusion limited[15].

### 1.1.3.2 Bi-Layer Heterojunctions

In a bilayer device, a donor and an acceptor material are stacked together with a planar interface where the charge separation occurs, mediated by a large potential drop between donor and acceptor. The bilayer is sandwiched between two electrodes matching the donor HOMO and the acceptor LUMO, for efficient extraction of the corresponding charge carriers. The bilayer device structure is schematically depicted in Figure 1.5, neglecting all kinds of possible band bending due to energy level alignments. Though the formation of a classical p/n-junction requires doped semiconductors with free charge carriers to form the electric field in the depleted region, the charge transfer in bilayer heterojunction between undoped donor and acceptor materials is due to the differences in the ionization potential and electron affinity of the adjacent materials. Upon photon absorption in the donor D, the electron is excited from the HOMO to the LUMO. A big advantage over the single layer device is the monomolecular charge transport.

After the excitons are dissociated at the materials interface, the electrons travel within the n-type acceptor, and the holes travel within the p-type donor material. Hence, holes and electrons are effectively separated from each other, and thus charge recombination is greatly reduced [15].

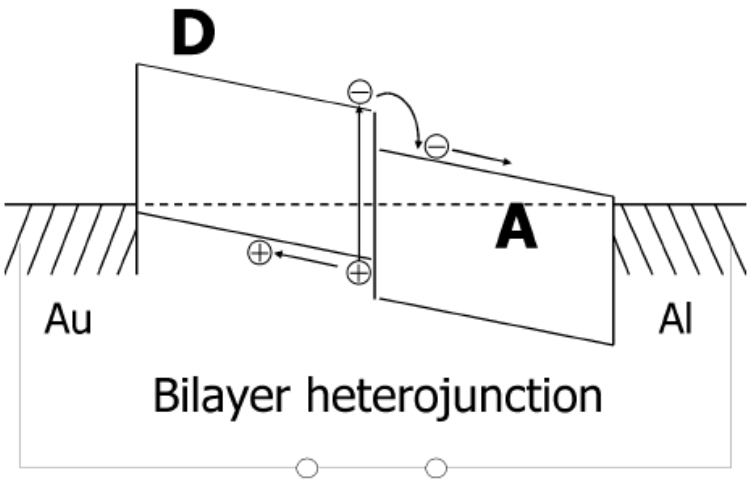


**Figure 1.5:** Schematic of a bilayer heterojunction device. The donor (D) contacts the higher and the acceptor (A) the lower work function metal, to achieve good hole and electron collection, respectively. Photogenerated excitons can only be dissociated in a thin layer at the heterojunction and thus the device is exciton diffusion limited[15].

#### 1.1.3.3 Bulk Heterojunctions

The essence of the bulk heterojunction is to intimately mix the donor and acceptor components in a bulk volume so that each donor–acceptor interface is within a distance less than the exciton diffusion length of each absorbing site. In Figure 1.6, the situation is schematically shown for a bulk heterojunction device, again neglecting energy level alignments and interface effects. The bulk heterojunction device is similar to the bilayer device with respect to the D-A concept, but it exhibits a largely increased interfacial area where charge separation occurs. Due

to the interface being dispersed throughout the bulk, no loss due to too small exciton diffusion lengths is expected, as ideally all excitons will be dissociated within their lifetime. Though in the bilayer heterojunction the donor and acceptor phase contact the anode and cathode selectively, the bulk heterojunction requires percolated pathways for the hole and electron transporting phases to the contacts. In other words, the donor and acceptor phases must form a bicontinuous and interpenetrating network. Therefore, the bulk heterojunction devices are much more sensitive to the nanoscale morphology in the blend.

Generally, bulk heterojunctions may be achieved by co-deposition of donor and acceptor pigments or solution casting of either polymer/polymer, polymer/molecule, or molecule/molecule donor–acceptor blends. The most common devices today are based on solution cast poly(3-hexylthiphene):phenyl-C61-butyric acid methyl ester (P3HT:PCBM) blends yielding above 3.5% power conversion efficiency under AM 1.5[15, 16].

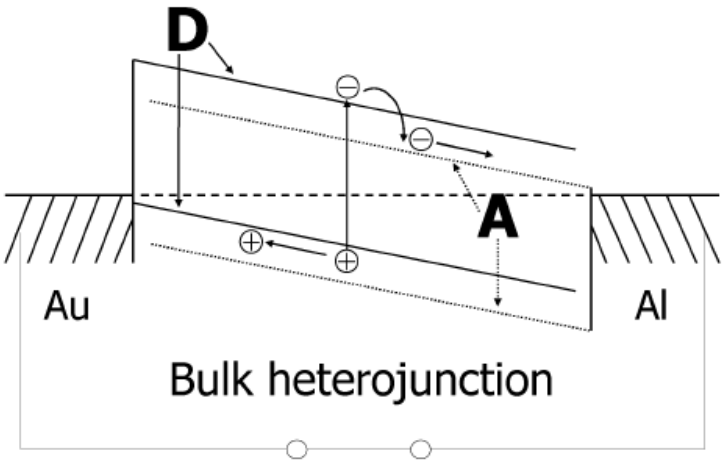


**Figure 1.6:** Schematic of a bulk heterojunction device. The donor (D) is blended with the acceptor (A) throughout the whole film. Thus, photogenerated excitons can be dissociated into charges at any place[15].

Bulk heterojunction OSCs are made with two structures. The 'normal' device structure usually consists of poly(3,4-ethylenedioxylenethiophene):polystyrene sulfonic acid (PEDOT:PSS) on indium tin oxide (ITO) glass as the anode and a low-work-function metal (usually, Al) as the cathode. A polymer−fullerene composite sandwiched between the electrodes is the active layer. The normal structure has a few drawbacks, such as the instability of PEDOT:PSS on ITO, as well as the top Al electrode, which degrade the performance of devices. To alleviate this problem, an 'inverted' device structure can be used. Here, the charge-collecting nature of the electrodes is reversed, with the ITO electrode as the cathode and a high-work-function metal (typically, Au or Ag) as the anode. Although more stable and potentially less costly, inverted OSCs generally have lower efficiencies compared with a normal device. Therefore, there is ongoing research to improve the inverted OSCs by implementation of new materials and exploration of new device structures[17-19]. Figure 1.7 compares the device structure and energy band diagrams of normal and inverted devices made using a P3HT:THBT (poly(3-hexylthiophene-co-benzothiadiazole)) active layer[20].

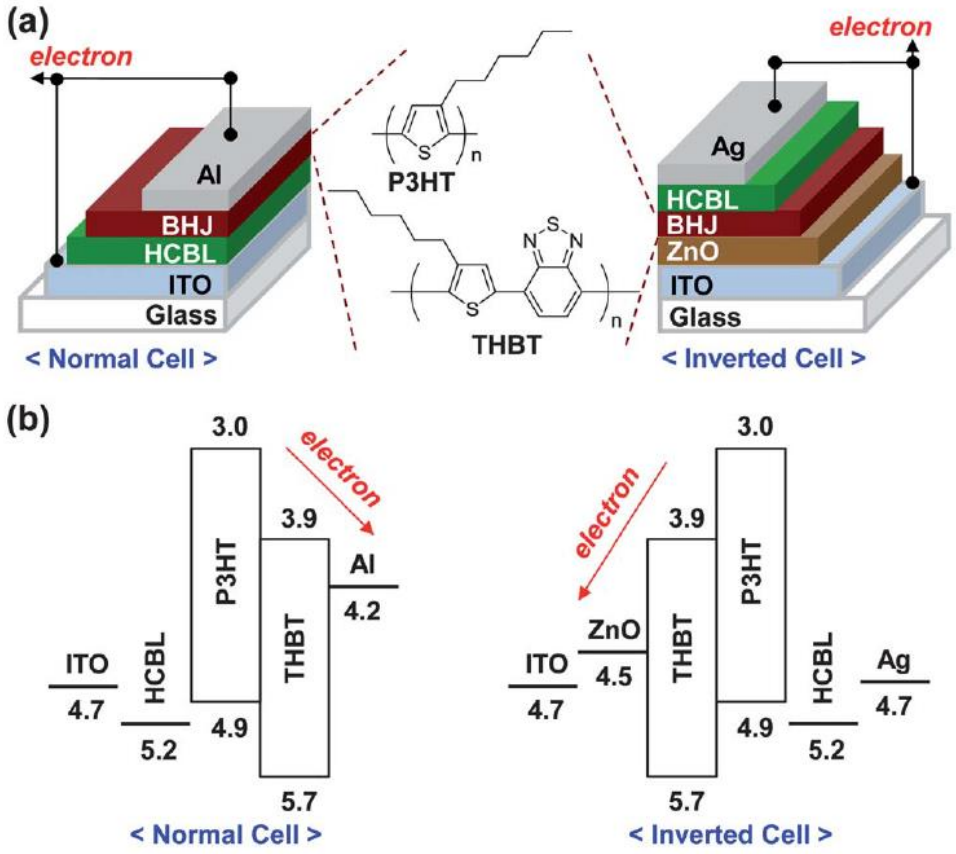


**Figure 1.7:** (a) Schematic illustration of normal and inverted polymer solar cells with the bulk heterojunction (BHJ) films of P3HT and THBT. (b) Flat energy band diagrams for the normal-type and inverted-type of the devices in (a). 'HCBL' denotes the hole-collecting buffer layer of PEDOT:PSS [20].

Figure 1.8 shows the schematic morphology of a bicontinuous interpenetration network, along with light absorption spectra and energy diagram for a typical OSC device with normal structure and P3HT:PCBM bulk heterojunction layer. The chemical structures of these organic materials as well as a number of others will be provided below.

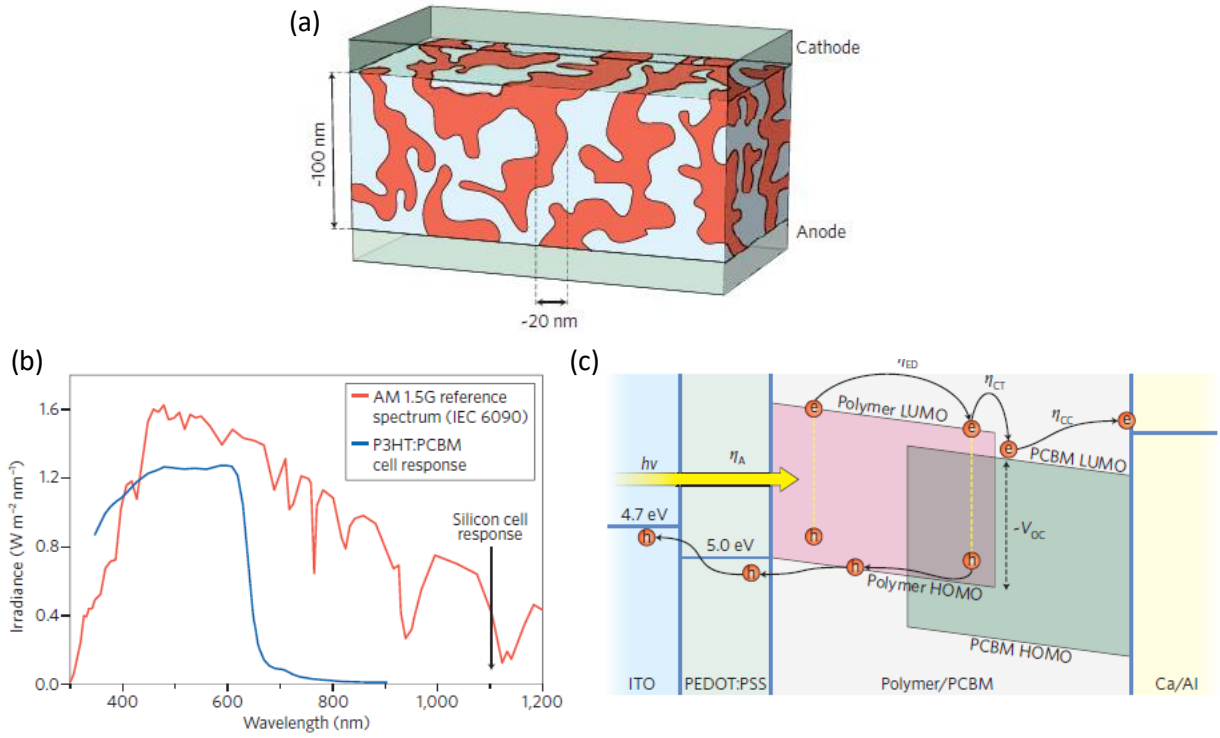


**Figure 1.8:** (a) The operating mechanism of a PSC. (b) Comparison between solar spectrum and the photoresponse of a P3HT:PCBM solar cell. (c) Conceptual morphology model with bicontinuous interpenetration network of the polymer and the acceptor[4].

### 1.1.4 Materials

The development of OSCs has always been accompanied by innovations in materials science. Figure 1.9 shows the chemical structures of some representative materials. One of the earliest OSC polymers is poly[2-methoxy-5-(2'-ethylhexyloxy)-p-phenylene vinylene] (MEH-PPV), which was developed by Wudl et al.[21]. Wudl also invented one of the most important fullerene derivatives, PCBM[22], which represents a milestone in the development of PSC acceptors and is still widely used today. In 1995, Yu et al. blended MEH-PPV with $C_{60}$ and its derivatives to give the first PSC with a high PCE[23]. This work opened a new era of polymer

materials for use in solar energy conversion. After significant optimization, researchers achieved PCEs of more than 3.0% for PPV-based PSCs[24, 25]. However, further improvement was limited by the relatively low hole mobility and narrow light absorption range. Soluble polythiophenes, especially poly(3-hexylthiphene) (P3HT)[16], with their higher hole mobility[26] and therefore a broader spectrum coverage than MEH-PPV, have become a standard for PSC materials in the recent years[27]. Morphology optimization[28] has provided PCEs of 4–5%, thus attracting worldwide interests in PSCs.

Many more high-performance polymers have been developed in recent years. One of these is poly[2,6-(4,4-bis-(2-ethylhexyl)-4H-cyclopenta[2,1-b;3,4-b']dithiophene)-alt-4,7-(2,1,3-benzothiadiazole)] (PCPDTBT), a low-bandgap polymer whose absorption extends up to 900 nm. PSCs made from this polymer have showed an initial efficiency of around 3%[29]. However, by incorporating alkanedithiol additives, researchers were able to achieve efficiencies of around 5.5%[30]. Leclerc et al. developed poly[N-9''-hepta-decanyl-2,7-carbazole-alt-5,5-(4',7'-di-2-thienyl-2',1',3'-benzothiadiazole)] (PCDTBT), which gave a PCE of 3.6%[31]. More recently, researchers increased this to 6.1% by incorporating a titanium oxide ($TiO_x$) layer as an optical spacer[32]. The most impressive high-performance polymers are those designed by Yu et al., which are composed of thieno[3,4-b]-thiophene (TT) and benzodithiophene (BDT) alternating units[33, 34]. This was the first polymer donor system capable of reaching PCEs of 7–8%. Following this work, PCEs of more than 7% were frequently reported with either new materials or novel device optimization techniques[35-38]. Research is ongoing in developing new donor and acceptor organic materials for high-efficiency OSCs[4]. The most established polymer:fullerene blend currently used in solution-processed bulk heterojunction solar cells is P3HT:PCBM, which will be the basis of the devices demonstrated in the present research.

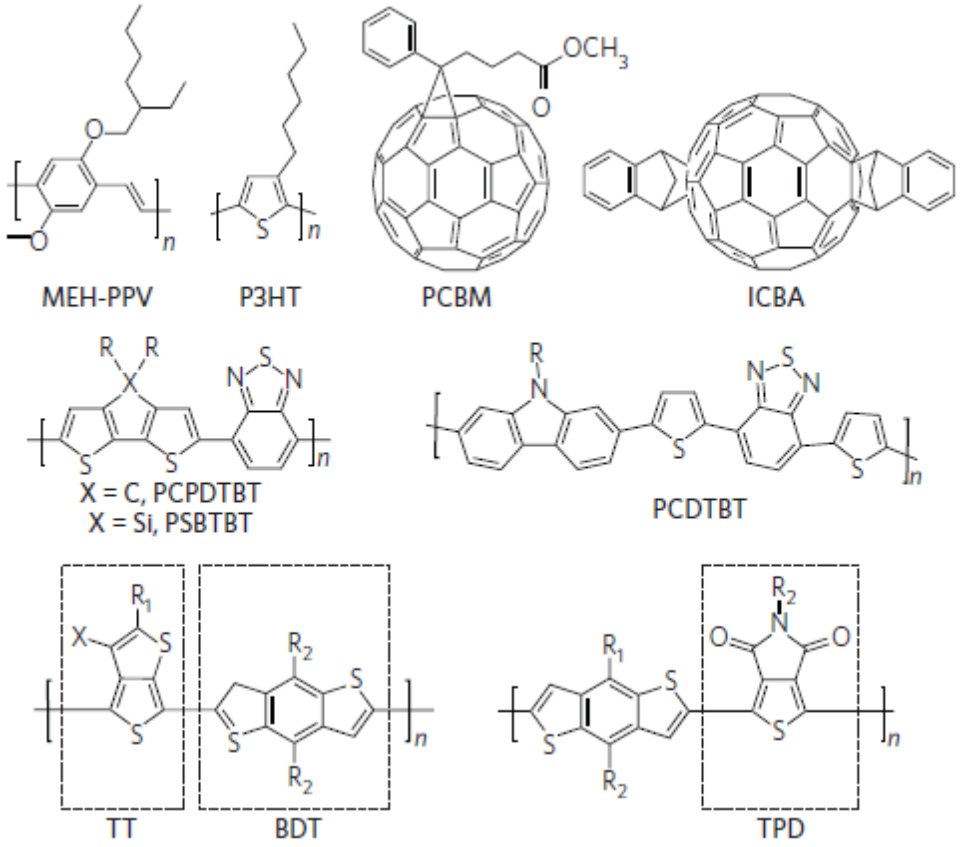


**Figure 1.9:** Chemical structures of representative donor and acceptor molecules used in PSCs[4].

### 1.1.5 Solution-Processed Organic Solar Cells

The two major classes of thin film fabrication techniques for OSCs are thermal evaporation and solution processing. While for evaporation thermal stability is required, materials for solution processing need to be soluble. Small molecules may be thermally more stable but less soluble than polymers, where solubility often is achieved by side-chain solubilization. Polymers will decompose under excessive heat and have too large a molar mass for evaporation. Hence for small molecules, evaporation is the best choice, whereas semiconducting polymers are mainly processed from solution. However, less soluble molecules like $C_{60}$ may become soluble

when modified by attaching solubilizing groups (e.g., PCBM) and short polymers or oligomers may also be evaporated[39, 40].

*Evaporation*: To grow films by thermal evaporation, usually a vacuum of $<10^{-5}$ mbar is applied. Thus, the mean free path of the evaporated molecule is longer than the distance between the evaporation source and the sample holder. In addition, contaminants like oxygen and water are reduced and can be eliminated further by ultra-high vacuum ($<10^{-9}$ mbar) or evaporation inside a glove box with an inert atmosphere. To create interpenetrating donor-acceptor networks or to achieve molecular doping, co-evaporation techniques can be applied[39, 41, 42].

*Solution Processing*: Solution processing is an attractive alternative to evaporation for the fabrication of polymer solar cells. Desirable features of solution processing include large-area processability[43], low-cost manufacturing[44], reduced energy payback time[45], and the high power-to-weight ratio[46]. The solution-processing method most commonly used for the fabrication of OSCs is spin-coating. Though advantageous in terms of fabrication accuracy and reproducibility, spin-coating has certain disadvantages, such as considerable waste of material, and in particular, lack of scalability, which limits its application to laboratory-scale fabrication[9, 10]. Recently, other solution processing methods have been used for the fabrication of OSCs, such as screen printing[47], doctor blading[48], inkjet printing[49] and spray-coating[43]. Among these methods, spray-coating is one of the most promising processes the fabrication of OSCs. Apart from the capability for large-area deposition, spray-coating offers several important advantages including lower material consumption, high production speed, high deposition-parameter adjustability[9], compatibility with a wide range of solution properties, and compatibility with various substrates[9, 10]. A more specific literature review of spray-coated OSCs will be discussed in Chapter 4 with regards to the motivations of this research.

## 1.2 Transparent Conductive Electrodes

### 1.2.1 Introduction

Transparent conductive electrodes (TCEs), which transmit light and conduct electrical current simultaneously are of increasing importance as an essential component in photovoltaic devices, as well as touch panels and displays[50-52]. So far, transparent conductive oxides (TCOs) and in particular indium tin oxide (ITO) electrodes have been the most popular TCEs. However, the limited supply of indium, as well as the lack of mechanical flexibility are among the reason that calls for the replacement of ITO electrodes. Various alternative structures and new materials, such as carbon nanotubes, graphene, and metal grids, films, or nanowires, have recently been suggested as candidates to replace ITO[50-52]. This section provides an overview of different types of transparent conductors and the requirements for TCEs.

### 1.2.2 Transparent Conductive Oxides

Due to their intrinsic transparency and low resistivity, transparent conducive oxides have dominated the field of transparent conductors for decades. Of the different possible TCO materials available, only $SnO_2$:X, ITO and ZnO:X (where 'X' is a dopant) have gained widespread attention, owing to their bandgap energy of > 3 eV, which allows for applications in the visible and near-ultraviolet spectral range (down to 300 nm), and their low resistivities of around $10^{-3}$ Ω cm or lower. Nowadays, ITO is the TCO material with the lowest resistivity on a commercial scale — of the order of $1–2 \times 10^{-4}$ Ω cm[53]. ITO is used almost exclusively as the transparent electrode in flat-panel displays[54].

Tin oxide doped with fluorine or antimony was the first TCO material used on an industrial scale, specifically for low-emissivity coatings on glass[55]. Today, it is also used as a

transparent electrode, especially in thin-film solar cells based on the absorber materials a-Si:H or CdTe[56]. The resistivity of tin oxide can be as low as $5 \times 10^{-4}$ Ω cm. With respect to its lowest values, ZnO is between ITO and $SnO_2$, with resistivities in the range of $2–4 \times 10^{-4}$ Ω cm. It is also used as a window and contact layer in thin-film solar cells, based on the absorber materials a-Si:H and $Cu(In,Ga)Se(S)_2$[57].

The past three decades have seen incremental improvements with respect to basic TCO properties. More recently, amorphous oxides were also developed as a new class of TCOs[58-61]. Novel amorphous semiconductors based on mixed oxides are particularly unique because their electron mobility is still of the order of 10 $cm^2 V^{-1} s^{-1}$ despite large structural disorders. This is in strong contrast with well-known amorphous semiconductors such as a-Si:H, which exhibit mobilities of only 0.1 $cm^2 V^{-1} s^{-1}$ or less. Other remarkable properties of amorphous TCOs are their high temperature stability, flexibility and potential for depositing films at low substrate temperatures (< 200 °C), thus allowing the use of flexible plastic substrates.

Another new material is doped $TiO_2$, which was introduced as a thin-film material by the Hasegawa group in 2005[62]. The researchers achieved resistivities of the order of $5 \times 10^{-4}$ Ω cm for epitaxially grown niobium- or tantalum-doped $TiO_2$. This could be reached only at relatively high substrate temperatures of more than 300 °C, which is a drawback for many practical purposes. A big advantage of doped $TiO_2$ is its excellent chemical stability, which can be exploited for use in transparent and conductive protection layers[63].

### 1.2.3 Replacements for Indium Tin Oxide

Around 2005, in parallel with the exponential rise of the flat-panel display industry, researchers began searching for alternatives to thin metal and ITO films[64]. Other fields of interest for these alternative TCE materials are solid-state lighting and cheap thin-film solar cells. These new research efforts were partly driven by the increasing price of indium, as the main component of ITO, which would make it a less viable option for future TCEs. Another reason is the quest for sheet resistances below 5 $\Omega\ \square^{-1}$, especially for large displays and large-area solid-state lighting[65]. The third motivation for seeking alternative TC materials is ITO's lack of mechanical flexibility, which calls for novel materials and structures which can be used for emerging flexible and stretchable electronic applications[52, 66].

Potential replacements for ITO are thin metal films combined with suitable oxidic films such as ITO, ZnO or $SnO_2$ [67]. Another alternative is the use of periodic metal grids or irregular metal nanowire networks, which are usually prepared by the lithography of metal films or direct deposition of metal nanowires from solutions[68-70]. Researchers have also replaced metal nanowires with single-walled carbon nanotubes. Although periodic metal grids look quite promising[71], nanowire and nanotube networks suffer from the intrinsic problem of percolation and large contact resistances between the many wires or tubes[70, 72]. Percolation theory for one-dimensional wires predicts a threshold areal wire density of $N_{th} = (4.236/L)^2/\pi$ ($L$ being the wire length), after which the onset of the conductivity occurs[73]. A highly transparent and conductive wire network requires long, thin nanowires with smooth surfaces, which imposes significant challenges on finding cheap synthesis and deposition techniques. Other challenges that need to be solved include long-term stability; high contact resistances between the metal grids and the active electronic materials; high uniformity; and large-scale fabrication.

A rapidly emerging subclass of TCE materials is based on carbon; on carbon nanotube networks[74], single- and few-layer graphene films[52], and conductive polymer films[75]. Single layers of graphene[76] exhibit the astounding properties of a two-dimensional electron gas at room temperature — that is, a very high electron mobility (up to around $5 \times 10^3$ cm$^2$ V$^{-1}$ s$^{-1}$) combined with high transmittance ($T \approx 1 - \pi\alpha = 97.7\%$, where $\alpha$ is the fine structure constant) — and have therefore attracted significant interest in both fundamental research and industry[76]. There are great expectations for graphene to be "an ideal photonic and optoelectronic material". For instance, the transmittance of single- (SLG) or few-layer graphene would be higher than that of ITO, which is today's 'best' TCO material. The minimum resistivity of undoped ($n_\square \approx 0$ cm$^{-2}$) graphene is $R_{SLG} \approx 6$ kΩ $\square^{-1}$, which is much higher than typical sheet resistances for TCO layers. However, real SLG samples are always doped by defects, the formation of graphene oxide or by other dopants, leading to carrier densities of $n_\square = 10^{12}$–$10^{13}$ cm$^{-2}$, which, with typical mobilities of $10^3$ to $2 \times 10^4$ cm$^2$ V$^{-1}$ s$^{-1}$, leads to sheet resistances comparable to that of TCO and metal films. For instance, Bae et al. demonstrated $R_{SLG} \approx 30$ Ω $\square^{-1}$ for graphene layers grown by chemical vapor deposition and layer-transferred to a polymer foil, which provided a transmittance of $T \approx 90\%$[52]. This gives graphene the potential for use in many optoelectronic devices, including photovoltaic cells, light-emitting devices, photodetectors, touch screens and lasers[77].

Although conductive polymers have been known for more than 30 years[78, 79], only over the past few years have they been investigated as TCEs for use in organic light-emitting diodes and thin-film solar cells. Recently, Kim et al. showed that PEDOT:PSS, which normally exhibits a resistivity of more than 0.1 Ω cm, can be treated in such a way as to achieve resistivities as low as $7 \times 10^{-4}$ Ω cm [75]. Previously, owing to its high resistivity and high work function, PEDOT

was used as an antistatic coating and as a hole-injection layer in organic devices, as mentioned in Section 1.1.3.3. Using PEDOT:PSS films, researchers demonstrated organic thin-film solar cells with efficiencies comparable to that of solar cells with ITO electrodes[63].

### 1.2.4 Requirements for Transparent Conductive Electrodes

The crucial requirements for a transparent electrode are high conductivity and high transparency — properties that are somewhat contradicting. From a practical point of view, these materials must be colorless and cheap to produce, preferably from non-toxic materials. For applications in flexible and wearable devices or on geometrically curved surfaces such as car windows and consumer electronics, these electrodes should also be flexible. Another important requirement in electronic devices is the formation of tailored interfaces between the TCE and the active electronic material, which is normally a typical semiconductor.

From a physical point of view, a material with a high conductivity $\sigma$ must have a high carrier concentration $n$ (electrons) of $p$ (holes) and/or a sufficiently high carrier mobility $\mu_{n,p}$ [80], giving

$$\sigma = en\mu_{\mathrm{n,p}} \quad \textbf{(Equation 1.4)}$$

where $e$ is the elementary charge. Owing to their small effective mass, electrons are much more mobile than ions and holes, which means good conductors exhibit electrons as charge carriers. Equation 1.5 is symmetrical in carrier concentration $n$ and mobility $\mu$; both quantities could in principle be increased to maximize the conductivity $\sigma$. However, the carrier concentration is limited by the absorption of light by free carriers (electrons). In the electrical field of a light

wave, the carrier gas (electrons) forms a collective plasma excitation (a 'plasmon')[81]. Classical Drude theory gives the plasma frequency as:

$$\omega_p = \sqrt{\frac{ne^2}{m^* \varepsilon_r \varepsilon_0}} \qquad \textbf{(Equation 1.6)}$$

where $m^*$ is the effective mass of the carriers and $\varepsilon_r\varepsilon_0$ is the permittivity of the material. The energy of the plasmon and its wavelength are given by $E_P = c\omega_P$ and $\lambda_P = 2\pi h^-/\omega_P$, respectively, where $c$ is the speed of light.

With respect to the carrier concentration, which determines both electrical (Equation 1.5) and optical (Equation 1.6) properties, three groups of TCE materials can be classified (Table 1.2): metals that exhibit very high carrier concentrations ($n >> 10^{22}$ cm$^{-3}$), medium mobilities and plasma wavelengths in the deep-ultraviolet ($\lambda_P < 0.2$ μm); oxide semiconductors with high carrier concentrations ($n \approx 10^{21}$ cm$^{-3}$), high mobilities and plasma wavelengths in the near-infrared ($\lambda_P \approx 1$ μm); and carbon-based materials with relatively low carrier concentrations ($n \approx 10^{20}$ cm$^{-3}$), low mobilities and plasma wavelengths in the mid-infrared ($\lambda_P > 1$ μm).

Table 1.2 lists typical electrical parameters and plasma wavelengths for these three material groups. Graphene is an exceptional TCE material owing to its outstanding two-dimensional electron gas at room temperature, leading to high mobility at low carrier concentrations ($n_\square \approx 10^{12}$ cm$^{-2}$, corresponding to a calculated carrier concentration of $n_G = 3 \times 10^{19}$ cm$^{-3}$ with a layer thickness of $d = 0.3354$ nm [82], which shifts the plasma wavelength to the far-infrared.

The best strategy for optimizing TCE materials is therefore to limit the carrier concentration and increase the carrier mobility. The maximum allowable carrier density depends on the required spectral window of transparency for the TCE layer. For flat-panel displays, the eye luminosity curve defines the requested spectral range, whereas for thin-film solar cells the spectral irradiance from the Sun (under AM1.5 conditions), in combination with the bandgap energy of the absorber material (such as silicon, CdTe or $Cu(In,Ga)Se_2$), sets the spectral limits for the transmittance of the TCE layer (Figure 1.10(a)).

Recently, researchers confirmed the classical Drude model by applying density functional theory calculations of the free carrier absorption (FCA) due to phonon-assisted intraband transitions in the conduction band of $SnO_2$, at least in the spectral range of 500–3,000 nm [83]. The absorptance $A$ is given by $A = nd\sigma_{FCA}(\lambda)$, where $n$ is the electron concentration, $d$ is the thickness of the layer and $\sigma_{FCA}(\lambda)$ is the absorption cross-section by free carriers. $\sigma_{FCA}(\lambda)$ is around $10^{-19}$ cm$^2$ at $\lambda$ = 500 nm but $8 \times 10^{-19}$ cm$^2$ at $\lambda$ = 1,000 nm, giving absorptances of 1% ($\lambda$ = 500 nm) and 8% ($\lambda$ = 1,000 nm) for a film with $n = 10^{21}$ cm$^{-3}$ and a thickness of $d$ = 1 μm.

The very high electron concentrations of metals (>$5 \times 10^{22}$ cm$^{-3}$) bring their plasmon energies into the deep-ultraviolet spectral range, thus endowing them with high absorption in the visible spectral range. Figure 1.10(a) shows spectral transmittance curves for different TCE films. The eye luminosity function and the spectral irradiance from the Sun under AM1.5 conditions are also displayed for comparison.

The Ag nanowire network exhibits a flat spectral transmittance, whereas the TCO/Ag/TCO layer stack shows a narrow spectral transmittance window that is well-fitted to the eye luminosity curve, reaching a maximum transmittance of 90% at around 530 nm.

The single TCO films (ITO, ZnO:Al and $SnO_2$:F) display an average transmittance of around 85% in the range of 400–1,000 nm. The oscillating *T* values are due to optical interference at the two film surfaces/interfaces. At a wavelength of around 1,200 nm, the transmittance of all three TCO films begins to decrease because of free carrier absorption (the 'Drude edge'), which, nevertheless, is well-suited to photovoltaic applications even for silicon and $Cu(In,Ga)Se_2$ absorber layers with bandgap energies of only 1.1 eV.

The dependency of sheet resistance on film thickness is shown in Figure 1.10(b) for different types of TCE layer. The data points mostly follow the inverse proportionality of $R_s = \rho_{film}/d$, which is expected for a thickness-independent resistivity $\rho_{film}$. For comparison, calculated $R_s$ curves for $\rho = 10^{-5}$–$10^{-2}$ Ω cm are also plotted. Graphene films exhibit the lowest resistivities (~$5 \times 10^{-6}$ Ω cm), followed by TCO/Ag/TCO films and Ag nanogrids (~$5 \times 10^{-5}$ Ω cm). The plotted ITO data are somewhat high at $\rho_{ITO} \approx 2$–$5\ 10^{-4}$ Ω cm, which is the lower range attainable by higher film thicknesses. The best ITO films today reach $\rho_{ITO} \approx 10^{-4}$ Ω cm for $d > 100$ nm, which would shift the ITO curve slightly to the left. PEDOT:PSS films and Ag nanowire networks exhibit the highest resistivities.

The challenge in terms of film preparation is to reach the intrinsic limits of the different TCE materials for large-area coating, which has nearly been achieved for TCO materials and TCO/Ag/TCO low-emissivity coatings. Single-layer graphene, owing to its excellent mobility, could surpass the limit set by established materials if its intrinsic mobility limit (~5,000 $cm^2\ V^{-1}\ s^{-1}$) can be transferred to large areas while avoiding wrinkles, cracks and other mobility-reducing defects.

**Table 1.1:** Electrical and optical properties of transparent conductive materials[63]

| Material class | Material | Bulk resistivity $\rho$ ($\mu\Omega$cm) | Carrier concentration $n$ ($10^{21}$cm$^{-3}$) | Mobility $\mu$ (cm$^2$V$^{-1}$s$^{-1}$) | Plasma wavelength $\lambda$ ($\mu$m) | $\sigma_{d.c.}/\sigma_{opt}$ |
|---|---|---|---|---|---|---|
| Metals | Al | 2.5 | 180 | 14 | 0.08 | 75 |
| | Ag | 1.5 | 58 | 72 | 0.14 | 215 |
| | Cu | 1.55 | 85 | 48 | 0.11 | 75 |
| Semiconductors | ITO | >100 | <3 | ≈20–100 | 0.77 | 120–240 |
| | $SnO_2$ | >500 | <1.0 | ≈15–50 | 1.1 | |
| | ZnO | >200 | <1.0 | ≈1–5 | 1.1 | |
| | $TiO_2$ | >500 | <4 | ≈10–70 | 1.27 | |
| | (Si) | >100 | <5 | | 0.95 | |
| Carbon | Polymers | >700 | <10? | <1? | 0.8? | |
| | SWNT | >150 | $3\times10^{-4}$ | <10 | 60 | 6–14 |
| | Graphene | >5 | <0.3 | <5,000 | 1.9 | 70 |

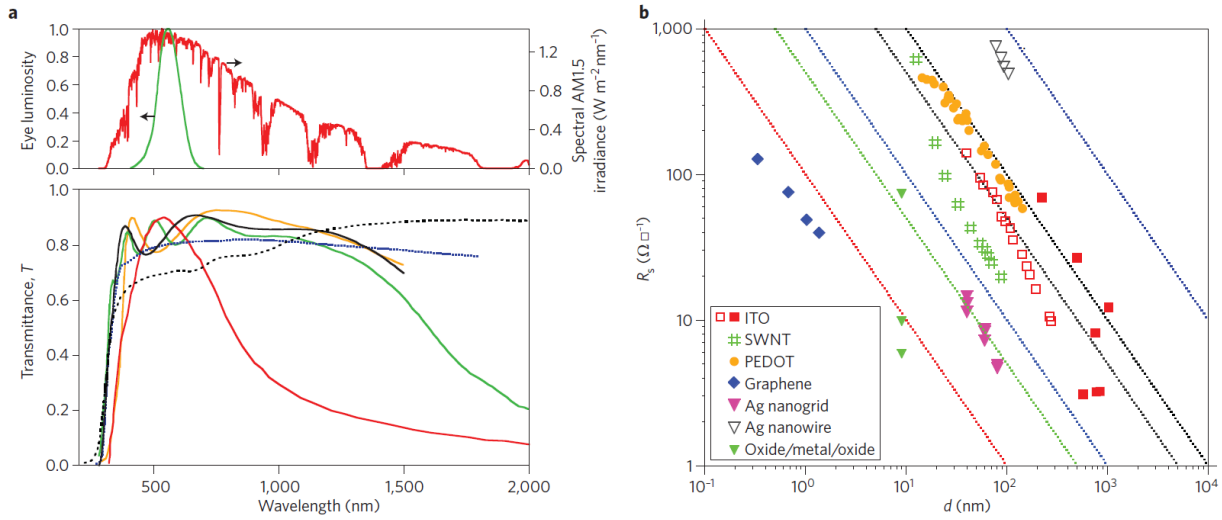


**Figure 1.10**: Optical transmittance T and sheet resistances $R_s$ of TCE layers. (a) Spectral transmittance of different TCE films: 12 $\Omega$ $\square^{-1}$, ITO (black); 10 $\Omega$ $\square^{-1}$, fluorine-doped $SnO_2$ (green); 56 $\Omega$ $\square^{-1}$, single-walled carbon nanotubes (dashed black); 23 $\Omega$ $\square^{-1}$, Ag nanowires (dotted blue); 50 $\Omega$ $\square^{-1}$, ZnO:Al (orange); and a low-emissivity coating 7 $\Omega$ $\square^{-1}$, $SnO_2$/Ag/$SnO_2$ (red). The upper part of a shows the luminosity function of the human eye, which is important for TCE applications in displays and LEDs; below is the spectral irradiance from the Sun under AM1.5 conditions, which is important for solar-cell applications of TCE layers.( b) Sheet resistance $R_s$ as a function of film thickness $d$ for different TCE films: Ag, Al and Cu metal grids; PEDOT-PSS; ITO films; SWNTs; Ag nanogrid; oxide/Ag/oxide films; and graphene. The dotted lines correspond to constant resistivities $\rho$ of $1\times10^{-5}$, $5\times10^{-5}$, $1\times10^{-4}$, $5\times10^{-4}$, $1\times10^{-3}$ and $1\times10^{-2}$ $\Omega$ cm (from left to right)[63].

One of the criteria to compare different TCO materials is to display the transmittance $T$ in the visible wavelength range as a function of sheet resistance $R_s$ (Figure 1.11). According to theory, these dependences can be described by the formula[84]:

$$T = \frac{1}{\left(1 + \frac{Z_0 \sigma_{opt}}{2 R_s \sigma_{d.c.}}\right)} \qquad \textbf{(Equation 1.7)}$$

where $Z_0$ is the vacuum impedance ($Z_0 = 1/\varepsilon_0 c = 377\ \Omega$) and $\sigma_{opt}$ and $\sigma_{d.c.}$ are the optical and d.c. conductivities of the material, respectively. $T$ is typically measured in the visible range at a wavelength of 550 nm, which corresponds to the maximum of the human eye luminosity curve (Figure 1.10(a)). According to Equation 1.7, the ratio $\sigma_{d.c.}/\sigma_{opt}$ can be maximized for high transmittance at a particular sheet resistance. This formula, although often used in literature, is not well substantiated; it is not clear for which wavelength the optical conductivity $\sigma_{opt}$ must be taken. Most experimental data for $T(R_s)$ have been reported for a wavelength of 550 nm. For nanowire and carbon nanotube networks, one must also take into account percolation in these films, as pointed out by De et al.[70]. Figure 1.11 shows the experimental $T(R_s)$ data for a number of different TCEs, along with a theoretical fit based on Equation 1.7. The large scattering of the data points is due to the different materials and preparation procedures. The main fit parameter is the ratio $\sigma_{d.c.}/\sigma_{opt}$ (see Table 1.2), which is highest for metal structures (films and nanowires) and ITO films, slightly lower for graphene films, and lowest for single-walled carbon nanotubes. This can also be inferred from Figure 1.11, in which ITO, graphene and Ag grids are the materials that fit best to the application target (the dashed rectangle). Most of these

data are given for $T$(550 nm); that is, at the maximum of the eye luminosity function. For TCE applications in thin-film solar cells, a better measure for the transmittance would be the average of $T$ over the spectral range of 400–1,000 nm, or a weighted transmittance that takes into account the spectral irradiance of the Sun (Figure 1.10(a)) and bandgap energy of the specific solar absorber[85]. In summary, this semi-empirical $T(R_s)$ relation can be used to judge thin-film TCE materials for a prospective application. Attaining a better fundamental understanding requires a firm theoretical analysis of the optical conductivity $\sigma_{opt}$ based on density functional theory calculations beyond the well-known Drude theory[63].

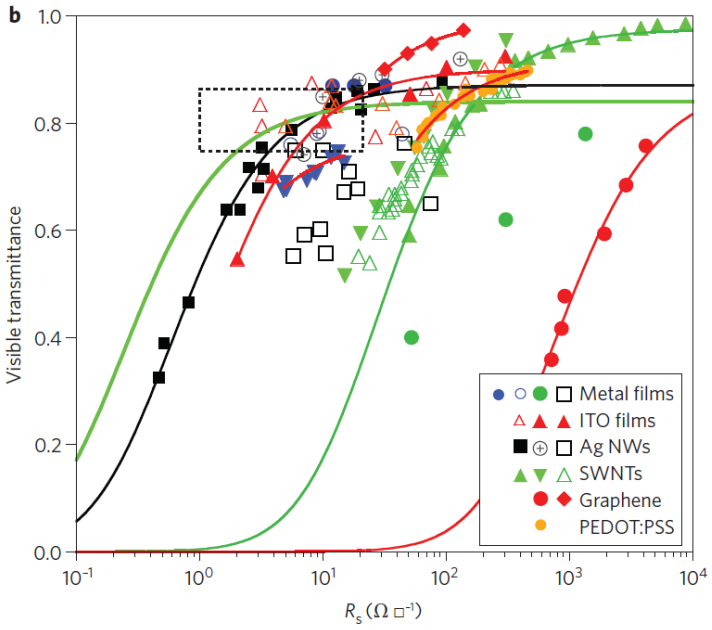


**Figure 1.11:** Transmittance $T$ in the visible range as a function of the sheet resistance $R_s$ for TCE films: ITO films[77, 85], graphene films[70, 77], single-walled carbon nanotubes[70, 77, 85], metal films[69, 86, 87], Ag nanowires[52, 70, 71, 74, 75, 88] and PEDOT films[75]. The dotted rectangle marks the $T$–$R_s$ target region for TCE applications. The lines are fits to some of the data points using Equation 1.7 (freestanding films) or a modified version of it (films on a glass substrate)[63].

## 1.3 Research Objectives

As the efficiency of laboratory-scale devices increases, developing materials and processes that would enable low-cost roll-to-roll fabrication of such devices gains increasing research interest. To promote the OSCs as a viable substitute for the conventional silicon-based solar cells, it is therefore necessary to focus on materials that can offer high performances, roll-to-roll processability, and potential for flexibility, via processes that are scalable, and do not rely heavily on costly fabrication conditions, such as high temperatures, vacuum processing, or inert atmospheres.

Within this scope, the goal of this research is to develop materials and fabrication processes for OSCs, which can offer a low-cost and scalable replacement for the conventional materials (electrodes and charge transport layers fabricated through vacuum deposition techniques) as well as solar cell fabrication processes (dominated by laboratory-scale processes). The research is carried out with two major areas of focus. The first part of the research concerns the fabrication of nanostructured transparent conductors with low sheet resistance, high optical transmittance, and high mechanical flexibility, that can be fabricated through a low-cost, scalable process. The second part involves the fabrication of organic solar cells using a scalable, low-temperature and low material consumption spray-coating process in air.

## 1.4 Thesis Overview

In the present chapter, the background and fundamental aspects were discussed regarding the organic solar cells and transparent conductive electrodes as a main component of the OSCs. The chapter concluded with discussing the major objectives of this research and an outline of the thesis (the present section).

In Chapter 2, the fabrication process, material characterization, and performance results will be presented for highly stretchable transparent conductors fabricated by metallizing sparse meshes of flexible polyacrylonitrile (PAN) nanofibers. Low sheet resistance, high optical transmittance, and high electromechanical stretchability of these TCEs will be analyzed in terms of material microstructure, and in comparison with other TCEs in the literature.

Chapter 3 discusses the fabrication of charge-selective TCEs based on the metallized nanofibers (NFs) introduced in Chapter 2. The metallized electrospun NFs are incorporated into a composite structure using solution-processed electron- or hole-selective metal oxides as the matrix. The fabrication and heat treatment processes leading to low sheet resistance and high optical transmittance in charge-selective TCEs will be discussed. The results will be analyzed in terms of material microstructure and in comparison with ITO and uncoated NF TCEs introduced in Chapter 2. In the second part of Chapter 3, a few approaches will be proposed to render the introduced charge-selective composite TCEs flexible. Sheet resistance, optical transmittance, and electromechanical stretchability of the introduced TCEs will be compared with one another and with the relevant literature.

Chapter 4 discusses the fabrication of OSCs using a low-temperature, low material consumption spray-coating process. Various stages of process development will be discussed, leading to a single-pass spray-coating process for the deposition of large-area, low-roughness

P3HT:PCBM photoactive layers at 25 °C substrate temperature and in air. Thin film characteristics, microstructure and photovoltaic performance of the fabricated devices will be discussed with reference to spun reference samples and relevant reports from the literature. Application of the developed process will be demonstrated in the fabrication of all-sprayed OSCs as well as large-area deposition of OSCs.

A summary and conclusions of this research will be presented in Chapter 5. Research contributions and suggested future work based on the findings will be discussed.

Each of the chapters 2 through 4, or the sub-sections within the chapters is structured as follows:

- Introduction, discussion of relevant literature and motivations,
- Overview of the chapter,
- Experimental details,
- Results and discussions,
- Summary.

# Chapter 2: Highly Stretchable Metallized Electrospun Nanofibers as Transparent Conductors

## 2.1 Introduction and Motivation

Transparent conductors (TCs) are essential in solar cells, touch panels and large-area displays. Indium tin oxide (ITO) currently dominates most of the commercial TC applications[89]. Despite its exemplary combination of sheet resistance and transparency ($R_s$ ~10 Ω/□ at $T$ ~90%) as well as its unlimited scalability, ITO has certain drawbacks: 1) rising prices caused by the scarcity of indium and increasing demands of the market; 2) high-temperature vacuum processing used in its fabrication, and 3) its brittleness. These drawbacks limit the applicability of ITO in future electronic devices which demand transparent conductors with low-cost large-area processability and compatibility with polymer substrates required for emerging flexible and stretchable devices. There have been several attempts to find a substitute for ITO, intended to address all or some of these drawbacks. There are two fundamental strategies to replace ITO thin films as TCs. The first involves the modification of the metal oxide structure, either by replacing indium with other metals [90, 91] or by crafting ITO into more flexible nanostructures [92-94]. The former overcomes the issues associated with indium yet leaves the other two issues, especially that of flexibility unattended. While, the latter improves the flexibility yet retains the use of indium. Besides, considerably high sheet resistances ($R_s$ in the order of $10^3 – 10^6$ Ω/□) of ITO nanofibers make them an impractical candidate for transparent conductor applications. The second and more promising strategy involves the development of novel materials and structures. Such materials can be categorized in

three groups: carbon nanomaterials, metallic nanostructures and conductive polymers. The first and most widely investigated candidate for ITO-free TCs are carbon nanotubes (CNTs) [95-104] which are considered promising due to their high intrinsic conductivities, solution processability and potential for flexibility [105]. However, high junction resistances and the inconsistency of tube types lead to sheet resistances higher than ITO TCs by at least an order of magnitude ($R_s$ ~ 150-1000 Ω/□ with ~80% transparency) [96-104]. Research is ongoing to improve the sheet resistance of carbon nanotubes and $R_s$ values as low as 70 Ω/□ at 80% transmittance have been achieved by chemical modification of the tubes [95]. Graphene holds similar attractions as a transparent conductor as those of carbon nanotubes. The best combination of sheet resistance and transparency so far achieved for graphene is reported by Bae et al. [52]. They have used a multi-step process comprising of chemical vapor deposition (CVD) growth and chemical etching to produce large-scale graphene sheets with $R_s$ = 30 Ω/□ and 90% transmittance. This process, though scalable, requires high-temperature vacuum growth of graphene and involves multiple layer depositions to yield low sheet resistance. Conventional methods of graphene growth typically result in sheet resistances higher by at least an order of magnitude [106-109]. Transparent conductors made from carbon materials are fairly flexible, showing less than 100% increase in sheet resistance upon more than 15% strain [52, 98, 102, 108]. Metallic nanostructures have been used as an alternative to fabricate low sheet resistance TCs. Transparent conductors comprising of nano-sized patterns of metal grids yield an $R_s$ ~ 20 - 30 Ω/□ at ~ 80% transmittance [110-113]. The fabrication, however, involves elaborate photolithography and metal transfer steps and is therefore costly and difficult to scale up. Solution-processed random meshes of metal nanowires (NWs), especially silver nanowires provide a scalable and relatively inexpensive alternative to fabricate high-performance

transparent electrodes. Sheet resistances in the range of ~ 30 - 70 Ω/□ at ~ 85% transparency are typically achieved in silver nanowires TCs [66, 114, 115]. Drawbacks of silver NWs include stability of the wires[116], low aspect ratios (responsible for high junction resistances) and the use of polymer surfactants in the processing. The first issue imposes limitations on the lifetime of the TCs made from silver NWs while the last two lead to higher sheet resistances. Creating fused junctions is an effective way to mend the latter. Sheet resistances as low as 10 Ω/□ in the range of 80 – 85% transmittance have been achieved by local 'nano-welding' of nanowire junctions induced by heat [68, 117] or light [118]. This, however, involves a rather high temperature treatment and demands careful controlling of the heat treatment conditions to prevent over-melting and subsequent coalescence of silver nanowires [68, 117] or a controlled nitrogen atmosphere to conduct the nano-welding process [118]. Silver NWs show less flexibility than carbon materials, with ~200% increase in resistance upon ~16% strain[115, 117]. The problems of low aspect ratio and high junction resistance in metallic nanowires have recently been addressed in a more effective approach by Wu and coworkers [119]. They have used electrospinning process to produce copper oxide nanofibers with ultrahigh aspect ratios. By subsequent reduction of the oxide, they have succeeded in forming copper nanofibers with fused junctions, enabling very low junction resistances. Typical performances of $R_s$ = 12 Ω/□ at ~ $T$ = 80% and $R_s$ = 50 Ω/□ at ~ $T$ = 90% have been demonstrated by the TCs thus fabricated. This method provides high performance metallic TCs through a low-cost and scalable process. There are, however, three disadvantages to the method: 1) It involves high-temperature heat treatment steps to transform the initially electrospun nanofiber webs to the final metallic nanofibers. 2) Copper is oxidized when exposed to air, limiting device stability and necessitating encapsulation [119]. 3) The flexibility of the TCs is limited despite the high aspect ratios of the fibers. Copper

nanofibers show ~50% increase in resistance upon being bent to the radius of 6 mm [119], whereas CNTs show the same percentage of increase only after they are bent down to 2 mm [98]. The last class of potential candidates to replace ITO is the conductive polymers. The most widely used conductive polymer which is already extensively used in conjunction with ITO in solar cells is PEDOT:PSS. The low conductivity PEDOT:PSS (Rs ~ $10^3$ Ω/□) is the main obstacle in its successful application as a TC[111]. Strategies such as the addition of secondary dopants [75, 120, 121] and the use of metallic current-collector grids [111, 122, 123] have been used to improve the conductivity of PEDOT:PSS. However, the conductance of reported stretchable PEDOT:PSS TCs is not stable by increasing the strain [124].

Considering the diverse requirements of high stretchability, conductance and transparency for future TCs, this research presents a new class of electrospun nanofiber webs with conductive shells that demonstrate exceptional TC properties in addition to high stretchability. Scalable electrospinning process is used to produce PAN nanofibers, which are subsequently metallized with Au, to form conductive nanofibrous webs with high transmittance and low sheet resistances. Unlike other metallic nanostructures reported so far, polymer-metal core-shell structure of the metallized nanofiber webs enables accommodation of high levels of tensile strain with little change in sheet resistance.

## 2.2 Experimental

*Fabrication of Sparse Metallized Electrospun Nanofibrous TCs*: Sparse PAN NFs were prepared using the electrospinning as shown schematically in the Figure 2.1. PAN (Scientific Polymer Products Inc.) was dissolved in dimethylformamide (DMF) (10 wt% concentration, Fisher) and stirred at 60 °C for 24 h. The solution was loaded into a plastic syringe with a

blunted G18 needle for electrospinning (Kato Tech Co.). A constant volume of the solution was delivered to the needle (flow rate of 0.5 ml $h^{-1}$) and a constant potential (17 kV) applied to the needle with respect to the grounded substrate (a rectangular metallic frame) to form a sparse NF web (Figure 2.1). By changing PAN concentration from 9 to 11 wt% NFs with average diameter of 250–450 nm were prepared. NFs with average diameter of 300 nm (standard deviation of 25 nm) were used for making most of the TCs prepared for this work. The NF web was then coated with a thin layer of gold by sputtering (Edward Sputter Coater), which provides a uniform conformal coating on the NFs.

*Transfer of Nanofibers to Substrate*: The NF web was transferred to the target substrate to make rectangular samples (typically 20 × 10 mm). The transfer process is schematically depicted in Figure 2.1 (Step III). The metallic frame was placed on the surface of the desired substrate (glass, plastic or polydimethylsiloxane (PDMS)) which was first mounted on a raised surface. A drop of methanol was then added to enhance the physical adhesion between the NFs and the substrate surface. Finally, by lowering the frame past the substrate level, the NF web was separated from the frame and transferred to the substrate. Electrical contacts were then formed by application of silver paint (Ted Pella Inc.).

*Characterization of Metallized Electrospun Nanofibrous TCs*: The morphologies of the NFs were studied using scanning electron microscopy (SEM) (Hitachi S-4700) and confocal microscope (Olympus, LEXT OLS4000). To examine the cross-section of Au-coated NFs, the fibers were sandwiched between stainless steel rollers and mounted in an epoxy resin. The surface of the specimen was then polished and examined with the SEM (Figure 1c). For microstructural examination of the NFs under strain a home-made holder with adjustable grips was designed and built with a motorized linear stage (Zaber T-LS28M) to control the separation

of the grips for precise control of tensile extension of the NF TC webs. Thin films of Cr (5 nm)/Au (100 nm) were directly deposited on relaxed as well as pre-stretched PDMS substrates, using e-beam evaporation, to provide a reference of comparison for the sensitivity of sheet resistance to strain. The sheet resistance of NF web was obtained either by measuring the resistance between two contacts on the ends of rectangular samples or by the four-point probe measurements using the Van Der Pauw method to suppress effect of contact resistances. The electrical measurements were carried out using a Keithley 2400A source meter and a DMM4040 Tektronix multimeter.

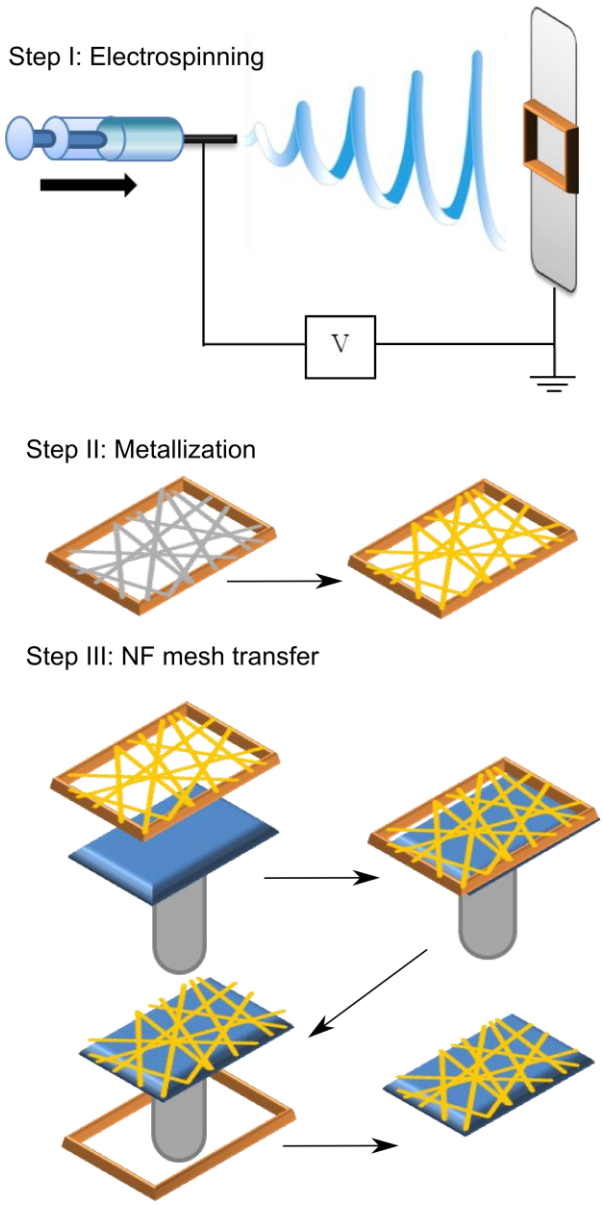


**Figure 2.1:** Schematic of the fabrication process steps of the nanofiber TC web: Step I - fabrication of sparse randomly oriented PAN nanofibers on the holder using electrospinning, Step II - Sputtering of a thin film of gold on the surface of the nanofibers, and Step III – transfer of the NF TC web to the desired substrate.

## 2.3 Results and Discussion

### 2.3.1 Characterization of the Metallized Nanofibers

Figure 2.2(a) and (b) show SEM micrographs of a thick layer of metallized electrospun NFs as well as a sparse NF TC web, illustrating the random arrangement of continuous NFs in a web. The diameter of NFs can be controlled by adjusting the electrospinning parameters including but not limited to solution concentration and the applied voltage. By changing PAN concentration from 9 wt% to 11 wt% NFs with average diameter of 250-450 nm were prepared. NFs with average diameter of 300 nm with standard deviation of 25 nm were used for making most of the TCs prepared for this study. The cross-sectional SEM micrograph of Au-coated NFs is illustrated in the Figure 2.2(c), revealing a conformal coating of gold on the surface of NFs. Figure 2.2(d) shows a transmission electron microscopy (TEM) micrograph of Au-coated and uncoated (inset) NFs. In contrast to the uncoated NFs, the coated NF is not transparent to the electron beam, due to the presence of a thin layer of gold. Figure 2.2(e) illustrates a photomicrograph of a single Au-coated NF on a glass substrate connected by two silver paint contacts. The current-voltage (*I-V*) characteristics of the NF are shown in the inset (a), signifying an Ohmic characteristic. To verify the uniformity of coated NFs, five NFs with different lengths were examined. The change in resistance of the NF vs. length for the samples is presented in the inset (b). The linear relationship between the resistance of the NF and the length of the segment under measurement confirms the uniformity of the NF diameter and the metallic shell.

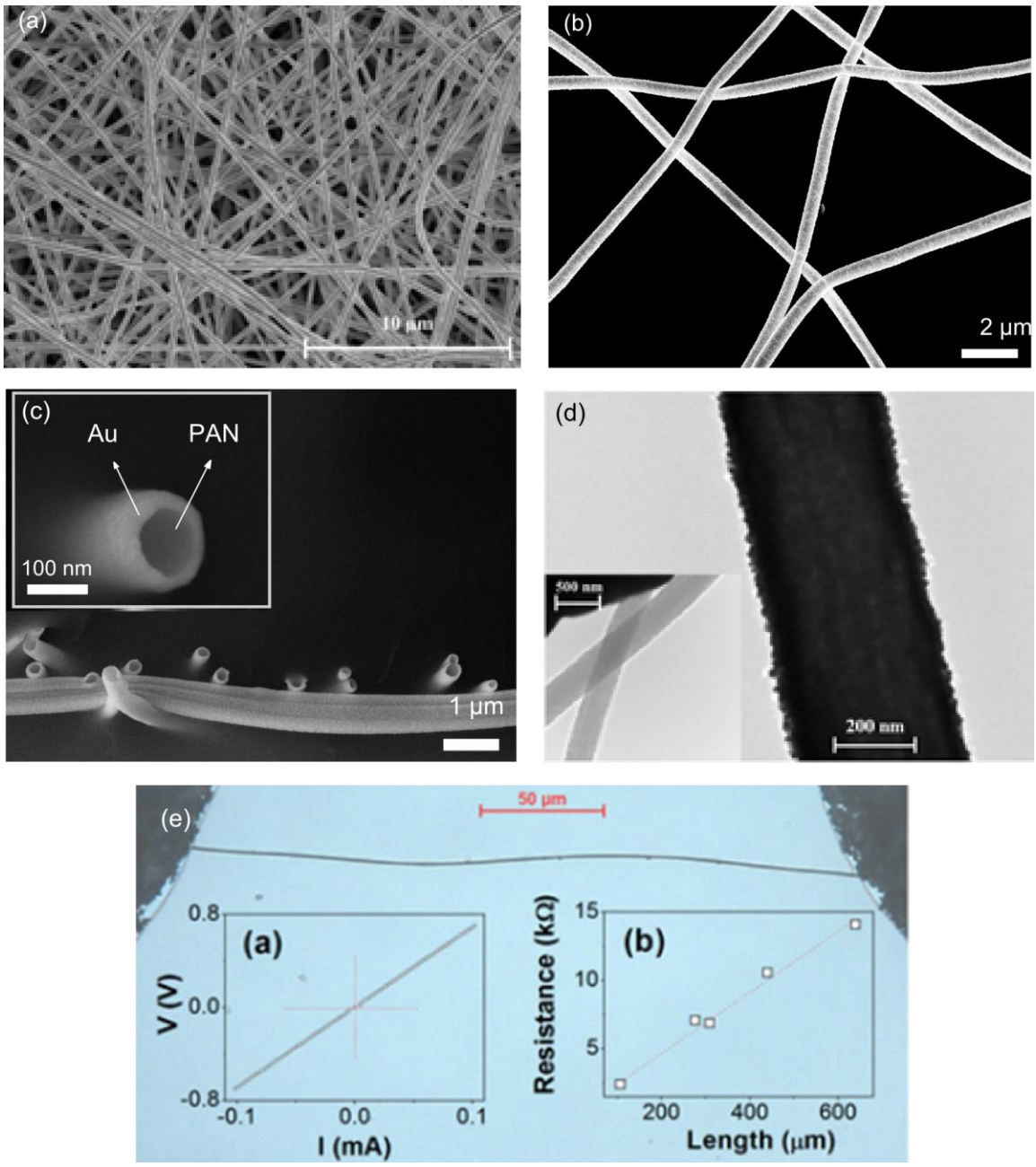


**Figure 2.2:** Microstructure and electrical properties of metallized electrospun nanofibers. (a) SEM micrograph of a thick layer of metallized electrospun NFs, (b) SEM micrograph of a sparse mesh of metallized electrospun NFs, typical of what is used in fabrication of the TCs, (c) cross sectional SEM micrograph of Au-coated NFs embedded in an epoxy resin. (d) TEM micrograph of Au-coated and uncoated (inset) NFs, (e) Optical micrograph of a gold coated NF between two silver paint contacts. Insets show the *I-V* curve of this fiber (a) and resistance vs. length for Au coated NF samples (b).

### 2.3.2 Characterization of Nanofibrous TCs

#### 2.3.2.1 Sheet Resistance and Optical Transmittance

Optical transmittance spectra and sheet resistances of NF TC webs prepared for different electrospinning durations are displayed in Figure 2.3(a). Corresponding optical micrographs of the webs are shown in Figure 2.3(b). By decreasing the duration of electrospinning, sparser NF webs are achieved, increasing both the optical transmittance and sheet resistance. Figure 2.3(c) illustrates the sheet resistance versus optical transmittance (at 550 nm) for metallized NF TCs, compared to other alternatives in the literature. Our NF TC webs show a performance comparable or superior to that of the ITO films, for instance, $R_s$ = 155 Ω □$^{-1}$ at $T$ = 95%, $R_s$ = 25 Ω □$^{-1}$ at $T$ = 81% and $R_s$ = 12 Ω □$^{-1}$ at $T$ = 71%. NF TC webs outperform carbon-based TCs by at least an order of magnitude. The sheet resistance of metallic nanostructures is in the same range as that of NF TC webs. Due to the virtually continuous fibers produced by electrospinning, the metallized NFs have extremely high aspect ratios (> 50000 compared to 100 – 1000 in the case of the typically micrometer-long nanotubes or nanowires[66, 95, 102, 114, 118]). Based on the percolation theory, this will considerably decrease the critical density of the fibers corresponding to the percolation threshold, making low sheet resistances possible at higher transmittance[72]. Slightly lower sheet resistances of electrospun copper NFs [119] and Ag NWs with fused junctions [117, 118] can be attributed to the low junction resistances and their all-metal structure, as opposed to the composite metal/polymer core-shell structure of NF webs. It should be noted, however, that this contributes to the higher strain sensitivity of sheet resistance and lower flexibility in Ag NWs and copper NFs in comparison to our composite TCs, as discussed in Section 2.3.2.3.

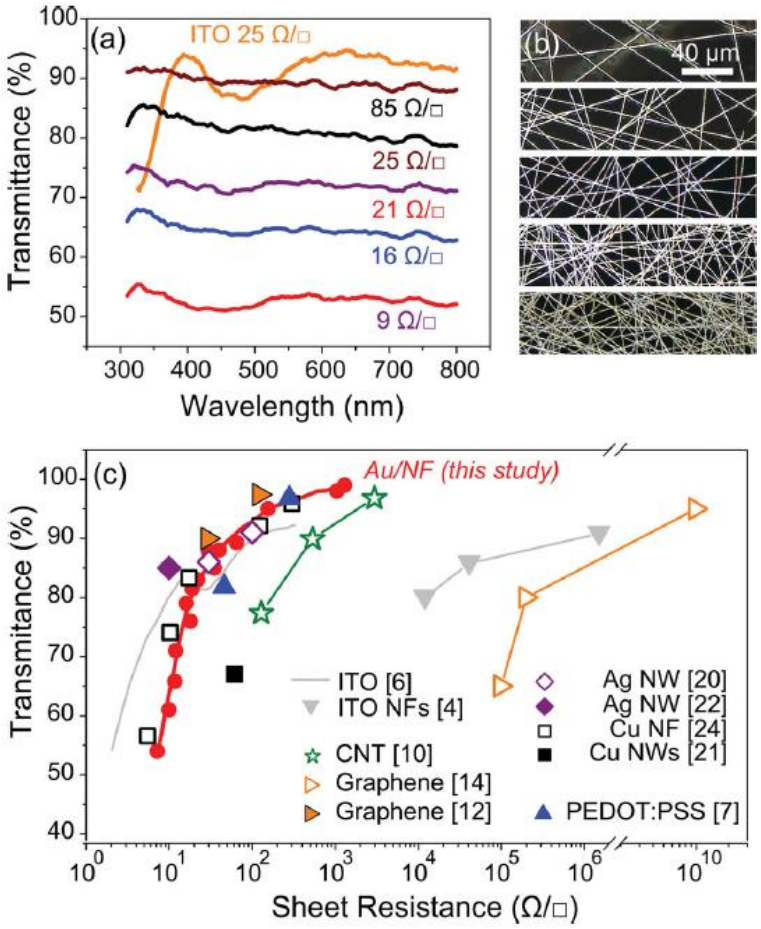


**Figure 2.3: (**a) Transmittance spectra of the Au-coated NF networks with different coverage and sheet resistances. (b) The corresponding confocal microscope photomicrographs of the samples from the highest to the lowest sheet resistance from top to bottom. (c) Sheet resistance vs. transmittance of NF TC webs in comparison to other alternatives in the literature. The lines are guides for the eye.

#### 2.3.2.2 Effect of Annealing

Figure 2.4 shows the effect of thermal annealing on sheet resistance and optical transmittance of a sparse metallized nanofiber TC. The sheet resistance is improved by more than 35% through annealing for 10 minutes at 250 °C. The decrease in sheet resistance continues with further annealing at the same temperature, with the value decreasing from 107 Ω $\square^{-1}$ (no annealing) to 58 Ω $\square^{-1}$ (45% decrease) after four successive annealing stages. A notable property of the fabricated TCs, as observed in Figure 2.4, is that the decrease in sheet resistance is achieved with no loss of transmittance. In fact, there is even a slight increase in transmittance values, from $T$ = 95.13% for the as-fabricated TC to $T$ = 96.53% after 10 minutes at 250 °C. To investigate the mechanism of the observed improvement in TC performance, the evolution of the microstructure of the TCs through annealing was studied using SEM. Figure 2.5 shows SEM micrographs of a metallized nanofiber TC before annealing and after annealing at 250 and 300 °C. To minimize the effect of possible variations in TC structure among different individual TCs, the characterizations are reported for the same sample through various heat treatment stages. Two distinctive trends can be observed in Figure 2.5. One is a gradual decrease in average fiber diameter as an effect of annealing (evident through comparing Figure 2.5 (a, b and c)). The second trend is the evolution of the nano-morphology of gold grains on the metal shell. High-magnification SEM micrographs (Figure 2.5 (g, h, i)) reveal a perceptible grain growth, which has resulted in partial coalescence of the grains through different annealing stages. The observed improvement in electrical conductance because of annealing agrees with the decrease in microstructural defects, in particular at the grain boundaries as observed in Figure 2.5. Our observation is in agreement with previous research where reduction in electrical resistivity of gold thin films is reported due to a drastic increase in grain size as the result of heat

treatment[125]. The decrease in the average diameter of NFs which can be attributed partly to compressive strains resulting from diffusion of gold atoms along the length of the NFs and partly to the shrinkage of the PAN NFs as a result of heating [126]. The decrease in the diameter of the NFs agrees with the increase in optical transmittance as exemplified in Figure 2.4.

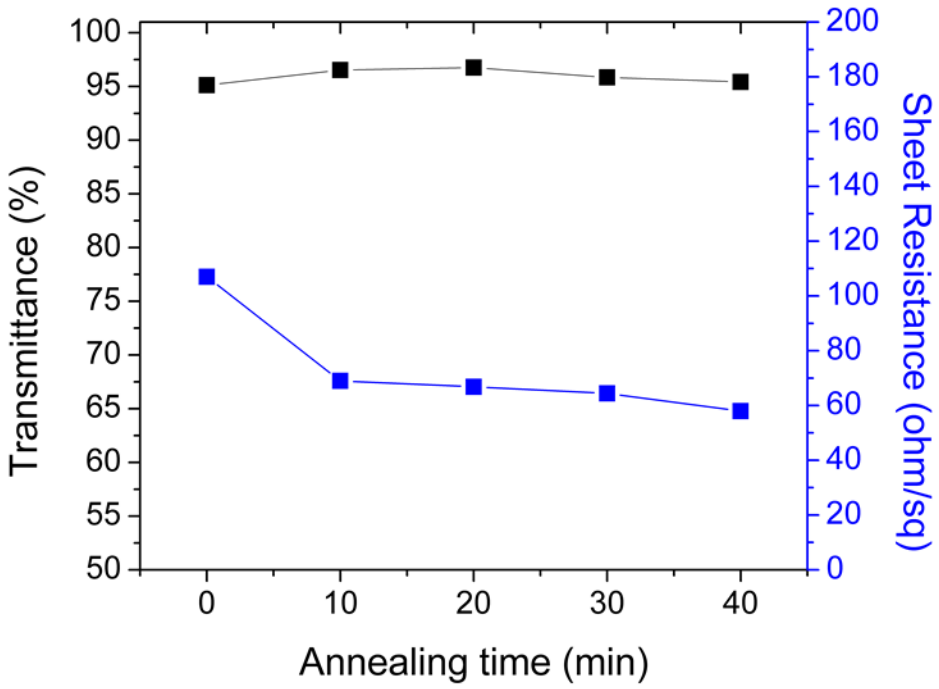


**Figure 2.4:** Effect of annealing time on sheet resistance and optical transmittance (at 550 nm) for a TC annealed at 250 °C.

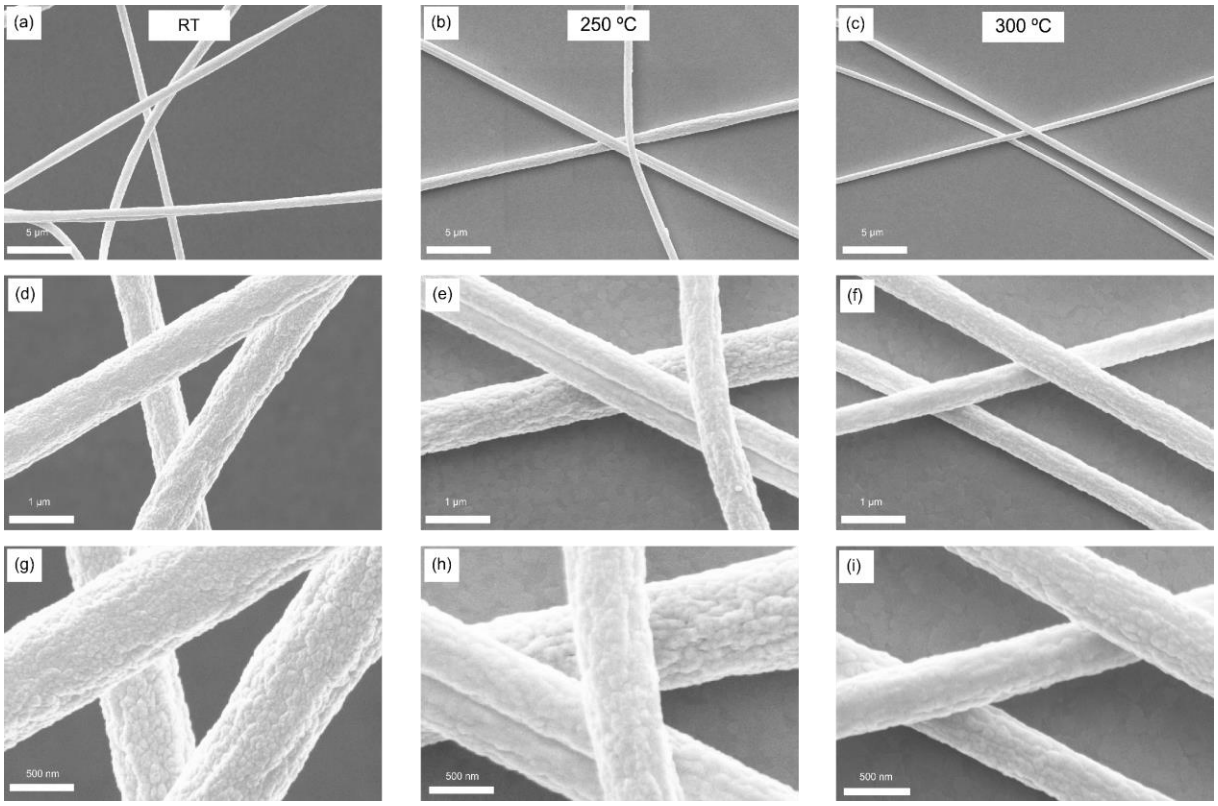


**Figure 2.5:** SEM micrographs of metallized NFs, showing the effect of thermal annealing on the diameter of NFs and morphology of the gold shell. Micrographs of the as-transferred TC (a, d, g) are shown in comparison with micrographs of the same TC annealed at 250 °C (b, e, h) and 300 °C (c, f, i).

#### 2.3.2.3 Electromechanical Stretchability

Figure 2.6(a) illustrates the relative change in resistance, $(R\text{-}R_0)/R_0$, as a function of tensile strain $\epsilon$ for the NF TC webs transferred to PDMS substrates. For comparison, results for thin gold films evaporated on PDMS substrates are also presented. Gold films deposited on relaxed PDMS can withstand up to 20% strain, but exhibit a sharp rise in electrical resistance beyond this value. Films evaporated on pre-stretched PDMS substrates (15% pre-strain) show negligible change in sheet resistance for up to 15% strain due to unbuckling of surface waves, but demonstrate a similar sharp rise in resistance at higher strain values. NF TC webs demonstrate

an unprecedentedly low sensitivity of sheet resistance, with only 56% increase in resistance and 6% increase in optical transmittance (Figure 2.6(c)) for 100% strain. In fact, the experiments show that NF webs can be stretched more than 200% without losing conductivity, and the stretchability is limited only by the failure of the contacts. Figure 2.6(b) illustrates the electromechanical performance of NF TC web in comparison to that of the ITO[127] and other TCs reported in the literature. As seen, the electromechanical stability of NF TC webs is far superior to that of other TCs. The two top flexible TCs, i.e. CVD-grown graphene films[52] and Ag NWs[117] fail upon 5–7% strain with ~60% increase in resistance at the point of failure. Highly stretchable PEDOT:PSS films withstand 188% tensile strain, however with 1700% increase in resistance at 100% strain[128]. The reason for the extremely low strain sensitivity of NF webs lies in their unique fibrous architecture that mimics the structure of natural systems. Extremely high aspect ratios of the NFs (in the order of $\sim 10^5$) coupled with the inherent mechanical flexibility of the polymer core enable them to accommodate high levels of strain through rearrangement and bending/unbending of percolating NF networks. Additionally, the conformal gold shell provides a virtually continuous conduction path on the surface, enabling low sheet resistance. The mechanical and electrical continuity of thin gold films on polymer substrates have been the subject of several studies[129-131]. Such thin films are shown to maintain electrical conductance at strain levels 1-2 orders of magnitude higher than that of freestanding gold films[131]. There are three mechanisms responsible for this behavior: 1) The actual bending strain in thin films is considerably low, by the virtue of the linearly decreasing bending strain with the thickness[132]; 2) The presence of a soft polymer substrate delocalizes the mechanical instability (i.e. necking) thus postponing the local ruptures (i.e. the initiation of the cracks) in the film[129, 130]; and 3) when formed, the cracks constitute a percolating

network thereby enabling gold islands to still maintain electrical continuity after >30% of applied tensile strain[131].

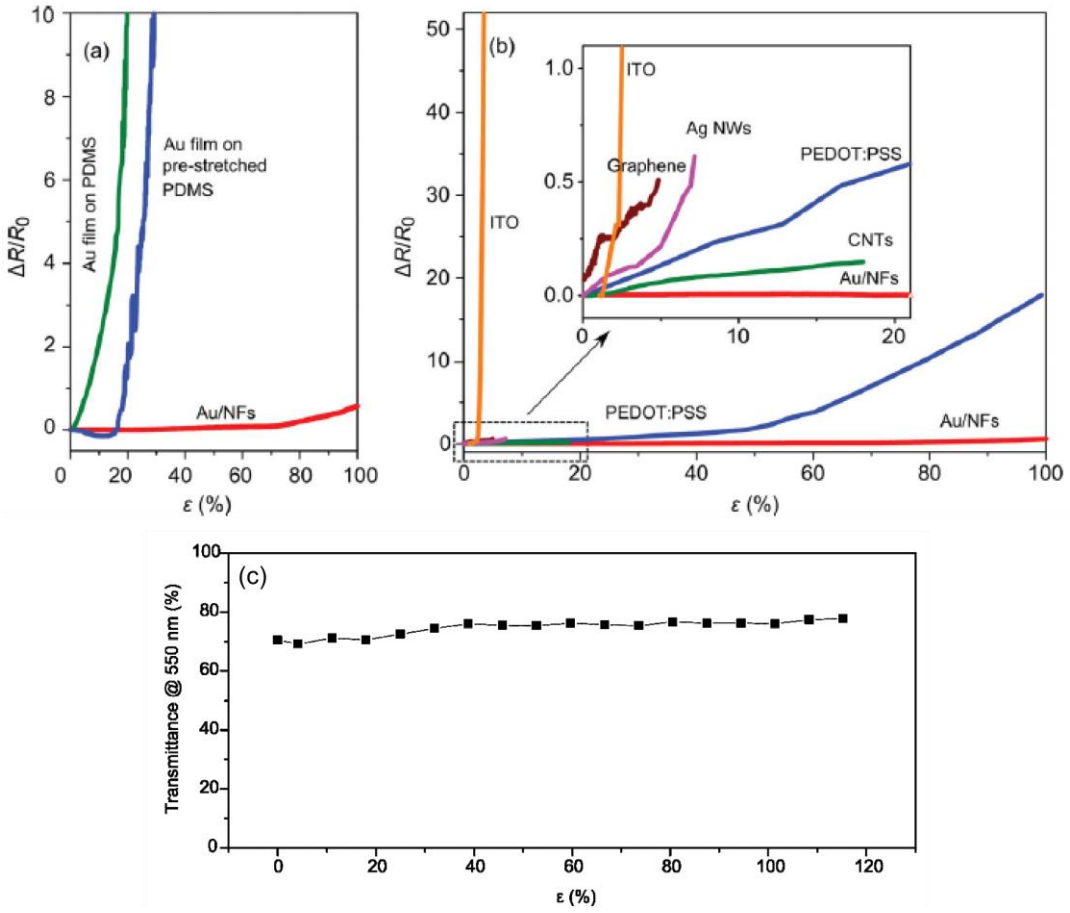


**Figure 2.6**: Strain sensitivity of the resistance of NF TC web on PDMS substrates. (a) The plot of $\Delta R/R_0$ vs. strain for NF TC webs compared to evaporated gold thin films on PDMS substrates, where $\Delta R = R\text{-}R_0$. (b) $\Delta R/R_0$ vs. strain of NF TC webs compared with other flexible TCs reported in the literature. The curve for ITO is also shown for comparison. (c) The evolution of optical transmittance (at 550 nm) of the NF TC during stretching

Study of the NF TC web at different tensile strains (Figure 2.7(a-c)) reveals no visible disconnection of the web, signifying that the rearrangement/reorientation of the NFs, rather than

the deformation of individual fibers, accommodates the strain. Even at 100% strain, the gold sheath of most fibers remains intact. As seen in Figure 2.7(e) and (f) for a sample under 100% strain, nano-cracks appear only on the surface of the fibers aligned with the applied strain. It is also notable that nano-cracks have not completely cut across the perimeter of the fiber, thereby leaving a conduction path along the fiber. Based on these observations, the randomly oriented network of NFs accommodates a large portion of the applied strain through rearrangement of the fibers, with little microstrain imposed on the individual fibers. As the applied strain increases, some nano-cracks form on the shell of a small fraction of fibers in the direction of strain. However, it appears that even at this stage, the severity of local bending/tensile strains is alleviated by the nanoscale diameter of the fibers and the delocalization of the cracks (this effect is evident through comparing the cracks on the surface of the NFs Figure 2.7(e) with micro-cracks formed on a gold thin film on a PDMS substrate, under the same amount of tensile strain, as shown in Figure 2.7(g)). These mechanisms provide an unprecedented stretchability and stability of sheet resistance in contrast to electrospun copper NFs or Ag NW meshes, where on the one hand the absence of a flexible core confines the deformation to the metallic nanostructure, thereby limiting the stretchability to the ductility of the freestanding metal, and on the other hand, the presence of fused metallic junctions act as stress concentration sites facilitating the localization of plastic deformation and contributing to a sharper increase in electrical resistance (Figure 2.6(b)). The evolution of the NF web under the applied strain is schematically illustrated in Figure 2.7(h) and (i).

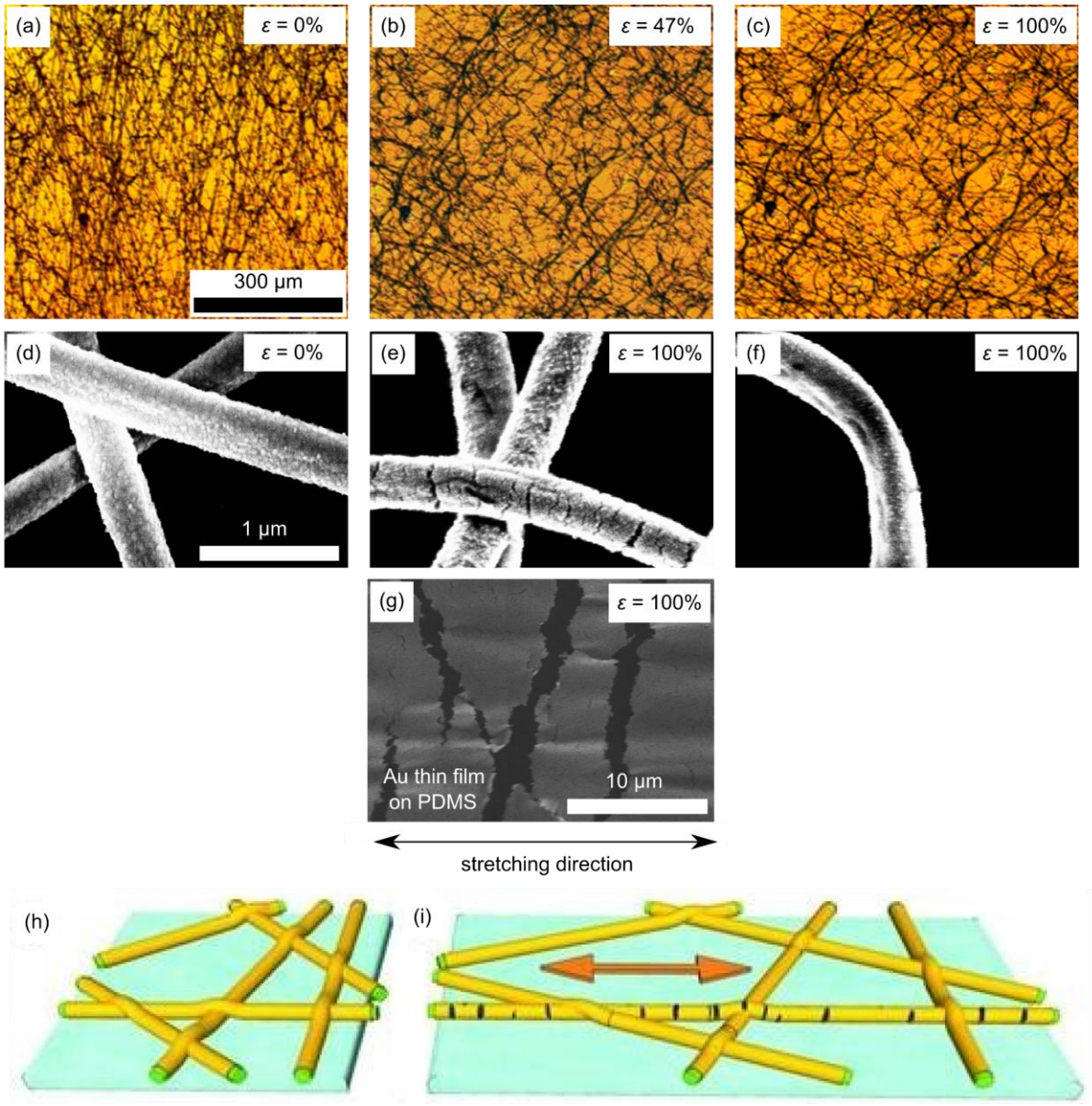


**Figure 2.7:** (a-c) Confocal optical micrographs of NF TC web, at different stretching levels. (d-f) SEM micrographs of NF TC before stretching (d) and under 100% stretching (e, f). The micrograph for Au thin film on PDMS substrate at under 100% strain is shown for comparison (i). (g, h) Schematics of the evolution of the NF web under the applied strain.

Cyclic endurance of the NF TC web under repeated stretching ($\epsilon_{max}$ = 10%) for 1000 cycles is shown in Figure 2.8. $\Delta R/R_0$ is almost unchanged over 1000 cycles. The variations in $\Delta R/R_0$ of

NF TC over 10 cycles for $\epsilon_{max}$ = 10% and 70% is shown in the inset (b), exhibiting a stable cyclic endurance under tensile strains as high as 70%.

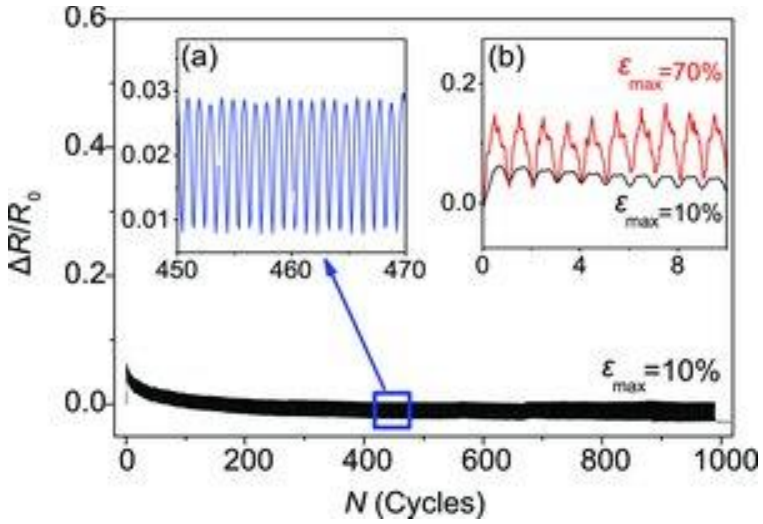


**Figure 2.8:** $\Delta R/R_0$ over 1000 cycles for Au-coated NF electrodes ($\epsilon_{max}$ = 10%). A close-up is shown in the inset (a). Inset (b) shows $\Delta R/R_0$ for the first 10 cycles for $\epsilon_{max}$ = 70% and $\epsilon_{max}$ = 10%.

## 2.4 Conclusions

High-performance TCs were fabricated by transferring sparse webs of metallized electrospun PAN NFs onto glass or PDMS substrates. The fabricated TCs show performances comparable to ITO, with $R_s$ of 155 Ω/□, 25 Ω/□, and 12 Ω/□ at $T$ of 95%, 81%, and 71%, respectively. 35-45% improvement in sheet resistance was achieved through annealing, with no drop in optical transmittance. TCs transferred onto stretchable PDMS substrates demonstrate unprecedented stretchability, with only 56% increase in resistance at 100% tensile strain (a sensitivity of ~ 0.5) and stable performance over 1000 stretching cycles. The high stretchability is due to reorientation of continuous nanofiber structures and stability of polymer core, as well as, formation of stable and movable junctions between nanofibers, the TC web.

# Chapter 3: Charge-Selective Transparent Electrodes Based on Metallized Electrospun Nanofibers

## 3.1 Introduction and Motivation

In Chapter 2, high-transparency, low-sheet-resistance TCs were introduced, which consisted of high aspect ratio metallized electrospun nanofibers with a core-shell structure. The introduced TCs show performances comparable or superior to conventional ITO TCs, typically with $R_s \sim 25\ \Omega/\square$ at $T \sim 81\%$ and have an unprecedented stretchability with only 56% increase in sheet resistance upon 100% strain. In the second part of this research, discussed in the current chapter, the idea is taken further, by integrating the metallized electrospun nanofibers into planar composite structures with different charge-selective nanoparticles as matrices. There are two major motivations for developing these composite TCs:

1. Integrating charge-selective (electron- and hole-selective) interface layers with the previously introduced TCs, to develop charge-selective TCs. Thus, the NF TCs can be used in organic photovoltaic devices as cathode or anode, depending on the choice of electron- or hole-selective nanoparticles, enabling normal and inverted device architectures.
2. Reducing the surface roughness of the original NF TCs, to enable them as bottom electrodes in organic photovoltaic devices.

The significance of each of the motivations is discussed further below.

### 3.1.1 Charge-Selective Interface Layers in Organic Solar Cells

Interface layers between the bulk heterojunction photoactive layer and the electrodes have different functions in OPVs. First, they reduce the energy barrier between the electrode and the photoactive layer, forming Ohmic contacts for effective charge extraction [4]. Secondly, they can be used as selective contacts for a single type of carrier (hole-selective/electron-blocking and vice versa). Thirdly, they act as protective layers to increase the durability of the electrodes as well as that of the electrode/photoactive layer interface [4, 15].

On the anode side (traditionally ITO), usually a p-type interface layer of PEDOT:PSS is applied, which has a high work function of 5.0 eV matching that of ITO. The acidic nature of PEDOT:PSS compromises long-term stability of the devices [4]. To get around this problem, transition metal oxides, such as $V_2O_5$, $WO_3$, NiO and $MoO_3$ have been suggested as replacements for PEDOT:PSS [133-135]. On the cathode side, usually low-work-function metals such as calcium, barium and magnesium are used to form Ohmic contacts at the cathode-polymer interface [4]. Researchers have introduced inorganic compounds such as thermally evaporated LiF layers to replace the reactive metals and improve the stability of the devices [4, 15]. Interface layers can be produced via different fabrication processes such as thermal or electron beam evaporation [135] and pulsed-laser deposition [136]. Solution-processed interface layers are often preferred over vacuum processes for realizing the full potential of bulk heterojunction devices [4], as well as their compatibility with low-temperature flexible substrates [137]. Jin et al. [138] have achieved 27% improvement in power conversion efficiency of OPVs, with 10 times increase in the long-term stability of the devices, using thermally evaporated $MoO_3$ as a hole transport layer. Girotto et al. [137] have shown that devices using solution processed $MoO_3$ nanoparticles can achieve a performance and lifetime comparable to those using

PEDOT:PSS or evaporated $MoO_3$. Ferreira et al. [139] have reported 18% increase in power conversion efficiency as well as extended lifetime by using ZnO nanoparticles as electron transport layer.

Although there have been several successful reports on the application of interface layers on conventional ITO electrodes and evaporated metal cathodes, there has been few reports on the deposition of metal oxide layers on novel nanostructured TCs. Chung et al. have used Ag NWs encapsulated in ITO nanoparticles to decrease the inter-wire junction resistances, decrease the surface roughness, and improve the mechanical adhesion of the TC to the substrate [140]. Their process, however, still uses indium, the replacement of which has been among the primary motives for the introduction of novel TC materials such as Ag NWs. Zhu et al. [50] have used a double layer of $TiO_2$ nanoparticles and PEDOT:PSS to form fused junctions in Ag NWs, thus decreasing the sheet resistance and improving mechanical stability. Here the $TiO_2$ layer has not been used as an electron transport layer and merely functions as a conductive encapsulating layer for the Ag NWs. Morgenstern et al. [141] have used Ag NWs coated with ZnO NPs which serves as electron transport layer while also decreasing the surface roughness of the Ag NW mesh. They have achieved photovoltaic performances comparable to a reference device with a similar structure based on ITO. There has been no report so far on the formation of charge-selective interface layers on high aspect ratio NFs. Furthermore, except in the case of Ag NWs encapsulated in ITO NPs [140], there has been no report on the application of interface layers in flexible and stretchable TCs. Their reported flexibility, however, is limited, with 30% increase in sheet resistance upon less than 2% strain [140].

In the present research, we propose the application of solution-processed charge transport coatings on high-aspect ratio metallized NF TCs. Also, stretchable charge-selective TCs are

fabricated by partly embedding the coated NFs near the surface of PDMS substrates. ZnO NPs are used as electron-selective and PEDOT:PSS and $MoO_3$ NPs as hole-selective coatings.

### 3.1.2 Addressing the Issue of Surface Roughness in Nanofibrous TCs

Despite their superior performance as TCs, the metallized electrospun NFs introduced in Chapter 2 have the drawback of high surface roughness (in the range of 400-600 nm) which limits their use as bottom electrodes in photovoltaic devices [1]. A similar issue has been reported in the case of Ag NWs [115] and CNTs [142]. Although there have been attempts to address the issue in Ag NWs by coating the NWs with a conductive encapsulating layer [141, 143] or making NW-polymer composites, using an inflexible polymer encapsulant [144], the problem has not yet been addressed in the case of high-aspect ratio NFs. Also, there has been no solution suggested to deal with the problem of surface roughness in flexible and stretchable TCs. In addition to their primary functions discussed in Section 3.1.1, here, the charge-selective nanoparticles are also employed to reduce roughness through covering the NFs via multiple layers of coating. Furthermore, stretchable metallized NF TCs with smooth surfaces are fabricated by partly embedding the NFs near the surface of PDMS substrates.

### 3.1.3 Overview of This Chapter

Section 3.2 discusses the results for the fabrication of composite, charge-selective TCs evolved from the metallized electrospun nanofibers discussed previously. A few materials and processes have been used to synthesize the electron- or hole-selective matrices for these composite TCs, each of which will be discussed in separate sub-sections under Section 3.2. Section 3.3 will discuss the suggested approaches to render such composite charge-selective TCs

stretchable. Section 3.4 compares the various composite TCs introduced in 3.2 and 3.3, with one another as well as with literature, in terms of different performance characteristics.

## 3.2 Composites of Metallized Electrospun Nanofibers in a Matrix of Charge-Selective Nanoparticles, as Charge-Selective Transparent Electrodes

Schematic structure of a planar composite of metallized electrospun nanofibers in a matrix of charge-selective nanoparticles is shown in Figure 3.2. A typical TC of this structure consists of a planar web of core-shell metallized NFs, introduced in Chapter 2, embedded in a matrix of nanoparticles that fully or partially cover the NFs (Figure 3.2(e) and insets). Different charge-selective layers are used as the matrix of the composite: zinc oxide colloidal nanoparticles (Sections 3.2.2), zinc oxide layers fabricated through sol-gel process (Section 3.2.2.2) as electron-selective layers, and molybdenum oxide layers fabricated through sol-gel process (Section 3.2.2.3) as hole-selective layers.

### 3.2.1 Experimental

*Zinc Oxide Colloidal Nanoparticles as Electron-Selective Matrices*: ZnO colloidal nanoparticles were synthesized by hydrolysis and condensation of zinc acetate dihydrate by KOH in methanol, based on the method of Pacholski et al. [145]. Figure 3.1 shows a TEM micrograph of the nanoparticles, showing diameters of ~ 10-15 nm. The solution in chloroform has a concentration of ~80 mg/ml. A diluted solution with a concentration of ~ 8 mg/ml was prepared, by adding isopropyl alcohol to the original solution. Both solutions have been used to deposit layers of ZnO NPs on the substrates, using spin-coating, as described below.

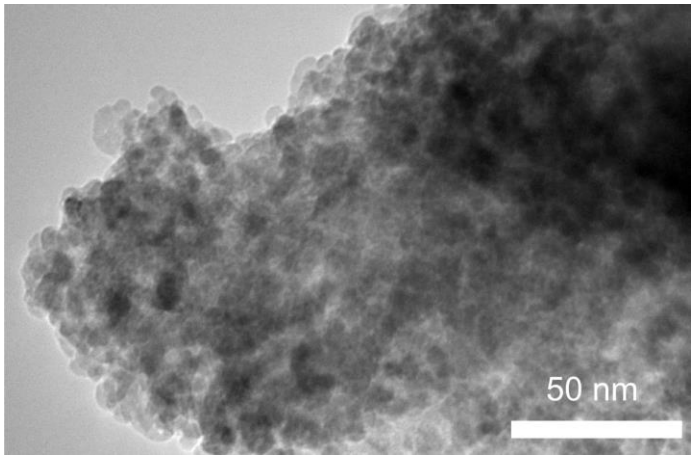


**Figure 3.1:** TEM micrograph of colloidal ZnO nanoparticles used to form electron-selective layers.

The fabrication is shown in Figure 3.2. Core-shell metallized electrospun NFs are produced as discussed in Section 2.2 (Figure 3.2a-c). The charge-selective matrix is formed by spin-coating the colloidal ZnO NP solution at 1000 rpm for 60 s. Partial coverage of NFs is achieved by using the diluted solution. Higher thicknesses are obtained by adding single or multiple coatings of the undiluted solution to the first layer.

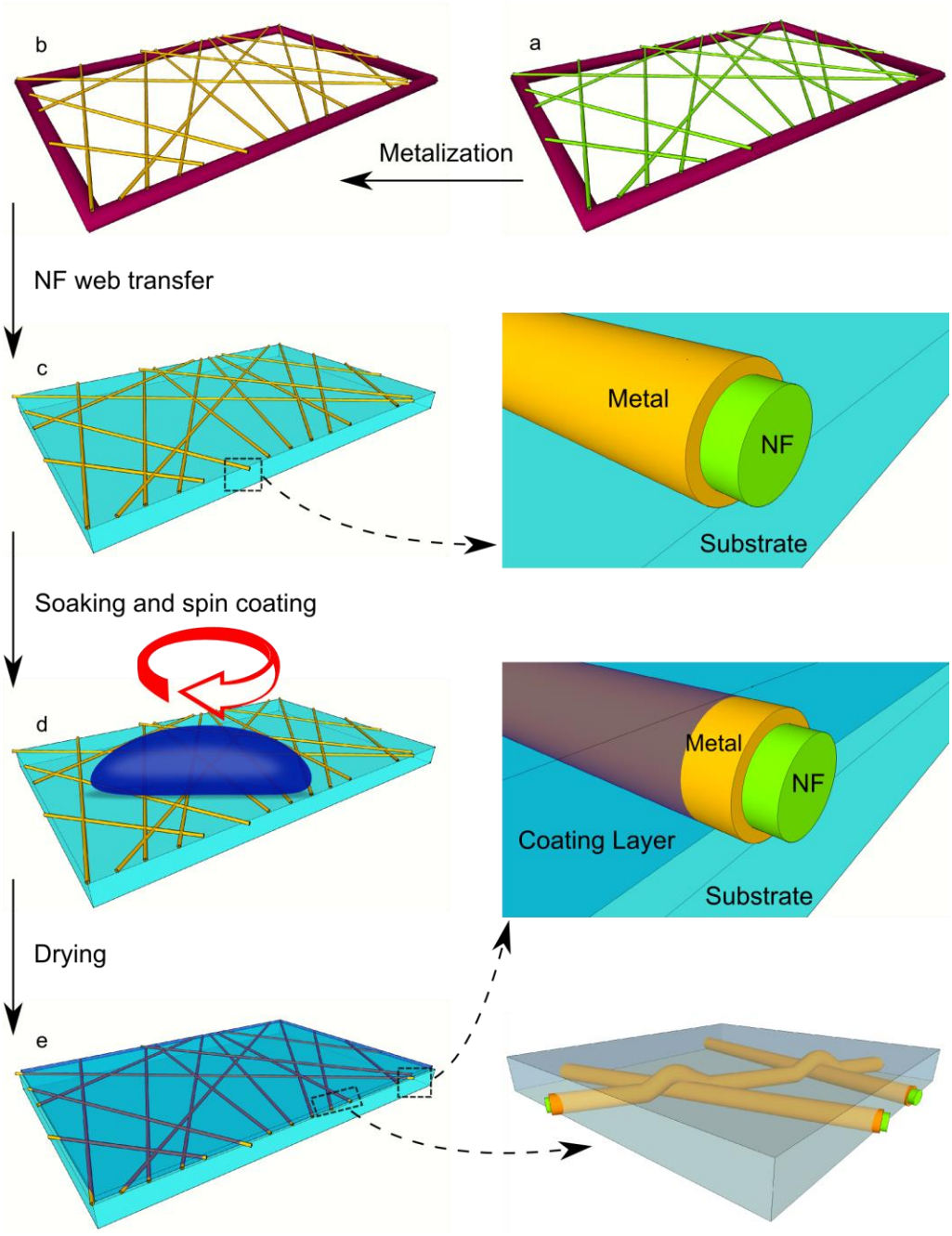


**Figure 3.2:** A schematic overview of the fabrication process (a-d) and eventual structure (e) of a typical charge-selective, composite TC, discussed in this section. The composite TC is composed of a planar web of core-shell metallized electrospun NFs in a matrix of charge-selective nanoparticles (e and the insets).

*Zinc Oxide Films Fabricated through Sol-Gel Process as Electron-Selective Matrices:* As a more facile alternative to nanoparticle synthesis, sol-gel method was used to form the electron-selective ZnO matrix. ZnO precursor solution was prepared by dissolving 0.5 M zinc acetate dehydrate in 0.5 M monoethanolamine and 2-methoxyethanol, using a process adapted from the work of Ong et al. [146]. The solution was dispensed on the nanofibers and spun at 1000 rpm for 15 s, followed by 20 s at 3000 rpm to strip away the remainder of the solution (Figure 3.2(d)). To obtain the ZnO film from the zinc acetate precursor, the film was annealed on a hotplate for 10 min, at a temperature ranging from 100 °C – 300 °C. To study the effects of annealing temperature, composite TCs were made by spin coating a single layer of ZnO precursor on a glass substrate. In successive steps, the samples were annealed at each temperature, cooled down to room temperature, measured for sheet resistance and optical transmittance, and then annealed at a higher temperature. Measurements were carried out for 100, 150, 200, 250 and 300 °C. To study the evolution of microstructure during annealing, similar procedure was used on TCs fabricated on ITO substrates.

*Molybdenum Oxide Films Fabricated through Sol-Gel Process as Hole-Selective Matrices*: Adapting the process used by Lin et al. [147], $MoO_3$ precursor solution was made by refluxing a 1 M solution of $MoO_3$ powder in $H_2O_2$ at 80 °C for 2 h. The viscosity and concentration of the solution was adjusted for spin coating, with diluting the original solution in ethylene glycol and 2-methoxyethanol (1:0.25:6.25 volume ratio) and further refluxing at 70 °C for 1 h, followed by cooling to room temperature for 24 h. The rest of the process is similar to that of the sol-gel ZnO TCs.

### 3.2.2 Results and Discussion

#### 3.2.2.1 Zinc Oxide Colloidal Nanoparticles as Electron-Selective Matrices

##### 3.2.2.1.1 Microstructure

Figure 3.3(a) and (b) show SEM micrographs of nanofibrous TCs coated with a thin and a thick coating of ZnO NPs, respectively. High-magnification images are provided in Figure 3.3(c) and (d). In the case of ZnO NPs spun from a diluted (8 mg/ml) solution (Figure 3.3(a) and (c)), the entire surface of the TC is uniformly covered with a thin layer of NPs. The coating (1) covers the inter-fiber spaces with a continuous thin film of electron-selective NPs, (2) forms a uniform shell of NPs on the NFs, extending along the fibers, and (3) surrounds the NF junctions, forming fused junctions (Figure 3.3(c) and inset). A composite TC consisting of 4 consecutive coatings of ZnO NPs from an undiluted solution (80 mg/ml) is shown in Figure 3.3(b) and (d). The NFs are completely covered by the electron-selective matrix. An AFM micrograph of this NF TC is shown in Figure 3.3(e). The surface roughness over the whole 10×10 μm area of the image, including the fiber, is $R_a$ = 43.1 nm. The roughness value over a 3×3 μm area on the ZnO film is $R_a$ = 5.91 nm. This shows considerable reduction in surface roughness, compared to uncoated metallized NFs, as will be discussed in more detail in Section 3.4.2.

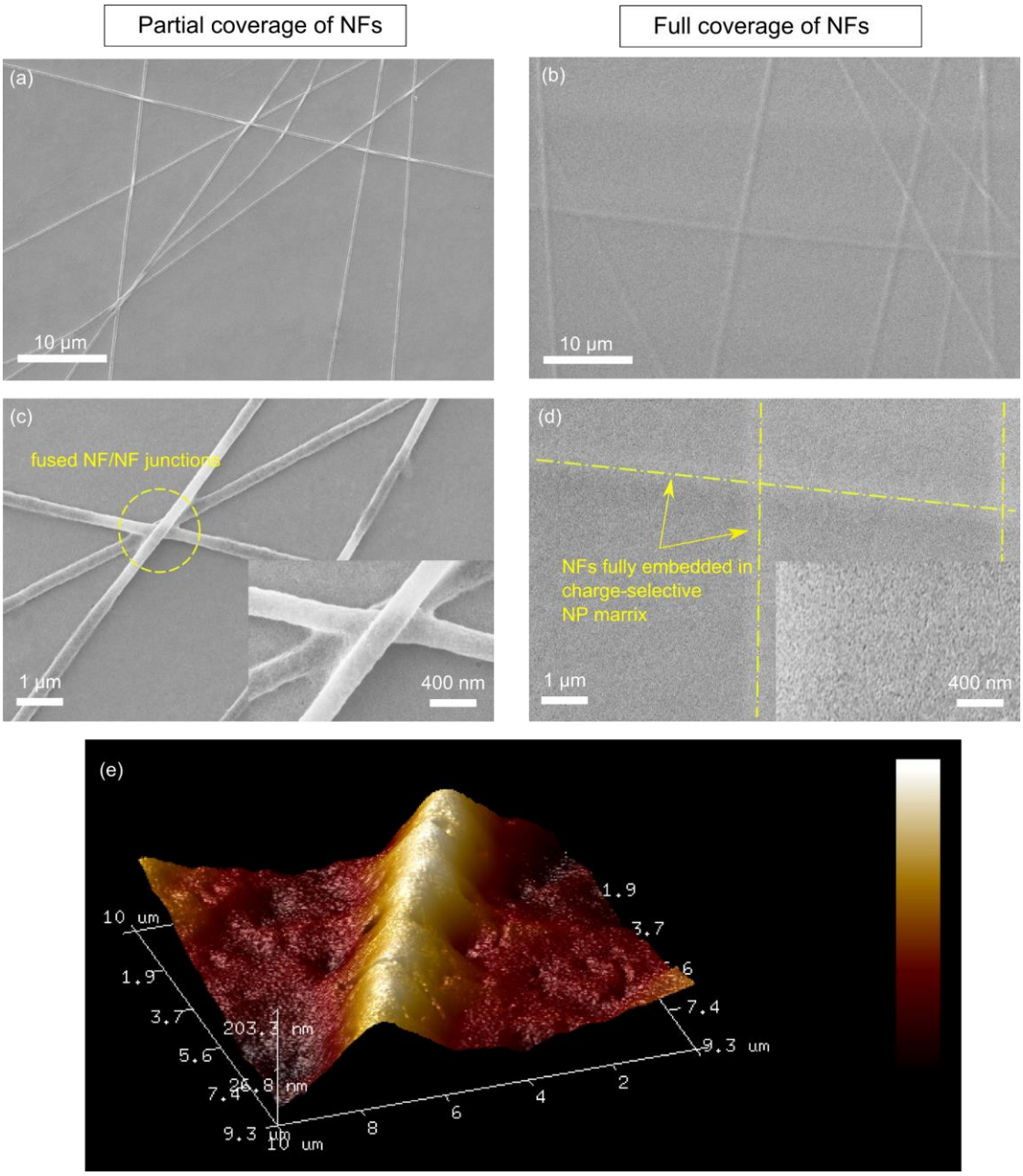


**Figure 3.3:** (a-d) SEM micrographs of metallized NFs coated with ZnO NPs; (a) a thin coating of NPs using a diluted solution, (b) a thick coating of NPs using multiple coatings from an un-diluted solution, (c) and (d) high-magnification micrographs of the same samples shown in (a) and (b). (e) 3D AFM image of NFs fully covered with ZnO NPs, using multiple coatings from an un-diluted solution.

#### 3.2.2.1.2 Sheet Resistance and Optical Transmittance

Figure 3.4(a) shows typical optical transmittance spectra of composite NF TCs with ZnO NPs as the electron-selective matrix. Performances of $R_s$ = 36.7 Ω/□ at $T$ = 86%, $R_s$ = 70.6 Ω/□ at $T$ = 95.3% and $R_s$ = 460 Ω/□ at $T$ = 97.5% are obtained. The performance of the composite TCs is shown on the sheet resistance-transmittance map, in comparison with those of uncoated metallized TCs and ITO. Composite TCs using ZnO NPs have performances superior to ITO, and comparable to the original uncoated TCs.

Figure 3.5 shows the evolution of sheet resistance and optical transmittance through successive coatings of ZnO NPs. The sheet resistance of the original NF TC is reduced by 16.4% after the first layer, consisting of a thin coating of ZnO from the diluted solution (Figure 3.3(a)). The decrease in sheet resistance continues, although with a decreasing rate, through more coatings of ZnO. The sheet resistance after 4 successive layers is 89.9 Ω/□, 22.5% less than the original value of 116 Ω/□ for the uncoated NF TC. The original noticeable decrease after the coating of a thin layer suggests that the formation of fused NF/NF junctions have a major contribution (Figure 3.3(c)). The decrease in sheet resistance can also be attributed to (1) the additional annealing of metallized NFs after every coating (see Section 2.3.2.2 for the detailed discussion) as well as (2) the emergence of inter-fiber charge conduction paths due to the formation of planar ZnO thin films. A remarkable characteristic observed in Figure 3.5 is that the optical transmittance does not decrease through multiple coatings. In fact, in most of the samples, optical transmittance increases by ~3-6% after the first layer of ZnO coating (from the diluted solution). The values of transmittance typically keep increasing over the subsequent coatings from the undiluted solution, with an additional 2-5% increase after another 4 layers of ZnO NPs (to provide a measure of statistical accuracy of this trend, normalized values of $R_s$ and

*T* are provided in Figure B.1 for multiple samples). The increase in optical transmittance can be attributed to (1) the anti-reflective quality of ZnO nanostructure (previously shown for silicon[148, 149] and dye-sensitized[150, 151] solar cells), (2) the decrease in the microstructural defects such as grain boundaries in the ZnO film, because of the annealing step carried out after each coating, and (3) the decrease in the average NF diameter as a result of the same annealing process (Section 2.3.2.2). This characteristic is valuable in the introduced composite TCs, as it enables us to achieve the reduction in the surface roughness of the TCs through multiple coatings (one of the motivations discussed in Section 23.1), while improving the sheet resistance and the optical transmittance.

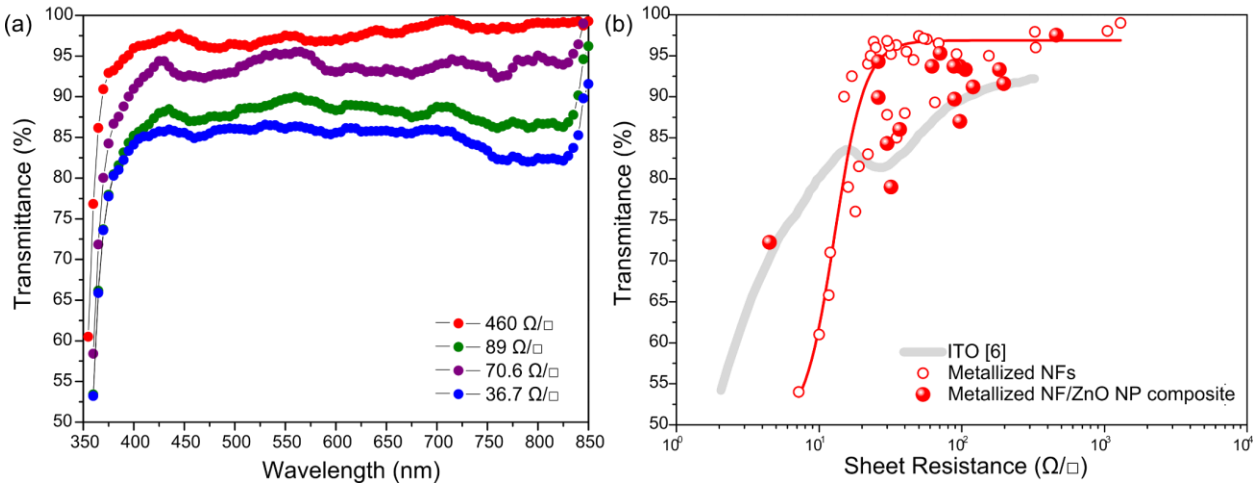


**Figure 3.4:** (a) Optical transmittance spectra of composite nanofibrous TCs using ZnO NPs as an electron-selective matrix, for sample TCs with various sheet resistances. (b) Sheet resistance vs. optical transmittance (at 550 nm) for the composite TCs, shown in comparison with uncoated metallized NF TCs and ITO.

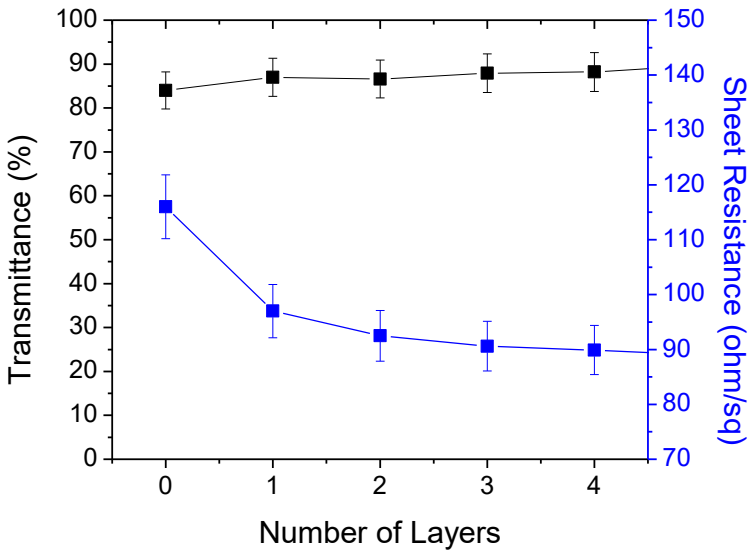


**Figure 3.5:** The evolution of sheet resistance and optical transmittance (at 550 nm) of the composite TCs through the coating of successive layers of ZnO NPs.

### 3.2.2.2 Zinc Oxide Films Fabricated through Sol-Gel Process as Electron-Selective Matrices

#### 3.2.2.2.1 Microstructure

Figure 3.6(a) shows the SEM micrograph of a composite NF TC with a single-layer coating of sol-gel ZnO. In contrast to the ZnO NPs (Figure 3.3), here the ZnO layer dos not cover the surface uniformly, but forms a preferential coverage with two distinct areas (bright and dark areas on Figure 3.6(a)). The preferential coating is a result of higher surface energy and lower vapor pressure of the solvent, resulting in slower evaporation of the solvent during the annealing process. Figure 3.6(b-d) show high-magnification SEM images of different areas indicated on Figure 3.6(a). The microstructure consists of an undisrupted coating of ZnO along the nanofibers and at NF/NF junctions (darker contrast, corresponding to Figure 3.6(b)), along with coffee-rings formed in inter-fiber areas. The latter consists of distinctive dark and bright

areas which at higher magnification are shown to be the areas covered with ZnO (darker contrast, corresponding to Figure 3.6(c)) surrounded by fringes of uncovered substrate (brighter contrast, corresponding to Figure 3.6(d)), identifiable by the characteristic grain structure of uncovered ITO. An AFM micrograph of a composite NF TC covered with 4 layers of sol-gel ZnO is shown in Figure 3.6(e). The surface roughness over 10×10 μm area is $R_a$ = 182 nm. The roughness value over a 3×3 μm area on the ZnO film is $R_a$ = 54.3 nm. Compared to the undiluted ZnO NP solution (Figure 3.3(e)), the sol-gel ZnO layer has higher surface roughness. This is due to the preferential coverage of the substrate surface by the sol-gel ZnO layer, as discussed above. Comparison of the surface roughness with other composite TCs in this research is discussed in Section 3.4.2.

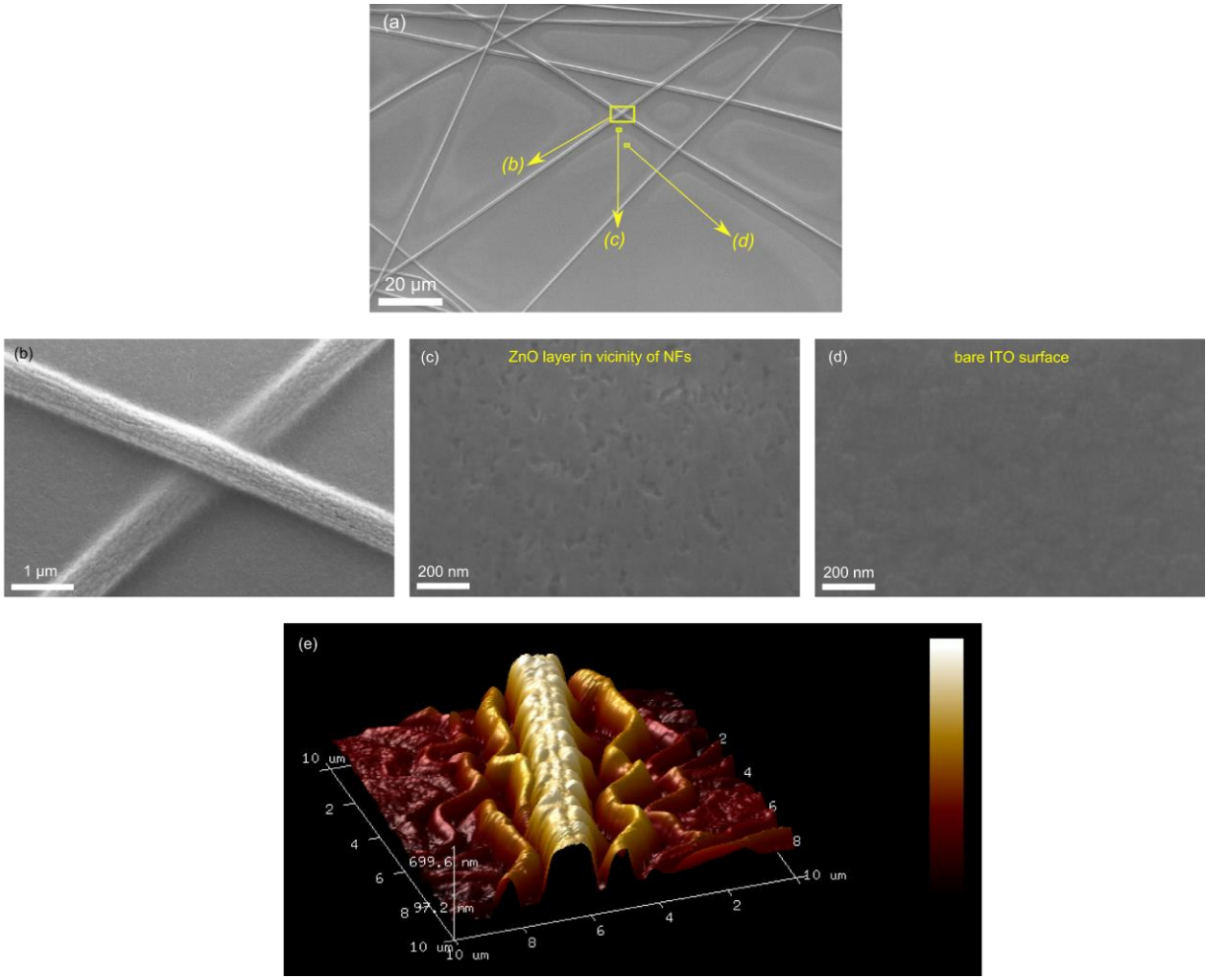


**Figure 3.6:** (a) SEM micrograph of a composite nanofibrous TC with sol-gel ZnO as the electron-selective matrix. (b-d) high-magnification SEM micrographs showing details of the microstructure at various points of the TC, as indicated on (a): (b) NFs partially covered by the ZnO layer, (c) ZnO film in vicinity of the NFs, (d) the bare ITO surface, indicating the ZnO-free area on the TC. (e) 3D AFM image of NFs covered with sol-gel ZnO, after multiple coating and annealing stages through sol-gel process.

#### 3.2.2.2.2 Sheet Resistance and Optical Transmittance

Figure 3.7(a) shows typical optical transmittance spectra of composite NF TCs with sol-gel ZnO layers as the electron-selective matrix. Outstanding combinations of sheet resistance and optical transmittance are achieved, with $R_s$ = 11 Ω/□ at $T$ = 90%, $R_s$ = 15 Ω/□ at $T$ = 93% and $R_s$ = 23 Ω/□ at $T$ = 95%. The performance is shown on the sheet resistance-transmittance map, in comparison with those of uncoated metallized TCs and ITO. The composite TCs using sol-gel ZnO layers have performances far superior to ITO and on a par with their best uncoated NF TC counterparts. High optical transmittance of these composite TCs (typically in the range of 90% to 95% at 550 nm) can be attributed to the preferential coverage of ZnO layers (Figure 3.6(a)). The charge-selective layer is mainly assembled along the length and at the intersections of the nanofibers, resulting in reduced junction resistance (enabled by fused NF/NF junctions, Figure 3.6(b)) but without covering the whole substrate area. After annealing, these TCs can even achieve lower sheet resistances and higher transmittances than the original uncoated TCs, as can be seen in Figure 3.7(b). Further discussion on the effects of annealing will follow.

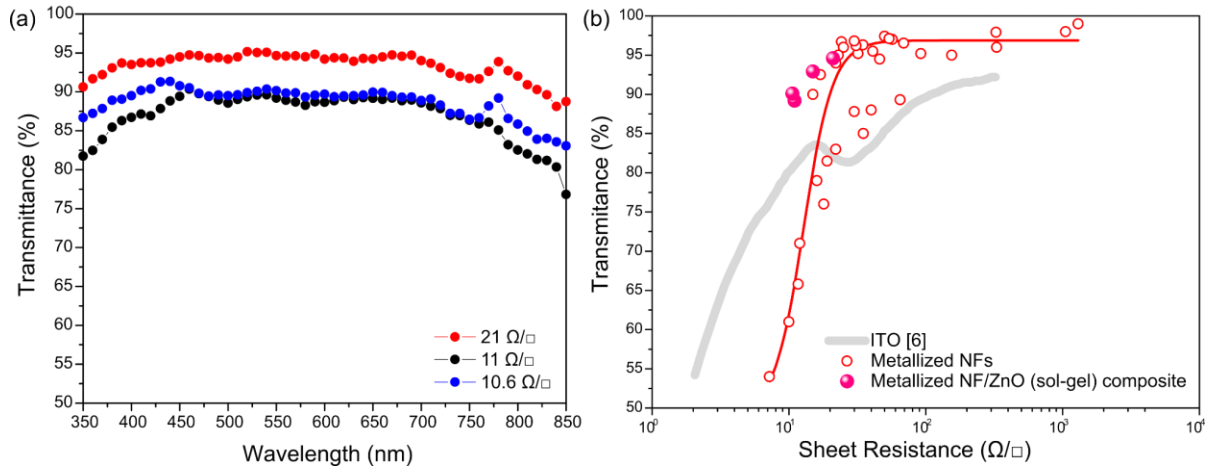


**Figure 3.7:** (a) Optical transmittance spectra of composite nanofibrous TCs using sol-gel ZnO layers as an electron-selective matrix. (b) Sheet resistance vs. optical transmittance (at 550 nm) for the composite TCs, shown in comparison with uncoated metallized NF TCs and ITO.

#### 3.2.2.2.3 Effect of Annealing

Figure 3.8 shows the effect of annealing at different temperatures on sheet resistance and optical transmittance of composite sol-gel ZnO NF TCs. The results for an uncoated metallized NF TC put through the same annealing procedure is also shown as a reference (hollow circles). The microstructures of the TCs after annealing at three selected temperatures within this range are shown in Figure 3.9. The sheet resistance of the composite TCs decreases with increasing the temperature. This is due to increasing crystallization of ZnO with increasing temperature [146, 152], as well as the continued annealing of the gold shell of the NFs, as discussed in Section 2.3.2.2. Optical transmittance of the composite TCs shows little change. Figure 3.9 shows the evolution of the microstructure of a composite TC after annealing at 100, 250 and 300 °C. Annealed at a low temperature (100 °C, Figure 3.9(a, d, g)), the ZnO precursor shows a distinct coffee ring effect characterized by preferential coating around the fibers as well as small

droplets scattered over inter-fiber areas. By increasing the temperature, the coffee-ring effect is alleviated through the coalescence of the small droplets and overall mass transfer towards the fibers. At higher temperatures, ZnO is also crystallized to a higher degree [146], giving the TC an outstanding combination of sheet resistance and transmittance.

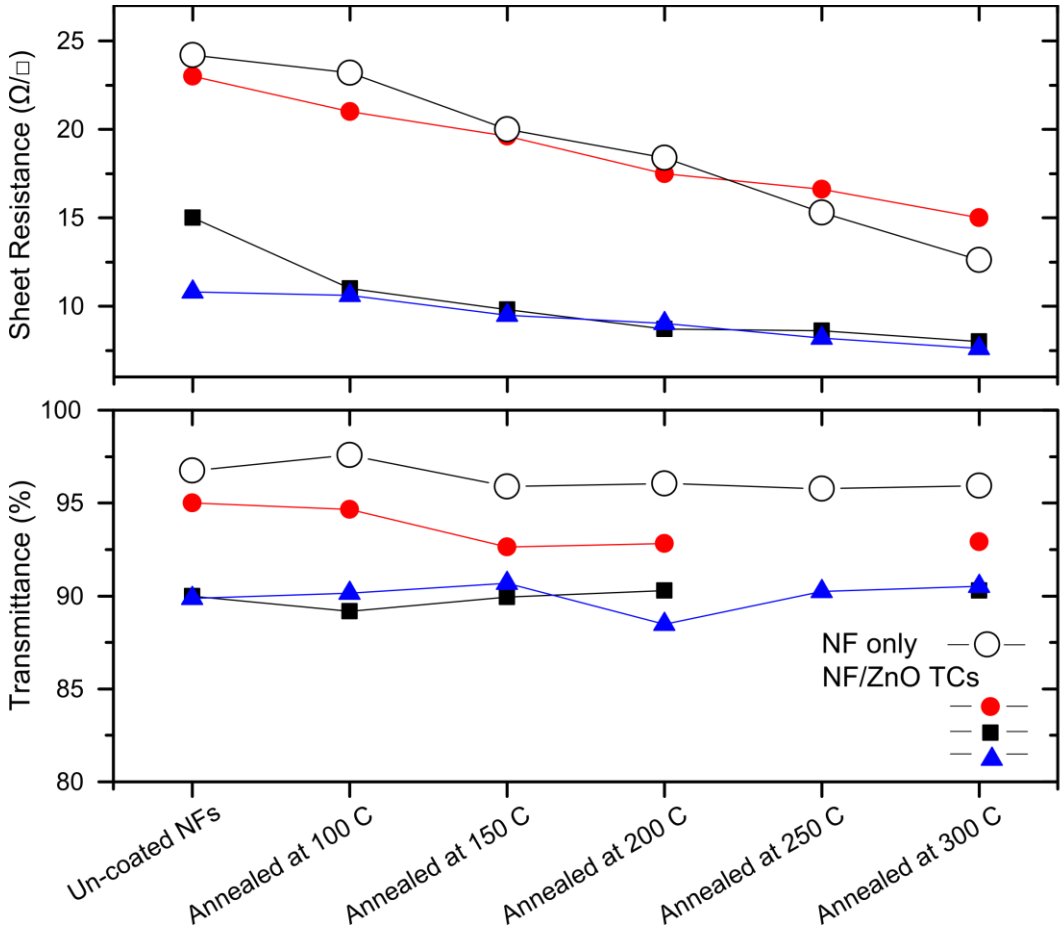


**Figure 3.8:** The effect of annealing at different temperatures on sheet resistance and optical transmittance (at 550 nm) of composite NF TCs using sol-gel ZnO layers as electron-selective matrices. The open circle represents the evolution of uncoated metallized NF TCs put through the same annealing procedure. The lines connecting data points are provided as a guide for the eyes.

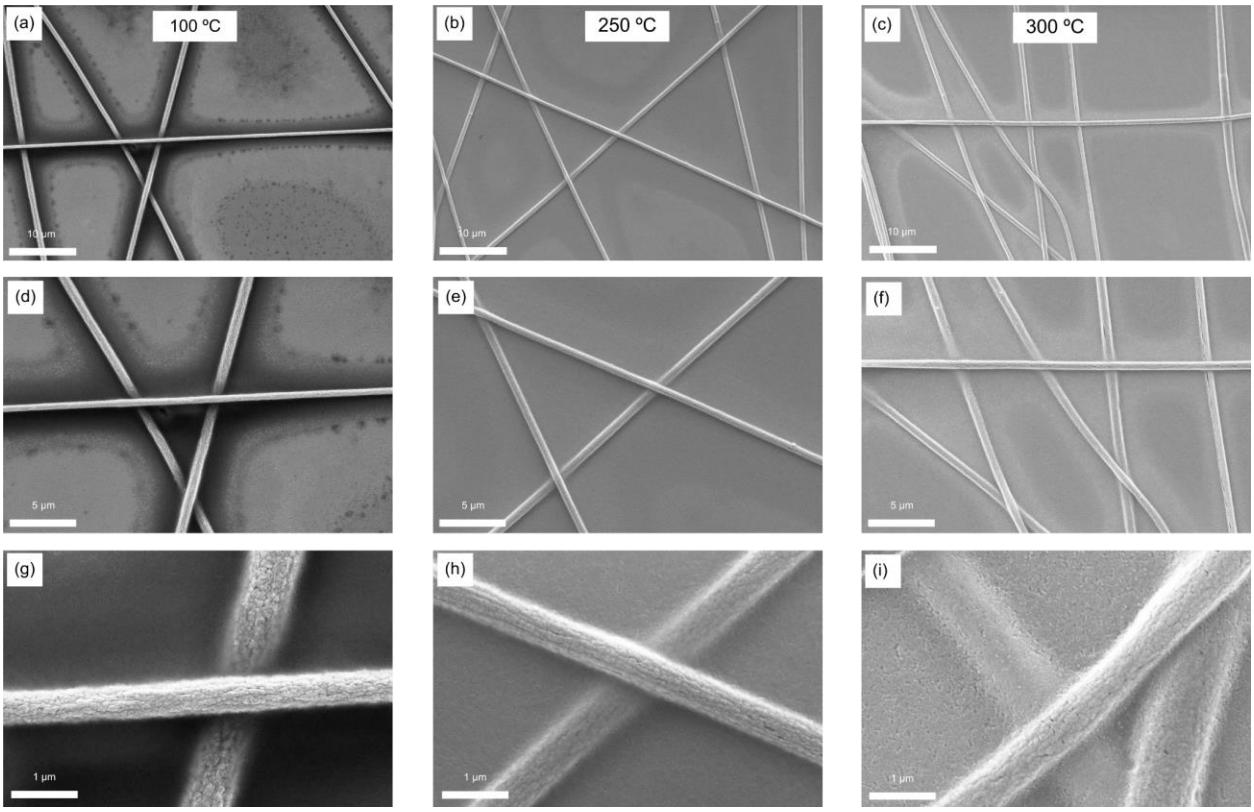


**Figure 3.9:** SEM micrographs of the NF TCs coated with sol-gel ZnO layers annealed at different temperatures, showing the evolution of the microstructure as the effect of annealing. Microstructures are shown at three magnifications after annealing at 100 C (a, d, g), 250 C (b, e, h) and 300 C (c, f, i).

### 3.2.2.3 Molybdenum Oxide Films Fabricated through Sol-Gel Process as Hole-Selective Matrices

#### 3.2.2.3.1 Microstructure

Figure 3.10(a) shows the SEM micrograph of a composite NF TC with a single-layer coating of $MoO_3$ hole-selective matrix fabricated through sol-gel process. As in the case of sol-gel ZnO (Figure 3.6(a)), the $MoO_3$ layer has formed a preferential coverage over the substrate, with distinct areas of bright and dark contrasts. High-magnification SEM images of the areas indicated on Figure 3.10(a) are shown in Figure 3.10(b) and (c). The coffee-ring effect is

alleviated through thermal annealing (Section 3.2.2.3.3). Figure 3.10(d) and (e) provide a comparison between composite TCs made with single-layer and multiple-layer (4 successive layers) coatings of $MoO_3$. Multiple coating has resulted in an increased coverage of the NFs. This is however at the cost of decreased optical transmittance (Section 3.2.2.3.2). An AFM micrograph of a TC covered with 4 layers of sol-gel $MoO_3$ is shown in Figure 3.10(f). The surface roughness over 10×10 μm area and a 3×3 μm sub-area on the ZnO film are $R_a$ = 170 nm and $R_a$ = 12.3 nm, respectively. Comparison of the surface roughness with other composite TCs introduced in this research will be discussed in more detail in Section 3.4.2.

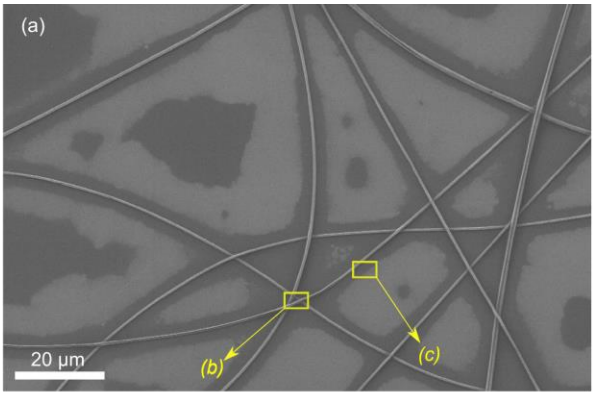
(a)
20 μm
(b)
(c)

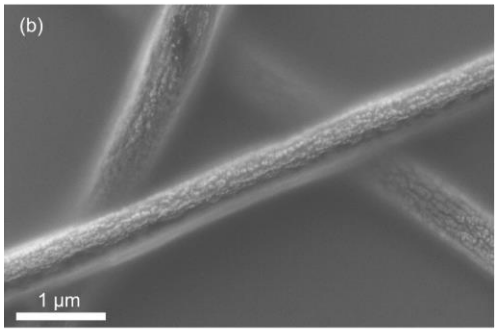
(b)
1 μm

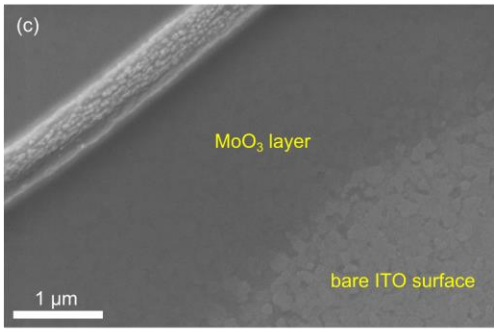
(c)
MoO3 layer
bare ITO surface
1 μm

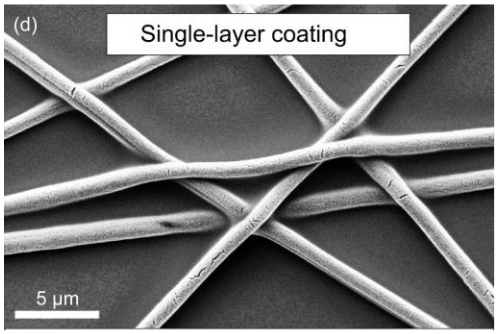
(d)
Single-layer coating
5 μm

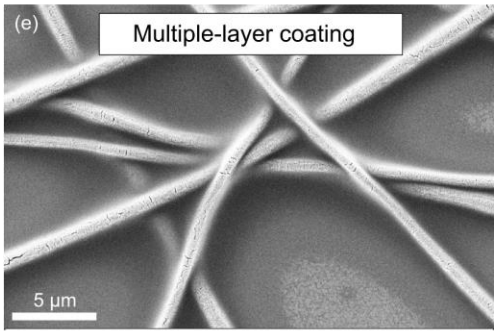
(e)
Multiple-layer coating
5 μm

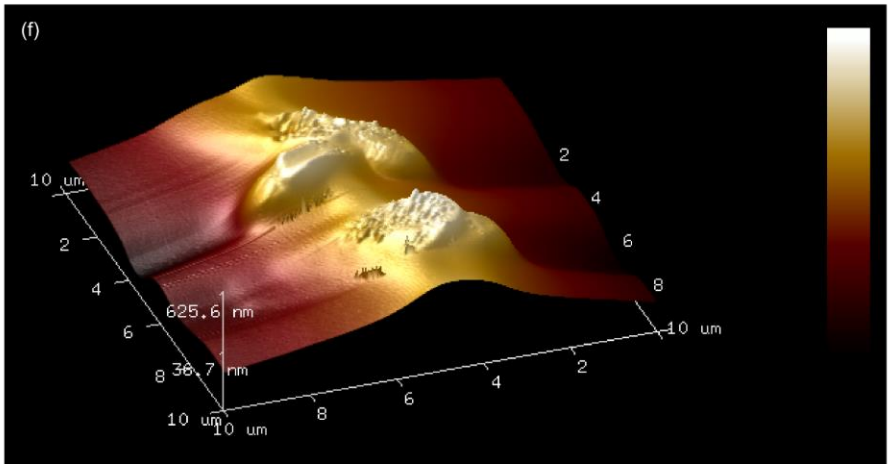
(f)
625.6 nm
38.7 nm
10 um
10 um
10 um
10 um

**Figure 3.10:** (a) SEM micrograph of a composite nanofibrous TC with sol-gel $MoO_3$ as the hole-selective matrix. (b, c) high-magnification SEM micrographs showing details of the microstructure at various points of the TC, as indicated on (a): (b) NFs partially covered by the $MoO_3$ layer, (c) Microstructure at the vicinity a NF, showing two distinct areas covered with and free of the $MoO_3$ layer. (d, e) Micrographs of composite TCs with single-layer and multiple-layer coatings of $MoO_3$. (e) 3D AFM image of NFs covered with sol-gel $MoO_3$, after multiple coating and annealing stages through sol-gel process.

#### 3.2.2.3.2 Sheet Resistance and Optical Transmittance

Figure 3.11(a) shows typical optical transmittance spectra of composite NF TCs with sol-gel $MoO_3$ layers as the hole-selective matrix. Performances of $R_s$ = 12.5 Ω/□ at $T$ = 91%, $R_s$ = 22.1 Ω/□ at $T$ = 93% and $R_s$ = 35.5 Ω/□ at $T$ = 94% are obtained. The sol-gel $MoO_3$ TCs have performances superior to ITO and on a par with their uncoated NF TC counterparts (Figure 3.11(b)). This is remarkable as, unlike ZnO, $MoO_3$ is not intrinsically transparent. High optical transmittance of the TCs is due to the preferential coverage of the surface (Figure 3.10(a), similar to the case of sol-gel ZnO, discussed in Section 3.2.2.2.2) and is enhanced through annealing as will be discussed in Section 3.2.2.3.3.

Figure 3.12 shows the evolution of sheet resistance and optical transmittance through successive coatings of sol-gel $MoO_3$. Normalized values of $R_s$ and $T$ are provided in Figure B.2 for multiple samples. The sheet resistance of the original NF TC is reduced from 21 Ω/□ to 16 Ω/□ after the first layer (23% reduction). The decrease in sheet resistance continues through more layers of $MoO_3$, resulting in $R_s$ = 15.6 Ω/□ after 4 layers. The improvement of sheet resistance through successive layers can be attributed to: (1) the formation of fused NF/NF junctions (Figure 3.10(e)), (2) increased conductivity of the $MoO_3$ film through annealing after each coating, (3) additional annealing of metallized NFs after every coating. The last two factors

will be discussed further in Section 3.2.2.3.3. Unlike the case of ZnO layers (Figure 3.5), the addition of successive $MoO_3$ layers leads to a linear drop in optical transmittance, due to lack of intrinsic transparency in the case of the latter. Nonetheless, high-performance hole-selective composite TCs, with 90-95% transparency, can be fabricated using a single layer coating of $MoO_3$ followed by heat treatment. Such TCs can be suitable for application as a top transparent electrode in organic photovoltaic devices.

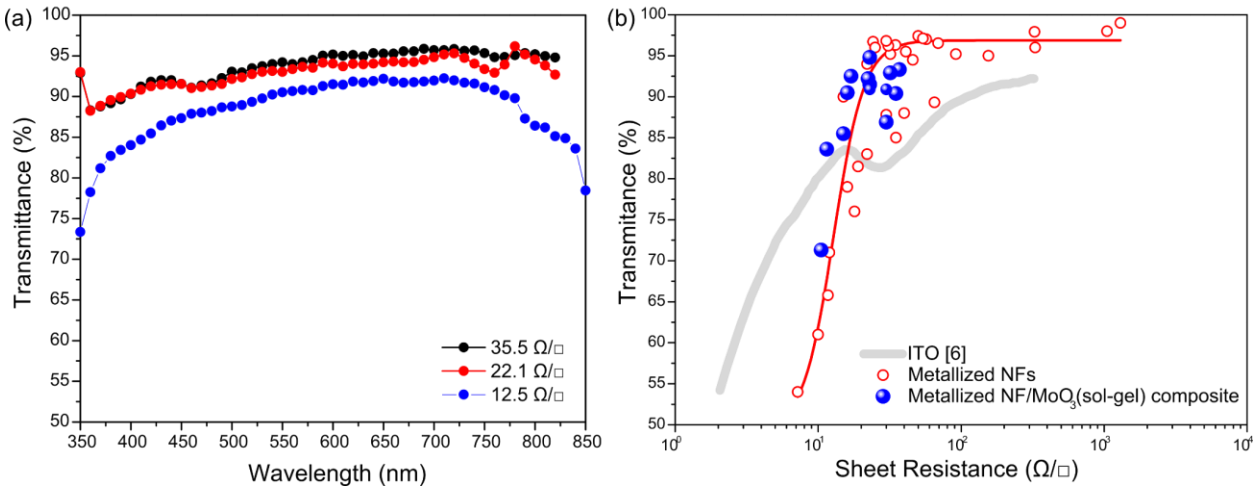


**Figure 3.11:** (a) Optical transmittance spectra of composite nanofibrous TCs using sol-gel $MoO_3$ layers as a hole-selective matrix. (b) Sheet resistance vs. optical transmittance (at 550 nm) for the composite TCs, shown in comparison with uncoated metallized NF TCs and ITO.

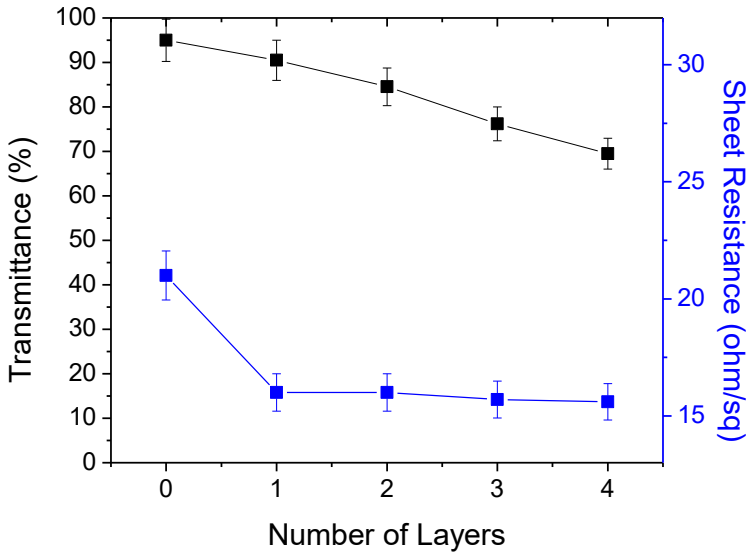


**Figure 3.12:** The evolution of sheet resistance and optical transmittance (at 550 nm) of the composite TCs through the coating of successive layers of sol-gel $MoO_3$.

#### 3.2.2.3.3 Effect of Annealing

Figure 3.13 shows the effect of annealing on sheet resistance and optical transmittance of composite NF TCs using sol-gel $MoO_3$ layers as hole-selective matrices. The microstructures of the annealed TCs are shown in Figure 3.14. As in the case of the ZnO-coated composite TCs, the sheet resistance decreases with increasing the temperature. Lin et have shown that the elimination of the absorbed water, evaporation of the solvents and oxidation of organic residues take place during annealing the films at temperatures up to 300 °C [147]. Even though the crystallization of the amorphous $MoO_3$ film does not begin at temperatures lower than 360 °C [137, 147], the removal of residual solvents and organics presumably contributes to the improvement of sheet resistance at higher temperatures. Given the similar decline in the uncoated NF TCs (hollow circles in Figure 3.13), the continued annealing of the gold shell of the NFs can also be a contributing factor, as discussed previously. The evolution of optical

transmittance of the composite $MoO_3$-coated TCs follows a characteristic trend, different to that of the uncoated TCs or the ZnO-coated composite TCs (Figure 3.8); this trend is characterized by an original decline in transmittance values up to 150 °C annealing temperature, followed by improvement at higher temperatures. As seen in Figure 3.13, the transmittance at 550 nm suffers an original drop from (typically) $T \sim 95\%$ to $T < 90\%$ for TCs annealed at 150 °C. This loss is mostly recovered at higher temperatures, with the transmittance approaching $T = 90 – 95\%$ for the samples annealed at 250 – 300 °C. Girotto et al. [137] have shown that the photovoltaic performance metrics ($V_{OC}$, $I_{SC}$, $FF$) of organic solar cells using sol-gel $MoO_3$ layers as hole injection layers improve through 175 – 275 °C annealing temperatures. They have reported temperatures of 250 – 275 °C as resulting in the best photovoltaic response. The same temperature range has led to the highest optical transmittance in our TCs. Figure 3.14 shows the microstructure of a composite TC after annealing at 100, 250 and 300 °C. The general effect of the annealing temperature is similar to that of sol-gel ZnO TCs (Section 3.2.2.2.3 and Figure 3.9). Annealed at a low temperature, the $MoO_3$ precursor shows a distinct coffee ring effect characterized by preferential coating around the fibers and isolated coated areas the inter-fiber regions (dark areas in Figure 3.14(a, d, g)). The effects of increasing temperature are similar to the case of sol-gel ZnO. Considering that the evaporation of the solvents takes place between 150 – 175 °C [147], the mass transfer from the inter-fiber regions towards the fibers presumably happens mostly in this temperature range. This claim can be supported by the considerable expansion of the dark regions observed in SEM micrographs from 100 °C (Figure 3.14(a)) to 250 °C (Figure 3.14(b)), which accounts for the decline of optical transmittance at annealing temperatures up to 150 °C. The film $MoO_3$ film thickness starts decreasing in 175 – 275 °C annealing temperatures [137, 147] which is a major factor in increased optical transmittance

beyond 150 °C. Annealing at a temperature between 250 - 300 °C can therefore be employed to improve the sheet resistance of the composite NF TCs coated with $MoO_3$ encapsulating layers, increase the coverage uniformity of the layers, and recover the optical transmittance of the composite $MoO_3$-coated NF TCs to a level close to that of uncoated TCs.

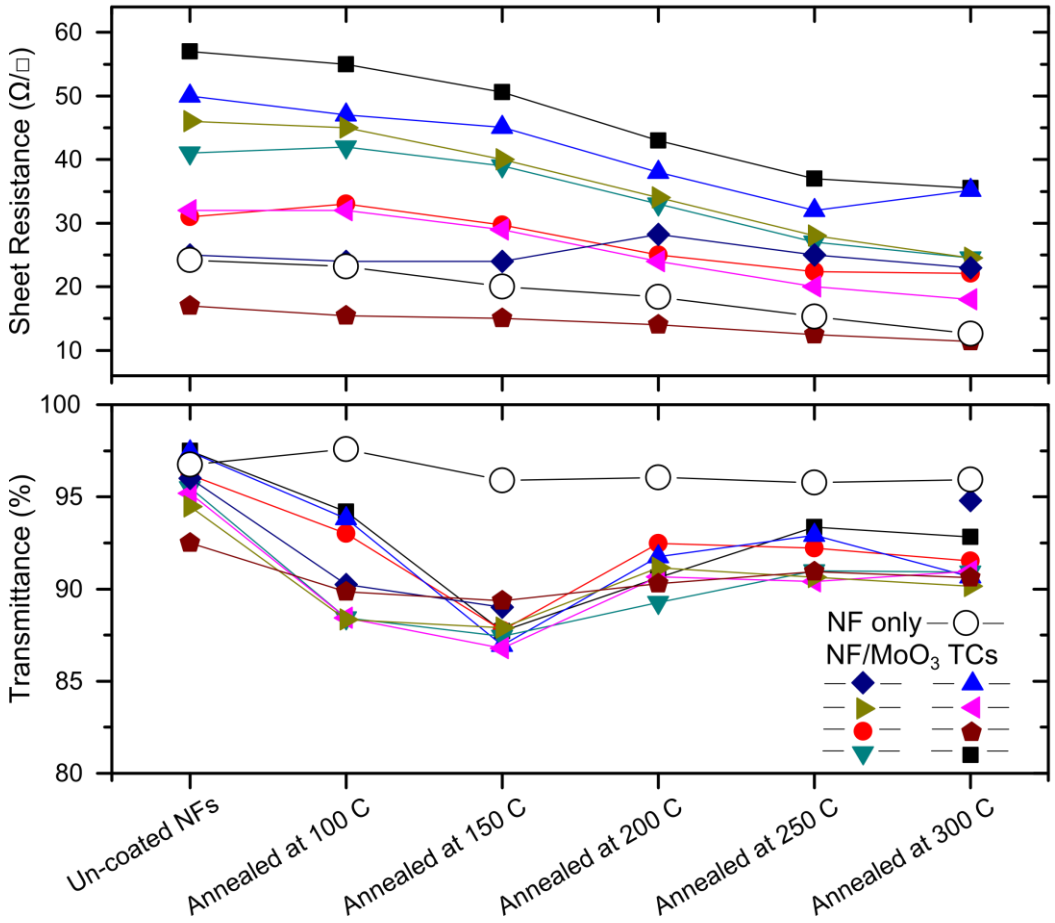


**Figure 3.13:** The effect of annealing at different temperatures on sheet resistance and optical transmittance (at 550 nm) of composite NF TCs using sol-gel $MoO_3$ layers as hole-selective matrices. The open circle represents the evolution of uncoated metallized NF TCs put through the same annealing procedure. The lines connecting data points are provided as a guide for the eyes.

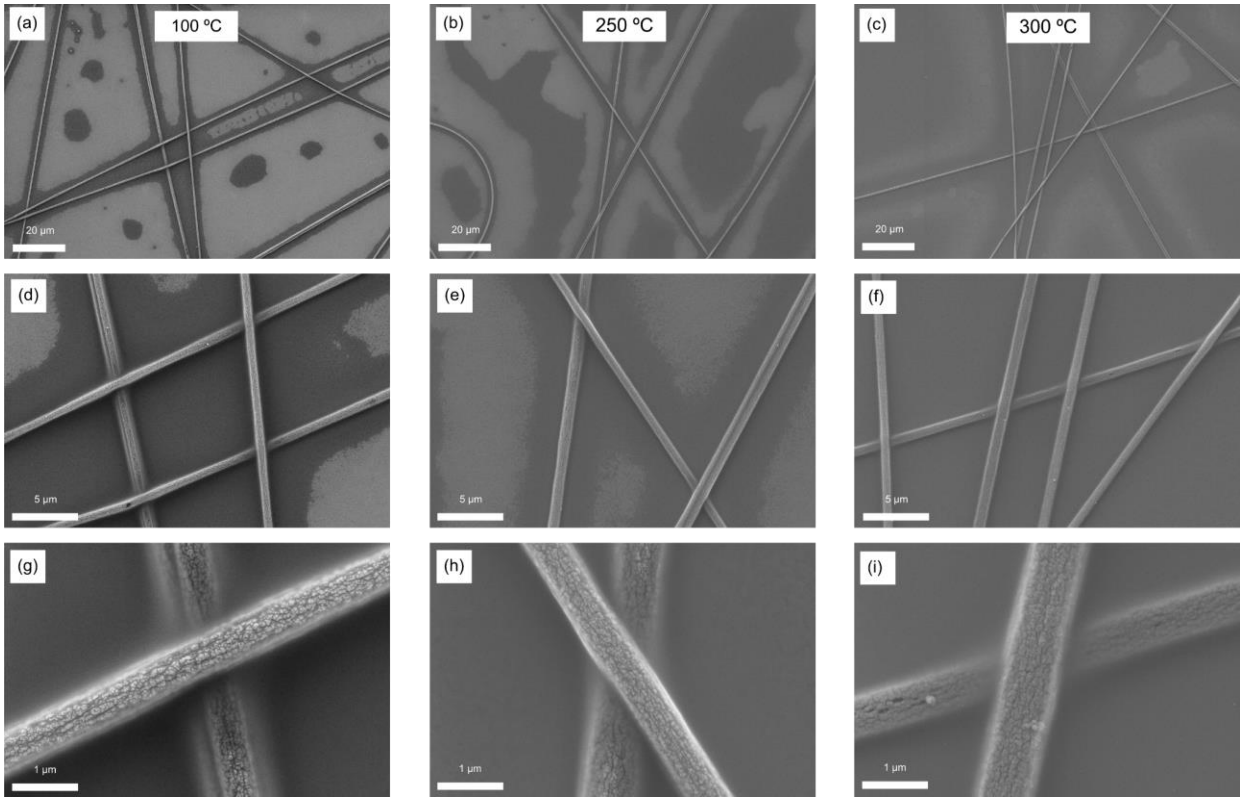


**Figure 3.14:** SEM micrographs of the NF TCs coated with sol-gel $MoO_3$ layers annealed at different temperatures, showing the evolution of the microstructure as the effect of annealing. Microstructures are shown at three magnifications after annealing at 100 C (a, d, g), 250 C (b, e, h) and 300 C (c, f, i).

## 3.3 Stretchable Transparent Conductors Based on Charge-Selective Layers

In this section, we focus on methods to enable repeatable electromechanical stretchability for charge-selective composite TCs. Three structures are introduced. We start with a simple approach, consisting of thin films of hole-selective PEDOT:PSS layers spun on pre-stretched PDMS in Section 3.3.2. Next, we will introduce stretchable charge-selective TCs, which build upon the metallized electrospun NFs. To render the composites of metallized NFs in charge-selective matrices flexible, a special architecture is suggested by embedding the NFs near the surface of a stretchable PDMS substrate. This will provide a framework for a stretchable low-roughness TC based on the metallized electrospun NFs. A charge-selective matrix is integrated into this framework either via direct spin-coating of a charge-selective ink on top of the partially exposed NFs (Section 3.3.2.2), or via fabrication and subsequent release of the composite NF TC on and from an intermediary glass substrate (Section 3.3.2.3). Details of the fabrication process and the performance results are discussed below for each of these TCs. A comparison of the stretchability of different TCEs introduced in this research, with one another as well as with selected results from the literature, will be discussed in Section 3.4.3.

### 3.3.1 Experimental

*PEDOT:PSS Films on PDMS Substrates*: Figure 3.15(a) shows the schematic of the procedure used to fabricate the TCEs on pre-stretched substrates. PDMS substrates are prepared by mixing Sylgard 184 (10:1 volume ratio between base and curing agent), pouring in a leveled petri dish, degassing in vacuum and curing at 70 ˚C. The substrates are mechanically pre-stretched to desired pre-strain value (5-50%) and fixed on a glass slide. The PDMS substrates are then treated in $O_2$ plasma (30 s at 150 W, 40 sccm $O_2$ flow, 300 mbar chamber pressure) to

activate the hydrophobic surface and enable the spin coating of PEDOT:PSS. The solution is spun at 1000 rpm for 60 s, and the samples are dried at 110 ˚C for 15 min. Finally, the pre-strain is released to provide the stretchable TCE.

*Composite of Metallized Nanofibers in a Matrix of PEDOT:PSS Embedded near the Surface of PDMS Substrates*: The fabrication process is schematically shown in Figure 3.19(a). The metallized NFs are temporarily transferred onto a flat substrate (Si or glass) and mechanically stabilized by adding a drop of methanol. A thin layer of PDMS is poured on the NFs, cured, and peeled off the temporary substrate, providing a PDMS film with NFs partly-embedded on the surface. PEDOT:PSS is spun (1000 rpm, 60s) on the partly-embedded NFs (the bottom row in Figure 3.19(a)). The surface of the NF/PDMS electrode is exposed to $O_2$ plasma before spin coating.

*Composite of Metallized Nanofibers/ Zinc Oxide Nanoparticles Embedded near the Surface of PDMS Substrates*: The fabrication process of is shown schematically in Figure 3.21(a). A glass substrate is mounted on the spin coater chuck and covered with the ZnO NP suspension (80 mg ZnO in 1 ml chloroform, diluted in methanol with 1:20 volume ratio). After placing and soaking the NF mesh on the wet substrate, spin coating is started (3000 rpm, 30s) to provide NFs, partly buried in NPs. PDMS is poured and cured against the surface and peeled off the glass to provide the final stretchable TCE.

### 3.3.2 Results and Discussion

#### 3.3.2.1 PEDOT:PSS Films on PDMS Substrates

Figure 3.15(b-e) shows the optical micrographs of the samples with different pre-strain values. The profilometry line scan is also shown for each sample. Releasing the pre-strain results in the formation of surface waves with the wavelength of ~10-20 μm. Increasing the pre-strain results in decreased wavelength and increased amplitude of the surface waves. At higher pre-strains the release also causes the formation of longitudinal cracks, due to tensile strains in transverse direction because of Poisson's effect.

The optical transmission spectra of TCEs with different pre-strain values are shown in Figure 3.16. Increasing the pre-strain has resulted in decreasing the transmittance because of increased light scattering by the buckled structure, and in increasing the sheet resistance given the increased density of defects, as observed in Figure 3.15.

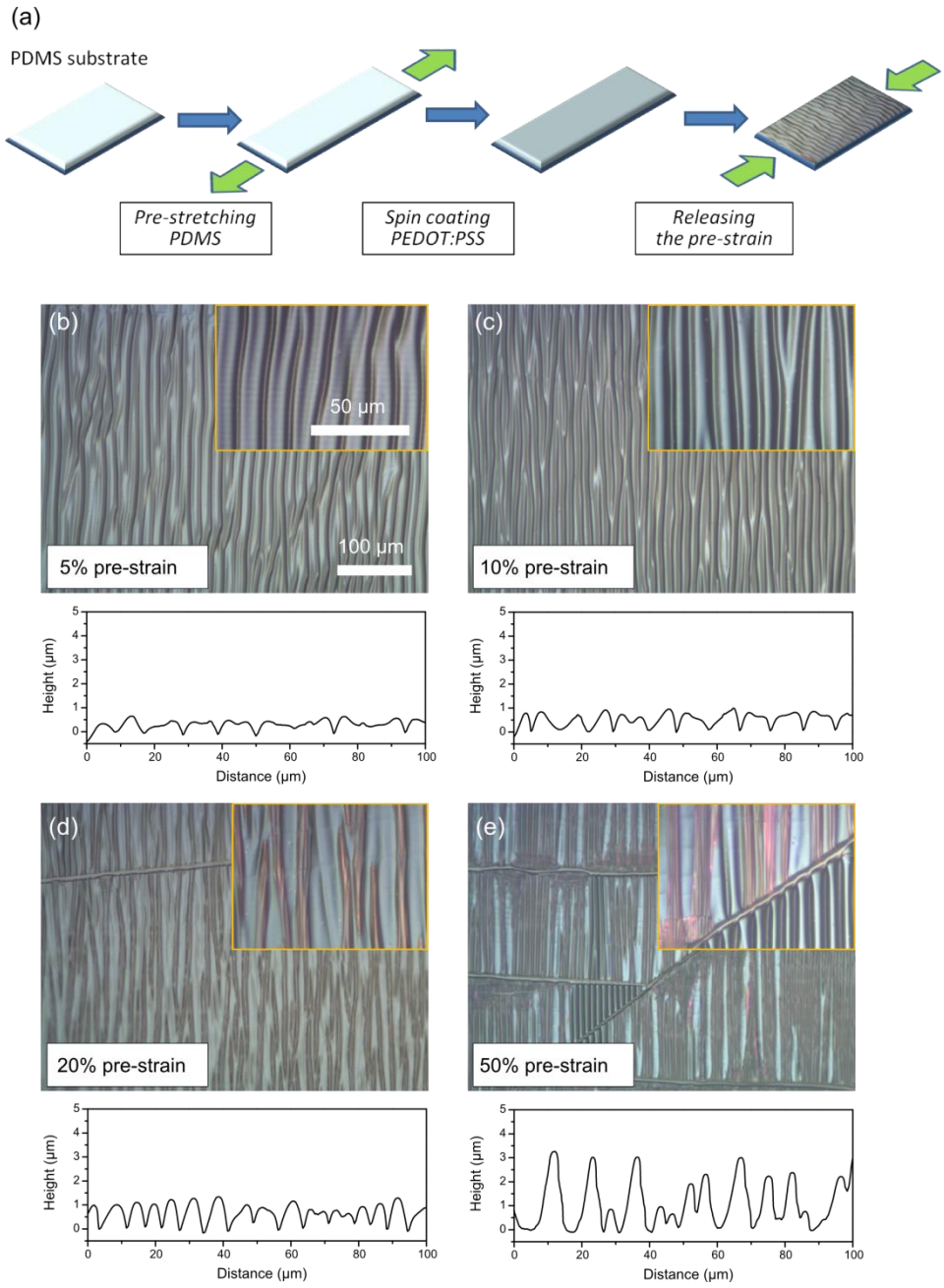


**Figure 3.15:** (a) Schematic procedure for the fabrication of PEDOT:PSS TCEs on stretchable PDMS substrates. (b-e) Optical micrographs of PEDOT:PSS TCEs after releasing the pre-strain, along with corresponding profilometry scans.

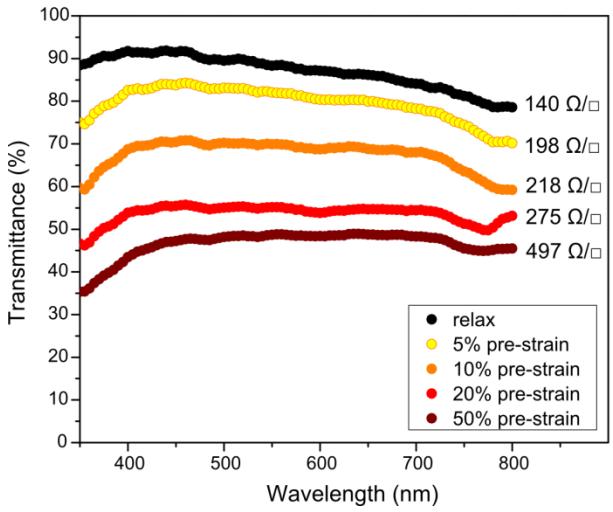


**Figure 3.16:** Optical transmission spectra of PEDOT:PSS TCEs with different pre-strain values.

Figure 3.17(a) shows the relative changes in resistance ($\Delta R/R_0$) with the strain, for specimens with different pre-strain values. The TCs show stable electrical conductance up to the strains equivalent to the original pre-strains, after which the resistance rises rapidly. Typical microstructural evolution of the pre-stretched samples during stretching, is shown in Figure 3.17(b-e). Up to the original pre-strain (in this case 5%), the tensile strain serves to unbuckle the surface waves. Therefore, there is no actual tensile strain imposed on the film, rather, the unbuckling of the waves leads to decrease in electrical resistance[132] (Figure 3.17(c)). Beyond the pre-strain value, perpendicular microcracks form as a result of tensile strain in the film, while transverse surface buckles appear as a result of compressive strains in the perpendicular direction (Figure 3.17(d)). Further increasing the strain leads to delamination of the thin film at the point of the microcracks and eventually to the permanent mechanical failure in the structure (Figure 3.17(e)).

Cyclic endurance of the TCEs is tested for 100 stretching cycles between 0 - 10% strain. Figure 3.18 shows the relative change in electrical conductance ($\Delta G/G_0$) over the cycles. The

close-up of first 5 cycles is shown in the inset. For the sample with 5% pre-strain, there is a maximum in each half-cycle, since the maximum strain is more than the pre-strain value, and hence the electrical resistance (conductance) decreases (increases) at $\varepsilon < 5\%$ before it starts to increase (decrease) at higher strains. For the rest of the TCEs, having pre-strain values equal to or higher than 10%, the conductance increases with increasing strain in each cycle. Samples with >20% pre-strain show negligible changes in resistance over the cycles.

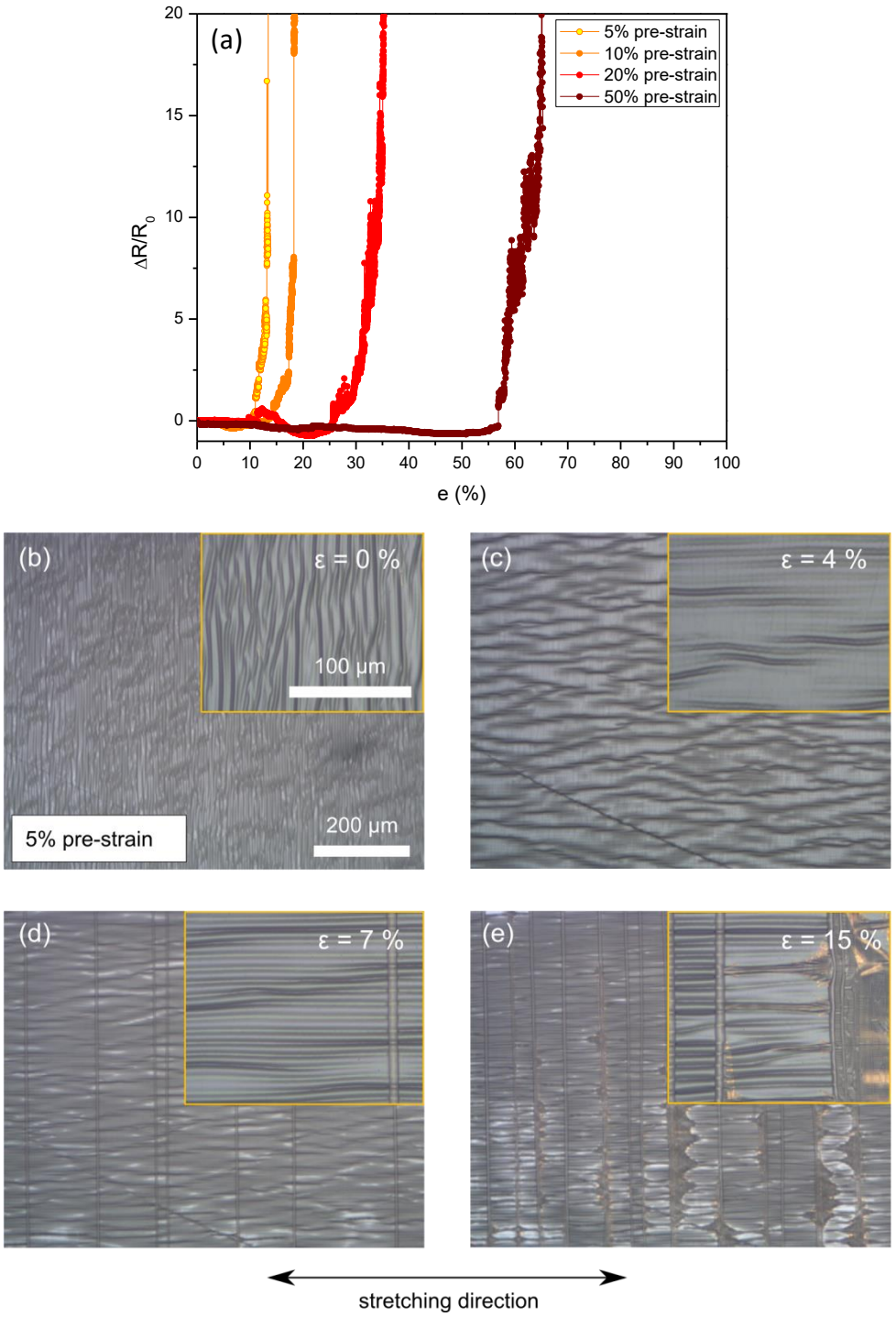


**Figure 3.17:** (a) $\Delta R/R_0$ versus tensile strain for pre-stretched PEDOT:PSS TCEs with different pre-strain values. (b-e) Optical micrographs showing the evolution of microstructure of the TCE at different strains, for a sample with 5% pre-strain.

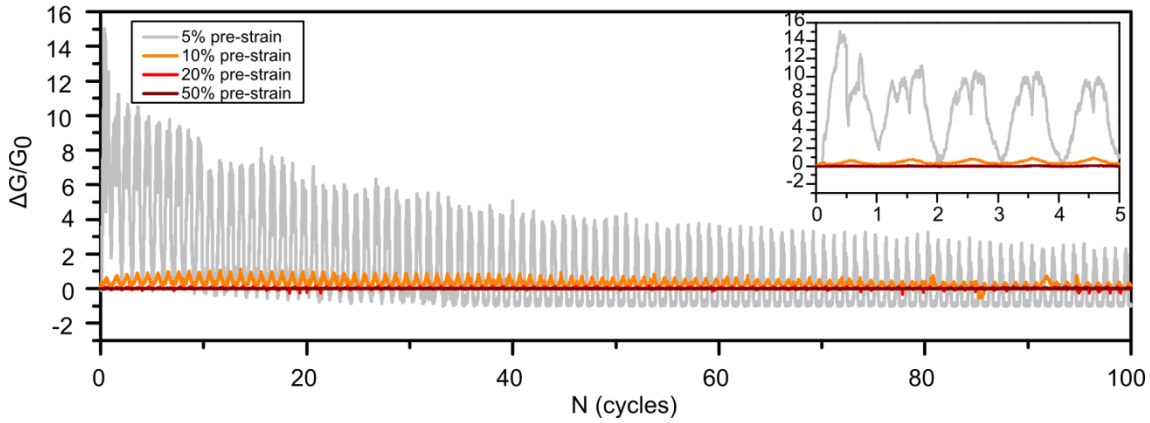


**Figure 3.18:** Cyclic endurance of PEDOT:PSS TCEs with different pre-strain values. Inset shows a close-up of the graphs for first 5 cycles.

### 3.3.2.2 Composite of Metallized Nanofibers in a Matrix of PEDOT:PSS Embedded near the Surface of PDMS Substrates

Fabrication of the TCE is shown in Figure 3.19(a) and described earlier. Figure 3.19(b) and (c) show the SEM micrographs of the TCE before and after the deposition of PEDOT:PSS encapsulating layer. Figure 3.19(d) shows the sheet resistance and transmittance spectra of TCEs made of partly-embedded NFs in PDMS, before the deposition of PEDOT:PSS. Figure 3.19(e) shows the original sheet resistance and transmittance spectra of individual components (PEDOT:PSS and partly-embedded NFs in PDMS) and the resulting bi-layer. The addition of PEDOT:PSS results in more than 73% drop in $R_s$ as the encapsulating layer effectively overs the NF/NF junctions and also provides an extra conduction path in addirion to that of the NFs. The drop in $R_s$ is accompanied by only 16% decrease in optical transmittance (at 550 nm).

Figure 3.20**(**a) shows the variations in $\Delta R/R_0$ versus strain for TCEs based on partly-embedded NFs in PDMS, PEDOT:PSS and the bi-layer of PEDOT:PSS on partly-embedded NFs. PEDOT:PSS film on PDMS shows a sharp rise of resistance at less than 10% strain. TCEs

based on partly-embedded NFs in PDMS can be stretched up to ε ~30%. The curve for the bi-layer falls in between. Examination of the microstructure of the TCEs after 50% strain reveals that the presence of the NFs has alleviated the cracking of the PEDOT:PSS film (Figure 3.20(c)), compared to single PEDOT:PSS layer (Figure 3.20(b)), presumably due to the fact that the NFs now partly accommodate the stress. On the other hand, comparing the microstructures of partly-embedded NFs without (Figure 3.20(d)) and with (Figure 3.20(e)) PEDOT:PSS encapsulating layer, shows that the presence of PEDOT:PSS layer gives rise to the rupture of NFs in the vicinity of cracks in the PEDOT:PSS film (Figure 3.20(e)), hence the decrease in the stretchability of the bi-layer, as compared to the uncoated NFs. It is observed both in Figure 3.20(d) and (e) that the encapsulation of the NFs in PDMS has resulted in the rupture of NFs, as opposed to the case of original metallized NFs (Section 2.3.2.3) which can freely rearrange under the strain.

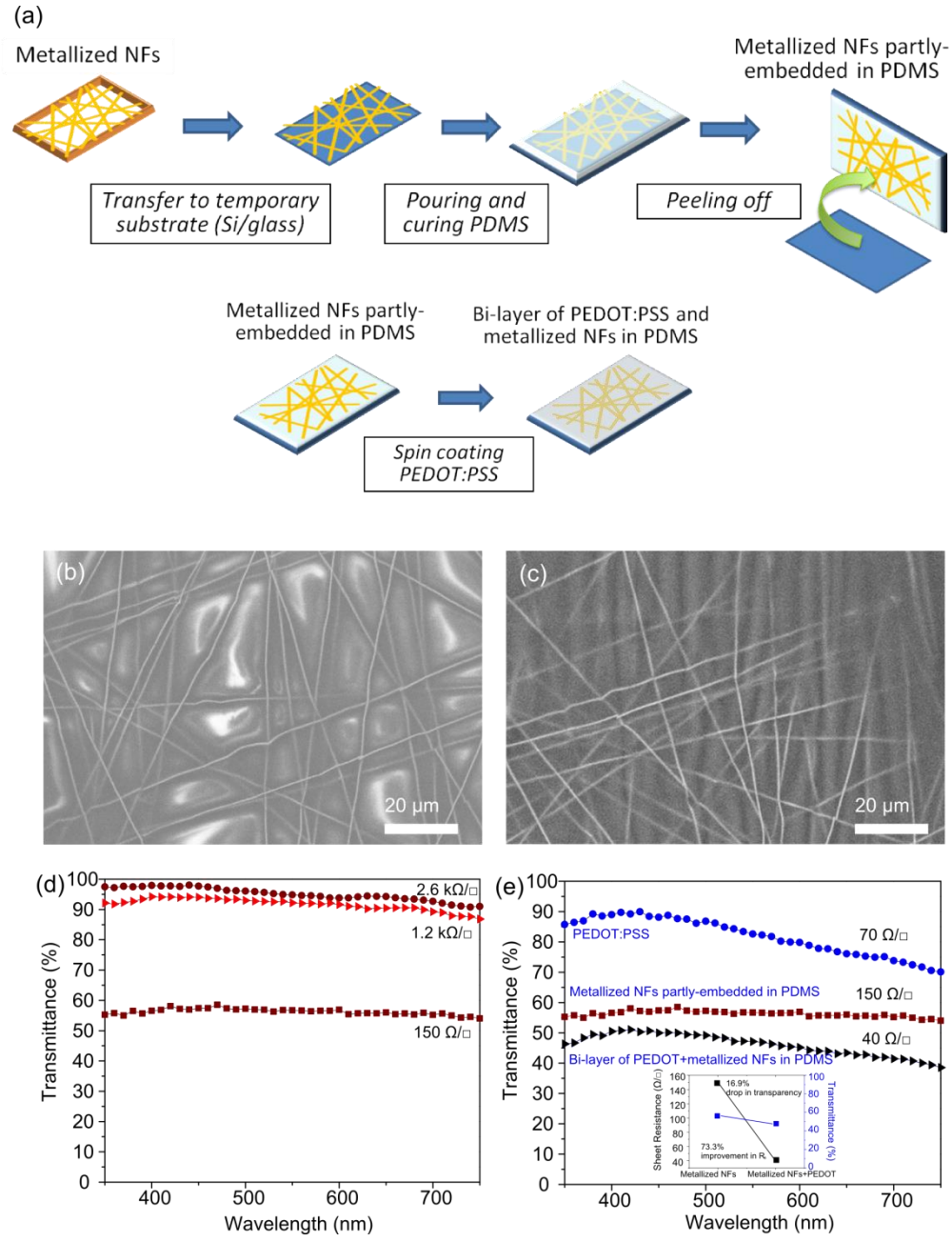


**Figure 3.19:** (a) Schematic procedure for the fabrication of partly-embedded NFs in PDMS, coated with PEDOT:PSS hole-collecting layer. (b) SEM micrograph of NFs partly-embedded in PDMS. (c) SEM micrograph of the bi-layer of PEDOT:PSS on NFs partly-embedded in PDMS. (d) Transmittance and sheet resistance of TCEs based on NFs partly-embedded in PDMS. (e) Variations of sheet resistance and transmittance as a result of creating the bi-layer.

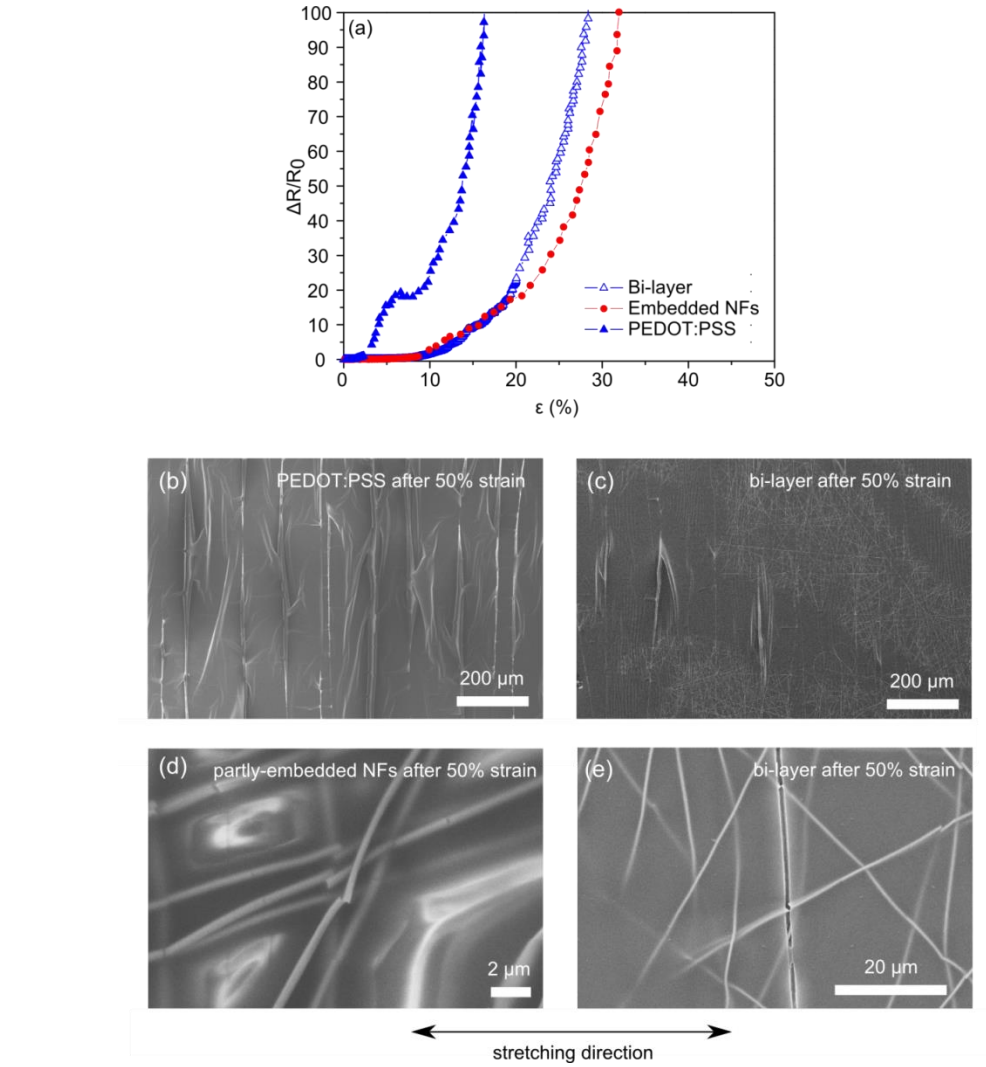


**Figure 3.20:** (a) Variations in $\Delta R/R_0$ versus strain for TCEs based on partly-embedded NFs in PDMS and its bi-layer with PEDOT:PSS. (b-e) SEM micrographs of the TCEs shown in (a), after 50% strain: single PEDOT:PSS layer (a), NFs partly-embedded in PDMS (d) and bi-layer of PEDOT:PSS on partly-embedded NFs (b,e).

#### 3.3.2.3 Composite of Metallized Nanofibers/ Zinc Oxide Nanoparticles Embedded near the Surface of PDMS Substrates

SEM micrographs of the TCE comprising of ZnO-coated NFs, partly-embedded in PDMS are shown in Figure 3.21(b and c) and a 3D AFM micrograph of the surface in Figure 3.21(d). Figure 3.21(e) shows the variations of sheet resistance and transmittance of original metallized NFs through coating and embedding stages. After embedding in PDMS, the TCE shows 63% improvement in $R_s$ compared to original NF TCEs, with < 14% loss of transmittance.

Figure 3.22(a) shows the variations of $\Delta R/R_0$ versus strain for stretchable TCEs based on partly embedded ZnO-coated NFs. The TCE withstands up to 10% strain. Figure 3.22(b-e) show the variations of the microstructure at different strains up to and beyond $\varepsilon$ = 10%. No rupture of the NFs is visible here even at $\varepsilon$ = 50% which suggests that the loss of conductance is not due to permanent rupture in the NFs. Figure 3.23 shows the cyclic endurance of the TCE over 100 stretching cycles from 0-10% strain. Although the TCE becomes non-conductive at $\varepsilon$ > 10%, the conductance at the relaxed state ($\varepsilon$ = 0%) has little change over 100 cycles, indicating reversible stretchability.

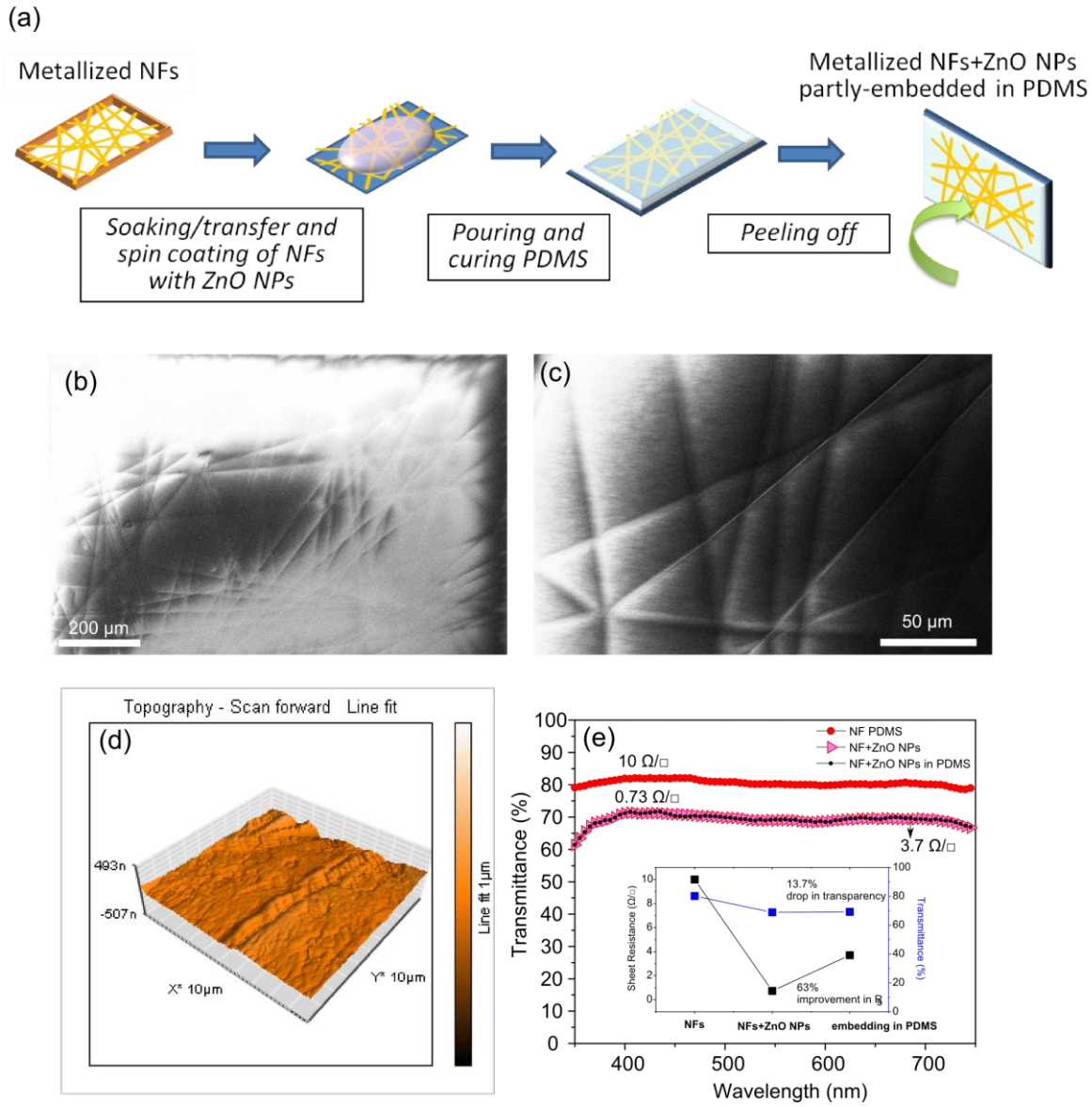


**Figure 3.21:** (a) Schematic procedure for the fabrication of metallized NFs coated with ZnO NPs, partly-embedded in PDMS. (b, c) SEM micrographs of the ZnO-coated NFs, embedded near the surface of a PDMS substrate. (d) AFM image of the ZnO-coated NFs partly-embedded in PDMS. (e) Variations of transmittance and sheet resistance of metallized NFs through the ZnO coating stage and after embedding in PDMS.

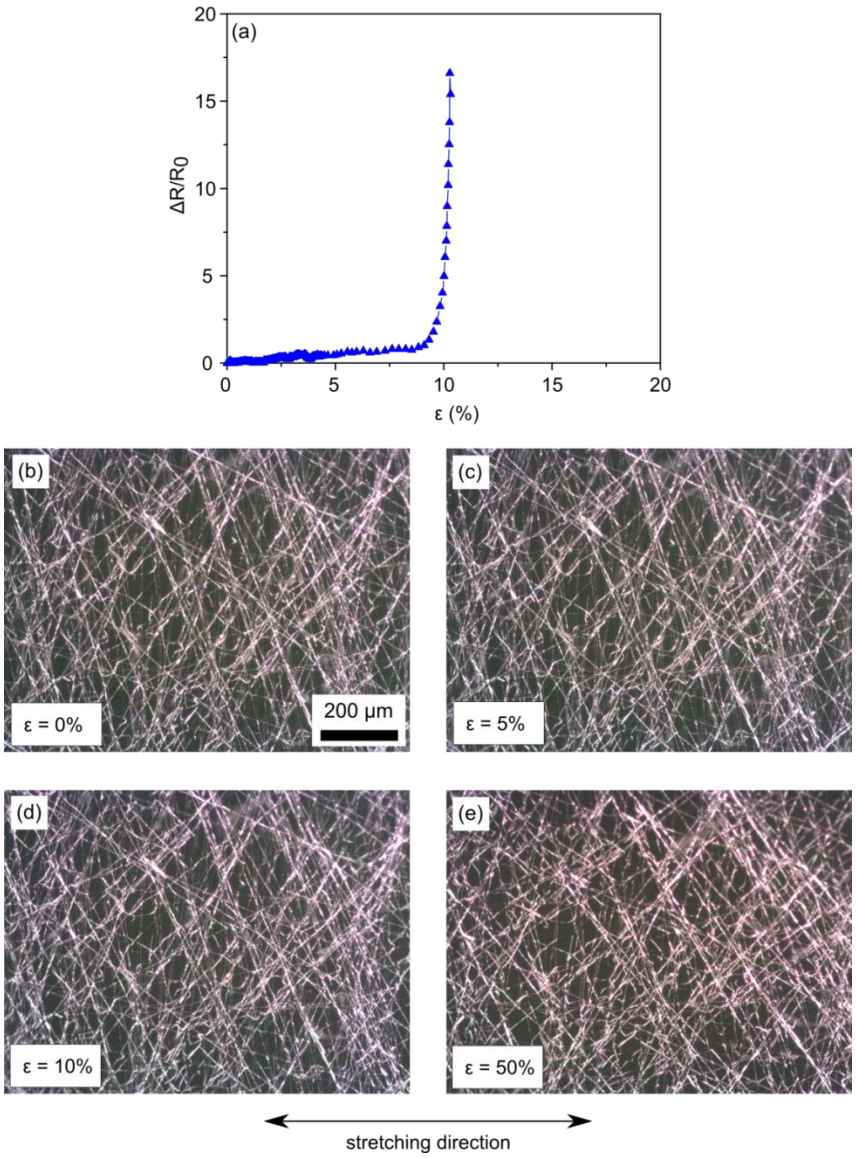


**Figure 3.22:** (a) Variations in $\Delta R/R_0$ versus strain for TCE based on ZnO-coated NFs partly-embedded in PDMS. (b-e) Optical micrographs showing the evolution of microstructure over stretching up to 50% strain.

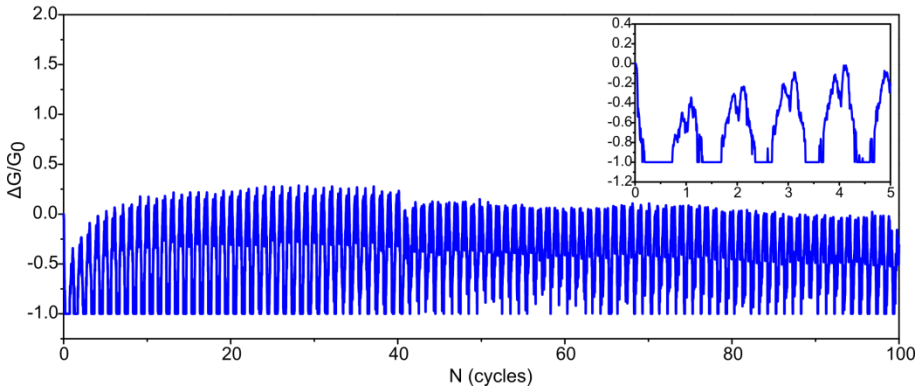


**Figure 3.23:** Cyclic endurance of ZnO-coated, partly-embedded NF TCE over 100 stretching cycles up to 10% strain. Inset shows a close-up of the graphs for first 5 cycles.

## 3.4 Comparison of the Introduced Transparent Electrodes

### 3.4.1 Sheet Resistance and Optical Transmittance

Figure 3.24 shows the sheet resistance and optical transmittance of various composite charge-selective TCs introduced in this chapter, in comparison with uncoated NF TCs (hollow red circles), ITO and selected nanostructured TCs from the literature. With the original uncoated NF TCs (introduced in Chapter 2), we have achieved performances exceeding that of conventional ITO TCs. The composite charge-selective TCs have generally maintained the performance level achieved by their uncoated counterparts. Electron-selective composite TCs using ZnO NPs as the matrix have performances comparable to the original uncoated TCs. Subjected to annealing, the composite TCs using sol-gel ZnO and $MoO_3$ layers as the charge-selective matrix achieve performances on a par with their uncoated NF TC counterparts. The best performance is observed in the case of sol-gel ZnO matrices, exemplified by outstanding combinations of sheet resistance and optical transmittance, namely, $R_s$ = 11 Ω/□ at $T$ = 90%, $R_s$ = 15 Ω/□ at $T$ = 93% and $R_s$ = 23 Ω/□ at $T$ = 95%.

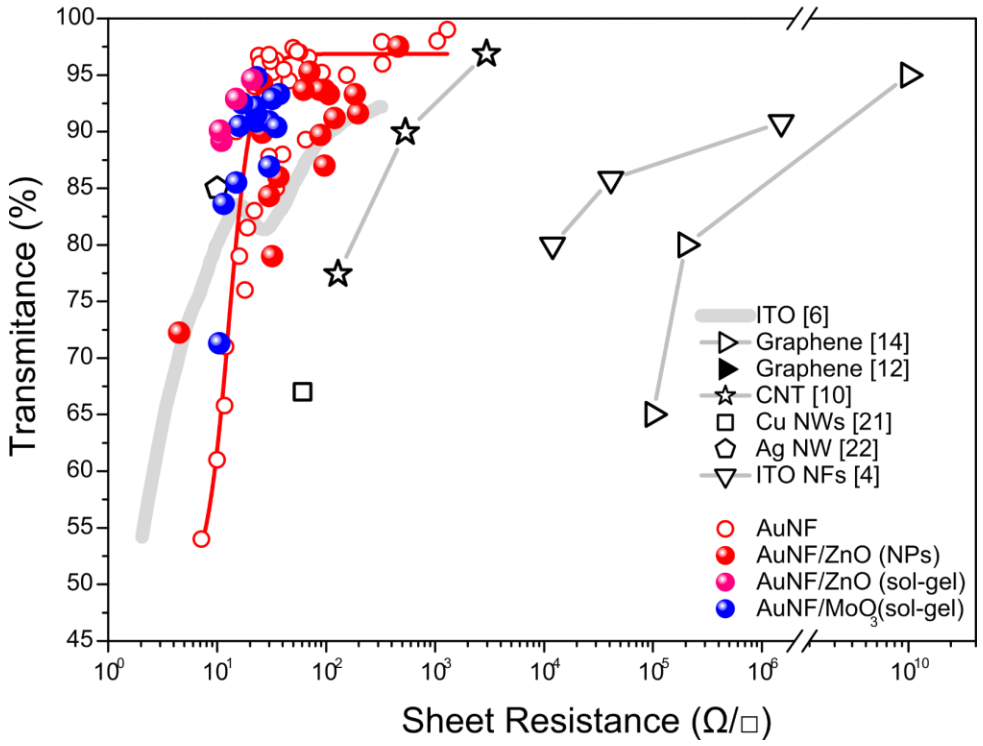


**Figure 3.24:** Sheet resistance vs. optical transmittance (at 550 nm) for various charge-selective composite TCs introduced in this chapter, shown in comparison with uncoated metallized NF TCs, ITO and some of the nanostructured TCs reported in literature.

### 3.4.2 Surface Roughness

Figure 3.25 compares the surface morphology and roughness of various charge-selective composite TCs introduced in Section 3.2. 2D topography AFM micrographs of the composite NF TCs, coated with multiple layers of a charge-selective material are shown in Figure 3.25(a, b and c). Surface roughness ($R_a$) values are shown on each micrograph, for the entire 10 × 10 µm area, as well as for the indicated 3 × 3 µm areas on the charge-selective layer. Cross-sectional line scans across the NF are shown in Figure 3.25(d, e and f). Reduction in roughness is achieved through multiple coatings of ZnO NPs, via coverage of the NFs by the charge-selective matrix. Roughness values of 5.9 nm and 46.7 nm are obtained for the ZnO surface and the entire

scanned area of the TC, respectively. The composite TC using sol-gel ZnO shows a higher roughness ($R_a$ = 54.3 nm for the ZnO surface and $R_a$ = 182 nm for the entire scanned area). The composite TC using sol-gel $MoO_3$ layers as the hole-selective matrix shows lower roughness values compared to the TC using sol-gel ZnO ($R_a$ = 12.3 nm for the $MoO_3$ surface and $R_a$ = 170 nm for the entire scanned area). The coverage of the NFs with charge-selective matrix is also very smooth (Figure 3.25(f)), which is presumably due to the absence of grain boundaries, given the fact that crystallization of $MoO_3$ has not yet commenced at the annealing temperatures used here. A notable difference can be observed in the uniformity of NF coverage by the charge-selective matrix in Figure 3.25(a) in contrast to Figure 3.25(b, c). The colloidal ZnO nanoparticles have formed a uniform coating over the surface of TC (Figure 3.25(d)). Whereas using sol-gel process, the charge-selective layer tends to accumulate around the NFs, resulting in an increased coverage of the NFs (Figure 3.25(e and f)). This preferential coverage, also observed in SEM images (Figure 3.6 and Figure 3.10), is responsible for high transmittance values of these TCs, but makes them unsuitable for application as bottom electrodes in organic photovoltaic devices. The composite TC using colloidal ZnO NPs on the other hand, can be a promising candidate as a bottom electrode.

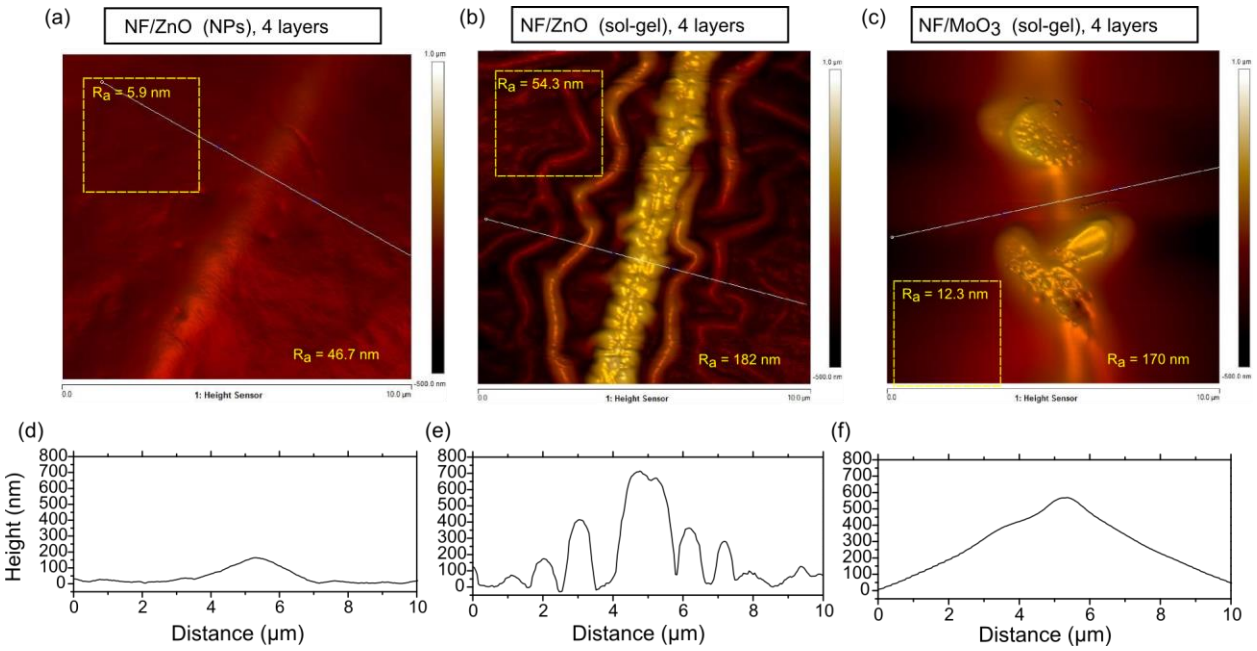


**Figure 3.25:** 2D topography AFM micrographs of the different composite NF TCs, coated with multiple layers of a charge-selective material (a - c), along with corresponding cross-sectional scans (d - f). (a, d) NFs coated with ZnO NPs, (b, e) NFs coated with ZnO sol-gel layers, and (c, f) NFs coated with $MoO_3$ sol-gel layers. The cross-sectional scans are taken along the lines indicated on the corresponding topography maps. Surface roughness ($R_a$) values are provided for the entire image as well as for the indicated 3 × 3 μm areas on the charge-selective layer.

Figure 3.26 shows the surface morphology and cross-sectional profile of the stretchable charge-selective composite TC introduced in Section 3.33.3.2.3, in comparison with uncoated NFs and NFs with a single-layer charge-selective coating. Figure 3.26(a, d) show the 2D topography micrograph and the corresponding height profile for an uncoated stretchable NF TC fabricated by transferring the NFs onto a PDMS substrate (introduced in Chapter 2). Although highly stretchable (see Section 2.3.2.3), these TCs have a considerable surface roughness, characterized by > 600 nm protrusion of the NFs from the surface (Figure 3.26(d)). Using the process shown in Figure 3.21(a), this value is reduced to ~ 50 nm for stretchable composite TCs.

The AFM micrograph and the corresponding height profile for the resulting stretchable TC are shown in Figure 3.26(c, f). The intermediate stage is shown in Figure 3.26(b, e), showing the NFs in (a) after coating a thin layer of ZnO NPs and before embedding in PDMS. NF protrusion from the surface is reduced from > 600 nm to ~ 450 nm as the result of spin-coating a single layer of ZnO NPs.

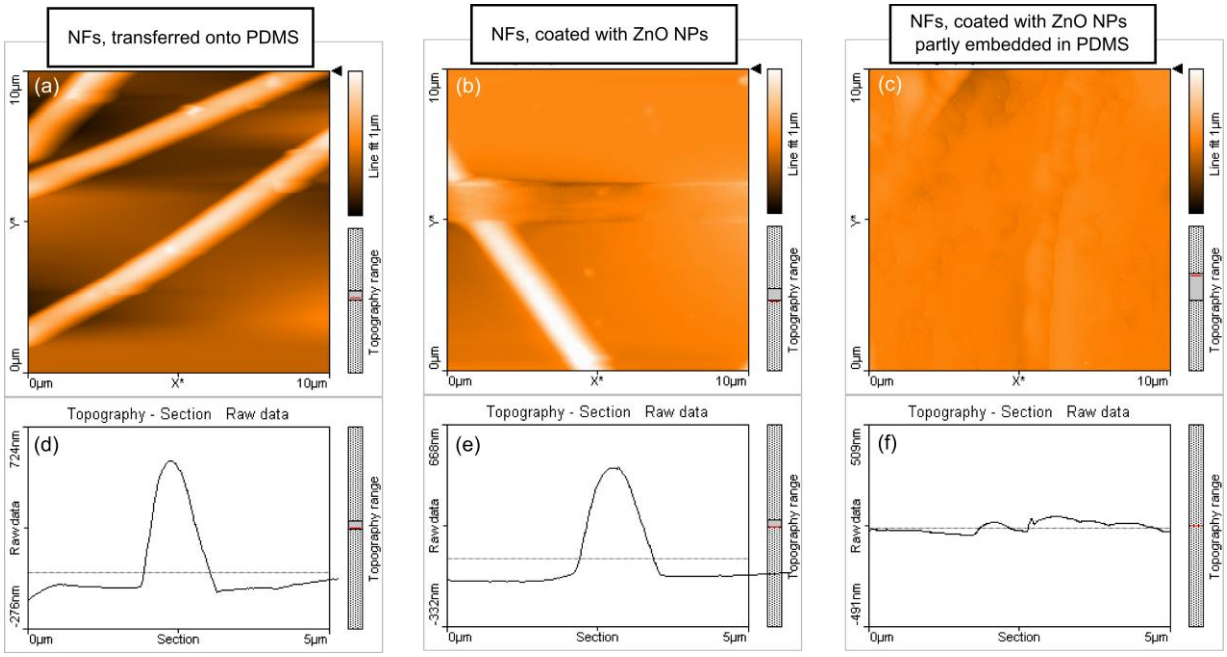


**Figure 3.26:** 2D topography AFM micrographs (a – c) and corresponding cross-sectional scans (d – f), showing the surface morphology and height profile of a stretchable charge-selective TC, in comparison with uncoated NFs and NFs with a single-layer charge-selective coating. (a, d) NFs directly transferred onto PDMS, (b, e) NFs coated with a single layer of ZnO NPs and (c, f) The TC shown in (b) after being partly embedded in PDMS.

### 3.4.3 Electromechanical Stretchability

Figure 3.27 shows the variations in $\Delta R/R_0$ versus strain for different stretchable TCs presented in this work, in comparison to the results reported in the literature. PEDOT:PSS TCs on pre-stretched PDMS and the uncoated metallized NFs on PDMS, both show superior stretchability compared to all of the results so far reported. Stretchable TCs based on the NFs partly-embedded in PDMS are less stretchable compared to their unencapsulated counterparts. However, they show 10 times less degradation in sheet resistance, compared to ITO-coated Ag NWs at a similar strain [140].

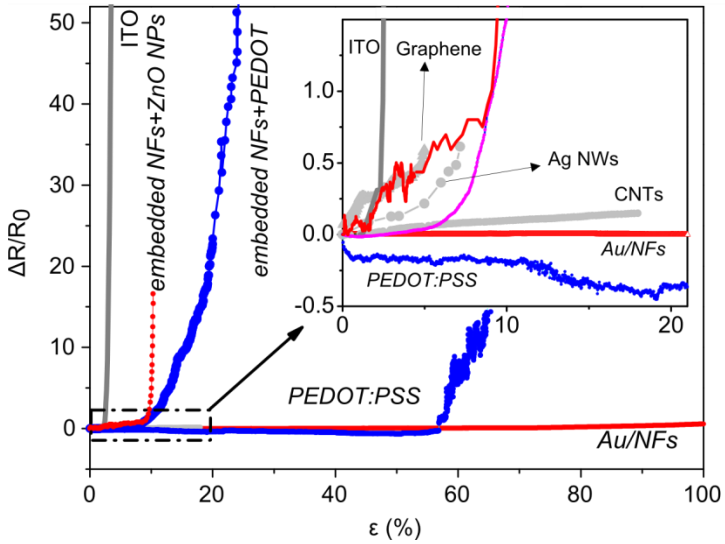


**Figure 3.27:** $\Delta R/R_0$ vs. strain for the stretchable TCEs presented in this work, in comparison with other results in the literature. Inset shows a close-up of the curves for strains smaller than 20%.

## 3.5 Conclusions

Expanding on the work presented in Chapter 2, in this chapter we discussed the microstructure and performance of composite nanofibrous TCs consisting of sparse metallized NFs incorporated in matrices of charge-selective materials. The motivations for this work were 1) integrating electron- or hole-selective interface layers with the previously introduced TCs, to develop charge-selective TCs that can be used as a cathode or an anode in organic photovoltaic devices, and 2) to reduce the surface roughness of the original NF TCs to enable them to be used as bottom electrodes in organic photovoltaic devices. Different materials/processes were used to synthesize the electron- or hole-selective matrix. Electron-selective composite NF TCs using colloidal ZnO NPs as the matrix show performances comparable to those of ITO, with transmittance values slightly lower than those of the original uncoated TCs. Performances of $R_s$ = 36.7 Ω/□ at $T$ = 86%, $R_s$ = 70.6 Ω/□ at $T$ = 95.3% and $R_s$ = 460 Ω/□ at $T$ = 97.5% are obtained using this charge-selective matrix. Reduction in surface roughness is obtained through multiple coatings of ZnO NPs from a concentrated solution. Coupled with annealing after each deposition stage, the successive coating also results in improved sheet resistance and optical transmittance. Therefore, reduction of roughness can be achieved concurrently with improvement of performance, making the introduced composite TC a promising candidate as a high-performance bottom electrode for inverted organic solar cells. As an alternate route to the elaborate process of nanoparticle synthesis, ZnO layers were also fabricated through sol-gel process. Electron-selective composite NF TCs using sol-gel ZnO layers as the matrix show outstanding performances, far superior to that of ITO and on a par with the best of the original uncoated TCs. Performances of $R_s$ = 11 Ω/□ at $T$ = 90%, $R_s$ = 15 Ω/□ at $T$ = 93% and $R_s$ = 23 Ω/□ at $T$ = 95% are obtained using this method. High performance is achieved through

preferential coating of the NFs. Heat treated at the right temperature, the composite TCs using sol-gel ZnO layers can achieve lower sheet resistances than the original uncoated TCs. Hole-selective composite TCs were fabricated using sol-gel $MoO_3$ layers. Using the appropriate heat treatment, performances close to those of the uncoated TCs are achieved, namely, $R_s$ = 12.5 Ω/□ at $T$ = 91%, $R_s$ = 22.1 Ω/□ at $T$ = 93% and $R_s$ = 35.5 Ω/□ at $T$ = 94%. In summary, the sol-gel process was successfully used to fabricate charge-selective TCs based on the original metallized NF TCs with virtually no loss of performance.

The second part of this chapter suggested methods to enable repeatable electromechanical stretchability for charge-selective composite TCs. Three structures were introduced. The first stretchable charge-selective TC consists of thin films of hole-selective PEDOT:PSS layers spun on pre-stretched PDMS. Depending on the pre-strain, up to > 55% stretchability can be achieved using this structure. Two other stretchable charge-selective TC structures are suggested, which build upon metallized electrospun NFs. To render the composites of metallized NFs in charge-selective matrices flexible, a special architecture is suggested, consisting of NFs embedded near the surface of a PDMS layer. Exposed on one side and embedded on the other, the NFs offer reduced surface roughness while enabling repeatable stretchability up to ~ 10% strain. Composite charge-selective TCs based on this architecture were fabricated either via direct spin-coating of a charge-selective ink on top of the partially exposed NFs, or via fabricating a composite NF TC on an intermediary glass substrate, pouring and curing PDMS and releasing the TC by peeling or lifting off the glass. Composite TCs thus fabricated showed stretchability up to 10% strain with stable cyclic endurance over 100 cycles. The fabricated TCs, although less stretchable than the original metallized NF TCs transferred onto PDMS substrates, show less

degradation in sheet resistance, compared to most of other stretchable nanostructured TCs at a similar strain.

In summary, charge-selective nanofibrous TCs were fabricated by integrating the metallized NFs into a matrix of a charge-selective material. Different electron- and hole-selective layers were used as the matrix. The resulting TCs show outstanding combinations of sheet resistance and optical transmittance, which are far superior to that of conventional ITO TCs and comparable, or with appropriate heat treatment in some cases even superior, to the original uncoated metallized TCs. Features of charge-selectivity and high performance, along with the successful reduction in surface roughness in the case of ZnO-coated composite TCs, make the introduced TCs promising candidates as top or bottom electrodes for efficient organic solar cells.

# Chapter 4: Spray-Coating as a Low-Consumption, Scalable Process for Fabrication of Organic Solar Cells

## 4.1 Introduction and Motivation

Interest in solution processed organic solar cells (OSCs) is mounting as laboratory-based polymer:fullerene bulk heterojunction devices attain certified efficiencies of 9.1%. These high-performance devices often rely on deposition techniques, such as spin coating[9], which are precise and reproducible, but which involve large material waste, and are not compatible with large-area manufacturing[9, 10]. To achieve large-area devices, alternative deposition techniques need to be considered[153]. Recently, other solution processing methods have been used for the fabrication of OSCs, such as screen printing[47], doctor blading[48], inkjet printing[49] and spray-coating[43]. Among these, the spray process is considered as one of the most promising [10]. Apart from the capability for roll-to-roll deposition, spray-coating offers advantages including lower material consumption, high production speed, high deposition-parameter adjustability[9], compatibility with a wide range of solution properties, and compatibility with various substrates[9, 10]. Spray-coating has successfully been used to coat layers of photoactive materials[154-156], polymer interfacial layers[157], nanowires[118], alternative transparent electrodes[158, 159], transition metal oxides[137], and metal electrodes[160, 161], demonstrating its potential for fabricating a complete OSC[9]. A greater part of the ongoing research is focused on the optimization of the process for the deposition of polymer:fullerene active layers[9, 10, 154, 157, 162-172] and, in particular, the widely established P3HT:PCBM bulk heterojunction [9, 10, 155-157, 162, 167, 168, 170, 173-175].

There are two methods for spray-coating; the multi-pass method where a slow accumulation of quickly dried droplets forms a thick and rough layer, and the single-pass method where the deposited droplets are allowed to coalesce into a single wet film over the substrate before drying[9, 10]. The former, though effective in producing uniformity over the sprayed area, has not been very effective for fabricating OSCs[154]. This is due to the high roughness and high density of defects and pinholes caused by the loosely-linked droplets [10, 154]. The latter method has been more successful in the fabrication of thin and uniform layers of photoactive material with device performance approaching the material efficiency limit[9]. However there are challenges in scaling up this method due to loss of uniformity over large areas[10].

A few approaches are proposed to improve film uniformity and device performance using each of these methods. Thermal annealing is used to improve film morphology and OPV device performance for both multi- and single-pass methods[155, 170, 176]. Solvent annealing of the active layer has also been shown to increase the light absorbance and enhance the charge mobility through facilitating the self-organization of polymer and fullerene compounds[176]. The solvent annealing process, though effective, takes a considerable time and requires the use of an enclosed environment to contain the solvent vapor [177]. Conventional solvent annealing process is therefore not suitable for large-area fabrication processes such as spray deposition[162]. Researchers have suggested an alternative 'solvent spray annealing' process where the multi-layer spray-coating of the photoactive layer is followed by a second round of spraying a pure solvent or mix of solvents that would partially dissolve and re-form the previously sprayed film, resulting in improved film uniformity upon the secondary drying. This method has been shown to increase device efficiency compared to those with as-sprayed films[9,

10, 162]. In the case of single-pass spray-coating, due to the high amount of solvent present on the substrate after spray-coating, utilization of solvent blends has been instrumental in controlling the delicate balance of surface tension induced flows[178], and solvent evaporation timing[179] to realize thin and uniform layers with an optimal morphology. To avoid miscibility constraints and stability limitations inherent to many pre-mixed solution blends, recently Tait et al.[9] have used concurrent spray-coating of separate inks holding P3HT and PCBM solutes by coaxial pumping through spray-coater nozzle. They achieved desirable heterojunction morphology by making sure the final dried layer is sufficiently mixed[9]. In order to avoid coffee ring effects caused by prolonged drying times in the single-pass method, most of these groups have used elevated substrate temperature (50 – 150 °C) [9, 155, 162, 168]. All of the works reporting high solar cell efficiency by room-temperature and/or single-pass spray-coating have carried out the post-treatment of the photoactive layer and device performance measurements[10, 170] or all of the fabrication and measurement steps[9, 155, 157] in an inert glovebox atmosphere

In the current part of this research, we have aimed for the fabrication of OSCs with P3HT:PCBM photoactive and PEDOT:PSS hole-selective layers that can have performances approaching the established material limits, through a low-cost, low material consumption spray-coating process. The specific goals have been as follows:

1. Single-pass spray-coating of the inks at 25 °C substrate temperature,
2. Achieving optimum film characteristics, including film thickness, surface roughness and bulk heterojunction morphology without the use of separate ink and solvent spraying steps,

3. Achieving performances approaching the established material limits without the need to use an inert ambient for the deposition, post-treatment and measurement stages of OPV device fabrication,
4. Realizing the above over large substrate areas.

Section 4.2 will discuss three major stages for developing this process, starting from the primary results on multi-pass coating of P3HT:PCBM, and leading to the process we have developed for fully automated spray-coating and accelerated drying of the sprayed layers, which is capable of single-pass room-temperature fabrication of OPV devices in air. In Section 4.3,we demonstrate the application of the developed process in large-area fabrication of all-sprayed OSCs. Section 4.3.1 discusses our results for the fabrication of the devices with spray-coated PEDOT:PSS hole-selective layers in addition to the photoactive layer. Section 4.3.2 discusses the results for the fabrication of spray-coated devices over large substrate areas and with larger active device area. A summary of the results will be presented in Section 4.4 and discussed in comparison with relevant literature.

## 4.2 Development of Spray-Coating Process for Automatic, Low-Consumption Fabrication of P3HT:PCBM Photoactive Layers

In this section we will discuss the various stages undergone over the course of this research to realize the eventual goal of fabricating single-pass spray-coated devices which can approach the performance limits of P3HT:PCBM bulk heterojunction structure without the necessity to resort to elevated substrate temperatures and inert fabrication atmosphere. The evolution of the process will be discussed in three stages. Section 4.2.2.1 discusses the results of the primary stage of this project involving the multi-pass spray-coating of P3HT:PCBM. Section 4.2.2.2 presents the results of spray-coating process development for transitioning from multi-pass to bi-layer deposition. Section 4.2.2.3 discusses the process development, thin film characteristics, and OPV device performance results for a single-pass room-temperature spray-coating method we have developed in this research for the deposition of P3HT:PCBM photoactive layers in air. Here, we report low-roughness films with high uniformity obtained at 25 °C substrate temperature through accelerated drying of the ink by adding an additional drying stage using a handheld dryer gun. In order to further simplify the process and ensure the reproducibility of film quality, we have subsequently replaced the manual accelerated drying stage with an automatic process which is carried out using the spray-coater nozzle as drying air delivery system. The process development, thin film characteristics, and OPV device performance results for devices fabricated using single-pass spray-coating at 25 °C substrate temperature followed by automated nozzle drying are presented in the latter party of Section 4.2.2.3.

### 4.2.1 Experimental

All the spray-coating experiments have been carried out using ExactaCoat automatic spray-coating system equipped with a SonoTek AccuMist ultrasonic atomizing nozzle. Spray-coating parameters are adjusted using the ExactaCoat system. The films are spray-coated on glass or ITO substrates, previously cleaned with acetone, isopropyl alcohol (IPA) and deionized (DI) water.

*Fabrication of OPVs using multi-pass spray-coating:* P3HT:PCBM solution with 8 mg/ml concentration (1:1 weight ratio between the solutes) dissolved in dichlorobenzene (DCB) was used as the ink. Spray-coating was conducted using solution flow rate of $f$ = 0.20 ml/min, shaping air flow of 1.0 (as read from the equipment flow gauge), spray nozzle scan speed of $V_c$ = 50 mm/s and from a spray nozzle-to-substrate distance of $h_d$ = 90 mm. Substrate temperatures of $T_{sub}$ = 60, 80 and 100 °C were used, using the built-in hot plate. Sprayed P3HT:PCBM layers are formed by multi-pass coating of the ink with 5 – 40 successive layers. Microstructure, thickness and roughness of the films deposited on glass substrates were characterized using an Olympus BH2-UMA optical microscope and a Bruker Dektak XT profilometer. Organic solar cells were fabricated on 20 × 10 mm ITO substrates. The substrates were cleaned using the same procedure used for the glass substrates. PEDOT:PSS hole-selective layer with ~ 40 nm thickness was deposited from an ink diluted in IPA (4:1 PEDOT:IPA volume ratio) and spun at 5000 rpm, followed by drying at 120 ° C on a hot plate for 10 minutes. P3HT:PCBM photoactive layers were spray-coated using similar sets of parameters as those used on glass substrates. A top electrode consisting of 20 nm Ca / 100 nm Ag was thermally evaporated on the films, resulting in OPV devices with 20 $mm^2$ active area. Current-voltage measurements of devices were conducted on a computer-controlled Keithley 2400 source meter. A xenon lamp (150 W,

Newport Co.) equipped with an AM1.5G filter was used as the light source with optical power of 100 mW/cm$^2$.

*Spray-coating of P3HT:PCBM double layers:* P3HT:PCBM films were spray-coated on 20 × 20 mm glass substrates cleaned as described above. Temperatures of 25, 40, 50, 60 °C, solution flow rates of 0.25, 0.30, 0.35 ml/min, and nozzle scan speeds of 30, 50, 70 mm/s were used for deposition. Each film consists of two successive spray-coated layers with 10 s wait time between the two coatings. The films were left at the substrate temperature to dry out, before being transferred for microstructural and optical characterizations. To examine the macro-scale uniformity of the film over the whole substrate area, photographs were taken using the built-in camera on a Google Nexus 5 phone. Microstructural studies were carried out using an optical microscope (Olympus BH2-UMA) and an atomic force microscope (Nanosurf easyScan 2). Thickness and nano-scale surface roughness of the films were studied using a Bruker Dektak XT profilometer. The profilometry scans are taken across a scratch made near the centre of the substrates. Optical absorption was measured by scanning wavelengths from 400 – 800 nm in 5 nm steps, using a monochromator aligned with a xenon lamp and a Newport 818-UV photo-detector. The measurements were done on a spot on the P3HT:PCBM films near the centre of each substrate, using an uncoated glass substrate with the same thickness as a reference.

*Fabrication of OPVs using single-pass spray-coating followed by accelerated air drying:* Photoactive layers were spray-coated in air from an 8 mg/ml P3HT:PCBM solution (1:1 weight ratio) in a blend of DCB and mesitylene (7:3 volume ratio). Spray-coating parameters for each set of samples are shown in Table 4.1. The wet layer was left for 1 minute to re-distribute over the substrate before drying. Accelerated manual drying was carried out using a handheld VT-750C Varitemp Heat Gun. The dryer gun was kept at ~ 30 cm distance from the substrates and

moved around to provide an even air flow over the substrate. The films were dried using two different modes, the 'cold blow' done without switching on the heating element, and the 'warm blow' done with the gun's heating knob set to 4 on the Varitemp controller scale. The substrate temperature was measured to be 26 °C for the cold blow and 33 °C for the warm blow. After complete drying of the film, the substrates were annealed in air on a hotplate for 5 minutes at 150 °C. OPV devices were finished by thermally evaporating 20 nm Ca / 120 nm Ag on top of the photoactive layers through a shadow mask. Each substrate included 6 – 8 devices with 10 $mm^2$ active area, as shown schematically in Figure 4.1. Spun reference samples were made using a similar procedure from a 40 mg/ml solution in DCB spun at 700 rpm in a glovebox, forming a ~ 200 nm-thick active layer. For each set of parameters described in Table 4.1, three samples were deposited, providing 18 devices per parameter set. AFM images were taken using a Bruker Dimension Icon AFM.

**Table 4.1:** Details of fabrication parameters for single-pass spray-coated devices dried using a handheld dryer gun

| Solution | Nozzle-to-substrate Distance (mm) | T(Substrate) (°C) | flow (ml/min) | Shaping Air | V (mm/s) | Wait (s) | nozzle power | Numbe of Layers | Drying Method | Anneal | Comments |
|---|---|---|---|---|---|---|---|---|---|---|---|
| m+DCB (3:7), 8 mg/ml | 67 | 25 | 0.425 | 0.78 | 55 | 0 | 4-.57 | 1 | cold blow | 150 C, 5' | spray-coated |
| m+DCB (3:7), 8 mg/ml | 67 | 25 | 0.425 | 0.78 | 25 | 0 | 4-.57 | 1 | cold blow | 150 C, 5' | spray-coated |
| m+DCB (3:7), 8 mg/ml | 67 | 25 | 0.425 | 0.78 | 55 | 0 | 4-.57 | 1 | warm blow | 150 C, 5' | spray-coated |
| m+DCB (3:7), 8 mg/ml | 67 | 25 | 0.425 | 0.78 | 25 | 0 | 4-.57 | 1 | warm blow | 150 C, 5' | spray-coated |
| 40 mg/ml in DCB | | 25 | | | | | | | air dry | N | spun |

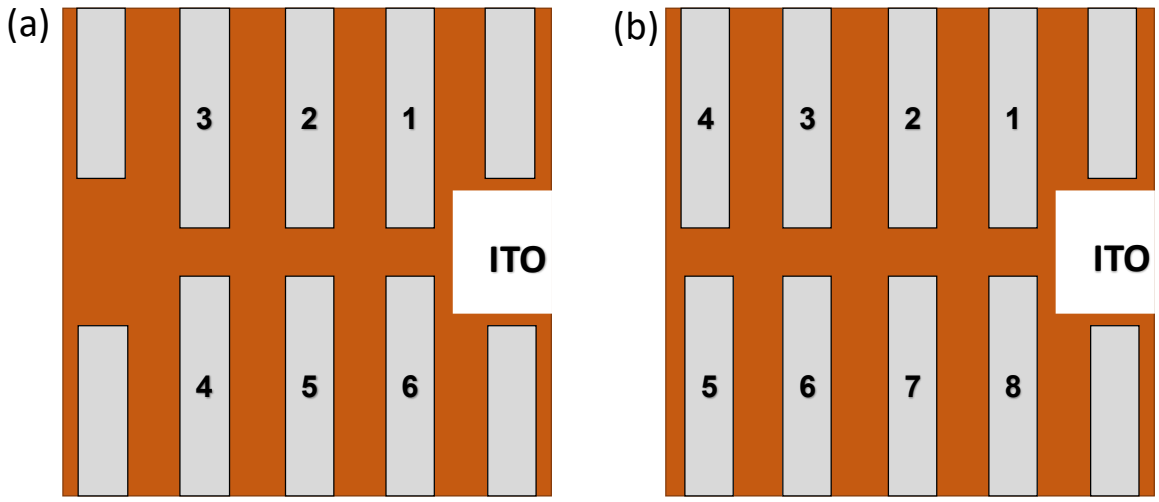


**Figure 4.1:** Schematic illustration of electrode patterns, showing OPV device position and numbering on 20 × 20 mm substrates with (a) 6 and (b) 8 devices per substrate.

Accelerated drying was carried out, in an alternative process, using the spray-coater nozzle by switching off the solution flow. Thus, the spray-coater shaping air could function as drying air delivered to the substrate using computer-controlled movement of the nozzle. The entire spray-coating and drying process was coded using the ExactaCoat software. Drying was done by repeated scanning movements of the nozzle in linear sweeps over the substrate area.

A two-stage drying process was used comprising the following stages:

- Stage 1: fast air blow from a higher nozzle-to-substrate distance in order to allow for uniform evaporation of extra solvent all across the substrate
- Stage 2: slow air blow from a closer distance to conduct the actual drying

Figure 4.2 shows a schematic picture of the process along with the parameters involved. The goal was to adjust the process parameters so as the onset of drying would be at the beginning of Stage 2 and the drying would be completed within 2-3 minutes. The parameters were chosen

through repeated cycles of deposition of films on glass substrates, observation of drying process and film uniformity, and subsequent adjustment of parameters. Details of the fabrication parameters are presented in Table 4.2. For the first stage of nozzle drying, the drying nozzle-to-substrate distance, $h_{d1}$, was 90 mm. The drying nozzle scan speed, $V_{d1}$, and scan line spacing, $d$, were 50 mm/s and 4 mm, respectively. Drying shaping air is set to 0.78 in the scale of the equipment controller. For the second stage, the shaping air and scan line distance were kept intact. $V_{d2}$ = 20 mm/s and two different drying nozzle-to-substrate distances, $h_{d2}$ = 75 and 50 mm, were tried.

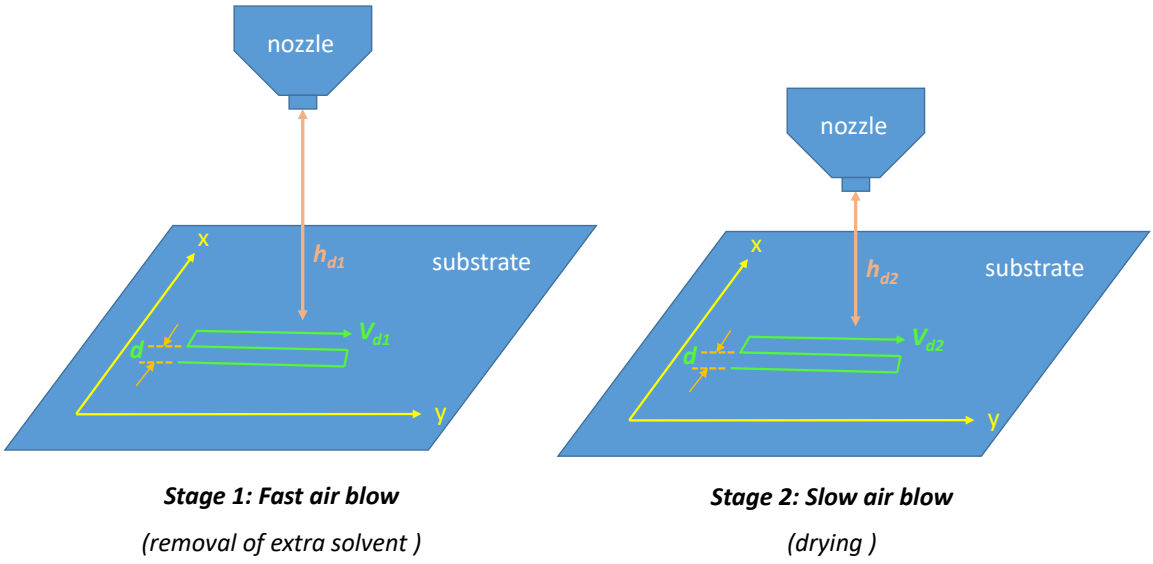


**Figure 4.2:** Schematic demonstration of two-stage drying recipe. Stage 1 (left) involves fast air blow from a higher nozzle-to-substrate distance to allow for the evaporation of extra solvent present on the substrate. Stage 2 (right) involves slower scan of the air-blowing nozzle for the actual drying of the film.

**Table 4.2:** Details of fabrication parameters for single-pass spray-coated devices dried using automated nozzle drying

| Solution | Nozzle-to-substrate Distance (mm) | T(Substrate) (°C) | flow (ml/min) | Shaping Air | V (mm/s) | nozzle power | Numbe of Layers | Drying Method | Anneal | Comments |
|---|---|---|---|---|---|---|---|---|---|---|
| m+DCB (3:7), 8 mg/ml | 67 | 25 | 0.425 | 0.78 | 35 | 4-.57 | 1 | nozzle | 150 C, 5 min | *h2* = 75 mm |
| m+DCB (3:7), 8 mg/ml | 67 | 25 | 0.425 | 0.78 | 35 | 4-.57 | 1 | nozzle | 150 C, 5 min | *h2* = 50 mm |
| m+DCB (3:7), 8 mg/ml | 67 | 25 | 0.425 | 0.78 | 45 | 4-.57 | 1 | nozzle | 150 C, 5 min | *h2* = 75 mm |
| m+DCB (3:7), 8 mg/ml | 67 | 25 | 0.425 | 0.78 | 45 | 4-.57 | 1 | nozzle | 150 C, 5 min | *h2* = 50 mm |

To correlate the performance of the OPV devices to the active layer thickness, profilometry scans were carried out on the substrates, after other characterizations had been completed. Photoactive layer thickness for each individual device was estimated by measuring the thickness at three points in vicinity of the device active area. The average of these measurements was used as estimated photoactive layer thickness.

*Fabrication of all-sprayed OPVs:* PEDOT:PSS inks for spray-coating were prepared by diluting Heraeus Clevios AI 4083 PEDOT:PSS in DI water and IPA, with three different volume ratios of 18:9:73, 9:18:73 and 9:28:63 (PEDOT:water:IPA). The inks were mixed on a hotplate-stirrer for 12 hours and filtered through a 45 µm filter. PEDOT:PSS inks were spray-coated on glass or ITO substrates at 25 °C substrate temperature, over a 30 × 40 mm deposition area. Spray-coating parameters were varied to achieve the desired thickness and uniformity. Spray-coating nozzle speeds of $V_c$ = 50, 75, and 100 mm/s and solution flow rates of $f$ = 0.6, 0.9, and 1.2 ml/min were used. The shaping air and nozzle-to-substrate distance were 0.6 and 75 mm, respectively. The films were deposited using single-pass spray-coating and left in the spray-coating chamber to dry. The films were annealed on a hotplate for 10 minutes at 120 °C to

remove the residual water. On glass substrates, profilometry scans were taken at 12 – 16 points over the sample to study the uniformity of thickness over the deposition area. OPV devices were made on 20 × 20 mm ITO substrates, using the procedure explained earlier. Four sets of OPV devices were fabricated using different combinations of spin- and spray-coated PEDOT:PSS and P3HT:PCBM layers.

*Spray-coating large-area OPVs:* Glass substrates with 75 × 50 mm dimension or ITO substrates with 75 × 75 mm dimension were used. Spray-coating of P3HT:PCBM was carried out using the single-pass deposition at 25 °C followed by automatic nozzle drying. To study the effect of deposition parameters on the uniformity of the films on glass substrates, deposition parameters of $V_c$ = 45, 112.5 mm/s, were used with proportionally adjusted values for ink flow, $f$ = 0.45, 1.06 ml/min. Accelerated nozzle drying was carried out from 90 mm nozzle-to-substrate distance, with drying nozzle speed of $V_d$ = 50 mm/s. Drying scan line distances of 4, 10, 25 mm were tried. Profilometry scans were taken from 12 points over the substrate area to study the uniformity of the resulting films. Large-area OPV devices were fabricated on 75 × 75 mm ITO substrates. ITO bottom electrodes were patterned using etching in boiling HCl, providing 7 mm – wide stripes. PEDOT:PSS layer was spun with thickness of ~ 30nm. Spray-coating parameters of $V_c$ = 112.5 and $f$ = 1.06 ml/min, and drying scan line distance of $d_d$ = 4 mm were used for the deposition of the P3HT:PCBM photoactive layer. Top electrodes were thermally evaporated through a shadow mask, resulting in total of 49 devices with 7 × 7 mm active area. The fabrication procedure is schematically shown in Figure 4.3. The large-area devices were set up for photovoltaic measurements were carried out using a home-made holder fabricated by 3D printing. A schematic design of the sample holder is shown in Figure 4.4. Reference small-area devices were fabricated on 20 × 20 mm ITO substrates using the procedure described previously,

with spray-coating parameters of $V_c$ = 45 mm/s, $f$ = 0.425 ml/s and drying scan line spacing of $d_d$ = 10 mm.

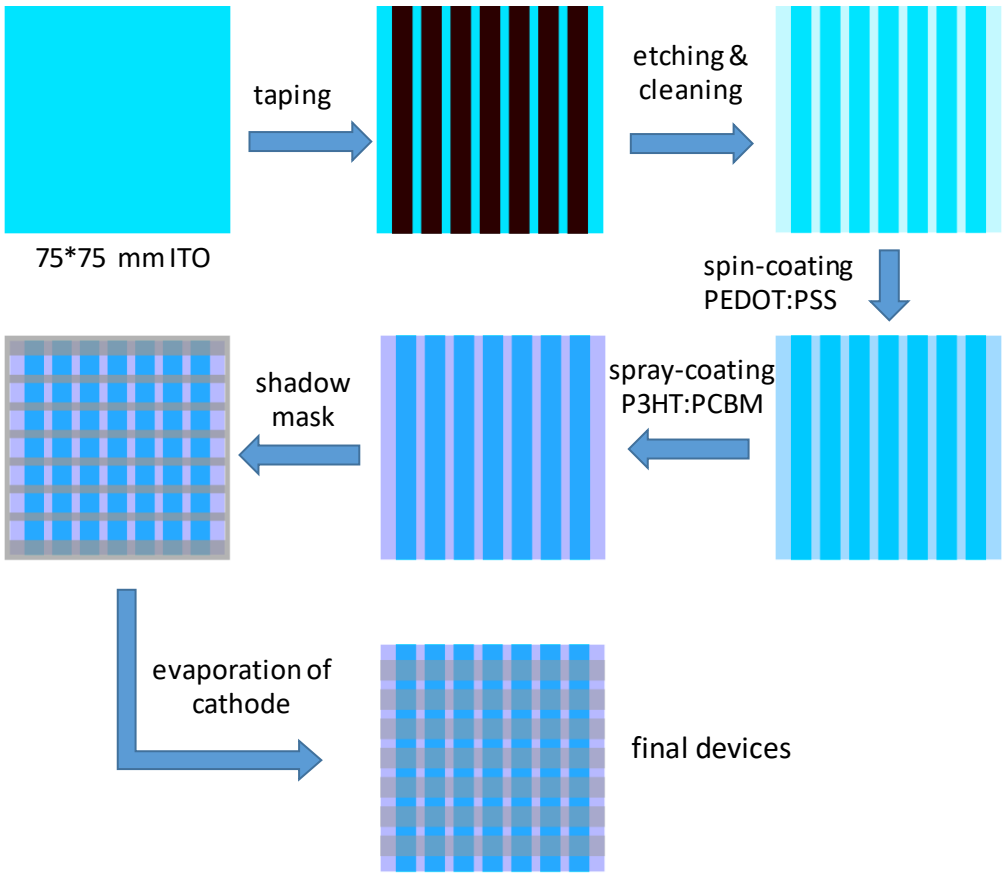


**Figure 4.3:** Schematic fabrication procedure for large-area organic solar cells (fabricated on 75×75 mm substrates).

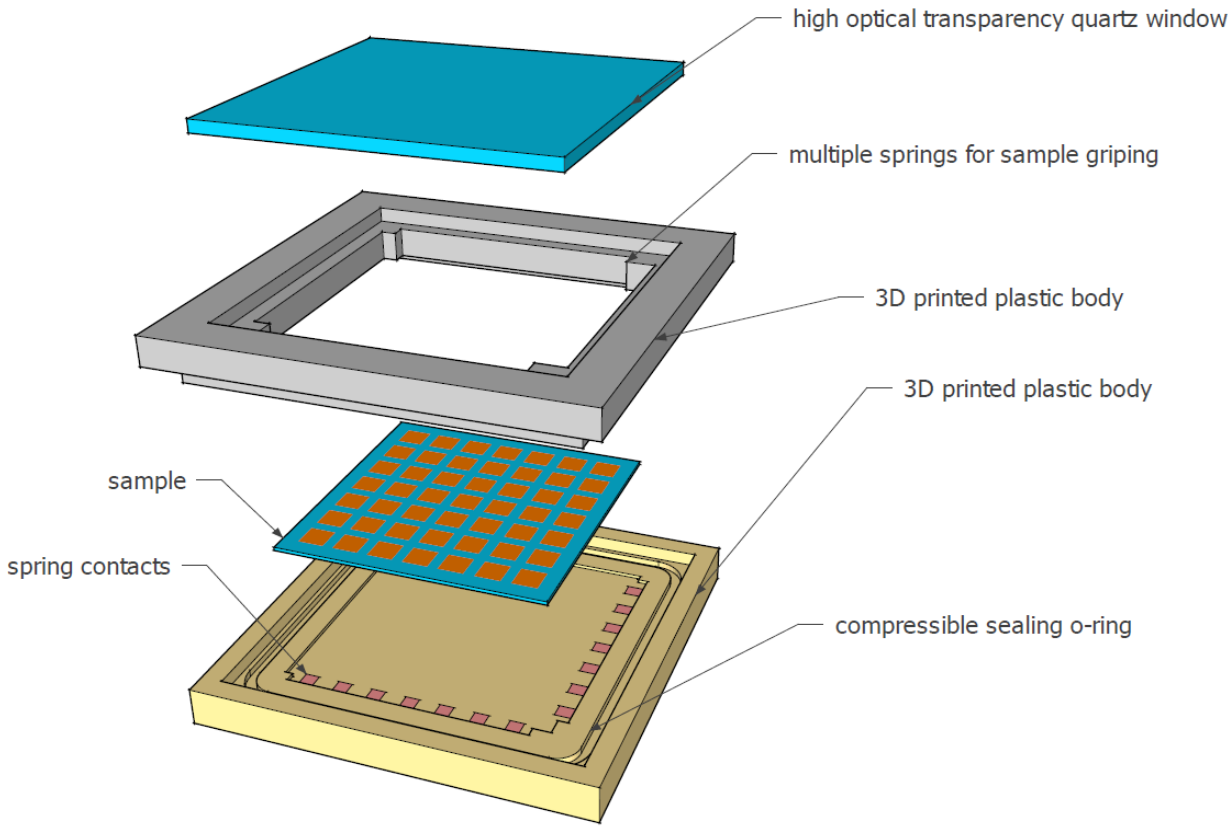


**Figure 4.4:** Schematic figure of design and different components of the sample holder for large-area OPV samples.

### 4.2.2 Results and Discussion

#### 4.2.2.1 Multi-Pass Spray-Coating

Figure 4.5 shows the effect of the number of layers on the optical microstructure of the films spray-coated at a single substrate temperature (100 °C). With 5 layers, a fairly complete coverage of the surface has been obtained. With increasing the number of coatings, the thickness of the layer increases, as is observed by the change in color and contrast of the transmission optical images. The surface coverage is enhanced through the accumulation of overlapping droplets.

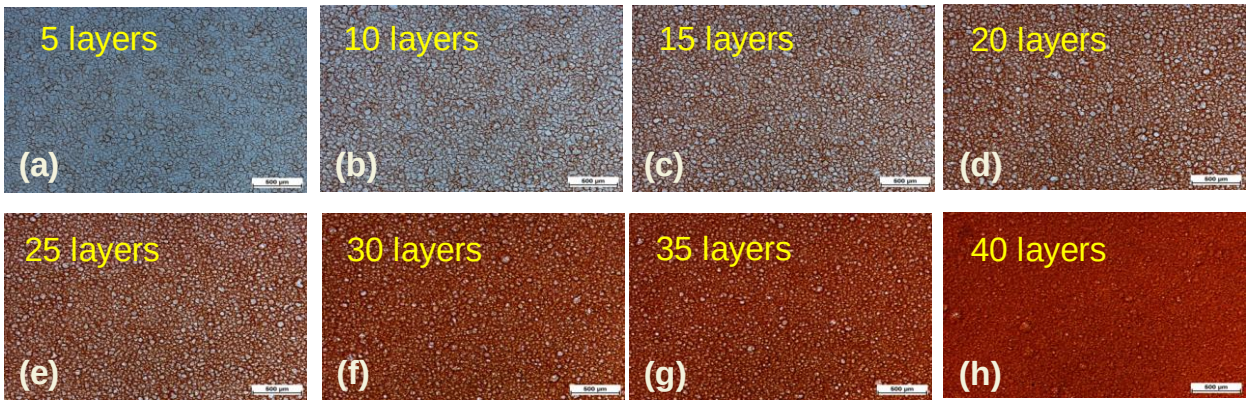


**Figure 4.5:** Effect of the number of layers on the optical microstructure of the films spray-coated at a single substrate temperature (100 °C). (a) 5 layers, (b) 10 layers, (c) 15 layers, (d) 20 layers, (e) 25 layers, (f) 30 layers, (g) 35 layers, and (h) 40 layers.

Figure 4.6 shows the effect of substrate temperature on optical microstructure of films spray-coated with the same number of layers (20 layers). Films deposited at 100 °C substrate temperature consist of droplets with 20 – 50 nm diameter. The droplets have well-defined boundaries as they dry almost instantly upon contact with the substrate. With decreasing the temperature, there will be more time for solute diffusion due to the prolonged drying time.

Therefore, the distribution of the solutes over each droplet is more uniform and the boundaries are more diffuse. This has also led to increased opacity of the films toward lower temperatures, as observed in Figure 4.6(a - c).

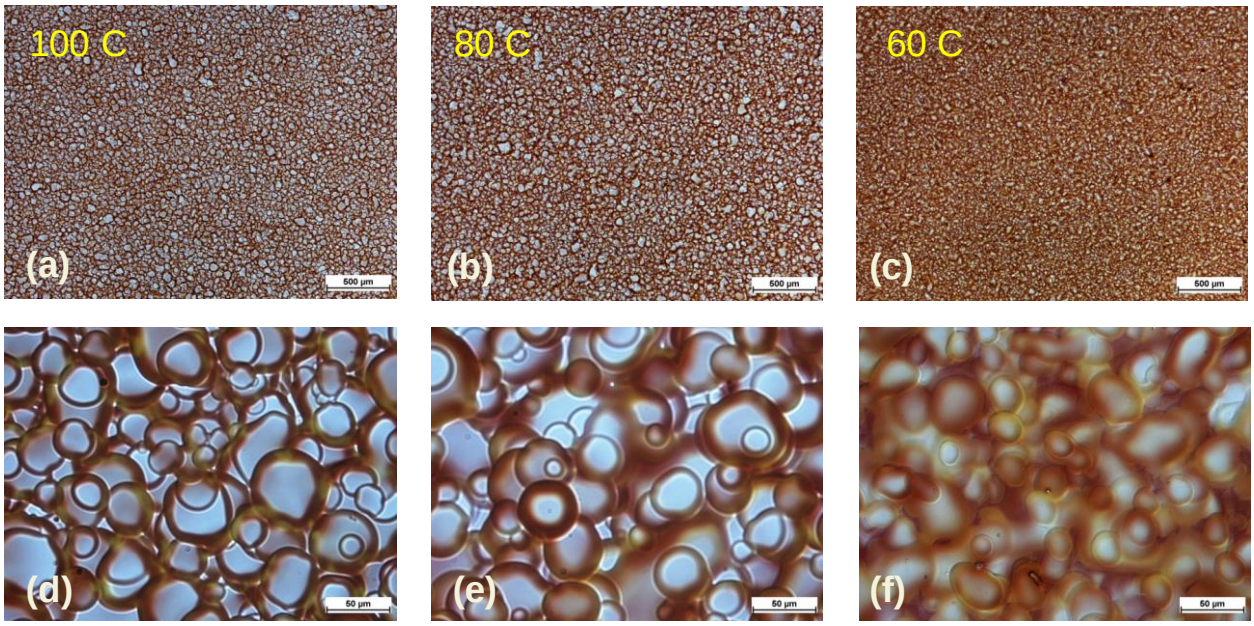


**Figure 4.6:** Effect of substrate temperature on optical microstructure of films spray-coated with the same number of layers (20 layers). (a, d) 100 °C, (b, e) 80 °C, (c, f) 60°C.

OPV devices fabricated using multi-pass spray-coating show very limited photovoltaic response under illumination, with $V_{OC}$ ~ 0.4 V and $I_{SC}$ ~ 0.4 mA/cm$^2$ in the case of the device with a photoactive layer spray-coated with 20 layers at 60 °C substrate temperature. Low performance metrics indicate poor charge transport, due to microstructural defects in the photoactive layer, induced by the granular structure of fast-dried individual droplets, as well as inefficient charge collection at the interfaces with the electrodes, caused by high roughness of the films. It is observed that $V_{OC}$, $I_{SC}$ and the efficiency increase with decreasing the substrate

temperature. This trend agrees with the microstructural observations (Figure 4.6) which show more diffuse interfaces between the droplets, as well as enhanced diffusion of the solutes within individual droplets.

Figure 4.7 provides a summary of photo-conversion efficiencies of the devices spray-coated using the multi-pass approach, at different substrate temperatures and with various number of layers. For each set of devices, the efficiency increases with reducing the temperature. Devices with photoactive layers deposited at 60 °C show non-zero efficiencies even with only 5 layers of coating. The best efficiency, approaching 0.1%, is obtained with 15 layers of successive coatings, corresponding to ~ 200 nm active layer thickness.

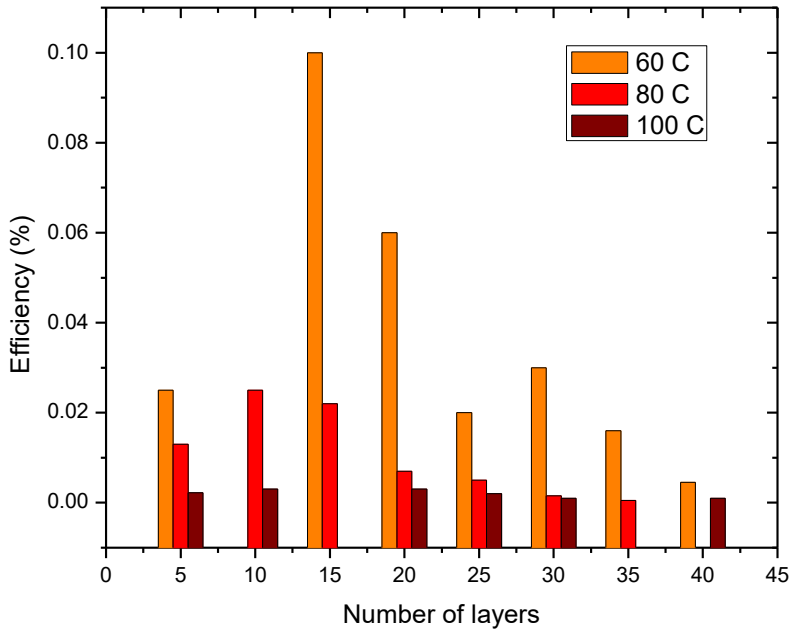


**Figure 4.7:** Comparison of photo-conversion efficiencies for devices spray-coated at different substrate temperatures and with various number of layers.

#### 4.2.2.2 Double-Pass Spray-Coating

According to the preliminary results obtained in the previous stage, here we have focused on improving P3HT:PCBM film uniformity at temperatures lower than 60 °C. Also, to reduce material waste, we have aimed to achieve the desired film thickness and quality with only two successive layers of coating. The effect of substrate temperature on macro- and micro-structure uniformity of the resulting films is evaluated using photography, optical microscopy, atomic force microscopy (AFM), and profilometry. Optical absorption of the sprayed films is measured to assess the suitability of the produced films as photoactive layers in organic solar cells.

Figure 4.8 shows the imaging results of the films spray-coated at different substrate temperatures starting from 60 °C and going down to room temperature. The flow rate and nozzle speed had fixed values of 0.30 ml/min and 50 mm/s, respectively. The sample spray-coated at 60 °C has a granular microstructure consisting of distinct droplets. At 50 °C the droplet boundaries are more diffuse. This agrees with the trend previously noted in Figure 4.6, where decreasing the temperature led to the formation of a more uniform film. This effect becomes more pronounced in the samples deposited at 40 °C and 25 °C. Sample photographs (Figure 4.8(a – d)) and micrographs show homogenous films without a granular structure. This is because at such low temperatures, the solution has enough time to spread over the surface of the specimen before the evaporation of the solvent takes over.

Apart from the microstructural morphology of the films, there are two features to be noted in comparing the samples. First is the difference in the macro-scale coffee ring effect or the 'edge effect' in samples deposited at lower temperatures as compared to those deposited at higher temperatures; As seen in Figure 4.8(a-d), in samples deposited at 60 and 50 °C, the uniformity of the film is similar all throughout the substrate, including the centre as well as the

edges. This changes in the case of samples deposited at 40 and 25 °C; Here, the film is uniform in the centre, but the color and consistency is different at the edges. The reason for this phenomenon is the slow evaporation of the solvent in the latter case, as opposed to that of higher temperatures; At high temperatures, the droplets are formed and solidified as they contact the substrate. Therefore, there is no redistribution of solution across the sample. At lower temperatures, the slow evaporation will allow 2-dimensional mass transfer before the completion of evaporation, which results in higher thicknesses in parts of the sample drying at later stages. Another feature of note in comparing the optical images in Figure 4.8 is the difference in color from sample to sample and/or at different locations on the sample. This effect indicates difference in light absorption among such areas of the films, which is attributed to varying degrees of P3HT crystallinity and P3HT:PCBM phase segregation, caused by different solvent evaporation rates. Further discussion will follow over Figure 4.10 and Figure 4.11.

Profilometry results of the films are shown in Figure 4.9. As expected, the average thickness of the film decreases with increasing the temperature (consistent with faster evaporation of the solvent at higher temperatures). The contrast between uneven granular structure at higher temperature and the uniform thickness at lower ones agrees with the microscopic images (Figure 4.8).

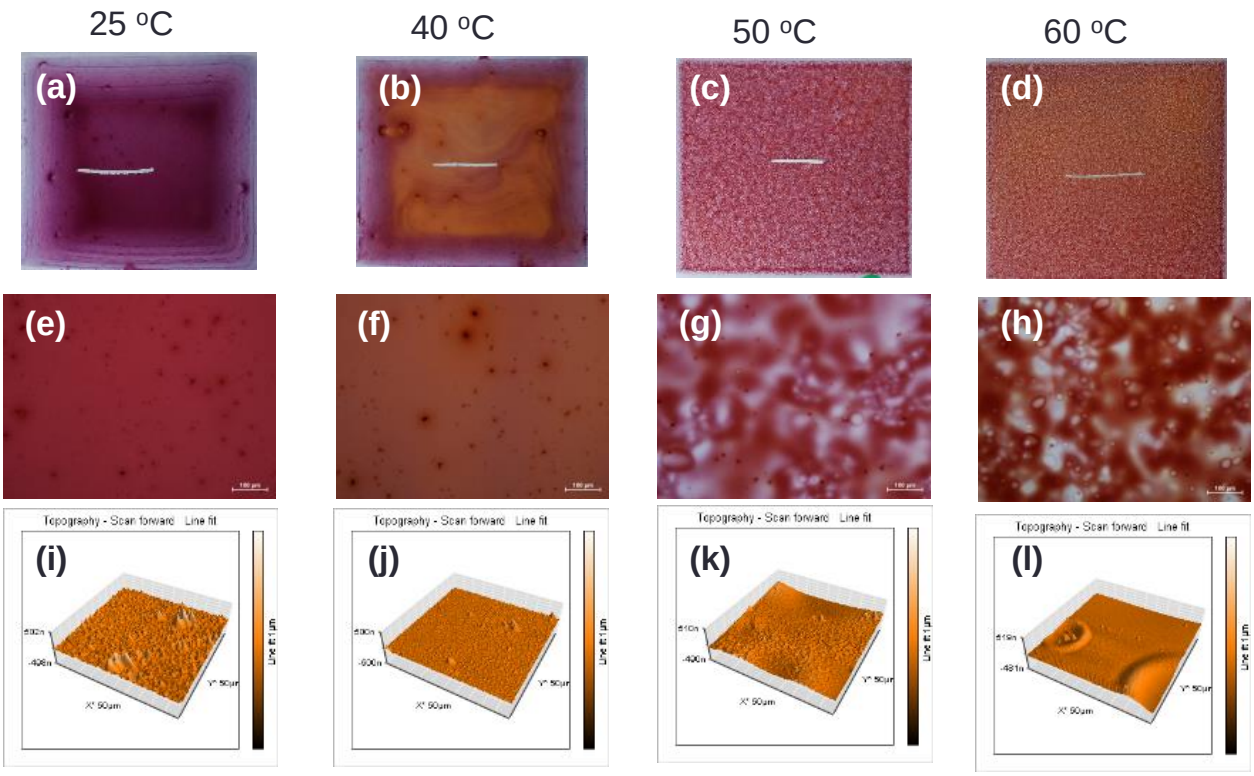


**Figure 4.8:** Imaging results for the films deposited at different substrate temperatures. (a-d) whole-area sample photographs, (e-h) Optical micrographs, (i-l) atomic force microscopy images.

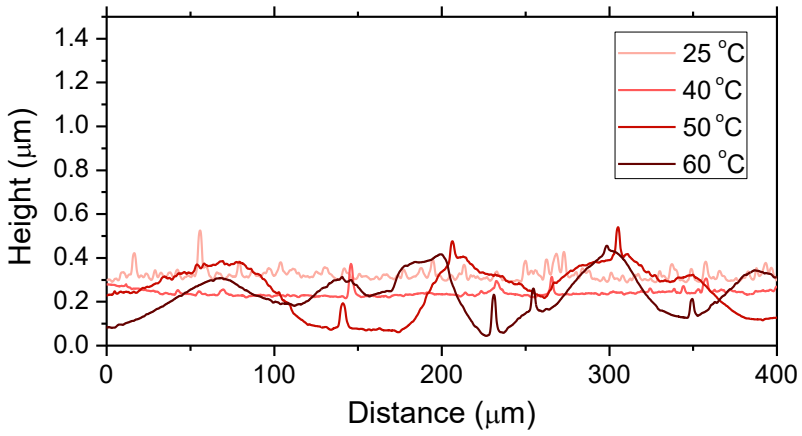


**Figure 4.9:** Profilometry results for the samples deposited at different substrate temperatures.

Figure 4.10 compares the optical absorption spectra of the films deposited at different substrate temperatures. The optical absorption can be analyzed in terms of the thickness, crystallinity and nano-morphology of the films. The former has an effect on the overall light absorption within P3HT:PCBM absorption peak (400 – 800 nm)[180]. The latter affects the shape of the spectrum, manifested in increased/decreased absorption at certain wavelengths or the appearance of more/less distinct shoulders at certain wavelengths[180, 181]. Figure 4.10 shows a slight gradual decrease in maximum light absorption as the temperature is increased, in agreement with the decreased thickness. In the case of the film deposited at 25 °C compared with that of 40 °C, the region around the absorption peak extends toward longer wavelengths. In addition, the shoulders around 545 and 600 nm are more pronounced. This can be attributed to the higher degree of P3HT crystallization as a result of slower solvent evaporation[180, 181]. A similar observation can be made between the films with the granular structure deposited at higher and lower temperatures (comparing the absorption spectra of the films deposited at 60 and 50 °C, respectively). The above difference in the effectiveness of light absorption in the range of ~ 570 – 600 nm can also be loosely correlated to the visible color of the films, manifested in a yellow shade of color in the case of the films, or regions on the films, formed at a faster solvent evaporation rate. To study the correlation of this difference in absorption to the nano-morphology of the P3HT:PCBM films, AFM images were taken from the films deposited at 25 and 40 °C (Figure 4.11). It is observed that the film deposited at lower temperature has a more ordered morphology, which is agreement with previous studies indicating a higher degree of P3HT crystallinity[180] and a finer phase segregation between P3HT and PCBM regions[181] in films dried at a lower rate of solvent evaporation.

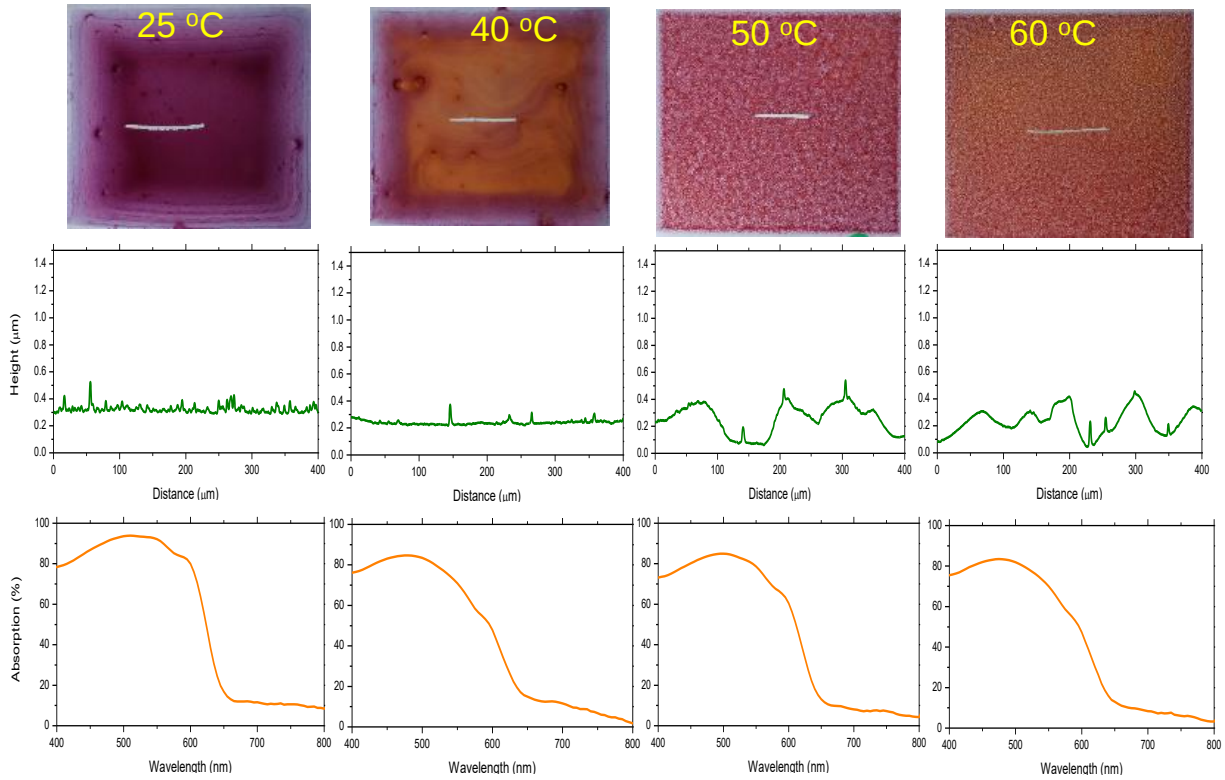


***Flow rate:*** *0.30 ml/mm,* ***Nozzle speed:*** *50 mm/s,* ***Wait time:*** *10 s*

**Figure 4.10:** Effect of substrate temperature on thickness and optical absorption of the samples.

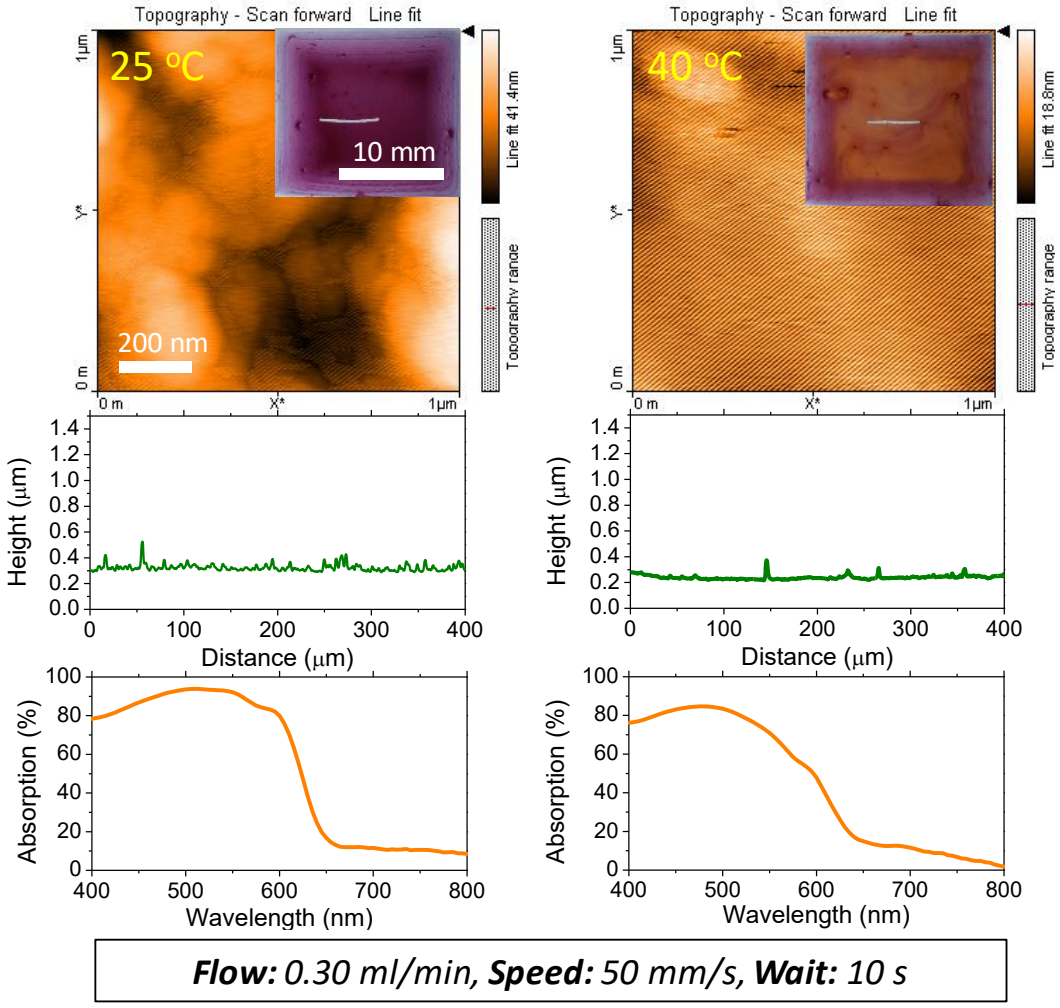


**Figure 4.11:** Comparison of film microstructure and optical absorption between slow-dried and fast-dried P3HT:PCBM films with a comparable thickness.

*Summary:* It was shown that a homogenous, low-roughness film can be obtained by maintaining a balance between the rate of solution delivery and that of solvent evaporation. Using a solution flow rate of $f$ = 0.30 ml/min and a nozzle speed of $V_c$ = 50 mm/s at the substrate temperature of 25 °C, a low-roughness film was obtained with ~ 250 nm thickness, micro-scale uniformity, and good optical absorption. This was however, at the cost of reduced macro-scale uniformity over the substrate area, because of stronger coffee-ring effects caused by prolonged

evaporation times[1]. To address this issue, a method is proposed for accelerated drying of the spray-coated solution while maintaining the low substrate temperature, which will be discussed in the following section.

#### 4.2.2.3 Single-Pass, Room-Temperature Spray-Coating Followed by Accelerated Drying

Continuing the development of the process for low-temperature, low-consumption deposition of P3HT:PCBM solutions for low-cost efficient organic solar cells, in this stage we have focused on:

1) Further reducing material consumption by using a single-pass spray-coating method,
2) Addressing the issue of macro-scale coffee-ring effects by introducing an accelerated air drying method while maintaining low substrate temperatures.

For the first objective, the ink composition was modified to increase the wetting of the substrate by the solution. For the second objective, a post-spraying drying stage was added, whereby drying is accelerated without resorting to higher substrate temperatures, using air flow delivered by a handheld dryer gun or by the spray nozzle itself. Details of the process, OPV device performances, and related characterizations will be discussed in this section.

To realize single-pass deposition of P3HT:PCBM, it was necessary to improve the wettability of the substrates by the ink and alleviate the coffee-ring effect observed in the previous stage. Girotto et al.[155] have shown that employing a blend of two solvents, comprising a low boiling point and a low surface energy component, is effective in improving

[1] The evaporation time for the samples deposited at 25 °C was is the order of several minutes, and up to 30 minutes in the case of the samples deposited at higher flow rates and lower spray nozzle speeds.

wettability. In addition , it is shown that using this approach is effective in alleviating coffee-ring effects, as the Marangoni flows caused by surface energy gradients in the ink, can reverse the coffee ring effect[155, 178]. Based on this approach, we have used a blend of DCB and mesitylene as the ink solvent, which has been recently used by some groups for spray-coating of single-pass[9, 155] and multi-pass[10] layers of P3HT:PCBM. Figure 4.12 shows the contact angle measurement results for this ink in comparison to inks made using the same solute concentration in pure chlorobenzene (CB) and DCB solvents. The ink made using the mesitylene and DCB blend has the smallest contact angle in comparison to the others, enabling a more effective wetting of the substrate surface for single-pass deposition.

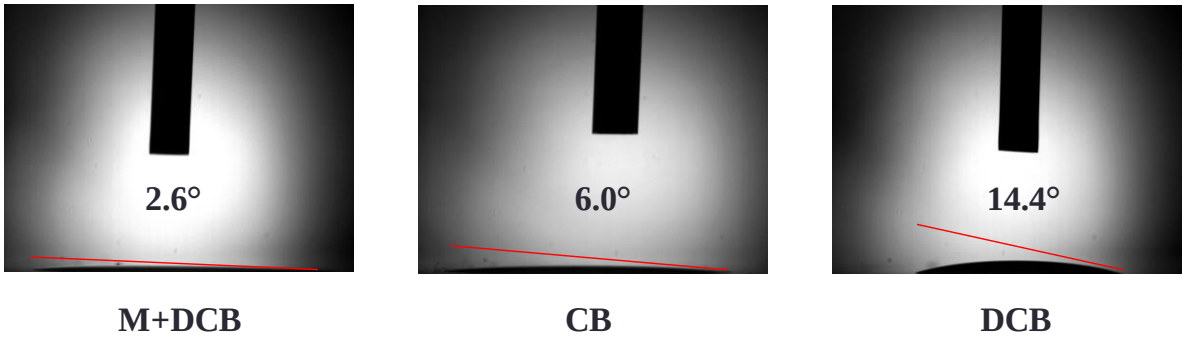


**Figure 4.12:** Contact angle measurement results for inks using DCB, CB, and a blend of mesitylene and DCB as solvents.

Table 4.3 shows the performance metrics for the best OPV devices fabricated using the single-pass spray-coating at 25 °C in air, and followed by accelerated drying using cold and warm air blow from a handheld dryer gun. *I-V* curves of the devices are shown in Figure 4.13. Two different nozzle speeds, $V_c$ = 55 and 25 mm/s, are used to consider the effect of different thicknesses. The best performances are obtained using 25 mm/s deposition speed. $V_{OC}$ = 0.52

V, $I_{SC}$ = 7.51 mA/cm$^2$ and $FF$ = 0.52 are obtained for the device dried using cold air, resulting in an efficiency of $PCE$ = 2.06%. For the device dried using warm air blow, these values are $V_{OC}$ = 0.56 V, $I_{SC}$ = 8.80 mA/cm$^2$ and $FF$ = 0.47, resulting in 2.35% efficiency. Both devices have performed better than the reference spun sample fabricated in a $N_2$ glovebox.

**Table 4.3:** Performance of single-pass spray-coated OPV devices dried using a handheld dryer gun

| Solution | Nozzle-to-substrate Distance (mm) | T(Substrate) (°C) | flow (ml/min) | Shaping Air | V (mm/s) | Numbe of Layers | Drying Method | Anneal | Comments | Voc (V) | Isc (mA/cm2) | PCE (%) | FF |
|---|---|---|---|---|---|---|---|---|---|---|---|---|---|
| m+DCB (3:7), 8 mg/ml | 67 | 25 | 0.425 | 0.78 | 55 | 1 | cold blow | 150 C, 5' | spray-coated | 0.54 | 5.62 | 1.64 | 0.53 |
| m+DCB (3:7), 8 mg/ml | 67 | 25 | 0.425 | 0.78 | 25 | 1 | cold blow | 150 C, 5' | spray-coated | 0.52 | 7.51 | 2.06 | 0.52 |
| m+DCB (3:7), 8 mg/ml | 67 | 25 | 0.425 | 0.78 | 55 | 1 | warm blow | 150 C, 5' | spray-coated | 0.56 | 6.50 | 2.18 | 0.59 |
| m+DCB (3:7), 8 mg/ml | 67 | 25 | 0.425 | 0.78 | 25 | 1 | warm blow | 150 C, 5' | spray-coated | 0.57 | 8.80 | 2.35 | 0.47 |
| 40 mg/ml in DCB | | 25 | | | | | air dry | N | spun | 0.53 | 7.22 | 1.82 | 0.47 |

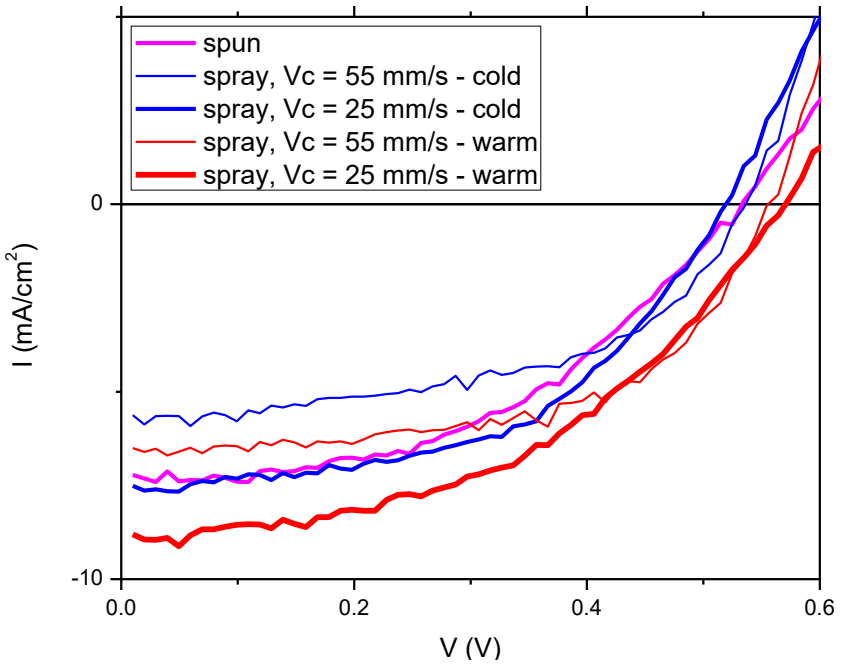


**Figure 4.13:** Comparison of the *I-V* characteristics of OPV devices fabricated through single-pass spray-coating and dried using a handheld dryer gun.

*Effect of Thermal Annealing*

Owing to the accelerated drying of the films in the method introduced here, the equilibrium formation of P3HT and PCBM phases is not possible. This is expected to lead to incomplete crystallization of P3HT, as well as non-equilibrium segregation of the phases, which has been reported elsewhere for fast-dried P3HT:PCBM bulk heterojunctions[180, 181]. To further improve the film uniformity, a post-deposition thermal annealing step was carried out immediately after spray-coating. Figure 4.14 shows the effect of this heat treatment (done at 150 °C) on macroscopic uniformity of the devices, optical absorption of the spray-coated films, and on solar cell performance. Annealing has improved the uniformity (decreased color contrast on the sample) and improved optical absorption (both through increasing peak absorption and increasing absorption at higher wavelengths (>550 nm). After annealing, the short-circuit current and the fill factor have increased and $V_{OC}$ has slightly decreased. The increase in $I_{SC}$ and *FF* compensate the effect of $V_{OC}$ and lead to the improvement of *PCE*. A similar effect has been reported by Sharma et al. [177] using solvent annealing of copolymer:fullerene solar cells. The increase in the *PCE* of the device upon annealing has been explained in terms of improvement in light absorption, by extending the conjugation length of the polymer chains, and balance charge transport, mainly due to the improved crystalline morphology of the polymer[177].

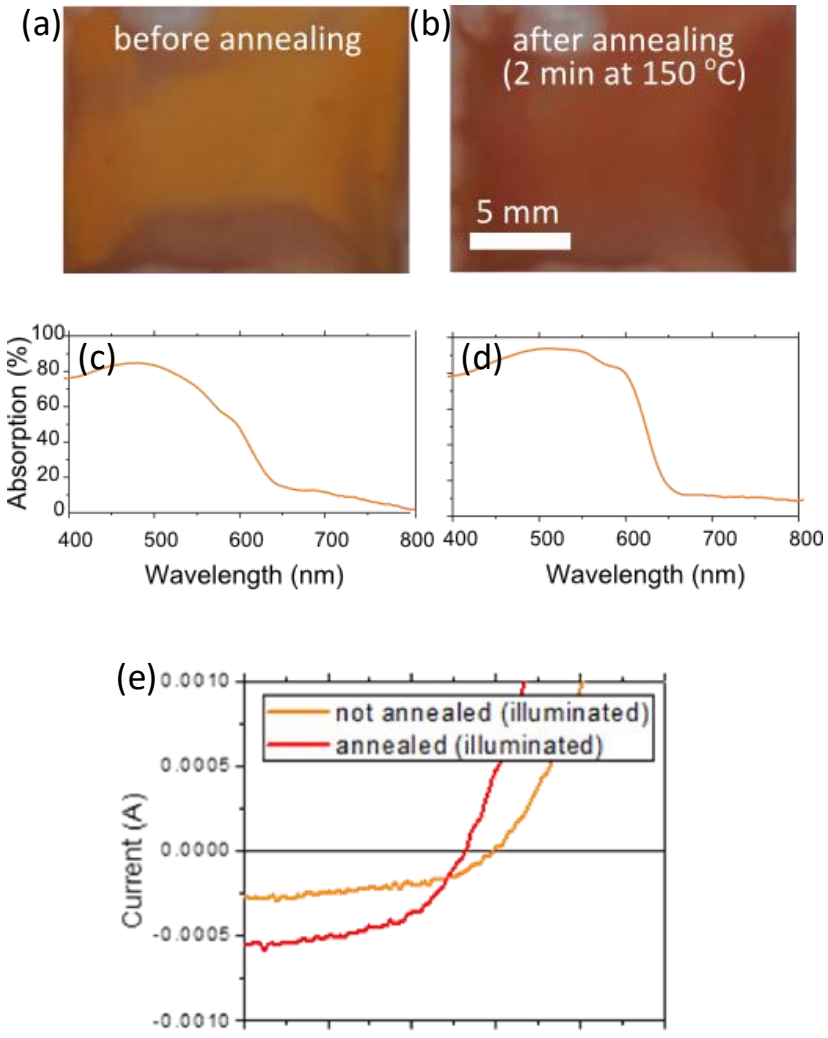


**Figure 4.14:** Effect of thermal annealing on macroscopic uniformity, optical absorption, and *I-V* characteristics of OPV devices fabricated through single-pass spray-coating and dried using a handheld dryer gun. (a, b) Photograph of the films before and after annealing, respectively, (c, d) optical absorption spectra of the films, (e) *I-V* curves of the devices measured before and after thermal annealing.

Figure 4.15 compares device performance metrics among all the devices fabricated through single-pass spray-coating and dried with cold and warm air blow using a handheld dryer gun. $V_{OC}$ and *FF* are consistent among the samples fabricated with various parameters, with the

average $V_{OC}$ in the range of 0.51 – 0.56 V and average *FF* in the range of 0.42 – 0.48. Devices dried with warm air have slightly higher $V_{OC}$ values. $V_{OC}$ and *FF* have the lowest standard deviation among devices deposited with $V_c$ = 25 mm/s and dried with warm air. $I_{SC}$ values show a clear correlation with spray-coating and drying parameters. Devices deposited at $V_c$ = 25 mm/s have higher $I_{SC}$ values compared to those deposited at $V_c$ = 55 mm/s, with the highest average and peak value being 7.06 ± 1.10 and 8.83 mA/cm$^2$, respectively, achieved in the case of the devices dried with warm air. Efficiency values are mostly controlled by current and follow the same general trends. The highest average and peak efficiency values are *PCE* = 1.80 ± 0.34% and 2.35%, respectively, achieved for the devices sprayed at $V_c$ = 25 mm/s and dried with warm air.

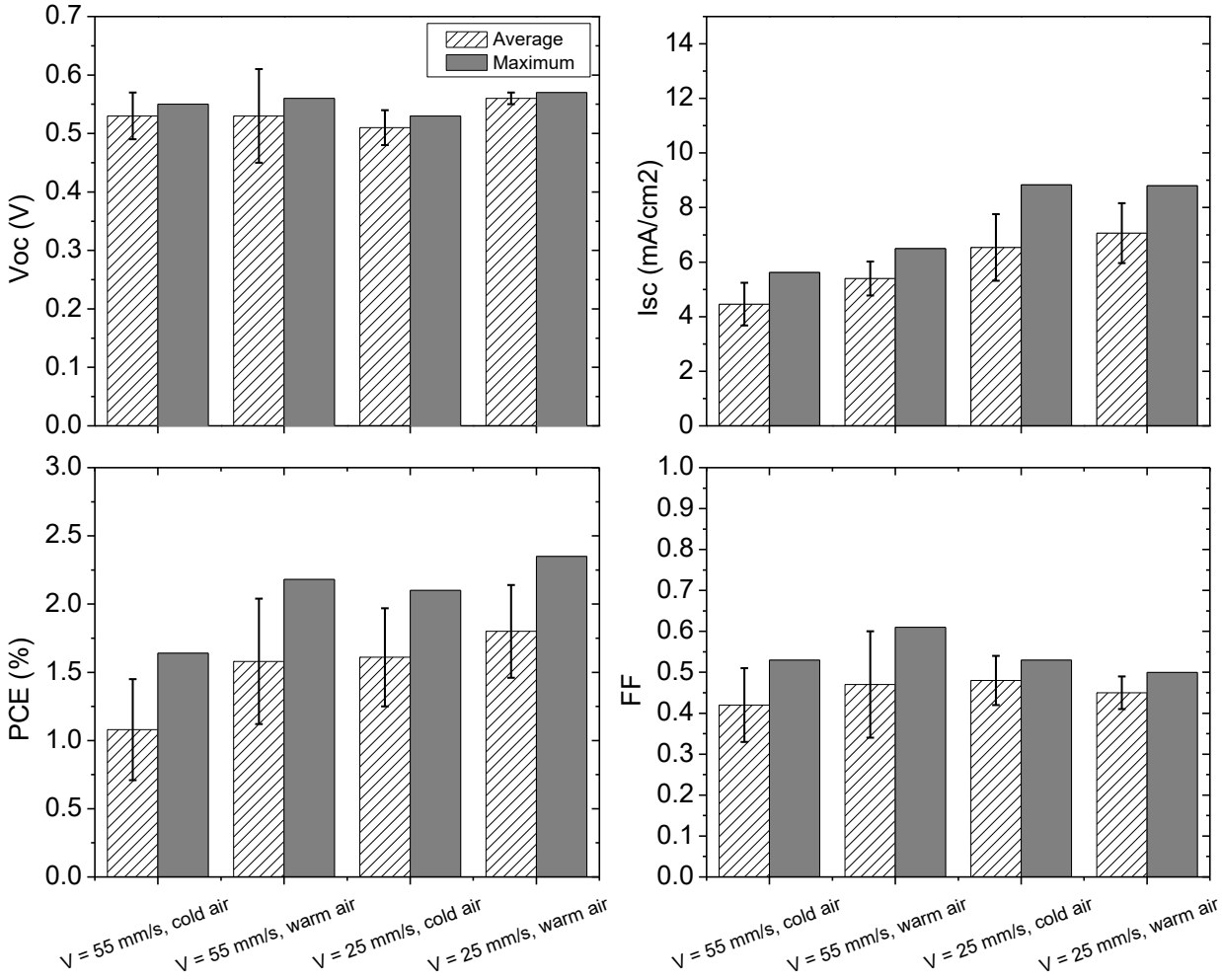


**Figure 4.15:** Comparison of OPV device performance metrics for among all the devices fabricated through single-pass spray-coating and dried with cold and warm air blow using a handheld dryer gun. Average and maximum values of $V_{OC}$, $I_{SC}$, *PCE* and *FF* are shown for devices with photoactive layers sprayed at two nozzle scan speeds ($V_c$ = 55, 25 mm/s) and dried with either cold or warm air.

Figure 4.16 shows the optical absorption spectra among photoactive films fabricated through single-pass spray-coating and dried with a handheld dryer gun. The spectrum for the spun reference sample is provided for comparison. Samples with thicker layers ($V_c$ = 55 mm/s) show higher absorbance than those with thinner active layer. Temperature of the drying air does not seem to have a clear influence on absorption.

Figure 4.17 shows the normalized external quantum efficiency (*EQE*) among selected devices. *EQE* graph of the spun reference sample is provided for comparison. Samples with thicker active layers show higher *EQE* at ~ 600 nm. Spun samples show a similar *EQE* to that of the sprayed sample deposited at $V_c$ = 25 mm/s.

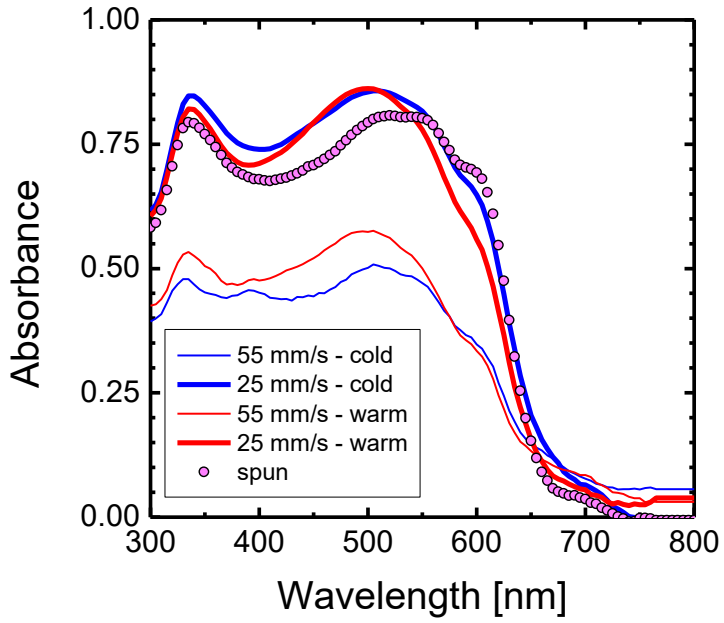


**Figure 4.16:** Comparison of optical absorption spectra among photoactive films fabricated through single-pass spray-coating using different nozzle scan speeds, and dried with cold and warm air blow using a handheld dryer gun. Optical absorption spectra for the spun reference sample is also provided for comparison.

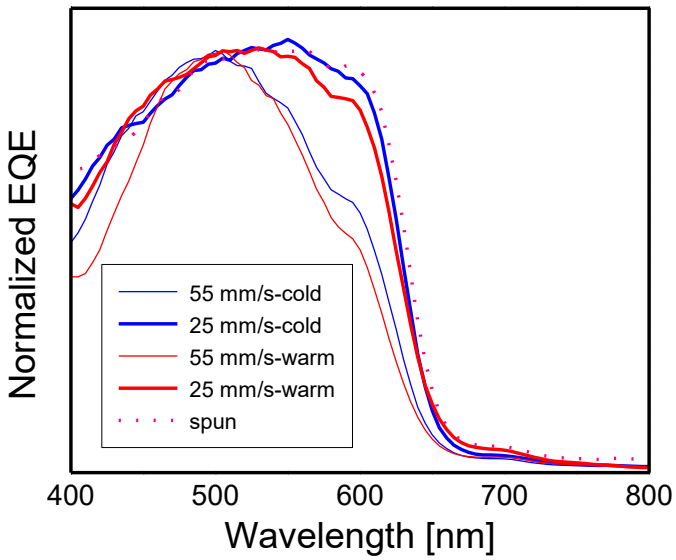


**Figure 4.17:** Comparison of external quantum efficiency (*EQE*) among devices fabricated through single-pass spray-coating using different nozzle scan speeds, and dried with cold and warm air blow using a handheld dryer gun. *EQE* graph of the spun reference sample is also provided for comparison.

Optical micrographs of the photoactive layer on near the device area is shown in Figure 4.18. The micrograph of the spun sample is provided as a reference. Spray-coated films have a pinhole-free structure with a better micro-scale uniformity than their spun counterpart. This can be attributed to the considerably lower drying times of the spray-coated samples compared to the spun films (~ 2 minutes in the case of the former, versus ~ 30 minutes in the case of the latter).

AFM micrographs of the surfaces of P3HT:PCBM films dried with cold and warm air are shown in Figure 4.19. Both films show a fine morphology of P3HT domains and have very low surface roughness values. The film dried with cold air blow has the roughness of $R_a$ ~ 2 nm while the one dried using warm air has achieved sub-nanometer roughness.

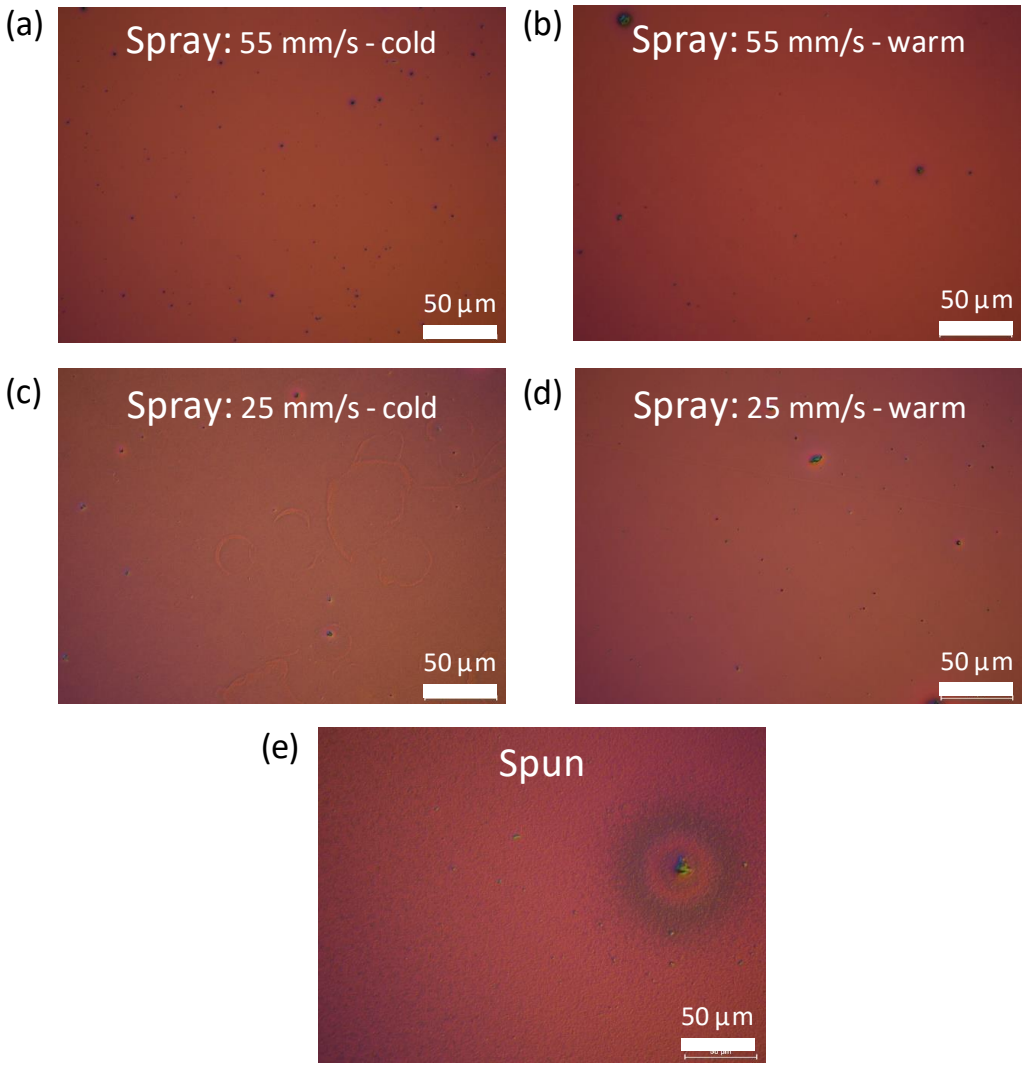


**Figure 4.18:** Optical micrographs of photoactive films on devices fabricated through single-pass spray-coating using a handheld dryer gun with (a) $V_c$ = 55 mm/s, cold drying air, (b) $V_c$ = 55 mm/s, warm drying air, (c) $V_c$ = 25 mm/s, cold drying air, (d) $V_c$ = 25 mm/s, warm drying air. Optical micrograph of the spun reference sample is also provided for comparison (e).

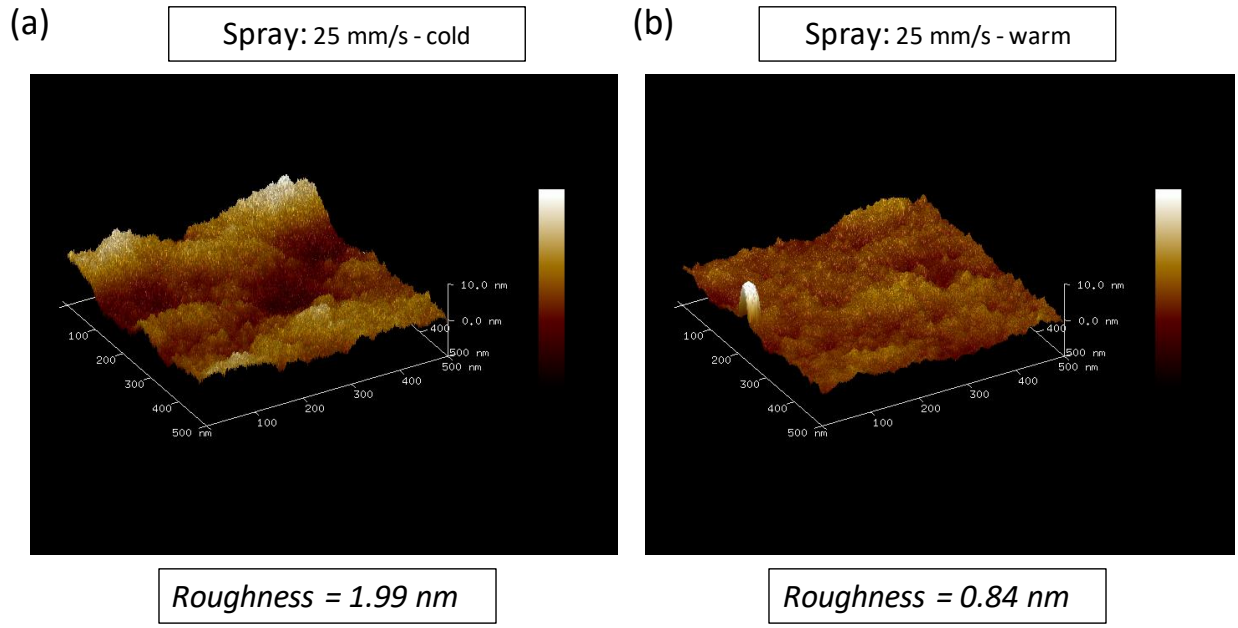


**Figure 4.19:** AFM micrographs of photoactive films on devices fabricated through single-pass spray-coating ($V_c$ = 25 mm/s) and dried with cold (a) and warm (b) air blow using a handheld dryer gun.

*Summary:* In this section we discussed the process we have introduced for single-layer spray-coating of P3HT:PCBM photoactive layers for organic solar cells. Using a modified ink composition and with the addition of a post-spraying air drying stage, OPV device efficiencies as high as 2.35% were obtained. The results were obtained by spray-coating in air at 25 °C substrate temperature. The spray-coated films show a high macro- and micro-scale uniformity and low surface roughness. Film morphology and device performance were superior to those obtained on a reference sample fabricated through spin-coating in $N_2$.

Above, we introduced a simple accelerated drying method for the fabrication of single-pass spray-coated OPV devices at 25 °C substrate temperature and in air atmosphere. In the next stage, we have focused on further improving the introduced process, considering our research goals (Section 4.1). Here, we have aimed for:

1) Improving the consistency and repeatability of the fabrication process by replacing the manual drying with an automated process,
2) Enabling large-area deposition,
3) Further reducing the fabrication power consumption by replacing warm air with cold air, without compromising device performance.

In this stage, we have introduced a drying process whereby the spray-coater nozzle itself is used to deliver a constant flow of drying gas to the spray-coated film. In addition to being completely computer-controlled, this method has the advantage of scalability through adjusting the drying nozzle scanning movement for desired substrate sizes. Details of OPV device performances and related characterizations will be discussed below.

Table 4.4 shows the performance metrics for the best OPV devices fabricated using single-pass spray-coating and dried using automated nozzle drying. Two spray-coating nozzle speeds of $V_c$ = 35 and 45 mm/s are used in the coating, and two drying nozzle-to-substrate distances, $h_{d2}$ = 75 and 50 mm, are used in the second stage of drying. The best performances are obtained from the devices coated at 45 mm/s deposition speed. Devices show high performance for both drying nozzle-to-substrate distances, with $V_{OC}$ = 0.58 V, $I_{SC}$ = 6.49 mA/cm$^2$, $FF$ = 0.53 and $PCE$ = 2.01% for the device dried from 75 mm distance, and $V_{OC}$ = 0.55 V, $I_{SC}$ = 12.09 mA/cm$^2$, $FF$ =

0.39 and *PCE* = 2.57% for the device dried from 50 mm distance. Using the nozzle drying method, all the devices have been dried within 2 – 2.5 minutes.

**Table 4.4:** Performance of single-pass spray-coated devices dried using automated nozzle drying

| Solution | Nozzle-to-substrate Distance (mm) | T(Substrate) (°C) | flow (ml/min) | Shaping Air | V (mm/s) | Number of Layers | Drying Method | Anneal | Comments | Voc (V) | Isc (mA/cm2) | PCE (%) | FF | Drying time (m:ss) |
|---|---|---|---|---|---|---|---|---|---|---|---|---|---|---|
| m+DCB (3:7), 8 mg/ml | 67 | 25 | 0.425 | 0.78 | 35 | 1 | nozzle | 150 C, 5 min | *h2* = 75 mm | 0.54 | 5.07 | 1.36 | 0.50 | 2:29 |
| m+DCB (3:7), 8 mg/ml | 67 | 25 | 0.425 | 0.78 | 35 | 1 | nozzle | 150 C, 5 min | *h2* = 50 mm | 0.48 | 5.10 | 0.90 | 0.37 | 2:25 |
| m+DCB (3:7), 8 mg/ml | 67 | 25 | 0.425 | 0.78 | 45 | 1 | nozzle | 150 C, 5 min | *h2* = 75 mm | 0.58 | 6.49 | 2.01 | 0.53 | 2:40 |
| m+DCB (3:7), 8 mg/ml | 67 | 25 | 0.425 | 0.78 | 45 | 1 | nozzle | 150 C, 5 min | *h2* = 50 mm | 0.55 | 12.09 | 2.57 | 0.39 | 2:02 |

Details of device performance for all the four conditions and all the devices are shown in Figure 4.20. In general, $V_{OC}$, $I_{SC}$, *PCE* and *FF* values are higher for devices deposited at $V_c$ = 45 mm/s and devices dried from $h_d$ = 75 mm drying nozzle-to-substrate distance. Lower standard deviation of performance metrics is observed in the case of the devices dried from a higher drying nozzle-to-substrate distance. This can be attributed to the fact that the drying air can create occasional disturbances on the surface of the sprayed film as it dries, creating randomly positioned pinholes on the dried active layer. Using $V_c$ = 45 mm/s and $h_d$ = 75 mm, highly consistent performance has been achieved using the nozzle drying method, with standard deviations of < 2% for $V_{OC}$ and *FF*, < 6% for $I_{SC}$, and < 9% for *PCE*. Short circuit currents exceeding 12 mA/cm$^2$ have been achieved, giving rise to the peak efficiency of *PCE* = 2.57% for the device deposited at $V_c$ = 45 mm/s and dried from $h_d$ = 50 mm.

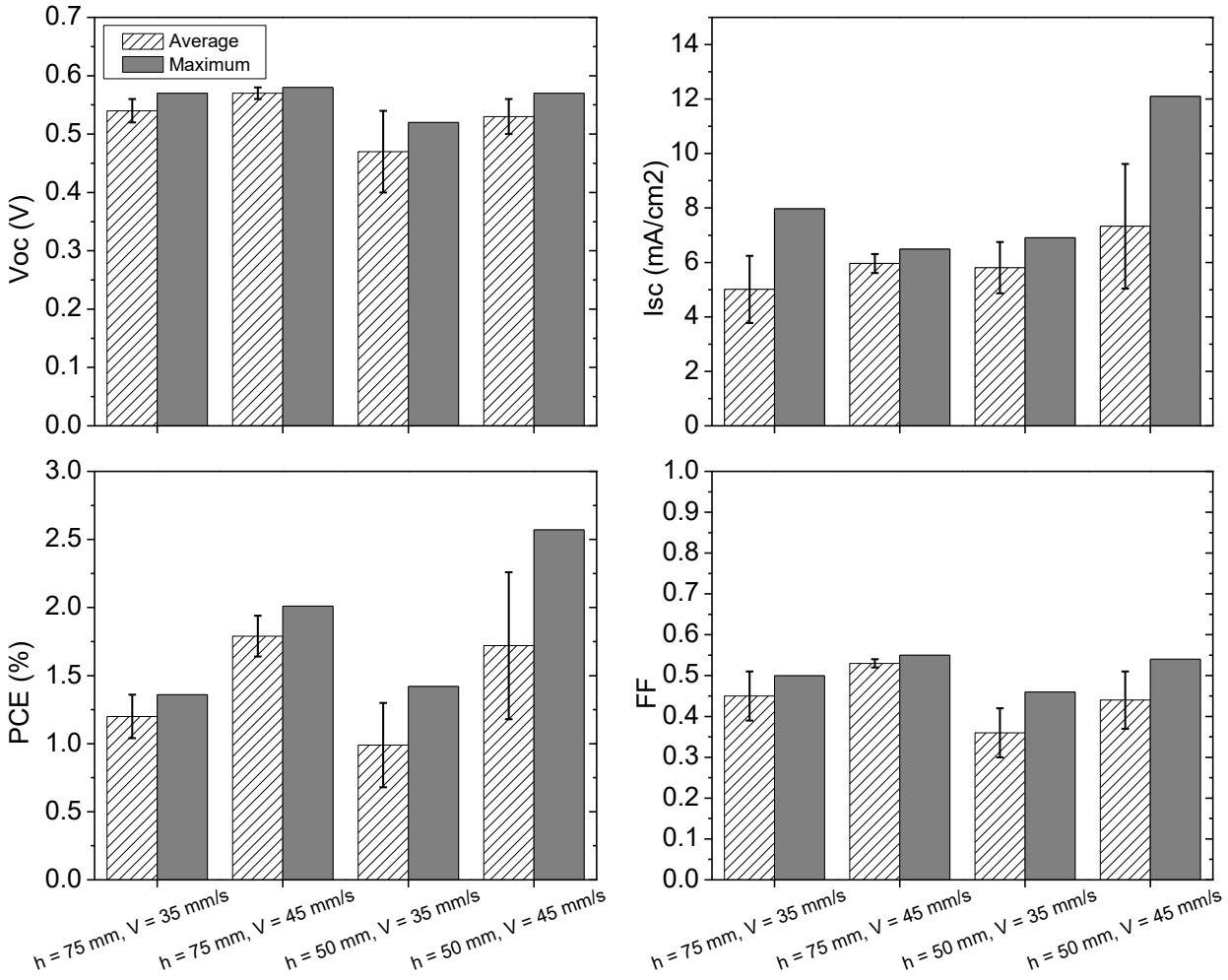


**Figure 4.20:** Performance of the OPV devices fabricated through single-pass spray-coating and dried using automated nozzle drying. Average and maximum values of $V_{OC}$, $I_{SC}$, *PCE*, and *FF* are plotted for the devices with photoactive layers sprayed using 35 mm/s and 45 mm/s coating nozzle scan speed and dried from 75 mm and 50 mm drying nozzle-to-substrate distance.

The thickness of the active layer at various points on the substrate is shown in Figure 4.21. Average thicknesses for the devices spray-coated at $V_c$ = 35 mm/s and $V_c$ = 45 mm/s are ~ 240 nm and ~ 160 nm, respectively. Further discussion on the correlation of OPV device performance to active layer thickness will be discussed at the end of this section.

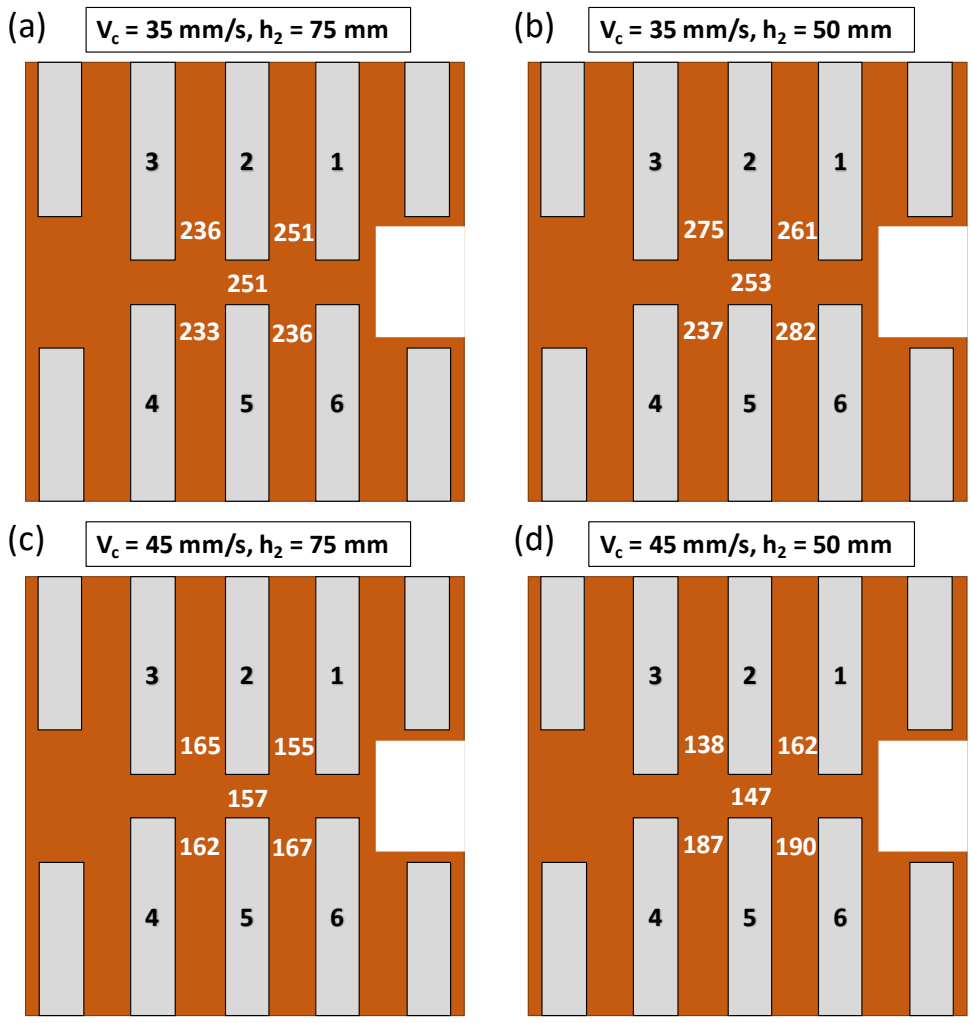


**Figure 4.21:** Photoactive layer thickness in vicinity of OPV devices fabricated through single-pass spray-coating and dried using automated nozzle drying. (a) $V_c$ = 35 mm/s, $h$ = 75 mm, (b) $V_c$ = 35 mm/s, $h$ = 50 mm, (c) $V_c$ = 45 mm/s, $h$ = 75 mm and (d) $V_c$ = 45 mm/s, $h$ = 50 mm.

Figure 4.22 shows the AFM micrograph of the photoactive film on a device dried using automated nozzle drying. The film shows a fine morphology of P3HT domains and a low surface roughness value of $R_a$ ~ 3 nm, which is comparable to the films dried using the handheld dryer gun (Figure 4.19).

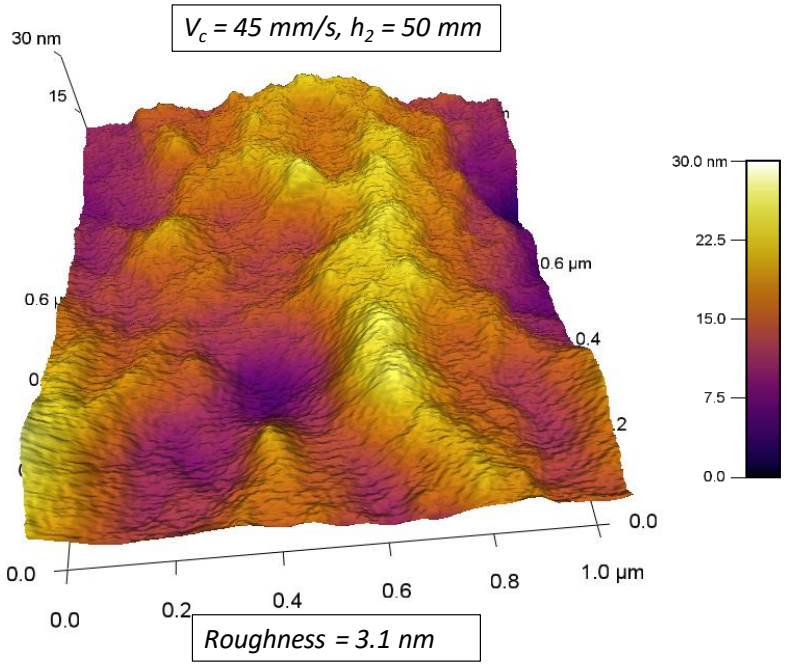


**Figure 4.22:** AFM micrograph of photoactive film on a device fabricated through single-pass spray-coating, and dried using automated nozzle drying.

*Summary:* Using single-pass deposition and nozzle drying, $V_{OC}$ = 0.58 V, $I_{SC}$ = 6.49 mA/cm$^2$, *FF* = 0.53 and *PCE* = 2.01% were obtained for the device dried from 75 mm nozzle-to-substrate distance, and $V_{OC}$ = 0.55 V, $I_{SC}$ = 12.09 mA/cm$^2$, *FF* = 0.39 and *PCE* = 2.57% in the case of the device dried from 50 mm nozzle-to-substrate distance. Figure 4.23 compares the performance of the nozzle-dried devices with those dried using the handheld dryer gun. In general, the devices dried using cold air with the nozzle-drying method have superior performances compared to those dried with either cold or warm air using the manual dryer gun. Using nozzle drying, devices with performance metrics as high as $V_{OC}$ = 0.58 V (0.57 ± 0.01 V in average), $I_{SC}$ = 12.10 mA/cm$^2$ (7.33 ± 2.29 mA/cm$^2$ in average), *PCE* = 2.57% (1.72 ± 0.54% in average) and *FF* = 0.55 (0.53 ± 0.01 in average) were obtained. In addition, devices nozzle-

dried from 75 mm drying nozzle-to-substrate distance show the smallest standard deviation, which indicates the effectiveness of this process for the fabrication of OSCs with reproducible performance.

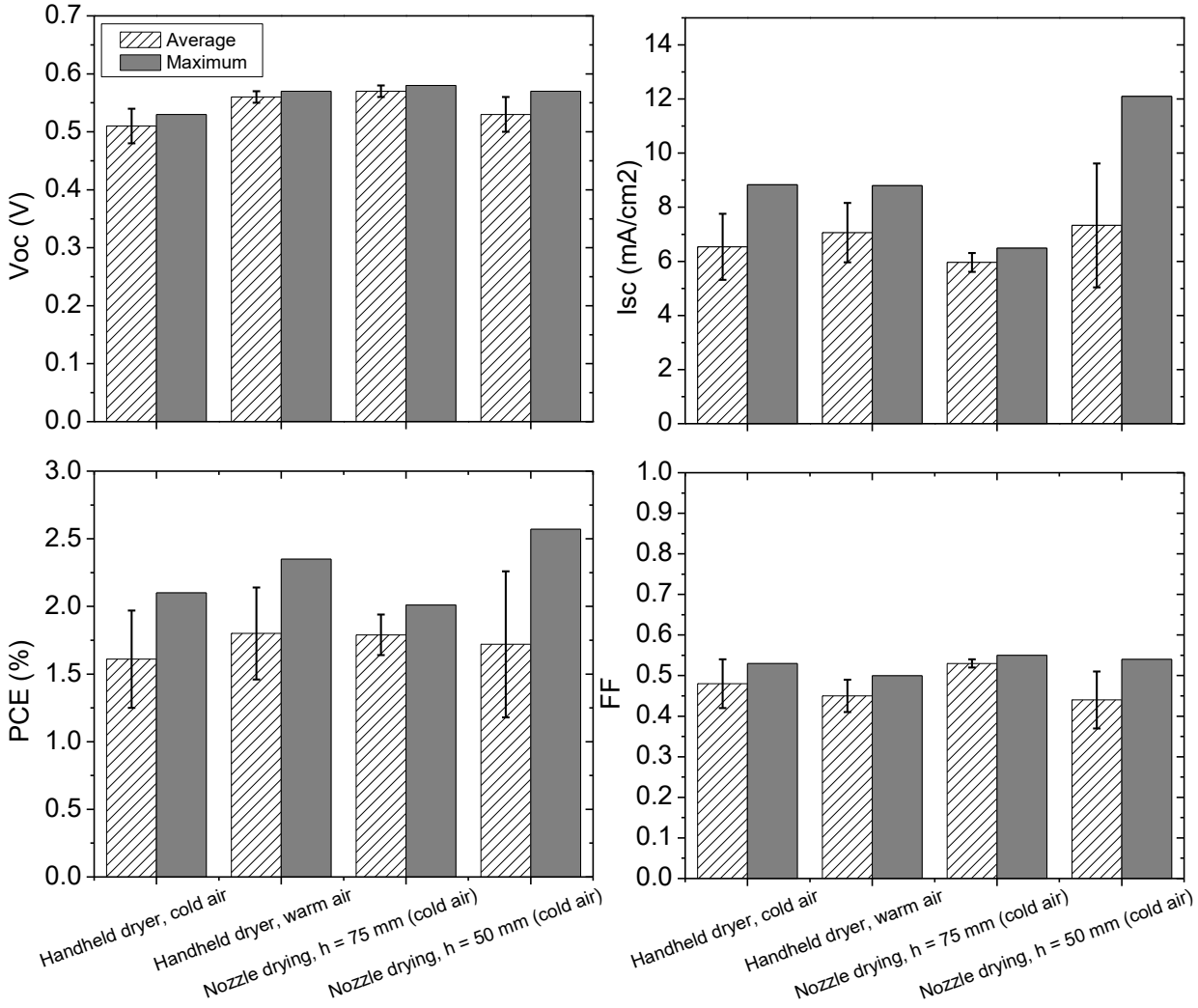


**Figure 4.23:** OPV device performance metrics for devices fabricated through single-pass spray-coating and dried using automated nozzle drying, in comparison with devices fabricated in the previous stage of this research employing a handheld dryer gun.

To separate the effect of active layer thickness in device performance, we have plotted the performance metrics against estimated active layer thickness for individual devices (Figure 4.24). $I_{SC}$ and *PCE* peak around 200 nm thickness. $V_{OC}$ and *FF* show no discernible dependence on thickness. Comparing different drying methods, nozzle-dried devices (cold air) have performances superior to their handheld gun-dried counterparts (warm and cold air). Among the latter, devices dried using warm air have higher currents and efficiencies.

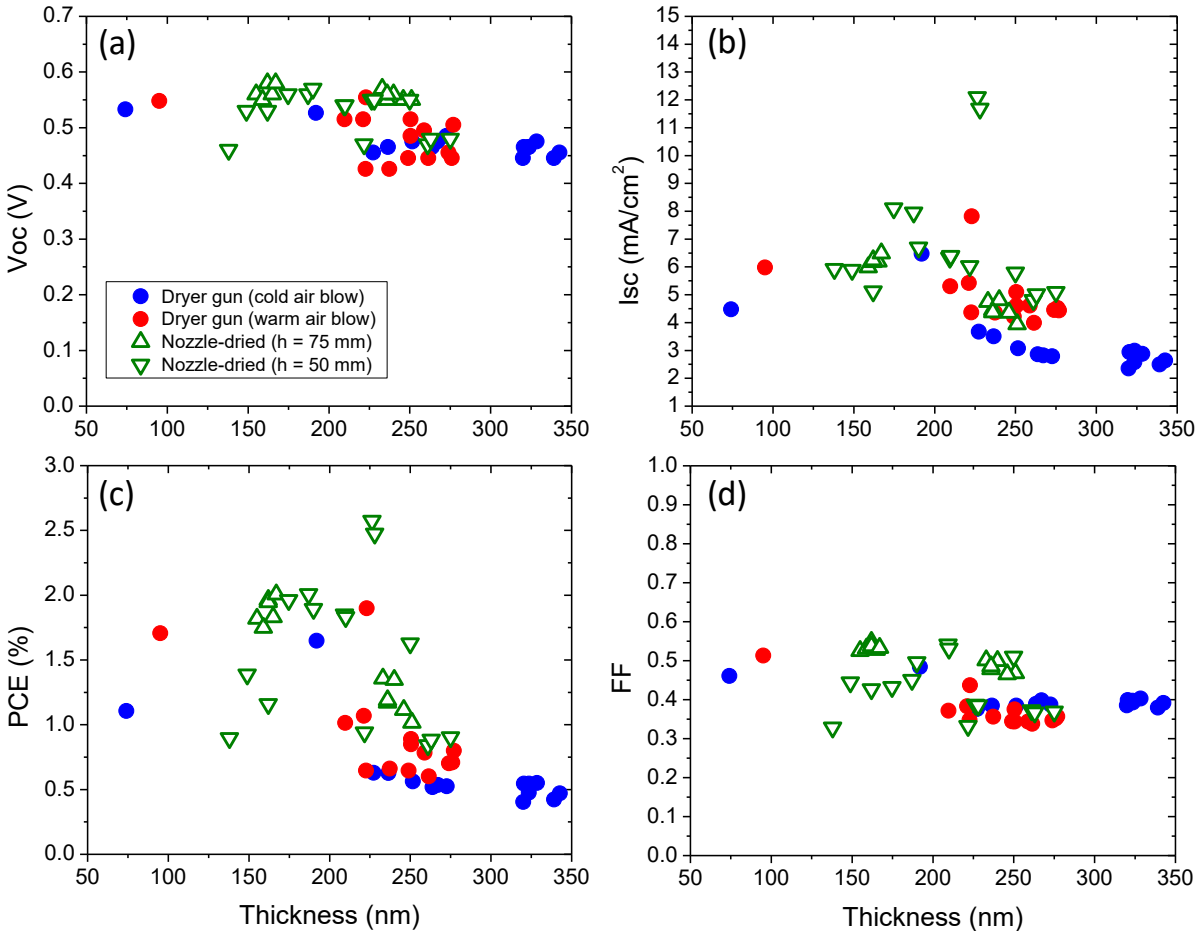


**Figure 4.24:** OPV device performance metrics plotted against estimated average photoactive layer thickness for devices fabricated through single-pass spray-coating followed by accelerated drying by a handheld dryer gun or automatic nozzle drying. (a) $V_{OC}$, (b) $I_{SC}$, (c) *PCE*, and (d) *FF*.

## 4.3 Applications of the Introduced Spray-Coating Process for Scalable Fabrication of Organic Solar Cells

In Section 4.2, we discussed the results obtained, during various stages of development of the present research, for low-temperature, low material consumption fabrication of OPV devices. Performances approaching the material limits were obtained through single-pass spray-coating of P3HT:PCBM photoactive layers in air, followed by accelerated air drying. To demonstrate the capability of this process for the fabrication of all-sprayed solar cells over large substrate areas, in Section 4.3.1, we will discuss room-temperature single-pass spray-coating of PEDOT:PSS hole transport layers, in addition to the active layer; In Section 4.3.2, we explore the effectiveness of the introduced process for large-area spray-coating of P3HT:PCBM.

### 4.3.1 Fabrication of Fully Spray-Coated Organic Solar Cells

As interest in using spray-coating for the fabrication of organic solar cells increases, in the past few years a few groups have moved toward the fabrication of fully spray-coated organic solar cells[155, 173, 182]. There have been several attempts for the fabrication of PEDOT:PSS hole transport layers via spray-coating[155, 158, 159, 165, 173-175, 183-185], although most of these works have not reported all-sprayed solar cells[158, 159, 165, 175, 183-185]. Because of the high surface energy of the solution[155] and slow evaporation of the solvent (water)[183], it is difficult to achieve a uniform, pinhole-free film of PEDOT:PSS using spray-coating. To overcome this challenge, different approaches have been used to assist the spray-coating process, including applying an electric voltage[183], adding substrate vibration[185], and substrate heating[155, 158, 173, 183, 185, 186]. The latter is the most commonly used strategy. A majority of the researchers have used elevated substrate temperatures, ranging from 30 – 80

°C[155, 158, 173, 186] and, in some cases, over 120 °C[175, 183, 185]. Zabihi et al.[185] have succeeded in fabricating PEDOT:PSS films at 25 and 125°C, by inducing ultrasonic vibrations in the substrate. They have reported significant decrease in surface roughness, film thickness, and the number of defects and pinholes[185]. They have not used the resulting film in a device. Kang et al.[173] have fabricated fully-sprayed inverted OSCs using PEDOT:PSS layers sprayed at 25 and 80 °C. They have achieved 1.25% efficiency for the device fabricated at 25 °C in an inert glovebox atmosphere[173].

In this section, we will investigate the possibility of the fabrication of all-sprayed solar cells, by using a room-temperature single-pass spray-coating process in air to fabricate PEDOT:PSS hole transport layers as well as the P3HT:PCBM photoactive layers. Our goal is to deposit pinhole-free PEDOT:PSS films with thickness and surface roughness comparable to spun films, without employing substrate heating. The effects of PEDOT:PSS ink composition and spray-coating parameters on the uniformity of the sprayed films are studied. The performance of OPV devices using different combinations of spin- and spray-coated PEDOT:PSS and P3HT:PCBM layers will be discussed.

As mentioned earlier, the major challenge for the deposition of PEDOT:PSS via spray-coating is its high surface tension which hinders the effective coverage of the substrate. Based on the work of Fanton et al. [17], Girotto et al.[155] have used a secondary solvent with a lower surface tension and a lower boiling point (higher evaporation rate). Using this two-solvent system not only has decreased the contact angle but also enhanced the substrate via surface tension gradients in the blend (the Marangoni effect). They have suggested isopropanol (IPA) as

the secondary solvent, since it can be used to dilute PEDOT:PSS whereby even small amounts of IPA can significantly reduce the surface tension of the IPA/water system (Figure 4.25).

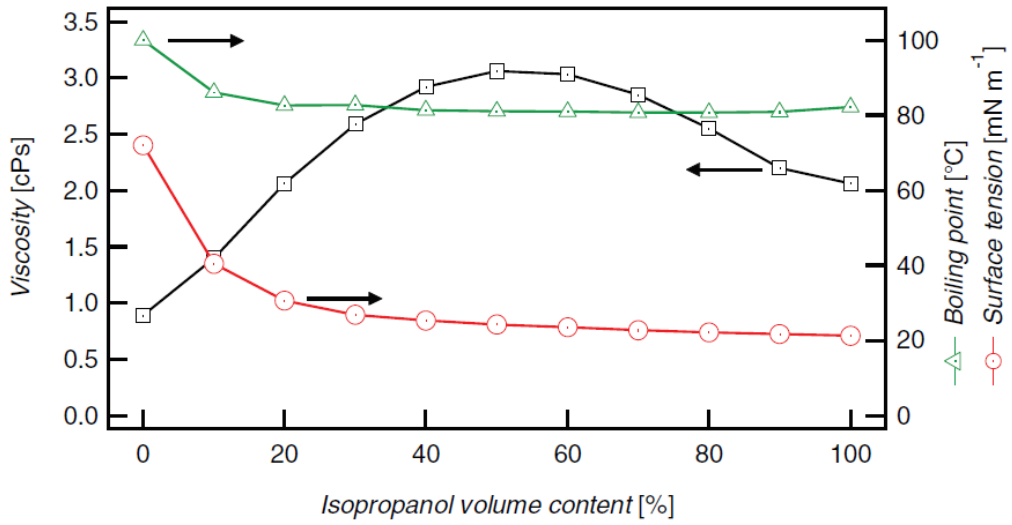


**Figure 4.25:** Viscosity, boiling point and surface tension of isopropanol/water mixtures at 25 °C as a function of isopropanol volume content [155].

Even though the addition of even 10% IPA significantly reduces the surface tension of the blend, Girotto et al. have shown that the volume ratio of IPA in the two-solvent blend should be kept between 55% and 89% in order to maintain a balanced evaporation of the two components while avoiding the instability of the solution[155]. To reproduce the PEDOT:PSS film thickness typically achieved with spin-coating (30 – 40 nm) through spray-coating at 25 °C substrate temperature, we have started with using an ink composition of 18:9:73 (PEDOT:water:IPA volume ratio). Figure 4.26(a) shows the distribution of thickness at various points over a 30 × 40 mm spray-coating area. Using a spray-coater nozzle speed of $V_c$ = 50 mm/s and nozzle-to-substrate distance of $h_c$ = 75 mm, this coating has resulted in an average thickness of ~ 50 nm

over the substrate, and a maximum thickness of > 70 nm, which are higher than the desired value (~ 30 nm). In order to reduce the thickness without changing ink viscosity, surface tension and solvent boiling point (see Figure 4.25), in the next sample we reduced the PEDOT:PSS content of the ink while maintaining the same IPA to water ratio (water content is defined as the sum of PEDOT:PSS and water[155]). Figure 4.26(b) shows the distribution of thickness obtained with an ink with 9:18:73 composition. Using this ink, the average thickness has been successfully reduced to ~ 20 nm. However, although a pinhole-free coating with thicknesses as low as ~ 11 nm is produced, the thickness is not uniform across the deposition area. In both Figure 4.26(a and b), it is observed that the points at lower left side of the substrate have a higher thickness. This directionality is in accordance with the trajectory of spray nozzle movement (which scans the deposition area by beginning from the lower-left and ending at the upper-right corner) and indicates that the solution deposited at earlier stages is partially dried before having the chance to re-distribute under the Marangoni effect towards the opposite corner of the substrate. To alleviate this effect, in the next attempt we reduced the ratio of IPA from 73% to 63%. As shown in Figure 4.25, decreasing the IPA to water ratio within this range results in an increase in ink viscosity, without having a significant effect on the surface tension or the boiling point of the blend. The effect will be an increase in Marangoni velocity, which will lead to a faster distribution of the ink across the substrate before the evaporation of the solvent prevails. The resulting distribution of the thickness for the film spray-coated using the 9:28:63 ink is shown in Figure 4.26(c). An average thickness of ~ 30 nm has been achieved, with higher thicknesses at the farther edges of the substrate, indicating a more balanced distribution of the solution. The thickness at the bottom-left of the substrate, corresponding to the starting nozzle position, is still

fairly high (60 nm), which still suggests that the solution has not been given enough time to travel across the substrate before the completion of evaporation.

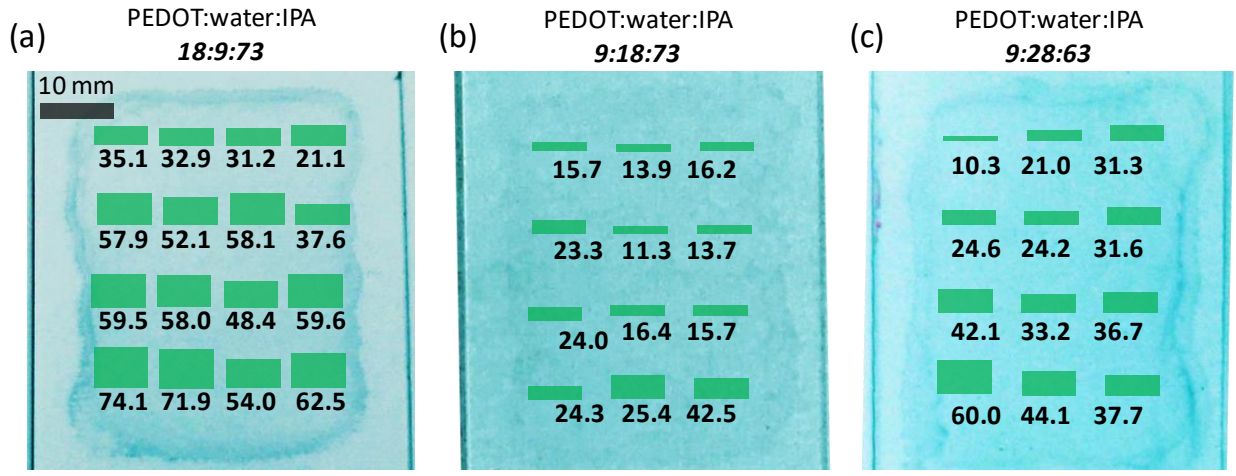


**Figure 4.26:** Distribution of sprayed PEDOT:PSS film thickness over a 30 × 40 mm deposition area, for the films sprayed from inks with three different compositions (expressed in PEDOT:water:IPA volume ratios). Results are provided for the inks with (a) 'high PEDOT content, high IPA:water ratio' (18:9:73), (b) 'low PEDOT content, high IPA:water ratio' (9:18:73), and (c) 'low PEDOT content, low IPA:water ratio' (9:28:63).

To address the latter issue, in the next stage we have focused on decreasing the deposition time without changing the overall amount of solution delivered to the substrate. The purpose is to reduce the time gap between the onset of drying (corresponding to the time of solution delivery to each point) at different positions on the substrate, thus providing a more balanced distribution of solution to begin with. To do so, we have proportionally increased the nozzle speed and flow rate values. Thereby, the solution delivery rate is increased while the overall volume of solution delivered to a given area remains constant. Three pairs of nozzle speed / flow rate values ($V_c$ = 50 mm/s, $f$ = 0.6 ml/min; $V_c$ = 75 mm/s, $f$ = 0.9 ml/min; $V_c$ = 100 mm/s, $f$ = 1.2

ml/min) were used. Figure 4.27(a-c) shows the distribution of film thickness resulted from spray-coating an ink with 9:28:63 composition using each of these paired values. By increasing the solution delivery rate, the uniformity of thickness across the substrate improves while the average thickness remains within the desired range (~ 30 nm).

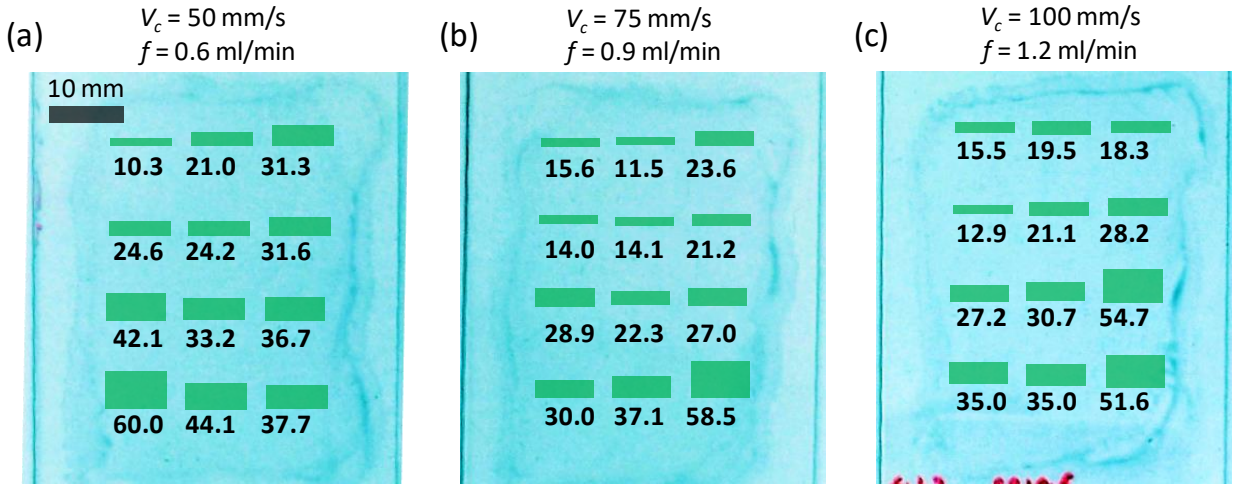


**Figure 4.27:** Distribution of sprayed PEDOT:PSS film thickness over a 30 × 40 mm deposition area, for the films sprayed at three different ink delivery rates (spray nozzle scan speed/solution flow rate paired values proportionally changed to deliver the same ink volume per substrate area). ). Results are provided for the paired values of (a) $V_c$ = 50 mm/s, $f$ = 0.6 ml/min, (b) $V_c$ = 75 mm/s, $f$ = 0.9 ml/min, and (c) $V_c$ = 100 mm/s, $f$ = 1.2 ml/min.

Figure 4.28 and Figure 4.29 show AFM micrographs of a film deposited using spray-coating in comparison with one deposited via spin-coating, on glass (Figure 4.28) and ITO (Figure 4.29) substrates. The micrograph of the bare glass or ITO surface is provided as a reference. It is observed that the spray-coated films have a surface roughness comparable, or slightly superior, to that of their spun counterparts.

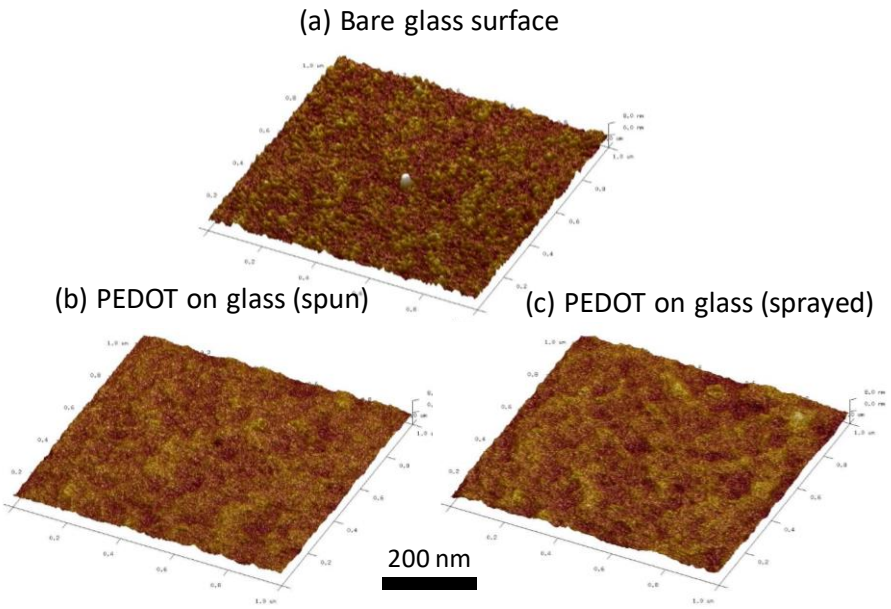


**Figure 4.28:** Comparison of surface morphology and roughness between spun and sprayed PEDOT:PSS films on glass. AFM micrographs of (a) bare substrate surface, (b) spun, and (c) sprayed PEDOT:PSS film.

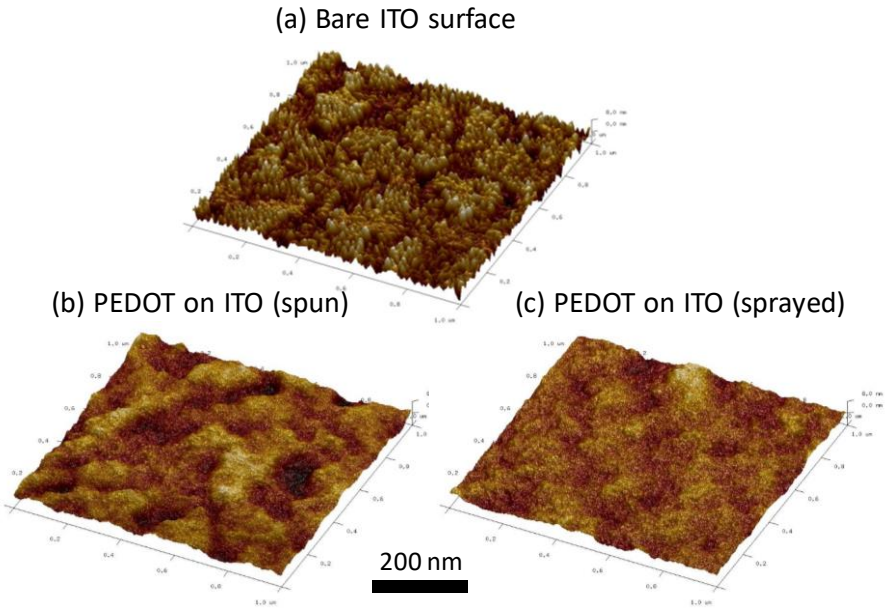


**Figure 4.29:** Comparison of surface morphology and roughness between spun and sprayed PEDOT:PSS films on ITO. AFM micrographs of (a) bare substrate surface, (b) spun, and (c) sprayed PEDOT:PSS film.

To demonstrate the application of the process for the fabrication of fully spray-coated solar cells, OPV devices were fabricated using various combinations of spin- and spray-coated layers. Figure 4.30 shows the *I-V* curves of the best devices with spray- and spin-coated PEDOT:PSS and P3HT:PCBM. Details of the performance of these four devices are provided in Table 4.5. For the devices with spun active layer, the device fabricated with sprayed PEDOT:PSS shows a performance similar to the all-spun reference device, with slightly higher $V_{OC}$, $I_{SC}$ and *PCE*, resulting in a *PCE* of 2.56%, as compared to 2.43% for the all-spun sample. For the devices with sprayed active layer, the device with sprayed PEDOT:PSS has shown a higher $I_{SC}$ but lower $V_{OC}$ and *FF* resulting in a *PCE* of 1%, as compared to 1.22% for the sample with spun PEDOT:PSS.

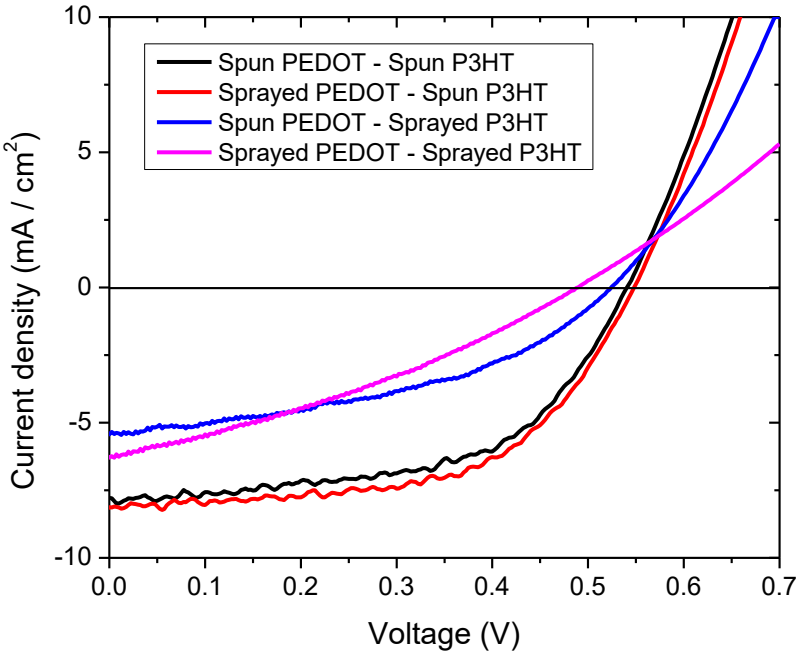


**Figure 4.30:** *I-V* curves of the devices fabricated using spray-coated vs. spin-coated PEDOT:PSS layers. *I-V* characteristics are compared for device structures with different combinations of spin- and spray-coated PEDOT:PSS and P3HT:PCBM layers.

**Table 4.5:** OPV device performance metrics for the devices with structures comprising different combinations of spin- and spray-coated PEDOT:PSS and P3HT:PCBM layers

| Deposition method | | Voc (V) | Isc (mA/cm2) | PCE (%) | FF |
|---|---|---|---|---|---|
| *PEDOT:PSS* | *P3HT:PCBM* | | | | |
| Spun | Spun | 0.54 | 7.78 | 2.43 | 0.57 |
| Sprayed | Spun | 0.55 | 8.12 | 2.56 | 0.57 |
| Spun | Sprayed | 0.53 | 5.43 | 1.22 | 0.43 |
| Sprayed | Sprayed | 0.49 | 6.27 | 1.00 | 0.33 |

*Summary:* Single-pass spray-coating was successfully used to deposit pinhole-free PEDOT:PSS films at 25 °C substrate temperature. The sprayed films have ~ 30 nm thickness over 30 × 40 mm substrate area, with surface roughness values comparable or superior to their spun counterparts. OPV devices using the sprayed PEDOT:PSS hole transport layer show a performance comparable to those with spun PEDOT:PSS, with a *PCE* = 2.56% for a device with sprayed PEDOT:PSS and spun P3HT:PCBM layer, and a *PCE* = 1.00% for the all-sprayed device.

### 4.3.2 Fabrication of Large-Area Spray-Coated Organic Solar Cells

In order to investigate the effectiveness of the introduced spray-coating process, here we have used it for large-area deposition of P3HT:PCBM layers (75 × 75 mm substrate size). The effect of spray-coating parameters on large-scale film uniformity will be discussed. The performance of OPV devices with larger device areas on large substrates will be discussed in comparison with those obtained on the smaller substrates using a similar spray-coating process.

As a preliminary to the fabrication of large-area devices using the spray-coating process, we have investigated the large-scale uniformity of film thickness over larger glass substrates. The effect of a number of spray-coating and nozzle drying parameters on improving the

uniformity was studied. Figure 4.31(a) shows the film deposited on a 75 × 50 mm glass substrate using the same parameters as used previously for 20 × 20 mm substrates. It is observed that the ink has not dried into a uniform film before drying. Rather, the trace of the spray-coating nozzle trajectory is distinguishable (characterized by parallel lines of reduced coverage corresponding to the vertical line distance between each horizontal pass). The effect suggests that the lines deposited at earlier stages are partially dried before the deposition of the next line, thus inhibiting the complete coalescence of the wet segments before the completion of drying. To overcome this effect, the nozzle speed and flow rate were proportionally increased to reduce the total deposition time while maintaining the amount of ink delivered to the substrate. Figure 4.31(b) shows the result of using modified deposition parameters. By increasing the deposition speed and flow rate to $V_c$ = 112.5 mm/s and $f$ = 1.06 ml/min, respectively, an observable improvement in film uniformity has been achieved.

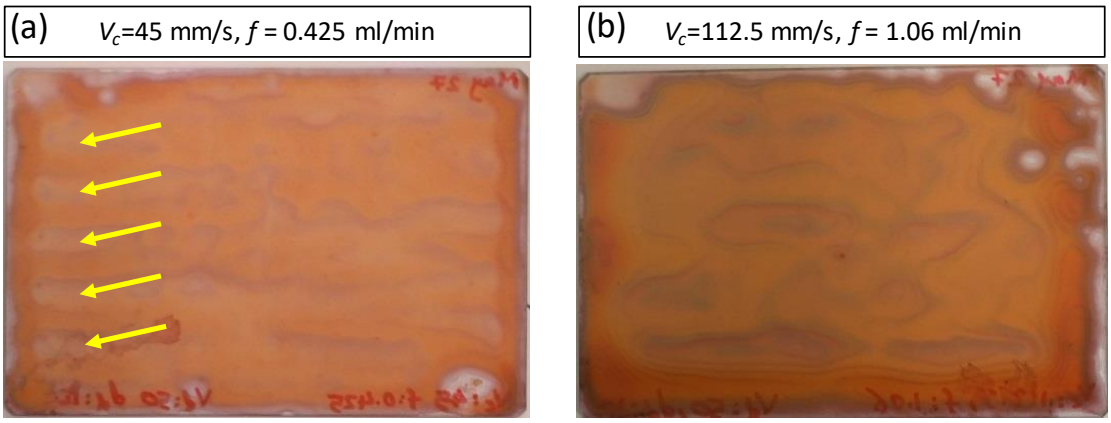


**Figure 4.31:** (a) Picture of a film deposited on 75×50 mm substrate, using the same parameters as used for 20×20 mm substrates. Arrows show the regions where the deposited lines are not effectively merged. (b) A film deposited on 75×50 mm substrate, using modified deposition parameters.

In search of the suitable set of parameters, the effect of changing the nozzle drying scan line distance ($d_d$, as defined in Figure 4.2) was also studied. Figure 4.32 compares the films spray-coated using two different solution delivery rates (adjusted through two pairs of nozzle speed/flow rate) and three drying nozzle scan spacing values. The measured film thickness at different points on the films is provided on the pictures. To provide a measure of evenness of the thickness along a horizontal profilometry profile, two different numbers are recorded for some of the points, which represent the film thickness at either side of the scratch used for the profilometry scan (examples can be seen in Figure 4.33). It is observed in Figure 4.32 that using a slower solution delivery rate ($V_c$ = 45 mm/s, $f$ = 0.425 ml/min) the issue of incomplete coalescence of the sprayed lines persists for all the drying line distances. Using a higher solution delivery rate ($V_c$ = 112.5 mm/s, $f$ = 0.425 ml/min), the solution successfully coalesces into a single wet layer before drying. The uniformity is improved by decreasing the drying scanning line distance. For the sample dried with $d_d$ = 25 mm, the trace of the drying nozzle trajectory is visible, in the form of two parallel horizontal regions approximately spaced by 25 mm. Reducing $d_d$ down to 4 mm has resulted in a uniform coating over the entire interior of the substrate. Using $V_c$ = 112.5 mm/s, $f$ = 1.02 ml/min and dd = 4 mm, an average thickness of ~ 180 nm is obtained, with a reasonable uniformity over the large substrate area. Examples of horizontally taken profilometry scans are shown in Figure 4.33 for the same samples. The films deposited at lower solution delivery rates and higher drying line distance have relatively uneven surfaces. The profile obtained from the film with $V_c$ = 112.5 mm/s, $f$ = 1.02 ml/min and $d_d$ = 4 mm shows a desirable thickness (~ 200 nm) evenly extended on either side of the scratch. Figure 4.34 shows the profilometry scans of the latter film, in comparison with that of a film on a 20 × 20 mm device typically used in this research. The film deposited on the 75 × 50 mm substrate

demonstrates comparable film uniformity and thickness to its small-area counterpart. Drying spreads quickly over most of the substrate area and only slows down toward the edges. Accordingly, the interior area of the substrate is uniform, with narrow margins of higher thickness near the edges. Drying time is ~ 3 minutes, which is comparable to that of smaller substrates (~ 2.5 minutes for 20 × 20 mm) despite the area of the former being ~ 14 times that of the latter.

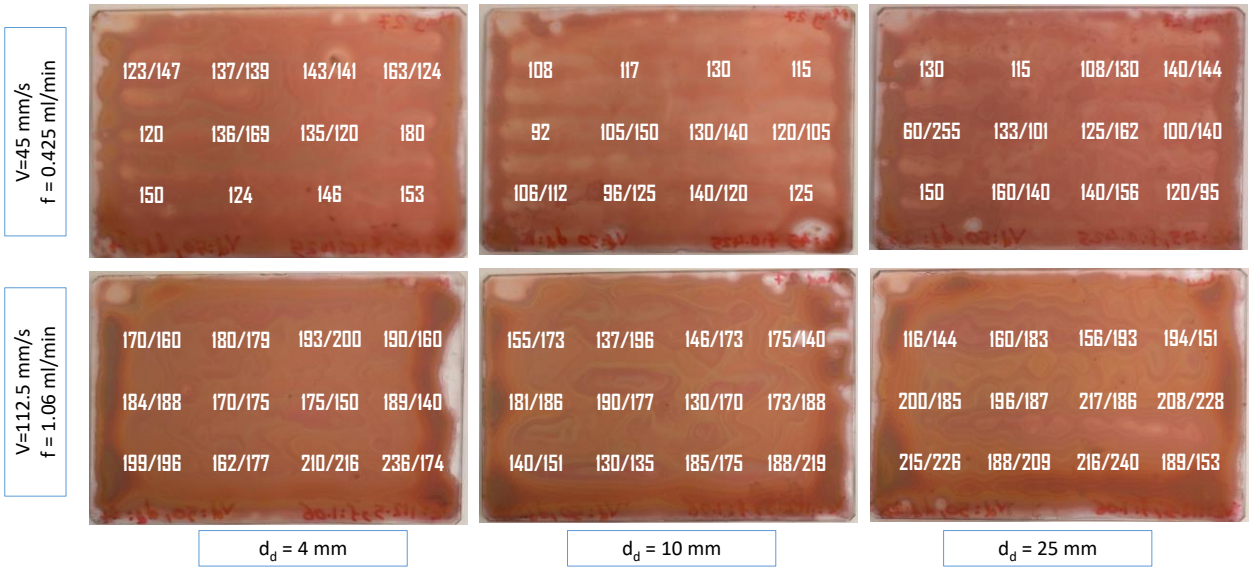


**Figure 4.32:** Thickness of the films at various points on the photoactive films spray-coated on large-area (75 × 50 mm) glass substrates, with different sets of spray-coating and nozzle drying parameters.

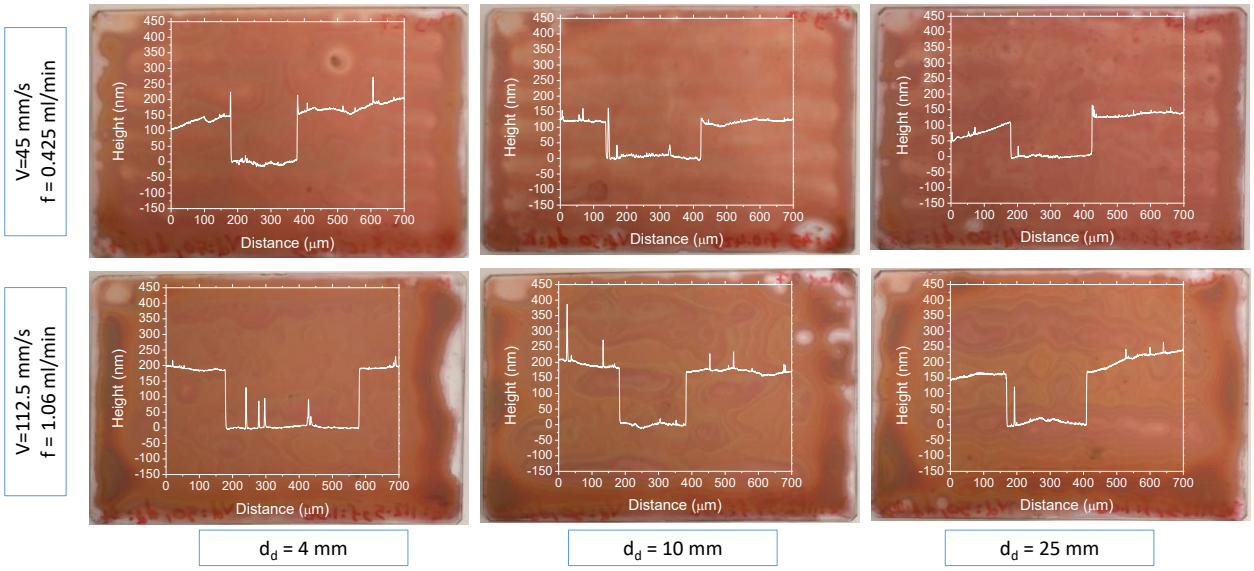


**Figure 4.33:** Thickness profiles across a scratch on the photoactive films spray-coated on large-area (75 × 50 mm) glass substrates, with different sets of spray-coating and nozzle drying parameters.

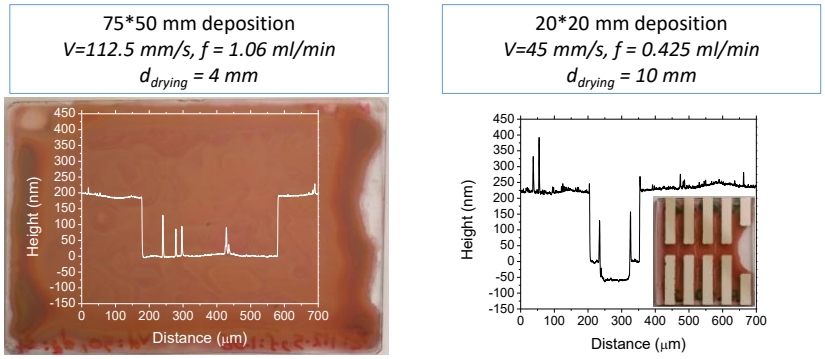


**Figure 4.34:** Comparison of thickness profiles between the films spray-coated over large and small areas.

Using the above findings, large-area OPV devices were fabricated on 75 × 75 mm ITO substrates. OPV devices on small area substrates were fabricated for comparison using the same ink and corresponding parameters. Figure 4.35 shows active layer uniformity and OPV performances for selected devices over the substrate. Figure 4.36(a) shows that the solution has effectively covered various parts of the substrate. Figure 4.36(b) shows a contour representation

of the variations in thickness over the area. In agreement with Figure 4.36(a), the distribution of thickness is uniform within the interior of the deposition area, with film thickness being in ~ 140 – 200 nm range. Figure 4.36(c-f) show the performance metrics for selected devices measured over the substrate. Open-circuit voltage and fill factor values are very consistent across the substrate, with $V_{OC}$ close to 0.5 V and *FF* over 0.25. Short-circuit current seems to vary according to the local thickness, approaching 7 mA/cm$^2$ near the edge of the substrate. Power conversion efficiency varies in accordance with $I_{SC}$, with maximum values approaching 1%.

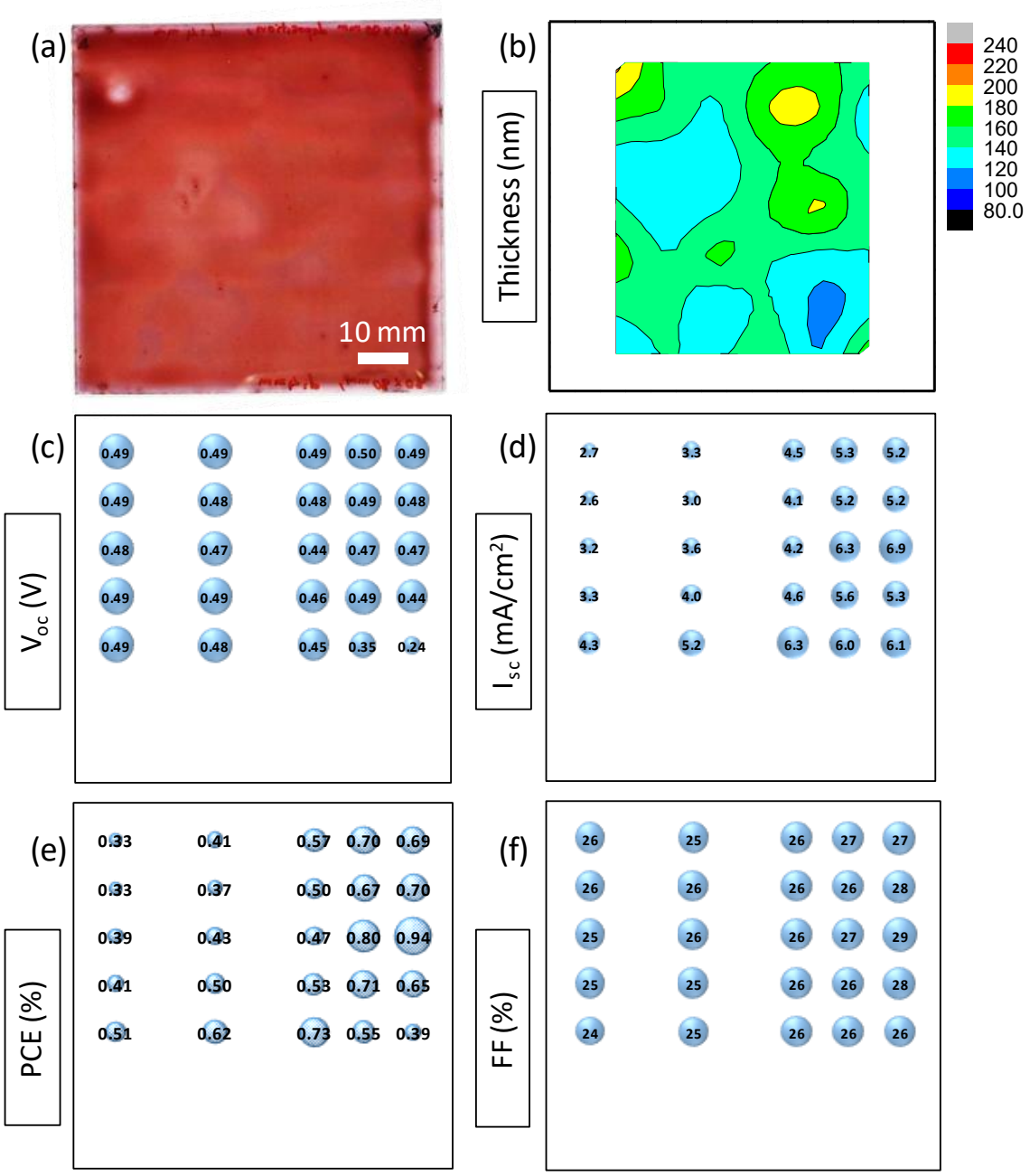


**Figure 4.35:** Photoactive film uniformity and OPV device performance for devices fabricated on large (75 × 75 mm) substrates. (a) Macro-scale film uniformity, and the distribution of (b) film thickness, (c) $V_{OC}$, (d) $I_{SC}$, (e) *PCE*, and (f) *FF* over the deposition area.

Figure 4.36 provides a graphical summary of the performance metrics for all the measured large-area devices, plotted against the estimated active layer thickness per device. The overall trends are similar to the case of the device discussed above. $V_{OC}$ and $FF$ values show little variation among different devices and for various active layer thicknesses. Average $V_{OC}$ ~ 0.45 V and peak $V_{OC}$ = 0.52 V are obtained. Average and peak $FF$ values are 0.26 and 0.31, respectively. The $I_{SC}$ values show more variation among different devices, with the average value of ~ 5 mA/cm$^2$ and the peak value of 7.46 mA/cm$^2$. $PCE$ values are mainly decided by $I_{SC}$, with the average value of ~ 0.6% and the peak value of 1.04%. Performance of the devices fabricated on 20 × 20 mm substrate areas (10 mm$^2$ active area) is provided for comparison. Devices on large substrates show photovoltaic properties comparable to those fabricated on small substrates, while having active device areas 5 times those on small substrates. Additionally, the performance of large-area devices seems to be less dependent on active layer thickness. It suggests that other factors such as photoactive layer nano-morphology and the interfaces between the layers play a more predominant role in device efficiency.

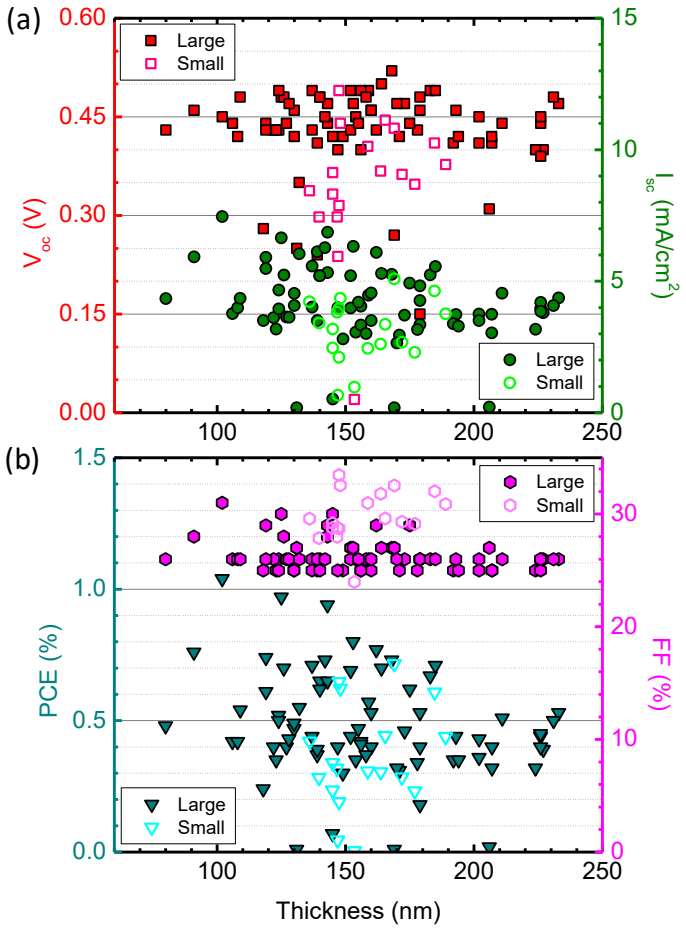


**Figure 4.36:** Comparison of OPV device performance between large- and small-area spray-coated devices, plotted against the estimated photoactive layer thickness. (a) $V_{OC}$ and $I_{SC}$, and (b) *PCE* and *FF*.

*Summary:* Single-pass spray-coating followed by accelerated nozzle drying was used for the fabrication of large-area OPV devices with 49 mm$^2$ active device area on 75 × 75 mm substrates. By adjusting spray-coating and nozzle drying parameters, uniform P3HT:PCBM films with ~ 180 nm thickness were deposited over a large deposition area with a drying time comparable to that of small-area substrates. OPV devices show performances comparable to small-area devices, with the peak performance of $V_{OC}$ = 0.52, $I_{SC}$ = 7.46 mA/cm$^2$, *FF* = 0.31 and *PCE* = 1.04%.

## 4.4 Summary and Comparison with Literature

In this chapter, we discussed various stages of development of the process for single-pass spray-coating of P3HT:PCBM photoactive layers at 25 °C substrate temperature in air. To achieve P3HT:PCBM films with macro- and micro-scale uniformity, low surface roughness, and desirable optical absorption, without the need to resort to elevated substrate temperatures, we introduced a post-deposition stage involving accelerated air drying of the spray-coated ink. Using a handheld dryer gun with warm air, efficiencies up to 2.35% were achieved. By replacing the handheld dryer with a computer-controlled nozzle drying process, we could achieve up to 2.57% efficiency using cold air. The application of the introduced spray-coating process was demonstrated through the fabrication of fully sprayed and large-area solar cells. Using spray-coated PEDOT:PSS layers produced via single-pass deposition at 25 °C substrate temperature, devices with a performance comparable to the spun counterparts were fabricated. Using spray-coating for the deposition of both PEDOT:PSS and P3HT:PCBM layers, efficiencies approaching 1% were achieved. The introduced process was successfully used for the deposition of P3HT:PCBM layers over 75 × 75 mm substrates, with thickness and uniformity comparable to those deposited on 20 × 20 mm substrates. With an active device area of 49 $mm^2$, efficiencies up to 1.04% were achieved on large substrates.

Table 4.6 and Table 4.7 summarize the fabrication parameters and solar cell performance of the best devices fabricated in the present research, in comparison with other reports in the literature using spray-coated P3HT:PCBM active layers. Most of the groups have used multi-pass spray-coating[10, 157, 168, 170] and elevated substrate temperatures[9, 155, 157, 162, 168] to achieve the desired active layer properties and solar cell performance. Susanna et al.[168] have reported efficiencies up to 4.1%, through multi-pass spray-coating at substrate temperatures from 25 to 70

°C. At $T_{sub}$ = 25 °C, they have achieved 2.7% efficiency. Using 50 sprayed layers, Steirer et al.[157] have achieved 3% efficiency at $T_{sub}$ = 25 °C. The efficiency is slightly improved by employing a solvent spray annealing post-deposition process. Lee et al.[10] have reported 0.97% efficiency by multi-pass deposition at room temperature. The efficiency is increased up to 2.44% by prolonged solvent spray annealing. Other groups have used single-pass deposition to improve the film uniformity and decrease material consumption. At 25 °C substrate temperature, Girotto et al.[170] have reported 2.84% efficiency using the single-pass method. Using a higher substrate temperature ($T_{sub}$ = 55 °C), Girotto et al.[155] have achieved 3.53% efficiency. Using a single-pass method at 55 °C substrate temperature, Tait et al.[9] have achieved 3.8% efficiency. They were able to improve the efficiency to 4% via coaxial spray-coating of P3HT:PCBM ink with pure solvent. It should be noted that most of these works have used an inert glovebox atmosphere for the post-processing and photovoltaic measurements[10, 170], or for all the spray-coating, post-processing and measurement stages[9, 155, 157]. The exceptions are the processes used by Susanna et al.[168] and Kim et al.[162]. The former group has achieved 2.7% efficiency by multi-layer spray-coating at $T_{sub}$ = 25 °C under a fumehood[168]. The latter has used single-pass deposition in air to fabricate devices with 1.1% efficiency which has been improved to 1.87% by solvent spray annealing. Both devices are fabricated at 150 °C substrate temperature[162]. In the present research, we have used single-pass deposition followed by accelerated air drying, at 25 °C substrate temperature. We have could achieve efficiencies as high as 2.35% through manual accelerated drying with warm air. By replacing the manual drying step with an automated nozzle drying process, we have achieved an efficiency of 2.57% using cold air. All the spray-coating, post-treatment and measurement stages have been carried out in air.

In terms of the properties of the spray-coated P3HT:PCBM film, different groups have reported thicknesses ranging from ~ 170 nm [10], up to over 400 nm[157, 162, 170]. The surface roughness values are generally high, due to the nature of the spray-coating or solvent spray annealing methods used in these researches. Reported roughness values mainly range from 10 nm to over 50 nm[9, 10, 155, 168, 170]. In a few cases, the roughness has been too high to be measured[157, 162, 170]. The lowest reported roughness value is 2.1 nm achieved with a ~ 250 nm-thick film using single-pass deposition at $T_{sub}$ = 55 °C[9]. In the present research, we have achieved surface roughness values as low as 0.84 nm in the case of a ~ 220 nm-thick film deposited using single-pass method at $T_{sub}$ = 25 °C and dried with warm air using a handheld dryer gun. The introduced process can produce low-roughness pinhole-free films within a wide range of thickness. P3HT:PCBM films with thicknesses as low as 75 nm have been successfully used in the fabrication of an OPV device with over 1% efficiency (see Figure 4.24).

**Table 4.6:** Spray-coating process parameters for different works reporting the fabrication of OPV devices using spray-coated P3HT:PCBM photoactive layers, in comparison with those of the present research

| Reference | Spraying process | Environment | | | Spraying parameters | | |
|---|---|---|---|---|---|---|---|
| | | Fabrication | Post-treatment | Measurement | Substrate temperature (°C) | Number of layers | Post-treatment |
| *Susanna at al., 2011* | handheld airbrush | *fumehood* | *fumehood* | *fumehood* | 25 - 70 | 3 | thermal annealing at 150 °C |
| *Girotto et al.,2009* | handheld airbrush | *air* | *inert* | *inert* | RT | single and multiple | thermal annealing at 140 °C |
| *Kim et al., 2012* | handheld airbrush | *air* | *air* | *air* | 150 | 1 | solvent spray annealing at 150 °C, whole device thermal annealing at 150 °C |
| *Steirer et al., 2009* | automatic with ultrasonic nozzle | *inert* | *inert* | *inert* | 25 - 78 | 50 | solvent spray annealingat 25 °C, thermal annealing at 110 °C |
| *Lee et al., 2011* | handheld airbrush | *air* | *inert* | *inert* | RT | multiple | solvent spray annealing at RT, thermal annealing at 150 °C |
| *Girotto et al., 2011* | automatic with ultrasonic nozzle | *inert* | *inert* | *inert* | 55 | 1 | thermal annealing at 110 °C |
| *Tait et al., 2013* | automatic with ultrasonic nozzle, coaxial spraying of two inks | *inert* | *inert* | *inert* | 55 | 1 | solvent spray annealing at 55 °C |
| ***This research, handheld gun drying*** | automatic with ultrasonic nozzle | *air* | *air* | *air* | 25 | 1 | thermal annealing at 150 °C |
| ***This research, automated nozzle drying*** | automatic with ultrasonic nozzle | *air* | *air* | *air* | 25 | 1 | thermal annealing at 150 °C |

**Table 4.7:** Sprayed film properties and OPV device performance from the references mentioned in Table 4.6, in comparison with the results achieved in the present research

| Reference | Sprayed film properties | | Device performance | | | | |
|---|---|---|---|---|---|---|---|
| | Thickness (nm) | Roughness (nm) | Description | Voc (V) | Isc (mA/cm2) | FF | PCE (%) |
| *Susanna at al., 2011* | 270 | 80 | *T(substrate) = 25 °C* | 0.57 | 10.62 | 44 | 2.7 |
| | | | *T(substrate) = 40 °C* | 0.64 | 10.98 | 59 | 4.1 |
| | | | *T(substrate) = 70 °C* | 0.63 | 9.6 | 49 | 2.9 |
| *Girotto et al.,2009* | 380 | 12.9 | *single-pass (as-produced)* | 0.61 | 9.2 | 0.51 | 2.84 |
| | 490 | high (couldn't measure) | *multiple-pass (as-produced)* | 0.68 | 1.8 | 0.32 | 0.4 |
| | 320 | | *multiple-pass (annealed)* | 0.63 | 5.2 | 0.5 | 1.64 |
| *Kim et al., 2012* | 400 | not reported | *pristine (sprayed P3:PC, no solvent annealing)* | 0.61 | 5.85 | 31 | 1.1 |
| | | | *solvent-annealed* | 0.63 | 7.12 | 45 | 1.87 |
| *Steirer et al., 2009* | 500 | high (numbers not reported) | *CB as solvent, T(substrate)= 25 °C* | 0.58 | 10.2 | 0.51 | 3 |
| | | | *CB as solvent, solvent annealing, T(substrate)= 25 °C* | 0.58 | 11.1 | 0.51 | 3.2 |
| | | | *p-xylene as solvent, T(substrate)= 25 °C* | 0.45 | 0.6 | 0.39 | 0.1 |
| | | | *p-xylene as solvent, T(substrate)= 78 °C* | 0.48 | 6 | 0.42 | 1.2 |
| *Lee et al., 2011* | 171 | 59.1 | *no solvent treatment* | 0.51 | 4.34 | 0.23 | 0.97 |
| | 215 | 31.1 | *DCB (their best)* | 0.58 | 6.7 | 0.5 | 1.95 |
| | 173 | 51.3 | *DCB (excess)* | 0.6 | 6.75 | 0.61 | 2.44 |
| *Girotto et al., 2011* | 220 | 10 | *standard device structure* | 0.575 | 8.84 | 69 | 3.53 |
| *Tait et al., 2013* | 249 | 2.1 | *singly sprayed P3HT:PCBM* | 0.61 | 9.1 | 0.69 | 3.8 |
| | 245 | 11.3 | *coaxial spraying (P3HT+PCBM)* | 0.62 | 9 | 0.7 | 3.9 |
| | 235 | 13.5 | *coaxial spraying (P3HT:PCBM + pure solvent)* | 0.61 | 9.1 | 0.77 | 4 |
| ***This research, handheld gun drying*** | 192 | 1.99 | *cold air blow* | 0.52 | 7.51 | 0.52 | 2.06 |
| | 223 | 0.84 | *warm air blow* | 0.57 | 8.80 | 0.47 | 2.35 |
| ***This research, automated nozzle drying*** | 167 | 3.1 | *Drying nozzle-to-substrate distance: 75 mm* | 0.58 | 6.49 | 0.53 | 2.01 |
| | 226 | | *Drying nozzle-to-substrate distance: 50 mm* | 0.55 | 12.09 | 0.39 | 2.57 |

# Chapter 5: Conclusion

## 5.1 Conclusions

Organic solar cells have had growing popularity as an emerging choice for harvesting solar energy, due to their potential for low-cost manufacturing and mechanical flexibility. As the efficiency of laboratory-scale devices increases, developing materials and processes that would enable low-cost roll-to-roll fabrication of such devices gains increasing research interest. To promote the OSCs as a viable substitute for silicon-based solar cells, it is necessary to focus on materials that can offer high performances, roll-to-roll processability, and potential for flexibility, via processes that are scalable, and do not rely heavily on costly fabrication conditions, such as high temperature, vacuum processing, or inert atmospheres.

This research had two major areas of focus. The first part of the research concerned the fabrication of nanostructured transparent conductors with low sheet resistance, high optical transmittance, and high mechanical flexibility. Using the scalable electrospinnig method followed by sputter coating, transparent conductors with performances comparable to conventional ITO electrodes, and with unprecedented electromechanical stretchability were fabricated. Expanding on this work, the metallized electrospun NFs were incorporated into matrices of solution-processed, charge-selective layers, to realize composite charge-selective TCs. By forming a selective coverage of solution-processed inorganic inks of ZnO or $MoO_3$ over the NF mesh, highly transparent electron- or hole-selective TCs were obtained. Followed by annealing at the appropriate temperature, these charge-selective TCs can achieve performances superior to ITO and on a par with the original (uncoated) NF TCs. The second part of the research, involved the fabrication of organic solar cells using a scalable, low-

temperature and low material consumption spray-coating process in air. By employing an accelerated air drying post-deposition stage, we were able to achieve uniform, large-area coating of P3HT:PCBM layers with sub-nanometer surface roughness, through single-pass spray-coating at 25 °C substrate temperature. OSCs fabricated using this method in air, can achieve performances comparable to the reference devices fabricated via spin-coating in an inert glovebox atmosphere. The introduced spray-coating process was successfully used in the fabrication of fully-sprayed OSCs, as well as in large-area deposition for large-area solar cells.

## 5.2 Contributions

- Highly stretchable, high-performance TCs were fabricated by metallizing sparse webs of electrospun polyacrylonitrile (PAN) nanofibers. By transferring the metallized NFs onto PDMS substrates, it was possible to realize TCs which demonstrate an unprecedented stretchability, with only 56% increase in resistance at 100% tensile strain, and stable performance over repeated stretching cycles. The fabricated TCs show performances comparable to ITO, with sheet resistances, $R_s$, of 155 Ω/□, 25 Ω/□, and 12 Ω/□ at transparencies, $T$, of 95%, 81%, and 71%, respectively.
- Electron-selective composite NF TCs were fabricated by using ZnO layers as a charge-selective matrix. Using colloidal ZnO NPs, typical performances of $R_s$ = 36.7 Ω/□ at $T$ = 86%, $R_s$ = 70.6 Ω/□ at $T$ = 95.3% and $R_s$ = 460 Ω/□ at $T$ = 97.5% were obtained. Surface roughness of the NF TCs was reduced by multiple coatings of ZnO NPs. Coupled with intermediate annealing steps, the reduction of roughness was achieved concurrently with improvement in both sheet resistance and transmittance, making the introduced TC a promising candidate as a bottom electrode for inverted organic solar cells.

- By employing sol-gel process for the synthesis of the ZnO matrix, electron-selective composite NF TCs were fabricated with performances far superior to that of ITO and on a par with the best of the original uncoated TCs. Using annealing heat treatment, the performance was improved to a level even higher than the uncoated TCs. Typical performances of $R_s$ = 11 Ω/□ at $T$ = 90%, $R_s$ = 15 Ω/□ at $T$ = 93% and $R_s$ = 23 Ω/□ at $T$ = 95% are obtained using this method.
- Hole-selective composite TCs were fabricated using sol-gel $MoO_3$ layers as the charge-selective matrix. Using the appropriate heat treatment, performances close to those of the uncoated TCs were achieved, despite the intrinsic opacity of the $MoO_3$ matrix, namely, $R_s$ = 12.5 Ω/□ at $T$ = 91%, $R_s$ = 22.1 Ω/□ at $T$ = 93% and $R_s$ = 35.5 Ω/□ at $T$ = 94%.
- Flexible charge-selective TCs were demonstrated by embedding the NFs near the surface of a stretchable PDMS substrate. Exposed on one side, the partially-embedded NFs offer the advantage of reduced surface roughness while enabling repeatable stretchability up to ~ 10%, with stable endurance over repeated mechanical cycles.
- We developed a process for single-pass, large-area spray-coating of P3HT:PCBM photoactive layers at 25 °C substrate temperature in air. By introducing a post-deposition stage involving accelerated air drying of the spray-coated ink, pinhole-free layers were obtained with thicknesses as low as 75 nm and roughness values as low as 0.84 nm, over deposition areas as large as 75 × 75 mm. Using a handheld dryer gun in the accelerated drying stage, efficiencies up to 2.35% were achieved in air. By replacing the handheld dryer with a computer-controlled nozzle drying process, we could achieve up to 2.57% efficiency using cold air. The process can provide macro- and micro-scale uniformity for a wide range of active layer film thicknesses over large deposition areas. The introduced

spray-coating process shows a path for low-cost, low-material consumption, and scalable fabrication of OSCs without relying on high temperatures or inert fabrication atmospheres.

## 5.3 Future Work

### 5.3.1 Fabrication of All-Sprayed Organic Solar Cells with Sprayed Electron- and Hole-Transport Layers

In Section 4.3.1, we demonstrated the fabrication of all-sprayed organic solar cells with spray-coated hole transport and photoactive layers. In Section 3.2, we used solution-processed ZnO and $MoO_3$ layers for fabricating composite electron- and hole-selective transparent electrodes. In the past few years, there have been a few researches on using spray-coating for the deposition of organic and inorganic charge transport interface layers[173, 182, 187, 188]. Kang et al.[187] have employed spray-coating for the fabrication of a sol-gel ZnO electron transport layer along with a spin-coated photoactive layer. Some groups have reported inverted OSCs with multiple sprayed layers [173, 182, 188]. In these works, ZnO[173, 182] or $Cs_2CO_3$[188] has been used as the electron-, and PEDOT:PSS as the hole-transport layer. Two of these groups have reported a fully-sprayed solar cell by using spray-coated top electrodes[182, 188]. Lewis et al.[188] have used sprayed PEDOT:PSS as the cathode as well as a charge-selective layer. Kang et al.[182] have taken a further step by spray-coating Ag NWs on top of the PEDOT:PSS layer. Like most of the other works in literature, these groups have employed high temperatures[173, 182, 187], and inert glovebox atmosphere[173, 182, 187, 188] or high vacuum[188] for the post-treatment of the devices in order to achieve a desirable efficiency.

In Chapter 4, we employed spray-coating, using blends of solvents and accelerated air drying, to deposit pinhole-free films of P3HT:PCBM (Section 4.2.2.3) and PEDOT:PSS (Section 4.3.1), at 25 °C substrate temperature, in air atmosphere, and over large areas. In Chapter 3, we demonstrated the use of solution-processed ZnO and $MoO_3$ inks to produce electron- and hole-selective layers at low to moderate temperatures. For the next stage of this research, we propose the fabrication of all-sprayed organic solar cells with sprayed electron- and hole-transport layers, deposited at room temperature and in air atmosphere. Figure 5.1(a) shows the schematic structure of an all-sprayed OSC fabricated on an ITO substrate, with spray-coated $MoO_3$, P3HT:PCBM, and ZnO, as hole transport, photoactive, and electron transport layers, respectively. Figure 5.1(b) shows the schematic structure for a fully-sprayed ITO-free inverted device. A low-roughness electron-selective composite transparent conductor (similar to what is introduced in Section 3.2.2 but with a spray-coated ZnO matrix) is used as the bottom electrode. Spray-coated P3HT:PCBM and $MoO_3$ layers are used photoactive and hole transport layers, respectively. In a further step toward a low-cost, scalable fabrication process, the thermally evaporated metal top electrode can be replaced with metallized NFs or spray-coated metal NWs.

Choice of solvent blends, spray-coating, and drying parameters will need to be investigated to achieve optimum film thickness, surface roughness and nanostructured morphology in the case of each individual film. Furthermore, considering different heat treatment requirements for different layers, post-treatment conditions will need to be carefully adjusted, such that an optimum film morphology and interface will be maintained with lowest possible temperatures and fewest possible number of heat treatment steps.

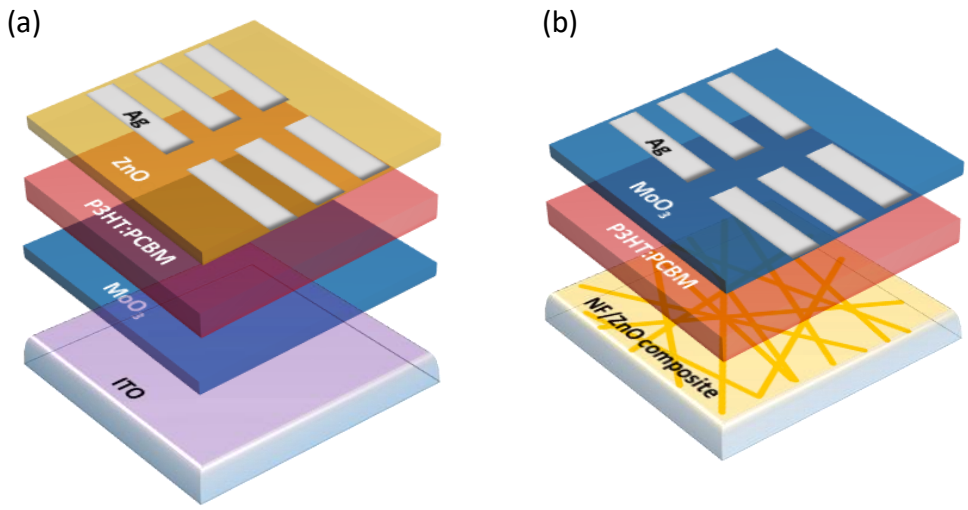


**Figure 5.1:** Schematic device structure of all-sprayed organic solar cells. (a) Normal structure with conventional ITO transparent electrode. (b) Inverted structure based on NF/ZnO composite transparent electrode.

### 5.3.2 Fabrication of Mechanically Stretchable Organic Solar Cells Based on Electrospun Nanofibrous Top and Bottom Electrodes

While the ongoing growth in stretchable electronics research has led to the fabrication of a variety of stretchable devices such as biological sensors, photodetectors and active-matrix displays, stretchable sources of power have so far received less attention[189]. A major roadblock to the realization of flexible solar cells is the fabrication of flexible and stretchable (top and bottom) electrodes. Wang et al.[190] have fabricated an organic solar cell on a flexible polycarbonate substrate. They have used nanoimprint lithography followed by sputter coating a layer of indium aluminum oxide to fabricate a flexible transparent electrode, and a thermally evaporated metal electrode as top electrode. Using this structure, they have achieved an efficiency higher than the reference device on ITO, although no performance results were reported under mechanical strain. Tait et al.[158] have reported a flexible OSC on a PET

substrate, by using spray-coated PEDOT:PSS as transparent electrode and thermally evaporated electron transport layer and top electrode. Their device has retained ~ 50% of its efficiency down to 1 mm bending radius. Although more flexible than the ITO-based reference device, their device can withstand no more than 1% strain. Finding mechanically flexible electrodes is even more challenging in the case of a stretchable device. Lipomi et al.[189] have achieved 27% stretchability by spin-coating PEDOT:PSS and P3HT:PCBM on a pre-stretched PDMS substrate. They have used a liquid metal as the top electrode, which is impractical for device applications. Kaltenbrunner et al.[46] have achieved an unprecedented stretchability of over 300% by fabricating the OSC on ultrathin PET substrates supported by a pre-stretched PDMS substrate. They have used PEDOT:PSS as the bottom transparent electrode, and evaporated metal as the top electrode. As far as we are aware, there are no reports on the fabrication of stretchable solar cells using viable stretchable electrodes as both bottom and top contacts. In addition, none of the works so far reported have used solution-processing for the deposition of all the photoactive, electron-, and hole transport layers.

In Chapter 2, we demonstrated highly stretchable TCEs based on metallized electrospun NFs, which can be used as stretchable top electrodes in OSCs. In Section 3.3.2.3, we demonstrated stretchable charge-selective NF TCEs. Partly embedded in a PDMS substrate on one side, and exposed for electrical contact on the other, these TCEs exhibit up to 10% stretchability. In Section 3.3.2, we demonstrated the use of pre-strain in engendering up to 50% stretchability in PEDOT:PSS electrodes deposited on PDMS. As another future course of research, we propose the fabrication of stretchable OSCs by using composite charge-selective NF electrodes as both top and bottom electrodes. Figure 5.2 shows the schematic structure and simplified fabrication procedure for the proposed device. A sparse mesh of metallized NFs in a

solution-processed $MoO_3$ matrix is partly embedded in PDMS, and used as the bottom transparent electrode. By pre-stretching this structure, a stretchable substrate will be provided, upon which P3HT:PCBM can be spin- or spray-coated. By transferring a dense mesh of metallized NFs onto the photoactive layer, followed by spin- or spray-coating of ZnO, a stretchable electron-selective top electrode will be obtained. Upon the release of pre-strain, a stretchable OSC will be obtained, which will be subjected to current-voltage and mechanical characterizations. In addition to the investigation of nanostructured morphology and layer-to-layer interface for and between each of these dissimilar materials, the stability of the interfaces under mechanical strain needs to be investigated. Considering the difference in mechanical properties of the various layers and the additional geometrical complexity of the NFs, the study of optimal film thickness and deposition, drying and post-treatment conditions will be of great importance, to achieve stable, defect-free interfaces. The study of charge transport mechanisms across the interfaces and across and over the nanofibrous composite layers is necessary to achieve a desirable photovoltaic performance.

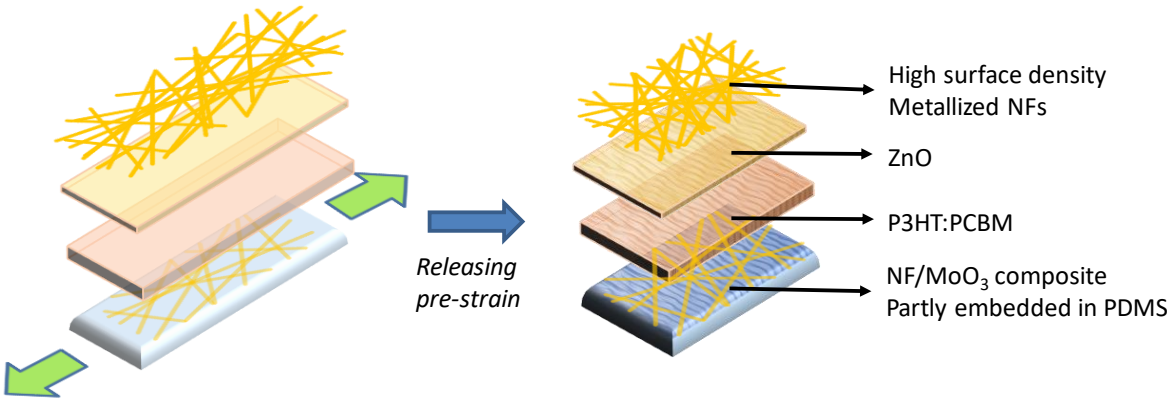


**Figure 5.2:** Schematic device structure and simplified fabrication procedure for stretchable organic solar cells based on stretchable metallized NF bottom and top electrodes.

## References


1. Soltanian, S., et al., *Highly Stretchable, Sparse, Metallized Nanofiber Webs as Thin, Transferrable Transparent Conductors.* Advanced Energy Materials, 2013. **3**(10): p. 1332-1337.
2. Coakley, K.M. and M.D. McGehee, *Conjugated Polymer Photovoltaic Cells.* Chemistry of Materials, 2004. **16**(23): p. 4533-4542.
3. Green, M.A., et al., *Solar cell efficiency tables (version 49).* Progress in Photovoltaics, 2017. **25**(1): p. 3-13.
4. Li, G., R. Zhu, and Y. Yang, *Polymer solar cells.* Nat Photon, 2012. **6**(3): p. 153-161.
5. Benanti, T.L. and D. Venkataraman, *Organic solar cells: An overview focusing on active layer morphology*. Photosynthesis Research, 2006. **87**(1): p. 73-81.
6. Brabec, C.J., N.S. Sariciftci, and J.C. Hummelen, *Plastic Solar Cells.* Advanced Functional Materials, 2001. **11**(1): p. 15-26.
7. Youn, H., H.J. Park, and L.J. Guo, *Organic Photovoltaic Cells: From Performance Improvement to Manufacturing Processes.* Small, 2015. **11**(19): p. 2228-2246.
8. Lipomi, D.J. and Z.A. Bao, *Stretchable, elastic materials and devices for solar energy conversion.* Energy & Environmental Science, 2011. **4**(9): p. 3314-3328.
9. Tait, J.G., B.P. Rand, and P. Heremans, *Concurrently pumped ultrasonic spray coating for donor:acceptor and thickness optimization of organic solar cells.* Organic Electronics, 2013. **14**(3): p. 1002-1008.

10. Lee, J.H., T. Sagawa, and S. Yoshikawa, *Morphological and topographical characterizations in spray coated organic solar cells using an additional solvent spray deposition.* Organic Electronics, 2011. **12**(12): p. 2165-2173.

11. Gregg, B.A. and M.C. Hanna, *Comparing organic to inorganic photovoltaic cells: Theory, experiment, and simulation.* Journal of Applied Physics, 2003. **93**(6): p. 3605-3614.

12. Gregg, B.A., *Excitonic solar cells.* Journal of Physical Chemistry B, 2003. **107**(20): p. 4688-4698.

13. Sze, S., *Physics of Semiconductor Devices (JohnWiley&Sons, NewYork, 1981).* There is no corresponding record for this reference: p. 790-838.

14. Parker, I.D., *Carrier tunneling and device characteristics in polymer light-emitting diodes.* Journal of Applied Physics, 1994. **75**(3): p. 1656-1666.

15. Hoppe, H. and N.S. Sariciftci, *Organic solar cells: An overview.* Journal of Materials Research, 2004. **19**(7): p. 1924-1945.

16. Padinger, F., R.S. Rittberger, and N.S. Sariciftci, *Effects of postproduction treatment on plastic solar cells.* Advanced Functional Materials, 2003. **13**(1): p. 85-88.

17. Yang, T., et al., *Solution-Processed Zinc Oxide Thin Film as a Buffer Layer for Polymer Solar Cells with an Inverted Device Structure.* The Journal of Physical Chemistry C, 2010. **114**(14): p. 6849-6853.

18. Ameri, T., et al., *Realization, characterization, and optical modeling of inverted bulk-heterojunction organic solar cells.* Journal of Applied Physics, 2008. **103**(8).

19. Sun, Y., et al., *Inverted Polymer Solar Cells Integrated with a Low-Temperature-Annealed Sol-Gel-Derived ZnO Film as an Electron Transport Layer.* Advanced Materials, 2011. **23**(14): p. 1679-1683.

20. Han, H., et al., *Poly(3-hexylthiophene-co-benzothiadiazole) (THBT) as an electron-accepting polymer for normal and inverted type all-polymer solar cells.* Polymer Chemistry, 2013. **4**(6): p. 2053-2061.

21. Wudl, F. and G. Srdanov, *Conducting polymer formed of poly (2-methoxy, 5-(2'-ethyl-hexyloxy)-p-phenylenevinylene)*. 1993, Google Patents.

22. Hummelen, J.C., et al., *Preparation and characterization of fulleroid and methanofullerene derivatives.* Journal of Organic Chemistry, 1995. **60**(3): p. 532-538.

23. Yu, G., et al., *Polymer photovoltiac cells: Enhanced efficiencies via a network of internal donor-acceptor heterojunctions.* Science, 1995. **270**(5243): p. 1789.

24. Brabec, C.J., et al., *Effect of LiF/metal electrodes on the performance of plastic solar cells.* Applied physics letters, 2002. **80**(7): p. 1288-1290.

25. Wienk, M.M., et al., *Efficient methano [70] fullerene/MDMO-PPV bulk heterojunction photovoltaic cells.* Angewandte Chemie, 2003. **115**(29): p. 3493-3497.

26. Bao, Z., A. Dodabalapur, and A.J. Lovinger, *Soluble and processable regioregular poly (3-hexylthiophene) for thin film field-effect transistor applications with high mobility.* Applied Physics Letters, 1996. **69**(26): p. 4108-4110.

27. Li, G., et al., *High-efficiency solution processable polymer photovoltaic cells by self-organization of polymer blends.* Nature materials, 2005. **4**(11): p. 864-868.

28. Ma, W., et al., *Thermally stable, efficient polymer solar cells with nanoscale control of the interpenetrating network morphology*. Advanced Functional Materials, 2005. **15**(10): p. 1617-1622.

29. Mühlbacher, D., et al., *High photovoltaic performance of a low-bandgap polymer.* Advanced Materials, 2006. **18**(21): p. 2884-2889.

30. Peet, J., et al., *Efficiency enhancement in low-bandgap polymer solar cells by processing with alkane dithiols.* Nature materials, 2007. **6**(7): p. 497-500.

31. Blouin, N., A. Michaud, and M. Leclerc, *A low-bandgap poly (2, 7-carbazole) derivative for use in high-performance solar cells.* Advanced Materials, 2007. **19**(17): p. 2295-2300.

32. Park, S.H., et al., *Bulk heterojunction solar cells with internal quantum efficiency approaching 100%.* Nature photonics, 2009. **3**(5): p. 297-302.

33. Liang, Y., et al., *Highly efficient solar cell polymers developed via fine-tuning of structural and electronic properties.* Journal of the American Chemical Society, 2009. **131**(22): p. 7792-7799.

34. Chen, H.-Y., et al., *Polymer solar cells with enhanced open-circuit voltage and efficiency*. Nature photonics, 2009. **3**(11): p. 649-653.

35. Price, S.C., et al., *Fluorine substituted conjugated polymer of medium band gap yields 7% efficiency in polymer− fullerene solar cells.* Journal of the American Chemical Society, 2011. **133**(12): p. 4625-4631.

36. Su, M.S., et al., *Improving device efficiency of polymer/fullerene bulk heterojunction solar cells through enhanced crystallinity and reduced grain boundaries induced by solvent additives.* Advanced Materials, 2011. **23**(29): p. 3315-3319.

37. Chu, T.-Y., et al., *Bulk heterojunction solar cells using thieno [3, 4-c] pyrrole-4, 6-dione and dithieno [3, 2-b: 2', 3'-d] silole copolymer with a power conversion efficiency of 7.3%.* Journal of the American Chemical Society, 2011. **133**(12): p. 4250-4253.

38. Amb, C.M., et al., *Dithienogermole as a fused electron donor in bulk heterojunction solar cells.* Journal of the American Chemical Society, 2011. **133**(26): p. 10062-10065.

39. Geens, W., et al., *Organic co-evaporated films of a PPV-pentamer and C 60: model systems for donor/acceptor polymer blends.* Thin Solid Films, 2002. **403**: p. 438-443.

40. Veenstra, S., et al., *Sexithiophene-C60 blends as model systems for photovoltaic devices.* Synthetic metals, 1997. **84**(1-3): p. 971-972.

41. Pfeiffer, M., et al., *Controlled p-doping of pigment layers by cosublimation: Basic mechanisms and implications for their use in organic photovoltaic cells*. 2000, Elsevier.

42. Tsuzuki, T., et al., *The effect of fullerene doping on photoelectric conversion using titanyl phthalocyanine and a perylene pigment.* Solar Energy Materials and Solar Cells, 2000. **61**(1): p. 1-8.

43. Reale, A., et al., *Spray Coating for Polymer Solar Cells: An Up-to-Date Overview.* Energy Technology, 2015. **3**(4): p. 385-406.

44. Søndergaard, R., et al., *Roll-to-roll fabrication of polymer solar cells.* Materials today, 2012. **15**(1): p. 36-49.

45. Espinosa, N., et al., *Solar cells with one-day energy payback for the factories of the future.* Energy & Environmental Science, 2012. **5**(1): p. 5117-5132.

46. Kaltenbrunner, M., et al., *Ultrathin and lightweight organic solar cells with high flexibility.* Nature Communications, 2012. **3**.

47. Shaheen, S.E., et al., *Fabrication of bulk heterojunction plastic solar cells by screen printing.* Applied Physics Letters, 2001. **79**(18): p. 2996-2998.

48. Schilinsky, P., C. Waldauf, and C.J. Brabec, *Performance analysis of printed bulk heterojunction solar cells.* Advanced Functional Materials, 2006. **16**(13): p. 1669-1672.

49. Hoth, C.N., et al., *High photovoltaic performance of inkjet printed polymer: Fullerene blends.* Advanced Materials, 2007. **19**(22): p. 3973-+.

50. Zhu, R., et al., *Fused Silver Nanowires with Metal Oxide Nanoparticles and Organic Polymers for Highly Transparent Conductors.* Acs Nano, 2011. **5**(12): p. 9877-9882.

51. Ellmer, K., *Past achievements and future challenges in the development of optically transparent electrodes.* Nature Photonics, 2012. **6**(12): p. 808-816.

52. Bae, S., et al., *Roll-to-roll production of 30-inch graphene films for transparent electrodes.* Nature Nanotechnology, 2010. **5**(8): p. 574-578.

53. Betz, U., et al., *Thin films engineering of indium tin oxide: large area flat panel displays application.* Surface and Coatings Technology, 2006. **200**(20): p. 5751-5759.

54. Katayama, M., *Tft-lcd technology.* Thin Solid Films, 1999. **341**(1): p. 140-147.

55. Chopra, K., S. Major, and D. Pandya, *Transparent conductors—A status review.* Thin solid films, 1983. **102**(1): p. 1-46.

56. Rech, B. and H. Wagner, *Potential of amorphous silicon for solar cells.* Applied Physics A: Materials Science & Processing, 1999. **69**(2): p. 155-167.

57. Klaus, E., K. Andreas, and R. Bernd, *Transparent Conductive Zinc Oxide: Basics and Applications in Thin Film.* Springer Series in Materials Science, New York, 2008. **104**: p. 140.

58. Hosono, H., et al., *Amorphous transparent electroconductor 2CdO· GeO2: Conversion of amorphous insulating cadmium germanate by ion implantation.* Applied physics letters, 1995. **67**(18): p. 2663-2665.

59. Narushima, S., et al., *Electronic structure and transport properties in the transparent amorphous oxide semiconductor 2 CdO· GeO 2.* Physical Review B, 2002. **66**(3): p. 035203.

60. Hosono, H., *Ionic amorphous oxide semiconductors: Material design, carrier transport, and device application.* Journal of Non-Crystalline Solids, 2006. **352**(9): p. 851-858.

61. Nomura, K., et al., *Room-temperature fabrication of transparent flexible thin-film transistors using amorphous oxide semiconductors.* Nature, 2004. **432**(7016): p. 488-492.

62. Furubayashi, Y., et al., *A transparent metal: Nb-doped anatase Ti O 2.* Applied Physics Letters, 2005. **86**(25): p. 252101.

63. Ellmer, K., *Past achievements and future challenges in the development of optically transparent electrodes.* Nat Photon, 2012. **6**(12): p. 809-817.

64. Kumar, A. and C. Zhou, *The race to replace tin-doped indium oxide: which material will win?* ACS nano, 2010. **4**(1): p. 11-14.

65. Eritt, M., et al., *OLED manufacturing for large area lighting applications.* Thin Solid Films, 2010. **518**(11): p. 3042-3045.

66. De, S., et al., *Silver Nanowire Networks as Flexible, Transparent, Conducting Films: Extremely High DC to Optical Conductivity Ratios.* Acs Nano, 2009. **3**(7): p. 1767-1774.

67. Bender, M., et al., *Dependence of film composition and thicknesses on optical and electrical properties of ITO–metal–ITO multilayers.* Thin Solid Films, 1998. **326**(1): p. 67-71.

68. Lee, J.Y., et al., *Solution-processed metal nanowire mesh transparent electrodes.* Nano Letters, 2008. **8**(2): p. 689-692.

69. Kang, M.G. and L.J. Guo, *Nanoimprinted semitransparent metal electrodes and their application in organic light-emitting diodes.* Advanced Materials, 2007. **19**(10): p. 1391-1396.

70. De, S., et al., *Size effects and the problem with percolation in nanostructured transparent conductors.* Acs Nano, 2010. **4**(12): p. 7064-7072.

71. Kang, M.-G., et al., *Toward low-cost, high-efficiency, and scalable organic solar cells with transparent metal electrode and improved domain morphology.* IEEE Journal of Selected Topics in Quantum Electronics, 2010. **16**(6): p. 1807-1820.

72. Hu, L., D. Hecht, and G. Grüner, *Percolation in transparent and conducting carbon nanotube networks.* Nano letters, 2004. **4**(12): p. 2513-2517.

73. Hu, L., H. Wu, and Y. Cui, *Metal nanogrids, nanowires, and nanofibers for transparent electrodes.* MRS bulletin, 2011. **36**(10): p. 760-765.

74. Doherty, E.M., et al., *The spatial uniformity and electromechanical stability of transparent, conductive films of single walled nanotubes.* Carbon, 2009. **47**(10): p. 2466-2473.

75. Kim, Y.H., et al., *Highly Conductive PEDOT:PSS Electrode with Optimized Solvent and Thermal Post-Treatment for ITO-Free Organic Solar Cells.* Advanced Functional Materials, 2011. **21**(6): p. 1076-1081.

76. de Heer, W.A., *Epitaxial graphene: A new electronic material for the 21st century.* Mrs Bulletin, 2011. **36**(08): p. 632-639.

77. Bonaccorso, F., et al., *Graphene photonics and optoelectronics.* Nature photonics, 2010. **4**(9): p. 611-622.

78. Shirakawa, H., et al., *Synthesis of electrically conducting organic polymers: halogen derivatives of polyacetylene,(CH) x.* Journal of the Chemical Society, Chemical Communications, 1977(16): p. 578-580.

79. Groenendaal, L., et al., *poly (3, 4-ethylenedioxythiophene) and its derivatives: past, present, and future.* Advanced Materials, 2000. **12**(7): p. 481-494.

80. Seeger, K., *Charge and Energy Transport in a Nondegenerate Electron Gas*, in *Semiconductor Physics*. 1991, Springer. p. 46-115.

81. Pankove, J.I., *Optical processes in semiconductors*. 2012: Courier Corporation.

82. Hass, J., W. De Heer, and E. Conrad, *The growth and morphology of epitaxial multilayer graphene.* Journal of Physics: Condensed Matter, 2008. **20**(32): p. 323202.

83. Peelaers, H., E. Kioupakis, and C.G. Van de Walle, *Fundamental limits on optical transparency of transparent conducting oxides: Free-carrier absorption in SnO2.* Applied Physics Letters, 2012. **100**(1): p. 011914.

84. Glover III, R. and M. Tinkham, *Conductivity of Superconducting Films for Photon Energies between 0.3 and 4 0 k T c.* Physical Review, 1957. **108**(2): p. 243.

85. Barnes, T.M., et al., *Comparing the fundamental physics and device performance of transparent, conductive nanostructured networks with conventional transparent conducting oxides.* Advanced Energy Materials, 2012. **2**(3): p. 353-360.

86. Dimopoulos, T., et al., *Characterization of ZnO: Al/Au/ZnO: Al trilayers for high performance transparent conducting electrodes.* Thin Solid Films, 2010. **519**(4): p. 1470-1474.

87. Gillham, E., J. Preston, and B. Williams, *A study of transparent, highly conducting gold films.* Philosophical Magazine, 1955. **46**(381): p. 1051-&.

88. Ahn, S.H. and L.J. Guo, *Large-area roll-to-roll and roll-to-plate nanoimprint lithography: a step toward high-throughput application of continuous nanoimprinting.* ACS nano, 2009. **3**(8): p. 2304-2310.

89. Tahar, R.B.H., et al., *Tin doped indium oxide thin films: Electrical properties.* Journal of Applied Physics, 1998. **83**(5): p. 2631-2645.

90. Bhosle, V., et al., *Gallium-doped zinc oxide films as transparent electrodes for organic solar cell applications.* Journal of Applied Physics, 2007. **102**(2).

91. Yang, F. and S.R. Forrest, *Organic solar cells using transparent SnO2-F anodes.* Advanced Materials, 2006. **18**(15): p. 2018-+.

92. Wu, H., et al., *Low Reflectivity and High Flexibility of Tin-Doped Indium Oxide Nanofiber Transparent Electrodes.* Journal of the American Chemical Society, 2011. **133**(1): p. 27-29.

93. Munir, M.M., et al., *Optical and electrical properties of indium tin oxide nanofibers prepared by electrospinning.* Nanotechnology, 2008. **19**(14).

94. Munir, M.M., et al., *Patterned indium tin oxide nanofiber films and their electrical and optical performance.* Nanotechnology, 2008. **19**(37).

95. Geng, H.Z., et al., *Effect of acid treatment on carbon nanotube-based flexible transparent conducting films.* Journal of the American Chemical Society, 2007. **129**(25): p. 7758-+.

96. Hellstrom, S.L., H.W. Lee, and Z. Bao, *Polymer-Assisted Direct Deposition of Uniform Carbon Nanotube Bundle Networks for High Performance Transparent Electrodes.* Acs Nano, 2009. **3**(6): p. 1423-1430.

97. Hu, L., D.S. Hecht, and G. Gruner, *Percolation in transparent and conducting carbon nanotube networks.* Nano Letters, 2004. **4**(12): p. 2513-2517.

98. Huang, Y.Y. and E.M. Terentjev, *Transparent Electrode with a Nanostructured Coating.* Acs Nano, 2011. **5**(3): p. 2082-2089.

99. Li, J., et al., *Organic light-emitting diodes having carbon nanotube anodes.* Nano Letters, 2006. **6**(11): p. 2472-2477.

100. McGehee, M.D., *Nanotube Networks as Transparent Electrodes for Solar Cells*. 2006.

101. Rowell, M.W., et al., *Organic solar cells with carbon nanotube network electrodes.* Applied Physics Letters, 2006. **88**(23).

102. Trottier, C.M., et al., *Properties and characterization of carbon-nanotube-based transparent conductive coating.* Journal of the Society for Information Display, 2005. **13**(9): p. 759-763.

103. Wu, Z.C., et al., *Transparent, conductive carbon nanotube films.* Science, 2004. **305**(5688): p. 1273-1276.

104. Zhang, M., et al., *Strong, transparent, multifunctional, carbon nanotube sheets.* Science, 2005. **309**(5738): p. 1215-1219.

105. Hu, L.B., D.S. Hecht, and G. Gruner, *Carbon Nanotube Thin Films: Fabrication, Properties, and Applications.* Chemical Reviews, 2010. **110**(10): p. 5790-5844.

106. Eda, G., G. Fanchini, and M. Chhowalla, *Large-area ultrathin films of reduced graphene oxide as a transparent and flexible electronic material.* Nature Nanotechnology, 2008. **3**(5): p. 270-274.

107. Khan, U., et al., *High-Concentration Solvent Exfoliation of Graphene.* Small, 2010. **6**(7): p. 864-871.

108. Kim, K.S., et al., *Large-scale pattern growth of graphene films for stretchable transparent electrodes.* Nature, 2009. **457**(7230): p. 706-710.

109. Li, F., et al., *Synthesis and Application of Widely Soluble Graphene Sheets.* Langmuir, 2010. **26**(14): p. 12314-12320.

110. Kang, M.G., et al., *Organic Solar Cells Using Nanoimprinted Transparent Metal Electrodes.* Advanced Materials, 2008. **20**(23): p. 4408-4413.

111. Tvingstedt, K. and O. Inganas, *Electrode grids for ITO-free organic photovoltaic devices.* Advanced Materials, 2007. **19**(19): p. 2893-+.

112. Galagan, Y., et al., *Current Collecting Grids for ITO-Free Solar Cells.* Advanced Energy Materials, 2012. **2**(1): p. 103-110.

113. Kang, M.G. and L.J. Guo, *Semitransparent Cu electrode on a flexible substrate and its application in organic light emitting diodes.* Journal of Vacuum Science & Technology B, 2007. **25**(6): p. 2637-2641.

114. Hu, L.B., et al., *Scalable Coating and Properties of Transparent, Flexible, Silver Nanowire Electrodes.* Acs Nano, 2010. **4**(5): p. 2955-2963.

115. Yu, Z.B., et al., *Highly Flexible Silver Nanowire Electrodes for Shape-Memory Polymer Light-Emitting Diodes.* Advanced Materials, 2011. **23**(5): p. 664-+.

116. Stahlmecke, B., et al., *Electromigration in self-organized single-crystalline silver nanowires.* Applied Physics Letters, 2006. **88**(5).

117. Madaria, A., et al., *Uniform, highly conductive, and patterned transparent films of a percolating silver nanowire network on rigid and flexible substrates using a dry transfer technique.* Nano Research, 2010. **3**(8): p. 564-573.

118. Garnett, E.C., et al., *Self-limited plasmonic welding of silver nanowire junctions.* Nature Materials, 2012. **11**(3): p. 241-249.

119. Wu, H., et al., *Electrospun Metal Nanofiber Webs as High-Performance Transparent Electrode.* Nano Letters, 2010. **10**(10): p. 4242-4248.

120. Nardes, A.M., et al., *Conductivity, work function, and environmental stability of PEDOT : PSS thin films treated with sorbitol.* Organic Electronics, 2008. **9**(5): p. 727-734.

121. Crispin, X., et al., *The origin of the high conductivity of poly(3,4-ethylenedioxythiophene)-poly(styrenesulfonate) (PEDOT- PSS) plastic electrodes.* Chemistry of Materials, 2006. **18**(18): p. 4354-4360.

122. Aernouts, T., et al., *Printable anodes for flexible organic solar cell modules.* Thin Solid Films, 2004. **451**: p. 22-25.

123. Glatthaar, M., et al., *Organic solar cells using inverted layer sequence.* Thin Solid Films, 2005. **491**(1-2): p. 298-300.

124. Vosgueritchian, M., D.J. Lipomi, and Z.A. Bao, *Highly Conductive and Transparent PEDOT:PSS Films with a Fluorosurfactant for Stretchable and Flexible Transparent Electrodes.* Advanced Functional Materials, 2012. **22**(2): p. 421-428.

125. van Attekum, P.M.T.M., et al., *Influence of grain boundaries and surface Debye temperature on the electrical resistance of thin gold films*. Physical Review B, 1984. **29**(2): p. 645-650.

126. Kalashnik, A.T., et al., *Properties and structure of polyacrylonitrile fibers.* Polymer Science Series A, 2010. **52**(11): p. 1233-1238.

127. Cairns, D.R., et al., *Strain-dependent electrical resistance of tin-doped indium oxide on polymer substrates.* Applied Physics Letters, 2000. **76**(11): p. 1425-1427.

128. Lipomi, D.J., et al., *Electronic Properties of Transparent Conductive Films of PEDOT:PSS on Stretchable Substrates.* Chemistry of Materials, 2012. **24**(2): p. 373-382.

129. Li, T. and Z. Suo, *Deformability of thin metal films on elastomer substrates.* International Journal of Solids and Structures, 2006. **43**(7-8): p. 2351-2363.

130. Xiang, Y., et al., *High ductility of a metal film adherent on a polymer substrate.* Applied Physics Letters, 2005. **87**(16).

131. Lacour, S.P., et al., *Stretchable gold conductors on elastomeric substrates.* Applied Physics Letters, 2003. **82**(15): p. 2404-2406.

132. Rogers, J.A., T. Someya, and Y.G. Huang, *Materials and Mechanics for Stretchable Electronics.* Science, 2010. **327**(5973): p. 1603-1607.

133. Sun, Y., et al., *Efficient, Air-Stable Bulk Heterojunction Polymer Solar Cells Using MoOx as the Anode Interfacial Layer.* Advanced Materials, 2011. **23**(19): p. 2226-2230.

134. Shrotriya, V., et al., *Transition metal oxides as the buffer layer for polymer photovoltaic cells.* Applied Physics Letters, 2006. **88**(7).

135. Irwin, M.D., et al., *p-Type semiconducting nickel oxide as an efficiency-enhancing anode interfacial layer in polymer bulk-heterojunction solar cells.* Proceedings of the National Academy of Sciences, 2008. **105**(8): p. 2783-2787.

136. Xi, F., et al., *Deposition temperature effect of RF magnetron sputtered molybdenum oxide films on the power conversion efficiency of bulk-heterojunction solar cells.* Journal of Physics D: Applied Physics, 2011. **44**(4): p. 045101.

137. Girotto, C., et al., *Solution-Processed MoO3 Thin Films As a Hole-Injection Layer for Organic Solar Cells.* ACS Applied Materials & Interfaces, 2011. **3**(9): p. 3244-3247.

138. Jin, F., et al., *Improvement in power conversion efficiency and long-term lifetime of organic photovoltaic cells by using bathophenanthroline/molybdenum oxide as compound cathode buffer layer.* Solar Energy Materials and Solar Cells, 2013. **117**(0): p. 189-193.

139. Ferreira, S.R., et al., *Effect of Zinc Oxide Electron Transport Layers on Performance and Shelf Life of Organic Bulk Heterojunction Devices.* The Journal of Physical Chemistry C, 2011. **115**(27): p. 13471-13475.

140. Chung, C.-H., et al., *Solution-processed flexible transparent conductors composed of silver nanowire networks embedded in indium tin oxide nanoparticle matrices.* Nano Research, 2012. **5**(11): p. 805-814.

141. Morgenstern, F.S.F., et al., *Ag-nanowire films coated with ZnO nanoparticles as a transparent electrode for solar cells.* Applied Physics Letters, 2011. **99**(18): p. 183307-3.

142. Yu, Z., et al., *Highly flexible polymer light-emitting devices using carbon nanotubes as both anodes and cathodes.* Journal of Photonics for Energy, 2011. **1**(1): p. 011003-011003-15.

143. Gaynor, W., et al., *Smooth Nanowire/Polymer Composite Transparent Electrodes.* Advanced Materials, 2011. **23**(26): p. 2905-2910.

144. Yu, Z., et al., *Silver Nanowire-Polymer Composite Electrodes for Efficient Polymer Solar Cells.* Advanced Materials, 2011. **23**(38): p. 4453-4457.

145. Pacholski, C., A. Kornowski, and H. Weller, *Self-Assembly of ZnO: From Nanodots to Nanorods.* Angewandte Chemie International Edition, 2002. **41**(7): p. 1188-1191.

146. Ong, B.S., et al., *Stable, Solution-Processed, High-Mobility ZnO Thin-Film Transistors.* Journal of the American Chemical Society, 2007. **129**(10): p. 2750-2751.

147. Lin, S.-Y., et al., *Electrochromic properties of MoO3 thin films derived by a sol–gel process.* Journal of Sol-Gel Science and Technology, 2010. **53**(1): p. 51-58.

148. Han, S.-Y., B.K. Paul, and C.-h. Chang, *Nanostructured ZnO as biomimetic anti-reflective coatings on textured silicon using a continuous solution process.* Journal of Materials Chemistry, 2012. **22**(43): p. 22906-22912.

149. Lee, Y.-J., et al., *ZnO Nanostructures as Efficient Antireflection Layers in Solar Cells.* Nano Letters, 2008. **8**(5): p. 1501-1505.

150. Chanta, E., et al., *Effect of ZnO Double Layer as Anti-Reflection Coating Layer in ZnO Dye-Sensitized Solar Cells.* Energy Procedia, 2015. **79**: p. 879-884.

151. Wahyuningsih, S., et al., *Thin Film ZnO Coated on FTO/TiO2 as an Anti Reflection Coatingfor EnhancingVisible Light Harversting in Dye Sensitized Solar Cells System.* Procedia Chemistry, 2016. **19**: p. 632-637.

152. Sekine, N., et al., *ZnO nano-ridge structure and its application in inverted polymer solar cell.* Organic Electronics, 2009. **10**(8): p. 1473-1477.

153. Krebs, F.C., *Fabrication and processing of polymer solar cells: A review of printing and coating techniques.* Solar Energy Materials and Solar Cells, 2009. **93**(4): p. 394-412.

154. Vak, D., et al., *Fabrication of organic bulk heterojunction solar cells by a spray deposition method for low-cost power generation.* Applied Physics Letters, 2007. **91**(8): p. 081102.

155. Girotto, C., et al., *High-Performance Organic Solar Cells with Spray-Coated Hole-Transport and Active Layers.* Advanced Functional Materials, 2011. **21**(1): p. 64-72.

156. Kang, J.-W., et al., *All-spray-coated semitransparent inverted organic solar cells: From electron selective to anode layers.* Organic Electronics, 2012. **13**(12): p. 2940-2944.

157. Steirer, K.X., et al., *Ultrasonic spray deposition for production of organic solar cells.* Solar Energy Materials and Solar Cells, 2009. **93**(4): p. 447-453.

158. Tait, J.G., et al., *Spray coated high-conductivity PEDOT:PSS transparent electrodes for stretchable and mechanically-robust organic solar cells.* Solar Energy Materials and Solar Cells, 2013. **110**: p. 98-106.

159. Colsmann, A., et al., *Inverted semi-transparent organic solar cells with spray coated, surfactant free polymer top-electrodes.* Solar Energy Materials and Solar Cells, 2012. **98**: p. 118-123.

160. Girotto, C., et al., *Nanoparticle-based, spray-coated silver top contacts for efficient polymer solar cells.* Organic Electronics, 2009. **10**(4): p. 735-740.

161. Hau, S.K., et al., *Spraycoating of silver nanoparticle electrodes for inverted polymer solar cells.* Organic Electronics, 2009. **10**(4): p. 719-723.

162. Kim, K.J., et al., *Enhancement of Active Layer Characteristics with Solvent Spray Annealing Treatment for Organic Solar Cell.* Japanese Journal of Applied Physics, 2012. **51**(8).

163. Wang, T., et al., *Fabricating High Performance, Donor–Acceptor Copolymer Solar Cells by Spray-Coating in Air.* Advanced Energy Materials, 2013. **3**(4): p. 505-512.

164. Nie, W.Y., et al., *High efficiency organic solar cells with spray coated active layers comprised of a low band gap conjugated polymer.* Applied Physics Letters, 2012. **100**(8).

165. Kumar, P., et al., *High-performance organic solar cells based on a low-bandgap poly-thienothiophene-benzodithiophene polymer and fullerene composite prepared by using the airbrush spray-coating technique.* Journal of the Korean Physical Society, 2013. **62**(8): p. 1169-1175.

166. Li, G., et al., *"Solvent annealing" effect in polymer solar cells based on poly(3-hexylthiophene) and methanofullerenes.* Advanced Functional Materials, 2007. **17**(10): p. 1636-1644.

167. Park, S.Y., et al., *Spray-coated organic solar cells with large-area of 12.25 cm(2).* Solar Energy Materials and Solar Cells, 2011. **95**(3): p. 852-855.

168. Susanna, G., et al., *Airbrush spray-coating of polymer bulk-heterojunction solar cells.* Solar Energy Materials and Solar Cells, 2011. **95**(7): p. 1775-1778.

169. Kim, S.S., et al., *Efficient polymer solar cells fabricated by simple brush painting.* Advanced Materials, 2007. **19**(24): p. 4410-+.

170. Girotto, C., et al., *Exploring spray coating as a deposition technique for the fabrication of solution-processed solar cells.* Solar Energy Materials and Solar Cells, 2009. **93**(4): p. 454-458.

171. Nie, W.Y., et al., *Exploring Spray-Coating Techniques for Organic Solar Cell Applications.* International Journal of Photoenergy, 2012.

172. Green, R., et al., *Performance of bulk heterojunction photovoltaic devices prepared by airbrush spray deposition.* Applied Physics Letters, 2008. **92**(3): p. 033301.

173. Kang, J.-W., et al., *Fully spray-coated inverted organic solar cells.* Solar Energy Materials and Solar Cells, 2012. **103**: p. 76-79.

174. Na, S.-I., et al., *Fully spray-coated ITO-free organic solar cells for low-cost power generation.* Solar Energy Materials and Solar Cells, 2010. **94**(8): p. 1333-1337.

175. Kim, K.-J., et al., *Inspection of substrate-heated modified PEDOT:PSS morphology for all spray deposited organic photovoltaics.* Solar Energy Materials and Solar Cells, 2010. **94**(7): p. 1303-1306.

176. Ma, W.L., et al., *Thermally stable, efficient polymer solar cells with nanoscale control of the interpenetrating network morphology.* Advanced Functional Materials, 2005. **15**(10): p. 1617-1622.

177. Sharma, G.D., et al., *Effect of Solvent and Subsequent Thermal Annealing on the Performance of Phenylenevinylene Copolymer:PCBM Solar Cells.* Acs Applied Materials & Interfaces, 2010. **2**(2): p. 504-510.

178. Hu, H. and R.G. Larson, *Marangoni effect reverses coffee-ring depositions.* Journal of Physical Chemistry B, 2006. **110**(14): p. 7090-7094.

179. Fang, G., et al., *Improving the nanoscale morphology and processibility for PCDTBT-based polymer solar cells via solvent mixtures.* Organic Electronics, 2012. **13**(11): p. 2733-2740.

180. Dang, M.T., et al., *Polymeric solar cells based on P3HT:PCBM: Role of the casting solvent.* Solar Energy Materials and Solar Cells, 2011. **95**(12): p. 3408-3418.

181. Tsoi, W.C., et al., *Effect of Crystallization on the Electronic Energy Levels and Thin Film Morphology of P3HT:PCBM Blends.* Macromolecules, 2011. **44**(8): p. 2944-2952.

182. Kang, Y.J., et al., *Progress towards fully spray-coated semitransparent inverted organic solar cells with a silver nanowire electrode.* Organic Electronics, 2014. **15**(10): p. 2173-2177.

183. Chaturvedi, N., et al., *Effect of electric field on the spray deposited poly (3,4-ethylenedioxythiophene): poly(styrenesulfonate) layer and its use in organic solar cell.* Journal of Applied Physics, 2013. **114**(18).

184. Weickert, J., et al., *Spray-deposited PEDOT:PSS for inverted organic solar cells.* Solar Energy Materials and Solar Cells, 2010. **94**(12): p. 2371-2374.

185. Zabihi, F. and M. Eslamian, *Substrate vibration-assisted spray coating (SVASC): significant improvement in nano-structure, uniformity, and conductivity of PEDOT:PSS thin films for organic solar cells.* Journal of Coatings Technology and Research, 2015: p. 1-9.

186. Steirer, K.X., et al., *Ultrasonically sprayed and inkjet printed thin film electrodes for organic solar cells.* Thin Solid Films, 2009. **517**(8): p. 2781-2786.

187. Kang, Y.J., et al., *Spray-coated ZnO electron transport layer for air-stable inverted organic solar cells.* Solar Energy Materials and Solar Cells, 2012. **96**(1): p. 137-140.

188. Lewis, J.E., et al., *Over 30% transparency large area inverted organic solar array by spray*. Solar Energy Materials and Solar Cells, 2011. **95**(10): p. 2816-2822.

189. Lipomi, D.J., et al., *Stretchable Organic Solar Cells.* Advanced Materials, 2011. **23**(15): p. 1771-+.

190. Wang, D.H., et al., *Polymer Solar Cells: Efficiency Increase in Flexible Bulk Heterojunction Solar Cells with a Nano-Patterned Indium Zinc Oxide Anode (Adv. Energy Mater. 11/2012).* Advanced Energy Materials, 2012. **2**(11): p. 1282-1282.

191. Soltanian, S., et al., *Highly piezoresistive compliant nanofibrous sensors for tactile and epidermal electronic applications.* Journal of Materials Research, 2015. **30**(1): p. 121-129.

# Appendices

## Appendix A Publication Not Included in this Thesis

In Chapter 2 we reported the application of sparse webs of metallized electrospun nanofibers in the fabrication of transparent conductive films with low strain sensitivity of electrical conductance, that were used in highly stretchable transparent conductive electrodes. In a different application, thick layers of similarly produced metallized NFs were encapsulated in PDMS layers, resulting in stretchable strain sensors with high strain sensitivity. The instigator and the lead investigator of this project was Dr. S. Soltanian. The author was responsible for the analysis of the electromechanical response of the strain sensors and the temperature dependence of the strain sensitivity, with reference to the thermal and mechanical properties of the constituent materials. The author was also responsible for writing the manuscript sections comprising the introduction, discussion of the electromechanical response of the sensors, and the discussion of performance in comparison with the literature. The experimental section as well as the characterization of individual NFs was written by Dr. S. Soltanian. The sections involving the application of the introduced sensors in tactile sensing and health monitoring were designed, conducted and written by Dr. A. Servati and Dr. S. Soltanian. The supervision of various stages of design, implementation, analysis and writing was done by Dr. P. Servati and Dr. F. Ko. All the authors were involved in the revision of the manuscript for publication, under the supervision of Dr. P. Servati. The results of this research are published in the following paper [191]:

- S. Soltanian, A. Servati, R. Rahmanian, F. Ko, P. Servati, '*Highly piezoresistive compliant nanofibrous sensors for tactile and epidermal electronic applications*', Journal of Materials Research, Vol. 30, No. 1, pp. 121-129, 2015

## Appendix B Effect of Successive Coating on Normalized Optical Transmittance and Sheet Resistance of Composite TCEs

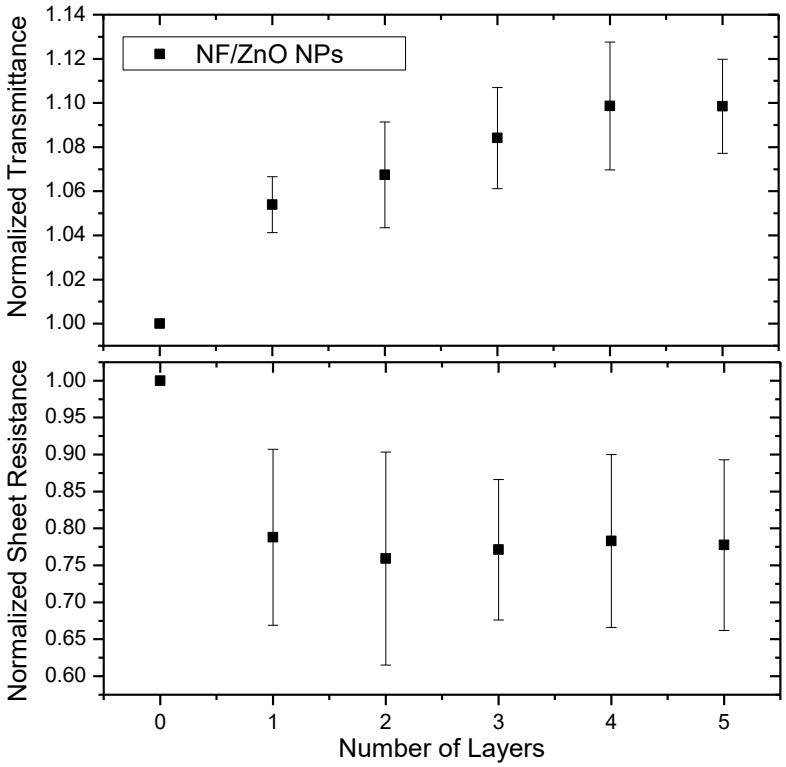


**Figure B.1:** Evolution of sheet resistance and optical transmittance of composite NF/ZnO TCEs through multiple coatings of ZnO NPs. To enable a comparison between multiple TCEs, the parameters are expressed as normalized values.

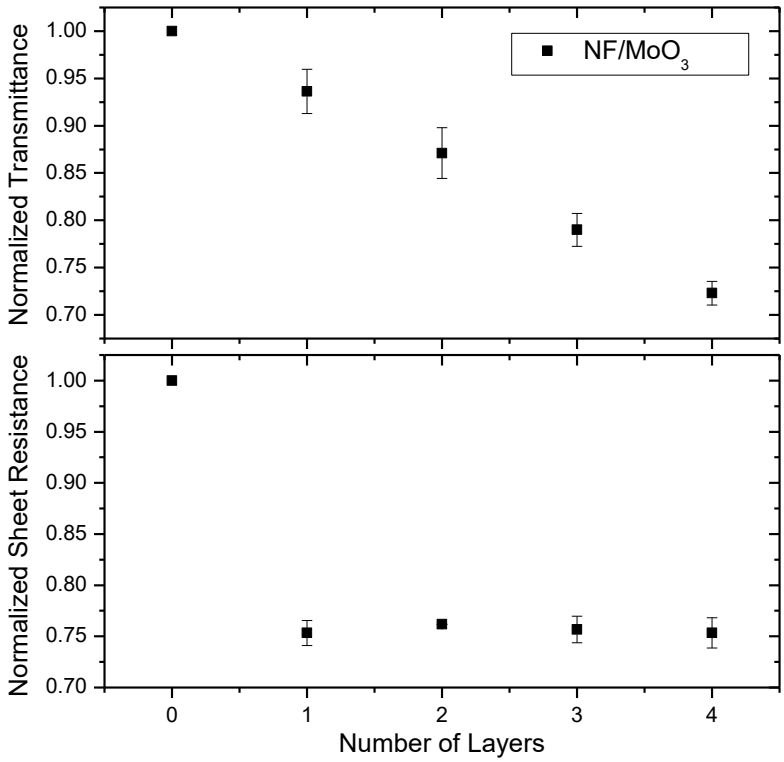


**Figure B.2:** Evolution of sheet resistance and optical transmittance of composite NF/$MoO_3$ TCEs through multiple coatings of $MoO_3$. To enable a comparison between multiple TCEs, the parameters are expressed as normalized values.

## Appendix C Additional Results of the Performance of Large-Area Spray-Coated Devices

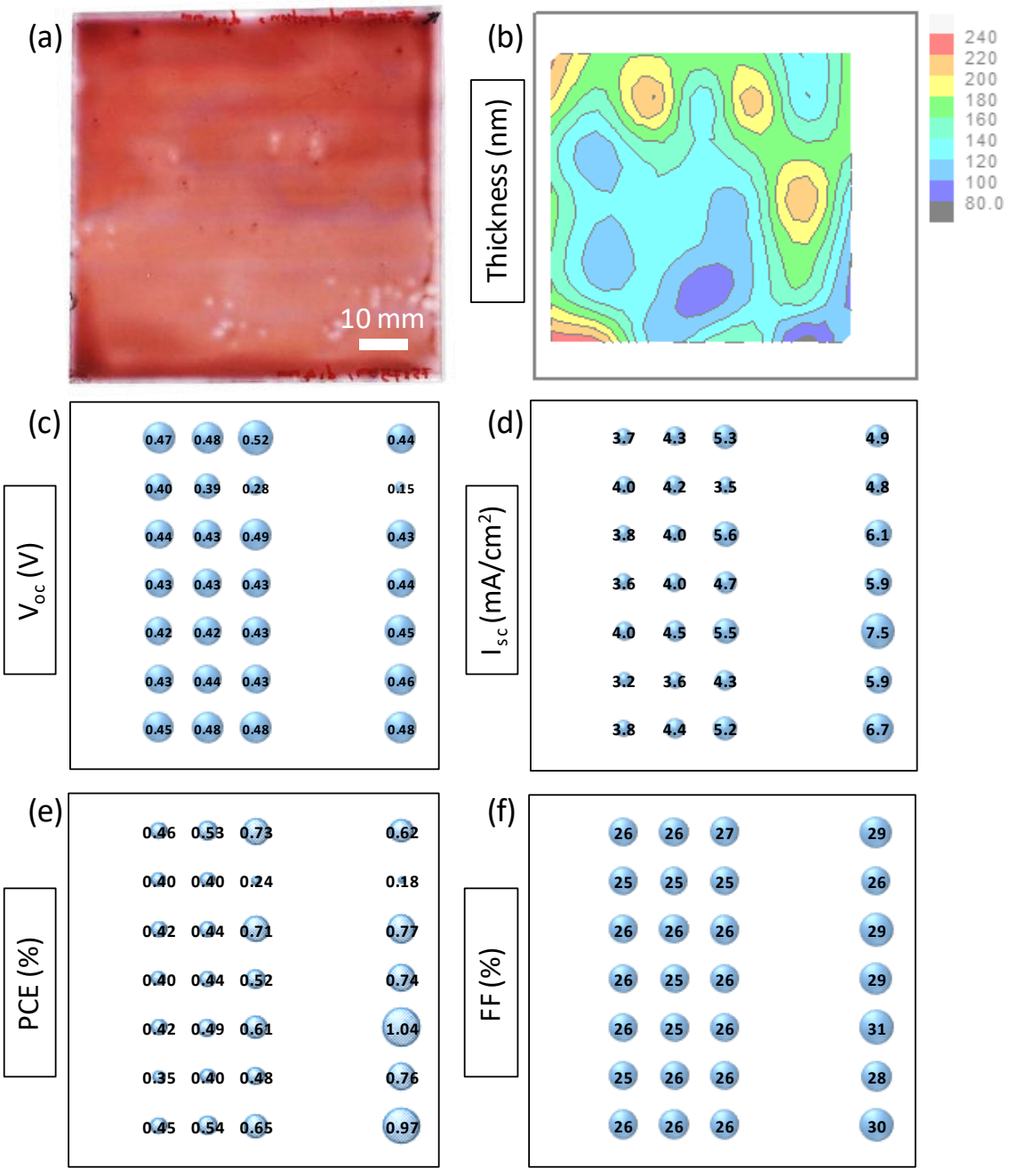


**Figure C.1:** Photoactive film uniformity and OPV device performance for additional batch of devices fabricated on large (75 × 75 mm) substrates. (a) Macro-scale film uniformity, and the distribution of (b) film thickness, (c) $V_{OC}$, (d) $I_{SC}$, (e) *PCE*, and (f) *FF* over the deposition area.